Neutron diffraction studies of perdeuterated urate oxidase complexes

McGregor, Lindsay

Awarding institution:
King's College London

KING'S COLLEGE LONDON

DOCTORAL THESIS

Neutron diffraction studies of perdeuterated urate oxidase complexes

---

Author:
Lindsay MCGREGOR

Supervisor:
Prof. Roberto A. STEINER
Dr. Matthew P. BLAKELEY

A thesis submitted in fulfillment of the requirements
for the degree of Doctor of Philosophy

in the

Steiner Research Group
Randall Centre for Cell and Molecular Biophysics

Abstract

Urate Oxidase (UOX) is the archetypal cofactor-free oxidase and has been the subject of several biochemical studies over the last 70 years. This enzyme plays a role in purine recycling, facilitating the O_2-mediated degradation of uric acid to 5-hydroxyisourate. The latter compound is then further degraded to the more soluble allantoin. However, there are significant thermodynamic and kinetic barriers associated with O_2-activation, and it is not yet completely understood how UOX is able to function in the absence of a redox-active metal or organic cofactor.

The main aim of this PhD project was to advance our mechanistic understanding of UOX catalysis by investigating the structure of UOX complexes using neutron macromolecular crystallography (NMX). Compared to the more popular technique of X-ray crystallography (MX), the main strength of NMX is that it allows the direct visualization of hydrogen atoms (typically in the form of deuterium atoms). As a correct understanding of enzymatic catalysis often relies on the proper identification of protonation states at different stages of the reaction, NMX is a very valuable tool in mechanistic enzymology studies.

This thesis is divided in six chapters. In the introductory Chapter 1, the subject of O_2 reactions in biology is presented, with reference to the challenges associated with O_2 activation. A historical overview of the current literature available on UOX is provided, including its clinical relevance, in addition to its structural and kinetic studies. Finally, the remaining mechanistic challenges associated with UOX are discussed. Chapter 2 briefly describes the main methodologies used in this work. In Chapter 3, I present the recombinant production, purification, and characterisation of perdeuterated UOX (DUOX) that was employed for all NMX/MX experiments described in this thesis. As the use of a perdeuterated sample presents significant advantages over the use of a H/D-exchanged one in terms of NMX data quality and maps interpretation, such an approach is a substantial improvement over previous NMX studies carried out on UOX by other authors. The joint NMX/MX refinement of the room-temperature complex between DUOX and the inhibitor 8-azaxanthine (AZA) is described in Chapter 4. This structure determines the

protonation states of the proposed catalytic triad, Thr57*-Lys10*-His256, and the relationships between this triad and the active site solvent network are determined.

In Chapter 5, I present the room-temperature NMX structure of DUOX in complex with 9-methyl-5-peroxyisourate (5-PMUA). The latter compound is trapped in the active site after co-crystallisation of DUOX with 9-methyl uric acid (9-MUA) under aerobic conditions, allowing the binding of O_2. From this structure, the trapped peroxide species is found to be negatively charged and is stabilized by the hydroxyl group of active site residue Thr57*. In addition, a proton-sharing relationship between residues Lys10* and His256 of the catalytic triad is established.

NMX was employed to obtain information on the protonation states of UOX complexes in two different environments: in the presence of an inhibitor that cannot be oxidised, and the trapped peroxide intermediate. The structures that are presented in this thesis are discussed with reference to the current knowledge of the UOX mechanism of action, and provide an exciting platform for future work into the structure of reactive intermediates in UOX catalysis.

Acknowledgements

Firstly, I would like to thank both of my supervisors, Professor Roberto A. Steiner and Dr Matthew P. Blakeley, for their help throughout this PhD project. I thank the Institut Laue-Langevin (ILL) for their funding and for providing such a fruitful environment for research. Thank you to my colleagues in the Large Scale Structures Group (LSS). I would also like to thank the Life Sciences Group (LSG) at the ILL, for accepting me into their group as one of their own. Thanks go to Professor Trevor Forsyth, Dr Michael Haertlein, and Dr Martine Moulin for participation in the deuteration labelling collaboration. Trevor, for always being supportive and willing to offer advice when I needed it. Martine, I will be eternally grateful for all that you have taught me over the years. Your patience and kindness, both in the lab and in our office, has always been appreciated. To all other past and present members of the LSG, thank you for creating a welcoming and helpful working environment, and for all of your help professionally and personally.

I would also like to thank the people who have contributed to my research in various ways. Thank you to Dr Nicolas Coquelle, ILL, for advice with my NMX studies. Thank you to Dr Jean-Luc Ferrer, from the ESRF, for his help with X-ray data collection and analysis, and Dr Matthew Bowler, from the EMBL, for also helping with data analysis. Thank you to the HTX Platform at the EMBL, from which the Thermofluor Assay results were obtained. Thank you to Dr Luca Signor, IBS, who conducted the Mass Spectrometry measurements and helped with the interpretation of the data.

On a personal note, I would also like to extend my gratitude to Dr Olivier Detante and the staff at the Neurology Department at CHU, Grenoble. Without their care the completion of this thesis would not have been possible. I would like to say thank you to all of my friends both in Grenoble and the UK who have been there for me over the last few years. All your visits and phonecalls have been invaluable to me and won't be forgotten. I would like to thank Dr Stuart Fisher for his time spent sorting through my thesis and for being a pillar of support to me during these interesting times, it will always be appreciated. Finally, I would like to say thank you to my parents Alison and Andrew, my brother Grant, and my grandparents, Celia and Peter, for all of your love and support that has been unwavering throughout this process. Any achievement that has come from this is because of you.

Contents

List of Figures

List of Tables

List of Abbreviations

5-HIU	5-hydroxyisourate
5-PIU	5-(hydro)peroxyisourate
8-HX	8-hydroxyxanthine
9-MUA	9-methyl uric acid
9-PMUA	9-methyl-5-peroxyisourate
ADP	Atomic Displacement Parameter
AI	After Induction
ASP	Ammonium Sulfate Precipitation
AZA	8-azaxanthine
BI	Before Induction
CCP4	Collaborative Computing Project 4
DEAE	Diethylaminoethyl
DHU	Dehydrourate
DLAB	Deuteration Laboratory
DNA	deoxyribonucleic acid
DSC	Differential Scanning Calorimetry
DSF	Differential Scanning Fluorimetry
DUOX	Perdeuterated Urate Oxidase
EPR	Electron Paramagnetic Resonance Spectroscopy
ESI-TOF	Electrospray Ionisation Time-Of-Flight
ESRF	European Synchrotron Radiation Facility
GF	Gel Filtration

HCDC	High Cell Density Cultures
HIC	Hydrophobic Interaction Chromatography
HOD	1-H-3-hydroxy-4-oxoquinaldine, 2,4-dioxygenase
HOMO	Highest Occupied Molecular Orbital
HUOX	Hydrogenated Urate Oxidase
IEC	Ion Exchange Chromatography
ILL	Institut Laue-Langevin
IPTG	isopropyl θ-D-1-thiogalatopyranoside
kan^R	kanamycin
LADI-III	Laue Diffractometer
LO	Lipoxygenases
LB	Luria Broth (Lysogeny Broth)
MAD	Multi-wavelength Anomalous Dispersion
MALDI-TOF	Matrix-Assisted Laser Desorption Ionization Time-Of-Flight
MW	Molecular Weight
MWCO	Molecular Weight Cutoff
NHE	Normal Hydrogen Electrode
NIP	Neutron Image Plate
NMX	Neutron Marcromolecular Crystallography
neutron density maps	neutron scattering length density maps
OD_{600}	Optical Density at 600 nm
O/N	overnight
P	Pellet
PDB	Protein Data Bank
PEG	Polyethylene Glycol
pI	Isoelectric Point
PRS	Proton Relay System
QOD	1-H-3-hydroxy-4-oxoquinoline, 2,4-dioxygenase
r.m.s.	root mean square

RNA	ribonucleic acid
ROS	Reactive Oxygen Species
RPM	Revolutions Per Minute
SAD	Single-wavelength Anomalous Dispersion
SDS-PAGE	sodium dodecyl sulfate-polyacrylamide gel electrophoresis
SN	Supernatant
SOC	Super Optimal broth with Catabolite repression
TcmH	Tetracenomycin-F1 monooxygenase
TLS	Tumor Lysis Syndrome
T_m	melting temperature
Tris	Tris(hydroxymethyl)aminomethane
TSA	Thermal Shift Assay
UA	Uric Acid
UOX	Urate Oxidase
WT	Wild Type
XO	Xanthine Oxidase

Declaration: In this thesis the term 'hydrogen' refers to the ^{1}H isotope, whereas 'deuterium' refers to the ^{2}H isotope (or D). Throughout this thesis, the term protonation state refers to the presence of either ^{1}H/^{2}H isotope attached to a heavy atom (C, N, O, S). When describing an atom or residue as unprotonated, this indicates an absence of either an ^{1}H/^{2}H atom. The term 'proton' specifically refers to the ^{1}H isotope, whereas to describe the ^{2}H isotope the term 'deuterated' is used, for clarity. A 'hydrogen bond' describes the interaction between either ^{1}H/^{2}H and the atom acting as a hydrogen bond acceptor (O, N, S).

For my parents

Chapter 1

Introduction

Abstract

The focus of this research project is the archetypal cofactor-free enzyme Urate Oxidase (UOX). This chapter introduces the topic of O_2-reacting enzymes, covering typical methods of O_2 activation. The role of UOX in biology is discussed with particular attention to the gene silencing event which caused its absence in humans, and subsequent clinical implications. A comprehensive review of the structural and functional studies of UOX is also conducted, addressing current mechanistic theories and further challenges. Finally, the aim and motivation for this thesis is presented, with reference to techniques employed during this research.

1.1 Oxygen-Reacting Enzymes

The oxidoreductases are a large family of enzymes that catalyse the transfer of electrons from an electron donor, or reductant, to an electron acceptor, or oxidant. Two important subclasses of oxidoreductases are the oxidases and the oxygenases. Molecular oxygen (O_2) is a vital reactant in these enzymatic reactions. Oxidase enzymes react with O_2 acting as the oxidant, reducing it by two or four electrons to either H_2O_2 or H_2O. Any oxygen atoms incorporated into the reaction product are commonly taken from the surrounding solvent, not from the O_2 molecule directly. Oxygenases operate differently by incorporating the atoms of O_2 into the structure of the organic product. Whether one or two of the O_2 atoms are bonded to the product of the reaction determines whether the enzyme is a monooxygenase or a dioxygenase [1].

Molecular oxygen is classed as an electrophile, and has the ability to accept electrons as it contains vacant orbitals. In fact, the ground state of O_2, the most abundant form, contains two unpaired electrons in the Highest Occupied Molecular Orbital (HOMO), as shown in the molecular orbital diagram in Figure 1.1. These two electrons are of the same spin state giving a total spin of $S = 1$, therefore the spin state is a 'triplet' denoted by $^3O_2$: this is considered a stable diradical. In comparison, an excited state of O_2 that contains paired electrons in the HOMO and is considered a 'singlet' species $^1O_2$, shown in Figure 1.1.

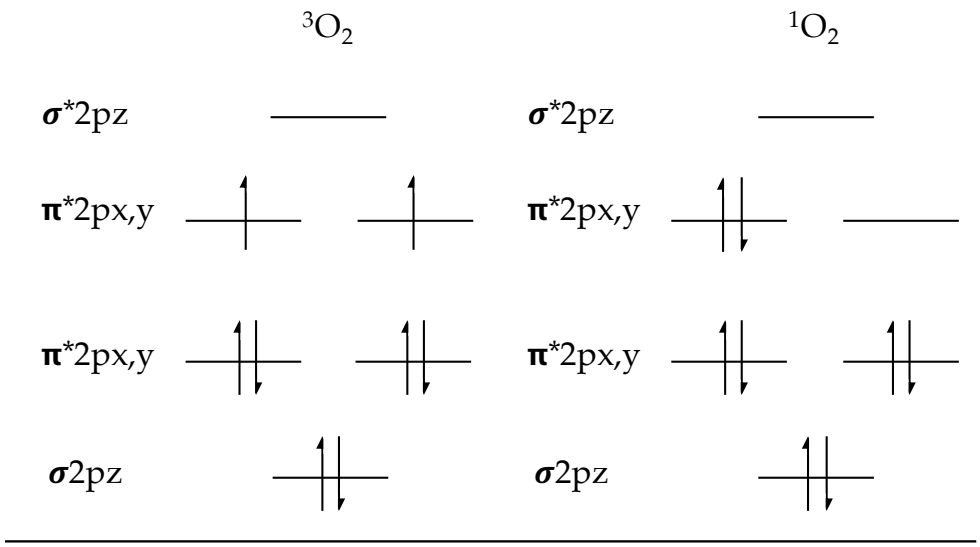

FIGURE 1.1: Molecular orbital diagrams for triplet ($^3O_2$) and singlet ($^1O_2$) dioxygen. Triplet O_2 has two unpaired electrons in the HOMO whereas singlet O_2 has one pair. Adapted from [2] with permission from Elsevier.

The standard reduction potential E^0 for the O_2/H_2O redox couple at pH 7 is + 0.815 V [3], indicating that O_2 has the potential to be a strong oxidising agent. The overall reduction reaction of O_2 is shown in Equation 1.1.

$$O_2 + 4H^+ + 4e^- \rightarrow 2H_2O \tag{1.1}$$

However, the reduction of O_2 to H_2O does not occur with a concurrent four-electron transfer, instead four one-electron reactions typically occur. The details of these four one-electron reactions are given in Figure 1.2. The first reduction occurs as O_2, a stable diradical triplet species, accepts an electron to form superoxide O_2^- or HO-O$^\cdot$, a radical doublet species. The second reduction results in the formation of hydrogen peroxide H_2O_2. This is followed by two further one electron transfers: the formation of a hydroxyl radical OH$^\cdot$ and one water molecule H_2O, finally, the termination of the reaction with an electron transfer resulting in a total of two water molecules [4]. The associated reduction potentials for each one- and two-electron reactions at pH 7.25 are shown in Table 1.1.

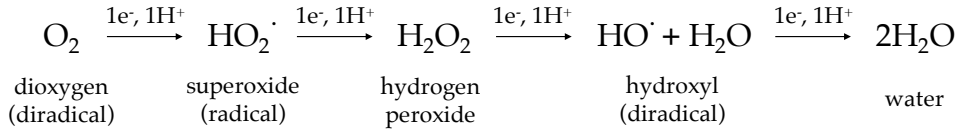

FIGURE 1.2: The reduction of O_2 to H_2O via a four stage electron transfer [4].

TABLE 1.1: Standard reduction potentials of one- and two-electron reduction of O_2 species in water. *NHE: normal hydrogen electrode. Values taken from [5]

										E^0 vs. NHE, pH 7.25
		O_2	+	e^-	→	O_2^-				- 0.33 V
O_2^-	+	e^-	+	$2H^+$	→	H_2O_2				+ 0.89 V
H_2O_2	+	e^-	+	H^+	→	$OH^·$	+	H_2O		+ 0.38 V
$OH^·$	+	e^-	+	H^+	→	H_2O				+ 2.31 V

Although the reaction between O_2 and organic molecules is both exothermic and thermodynamically favourable, it is not kinetically favourable due to a significant activation barrier to the reaction [3]. There are two factors that are considered responsible for this kinetic inertness and are related to the electronic structure of O_2. As shown in Table 1.1, all but one of the O_2 reduction reactions are thermodynamically favourable: the primary electron transfer to O_2 resulting in superoxide O_2^- has a reduction potential of - 0.33 V. This one electron transfer is considered thermodynamically unfavourable and, therefore, O_2 is the kinetically favoured molecule [6].

An additional restriction is due to the difference in spin states of O_2 and organic molecules. Organic molecules typically exist in a singlet state with no unpaired electrons, whereas ground state O_2 exists as a triplet, with two unpaired electrons [7]. The selection rule, or transition rule, stipulates that angular momentum must be conserved during a reaction. Therefore, a reaction between triplet state O_2 and

singlet state organic molecules to form singlet state products is considered 'spin forbidden'. The O_2 molecule itself can be excited to a singlet state, meaning the reaction with singlet organic molecules would be 'spin allowed'. The molecular orbital diagram of this O_2 species, showing the paired electronic structure, is shown in Figure 1.1. However, this reaction requires a high activation energy as the lowest energy singlet state of O_2 is 22.5 kcal/mol higher than energy than ground state triplet O_2 [2].

These kinetic restrictions result in the ability to closely control the reaction of O_2 with organic molecules in aerobic environments. As a result, O_2 can coexist with a variety of reducing agents inside living cells without reacting with them. This is considered crucial in biology as it prevents random O_2 reactions that may result in the destruction of essential components of the living cell [6, 7].

The barrier to the reactivity of O_2 with organic molecules is unfavourable, but reactions can occur. The oxidising ability of O_2 can be accessed by the presence of a suitability powerful reducing agent [6]. Such reducing agents capable of reducing O_2 include metal centres and organic cofactors, and are widely used in O_2-dependant reactions. These moieties can assist in the activation of either O_2 or the organic substrate directly.

Redox-active metal centres are commonly present in O_2-reacting enzymes, containing iron, molybdenum, or copper. There are three main ways that transition metals with unpaired electrons can activate O_2 for spin allowed reactions: orbital overlap, single electron transfer, and reaction with a substrate radical [2].

Orbital-orbital overlap can occur between O_2 and a transition metal ion when there are unpaired 3d electrons on the metal. The π^* orbitals of the complexed O_2 are able to overlap with those of the metal ion, creating a singlet species. This is then able to react with organic material in the singlet state as the reaction is 'spin-allowed', providing the overall number of electrons in the complex remains constant [2, 8].

When the protein contains a redox-active metal that has multiple oxidation states, such as Fe (II/III), a single electron transfer can occur to bound O_2, reducing it to form superoxide, O_2^-. The formation of a superoxide radical has an unfavourable activation potential (Table 1.1), however, superoxide can participate in further one- or two-electron transfer reactions favourably. Although this reaction is energetically unfavourable, the environment surrounding the O_2 binding site can favour the formation of superoxide through stabilisation interactions. These stabilisation effects have been noted in other enzymes. For example, in the case of myeloperoxidase, the enzymatic activity is highest at low pH, resulting in a protonated histidine residue located at the active site. It is suggested that this histidine is involved in the stabilisation of the superoxide bound to the heme centre [9]. Alternatively, enzymes may control the active site environment to stabilise either the oxidised or reduced form of the metal centre [10].

The reaction of O_2 with a substrate radical is also a method of activation, seen in ferric substrate-activating enzymes including lipoxygenases (LO) [11]. The oxidised metal centre in LO enzymes catalyses a hydrogen abstraction from the substrate to form a substrate radical. This facilitates the reaction of the substrate radical with O_2 as it is now a spin allowed process [2].

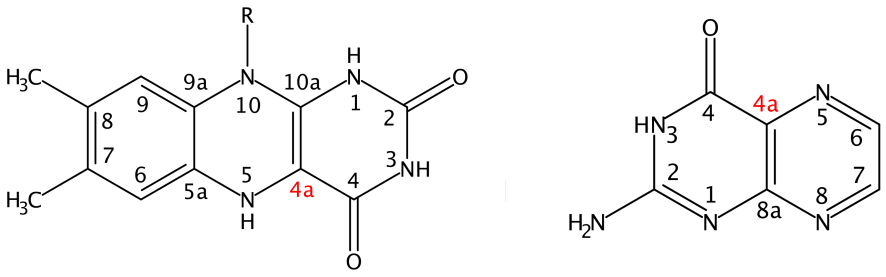

Flavin **Pterin**

FIGURE 1.3: Basic structures of the Flavin and Pterin cofactors that can be present in enzymes to facilitate the reaction of an organic substrate and O_2.

Conjugated organic cofactors that are able to form a stable radical intermediate

are also able to facilitate the transfer of electrons to O_2. Common organic moieties include Flavins and Pterins: a structural representation of these are shown in Figure 1.3. The ability of reduced Flavins and Pterins to delocalise and stabilise unpaired electrons is thought to be important in their reactions with O_2 [12].

The Flavin moiety acts as a redox cofactor, which is capable of existing in either a one- or two- electron reduced state [13]. These electrons can be received from a reduced substrate before delivering them to an electron acceptor. In this case, O_2 can be employed as an electron acceptor from a reduced Flavin, commonly resulting in the generation of H_2O_2. The general reaction of Flavin-containing enzymes with O_2 is that a one electron transfer occurs between the cofactor moiety and O_2, generating a radical pair consisting of the Flavin semiquinone and a superoxide molecule [14, 15]. This reaction circumvents the spin-forbidden aspect similarly to when there is a transition metal containing multiple oxidation states, described previously. This radical pair can result in a recombination reaction and the formation of a covalent adduct between the C4a position on the Flavin ring and O_2, generating a reactive C4a-(hydro)peroxide species [14]. The protonation state of this (hydro)peroxyflavin intermediate determines if the reaction is an electrophilic or nucleophilic attack [16, 17]. The formation of a C4a-(hydro)peroxyflavin intermediate is thought to be central to the mechanism seen in many Flavin monooxygenases, involved in reactions such as Baeyer-Villiger oxidations, hydroxylations, and epoxidations [17]. This C4a-(hydro)peroxyflavin intermediate has been well characterised via spectroscopic studies [14, 18, 19], however it has not been visualised structurally. A schematic describing the reaction of a Flavin cofactor with O_2 to form a C4a-(hydro)peroxyflavin intermediate before the expulsion of H_2O_2, commonly seen in Flavin-dependant monooxygenases, is shown in Figure 1.4 [2].

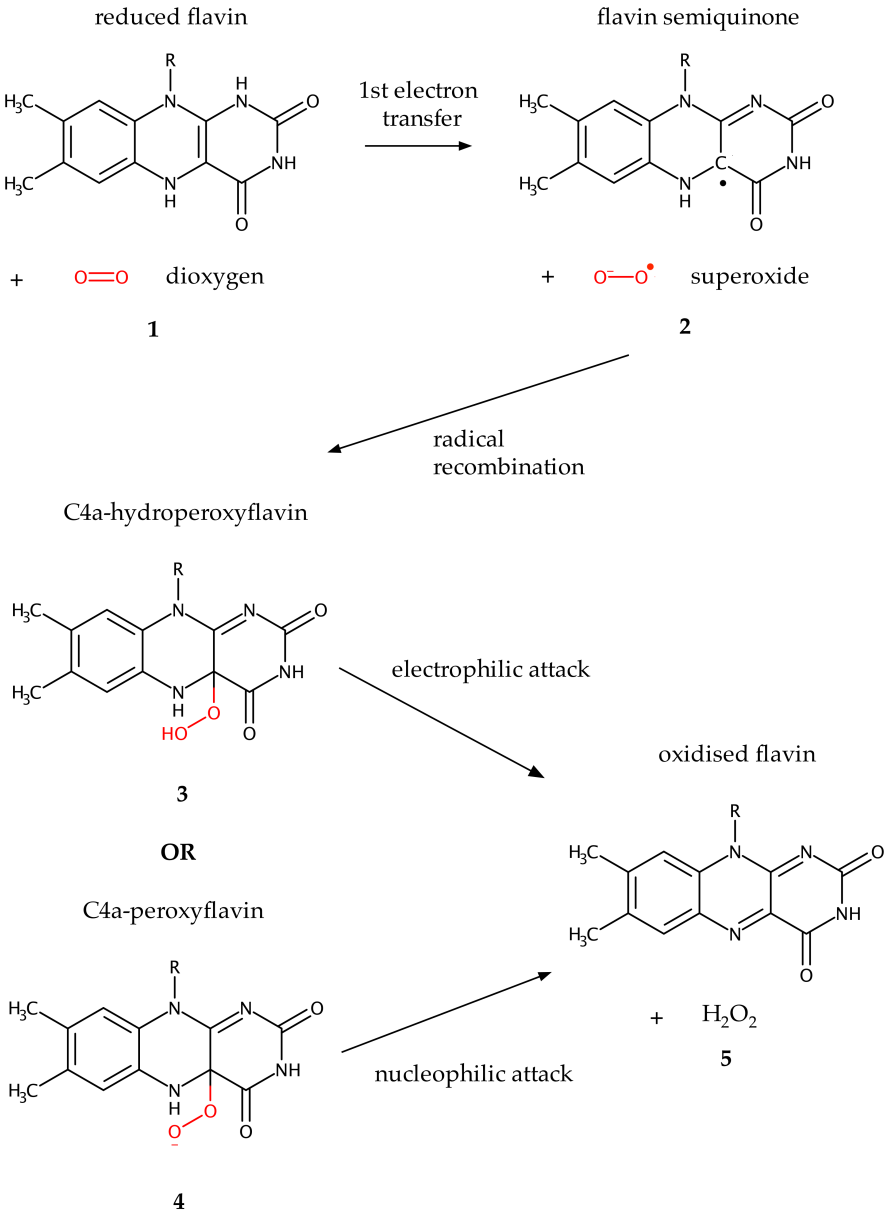

FIGURE 1.4: The activation of O_2 by electron transfer from a Flavin moiety, seen in Flavin-dependent monooxygenases. The reduced Flavin residue transfers an electron to an O_2 molecule (1) creating a Flavin semiquinone radical and superoxide (2). The pair then undergoes a radical recombination reaction to form a C4a-hydroperoxyflavin intermediate (3) or C4a-peroxyflavin intermediate (5). This flavin-oxygen adduct then breaks down to form oxidised Flavin and hydrogen peroxide (5). Adapted from [2] with permission from Elsevier.

Pterin-containing enzymes also commonly participate in enzymatic reactions involving O_2. Their basic structure and ability to delocalize and stabilise an unpaired electron is similar to that of Flavin moieties, shown in Figure 1.3 [14]. Less is understood about the intermediate structures of Pterin reactions, however, several Pterin-containing ezymes, such as phenylalanine hydroxylase, are thought to proceed through a similar C4a-intermediate as seen in Figure 1.4 [20, 21].

Interestingly, there are O_2-dependant enzymes that contain no metal centre or cofactor [3, 22]. The mechanism by which these enzymes are able to circumvent the selection rule is still not fully understood. It has been suggested that the reaction of a carbanion and O_2 is mechanistically possible if a stable radical can be accessed. However, there is little structural evidence to validate these claims.

1.2 Urate Oxidase

Purines are essential small molecules used as building blocks in DNA and RNA [23]. Many enzymes are involved in maintaining a balance of purines by promoting their synthesis or degradation [24]. Purine catabolism can also be referred to as a 'salvage pathway', where nucleotides are synthesised from intermediates from the degradation of other nucleotides.

A reaction scheme describing the breakdown of purine molecules to allantoin is described in Figure 1.5. Enzymes involved in this pathway include Xanthine Oxidase (XO) and Urate Oxidase (UOX). The final product of this pathway in humans is UA. This is explained in more detail in Section 1.2.1.

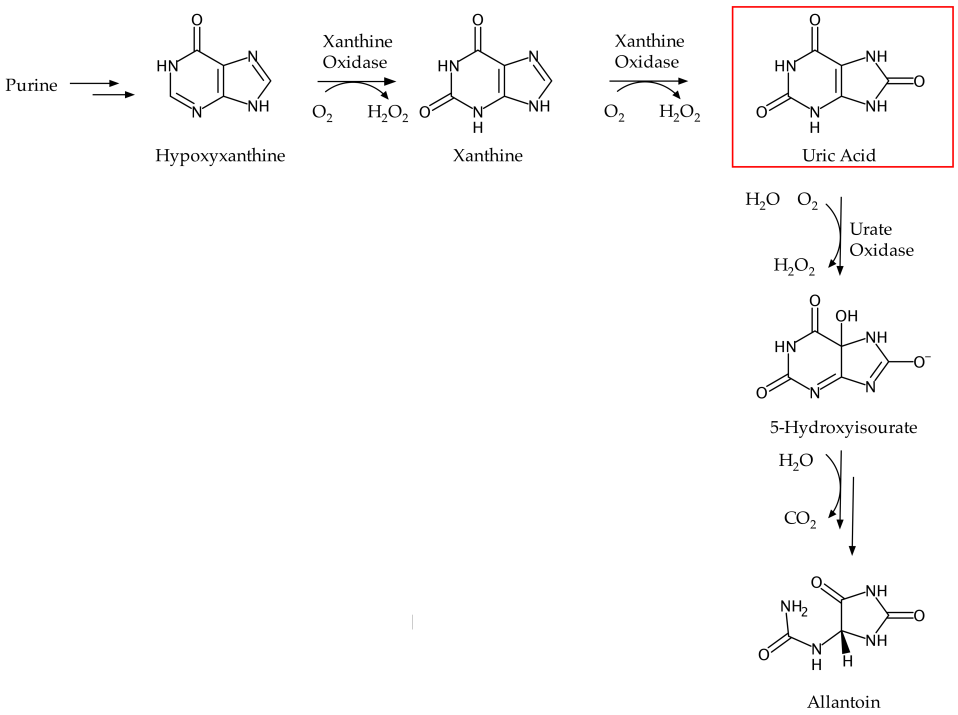

FIGURE 1.5: Reaction scheme describing the breakdown of purine molecules to Allantoin. Enzymes such as Xanthine Oxidase and Urate Oxidase participate in this salvage pathway. In the case of humans the final product is Uric Acid (highlighted in the red box).

UOX is a peroxisomal cofactor-free oxidase that participates in this purine degradation pathway. It is responsible for the enzymatic catalysis of UA to 5-hydroxyisourate (5-HIU), reacting with O_2 and producing hydrogen peroxide (H_2O_2) as a by-product.

1.2.1 Gene Silencing Event

UOX is found in all three domains of life: Archaea, Bacteria and Eukarya. However, in humans, certain primates, birds, and reptiles, the gene encoding for UOX is silenced [25, 26]. As a result, the final product of the purine degradation pathway is UA. Due to its presence in both prokaryotes and eukaryotes it is clear that UOX is of ancient origin [27]. As other primates have retained the production of

UOX, this gene silencing is assumed to have happened during the period of primate evolution, in a hominoid ancestor after divergence from Old World Monkeys [28, 29].

The loss of UOX activity has been shown to be due to nonsense mutations [30, 31], however, exactly how and why this happened is still not fully understood. Several mutations have been identified in the human UOX gene that may be relevant to the inactivation of this enzyme. Two nonsense mutations, at positions 33 and 187 coding for arginine, have been identified as premature stop codons [30], with the mutation at position 33 suggested as the primary cause of UOX silencing in humans [27].

It has been suggested that the gene silencing event was a multistep process: some monkeys have retained a lower level of UOX production, implying a gradual reduction [28, 32–35]. This is supported by a study that found blocking UOX activity in mice resulted in fatality: attributed to the inability of the mice to manage the sudden increase in UA [36]. In addition, the examination of ancestral UOXs provided evidence that the enzymatic activity had decreased gradually, via stepwise mutations [30, 35]. There are two suggestions for the systematic removal of UOX. One suggestion is that ancient apes slowly decreased the transcription of UOX via mutations in the UOX promoter before the pseudogenisation events [27, 35]. Alternatively, a reduction in UOX activity before pseudogenisation would also prevent the sudden increase in UA [35, 37]. This may be considered a more robust method for abolishing UOX activity in comparison to genetic mutations, which may result in compensatory changes that would up-regulate UOX expression [35].

An increase in UA is argued to be the main benefit of UOX silencing due to its free radical scavenging activity and reducing the likelihood of age-related cancers [33]. In addition, the loss of UOX may have had a 'survival advantage' at the time of silencing, relating to the change in diet of our ancestors [35]. Contrasting the other proposals, it was suggested that the loss of UOX activity in humans occurred

through a single mutation event [29, 30]. Furthermore, it has been postulated that this event and silencing of UOX was accidental, and the resultant side effects such as gout and hyperucemia are unwanted [25]. Nevertheless, the absence of UOX in humans, and the resultant increase in UA, have clinical implications.

1.2.2 Importance and Clinical Implications

Oxidative stress is a result of chemical and biological reactions that produce unwanted by-products and side effects. Free radicals are unstable molecules that can cause damage to other molecules and are usually by-products of essential cell processes or metabolism. For example, the metabolism of O_2 generates $^{\cdot}OH$, $O_2^{\cdot -}$ and H_2O_2 [38]. These Reactive Oxygen Species (ROS) have implications in neurodegenarative diseases, cancers, and ageing [38, 39].

Free radical scavengers, or antioxidants, are molecules that can react with unstable free radicals and convert them to stable, unreactive, and less harmful compounds. One such important antioxidant and free radical scavenger is uric acid (UA) [33, 40]. As previously described in Section 1.2.1, the UOX gene silencing event has resulted in an increased concentration of UA in humans. As a result the level of UA in the blood is typically fifty times higher than in other mammals [25]. Excess UA that is accumulated due to the lack of UOX is excreted in urine.

Specifically, UA is found in the plasma, where it is responsible for around two thirds of radical scavenging activity [41]. It has been found to be effective both *in vitro* and *in vivo* [33, 42, 43], and shown to scavenge both hydroxyl radicals [44] and oxo-heme oxidants [33, 44]. In particular, it is efficient at scavenging peroxynitrite ($ONOO^-$) in the presence of ascorbic acid and thiols [45–47]. Peroxynitrite can disrupt cell signalling pathways and react with lipids, DNA, and proteins. The essential role of UA is supported by the fact that neither ascorbic acid or thiols can

prevent the reactions of peroxynitrite alone. This UA radical scavenging pathway is shown in Figure 1.6 [47].

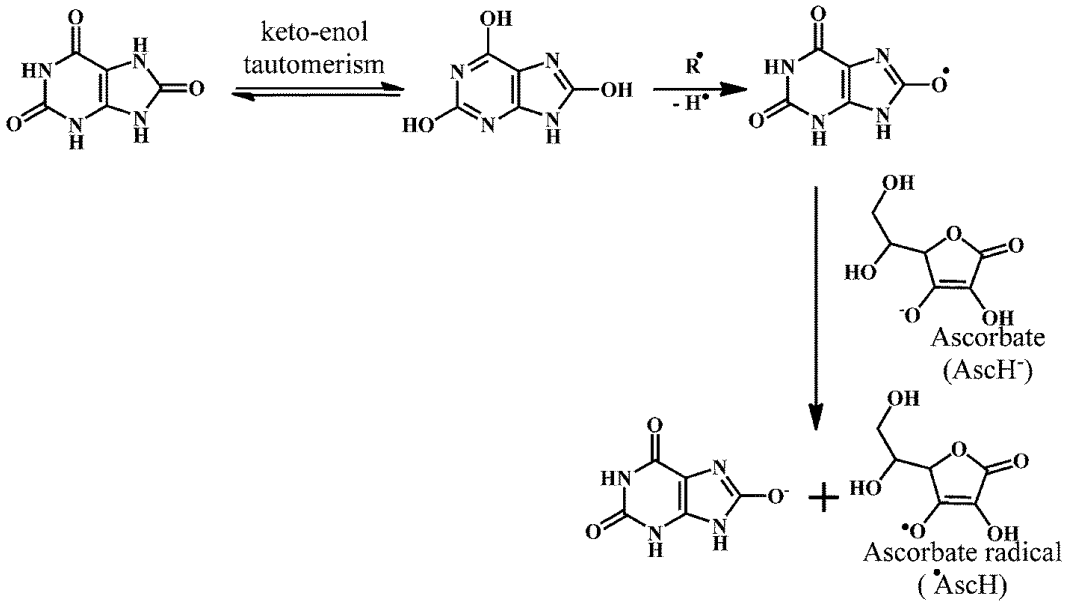

FIGURE 1.6: The free radical scavenging mechanism of uric acid (UA) in conjunction with ascorbic acid. Figure taken from [47], published by The Royal Society of Chemistry.

Although this has the possible evolutionary benefits discussed previously, there are a number of side effects that can have serious, even fatal, consequences when UA concentration is high.

Gout is an painful inflammatory disease that results from the accumulation of monosodium urate crystals in joints [48, 49]. This can be caused by the body over-producing large quantities of UA, or a build up of UA resulting from the failure of the kidneys to maintain physiological concentrations by UA excretion. It is important to note that the overproduction of UA is responsible for $\sim$ 10% of cases of gout whereas 90% of cases are as a result of problems with renal excretion [49]. Although there is no cure for gout, there are therapies that reduce the concentration of UA and minimise long term damage [48].

Tumor Lysis Syndrome (TLS) is an unwanted side effect of chemotherapy treatment. When the tumor cells are killed or lysed, the cells contents are released into the bloodstream [50]. The contents include metabolites that are converted to, amongst other compounds, UA. When the accumulation of UA occurs faster than the body is able to excrete, complications such as hyperucemia, and the deposition of UA crystals in the kidneys, can lead to renal failure [51].

Hyperuricemia, hypertension, renal, and cardiovascular diseases have all been found to be related to UA excess. There are several treatments available in order to combat these medical issues. A recombinant form of UOX, produced by a genetically modified strain of *Saccharomyces cerevisiae* with the cDNA cloned from a strain of *Aspergillus flavus* is commercially available as Rasburicase, Fasturtec, or Elitek by Sanofi [52–54]. It acts by catalysing UA to soluble allantoin, which can be rapidly excreted without interfering with any other step in the purine degradation process. However, in terms of typical therapy, it is more common to inhibit the conversion of xanthine to UA than to breakdown the accumulated product, using drugs such as allopurinol [55].

1.2.3 UOX and T-Fold Enzymes

A variety of enzymes of independent origin have been found to play a role in UA oxidation, however, this thesis will focus specifically on UOX. The most prevalent form of UOX in Gram-negative bacteria has been shown to contain an integral membrane cytochrome c [37, 56], in addition to two distinct Flavoenzymes [37, 57, 58]. However in eukaryotes, as well as some bacteria such as *B. subtilis*, UOX has been found to be cofactor-free [37, 59].

UOX was initially considered a copper-containing enzyme due to the presence of a type 2 binding motif, commonly found in other copper-binding proteins [30, 60]. However, UOX from yeast [61], and fungi [62] have been found to be copper-free.

The UOX found in soyabean root nodules was also examined and found to only contain trace quantities of copper [63]. Additionally, MALDI-TOF mass spectrometry measurements showed the absence of any organic cofactor [64]. The first X-ray structure was taken from *Aspergillus flavus* UOX and published by Colloch *et al.* [65]. This structure was able to unambiguously determine the absence of any additional metal centre or cofactor present in the enzyme, confirming UOX as a cofactorless enzyme in *Aspergillus flavus* [65]. This study was also the first to present cofactor-free UOX as a member of the tunnelling-fold (T-fold) superfamily.

The T-fold tetrameric structure is found in multimeric proteins crossed by a channel, forming a 'T' shape. It consists of an antiparallel β-sheet of four sequential strands, sandwiching two antiparallel α-helices between the second and third strands and is denoted by the topology $\beta\beta\alpha\alpha\beta\beta$ [65–67]. Multiple T-fold motifs assemble to form a $\beta_{(2n)}\alpha_{(n)}$ barrel, providing an efficient scaffold for building large multimeric proteins.

Each UOX monomer contains two successive T-fold domains of 137 and 164 residues in length, shown in Figure 1.7 (a). The topology of the two domains is identical and the sequence similarity is 52.3%, however, the sequence identity is low, 8.3% [66]. Two monomers associate to form a dimer related by a two-fold axis, with the active site located at the interface, this is shown in Figure 1.7 (b) [65]. UOX is functionally active as a tetramer, binding a total of four substrate molecules: one at each dimer interface. The barrel-shaped quaternary structure of UOX is shown in Figure 1.7 (c) and (d). The PDB used in Figure 1.7 was one of the first *Aspergillus flavus* UOX structures to be published (1R51): the deposition by Colloch *et al.* is no longer available in the PDB (1UOX) [65, 68].

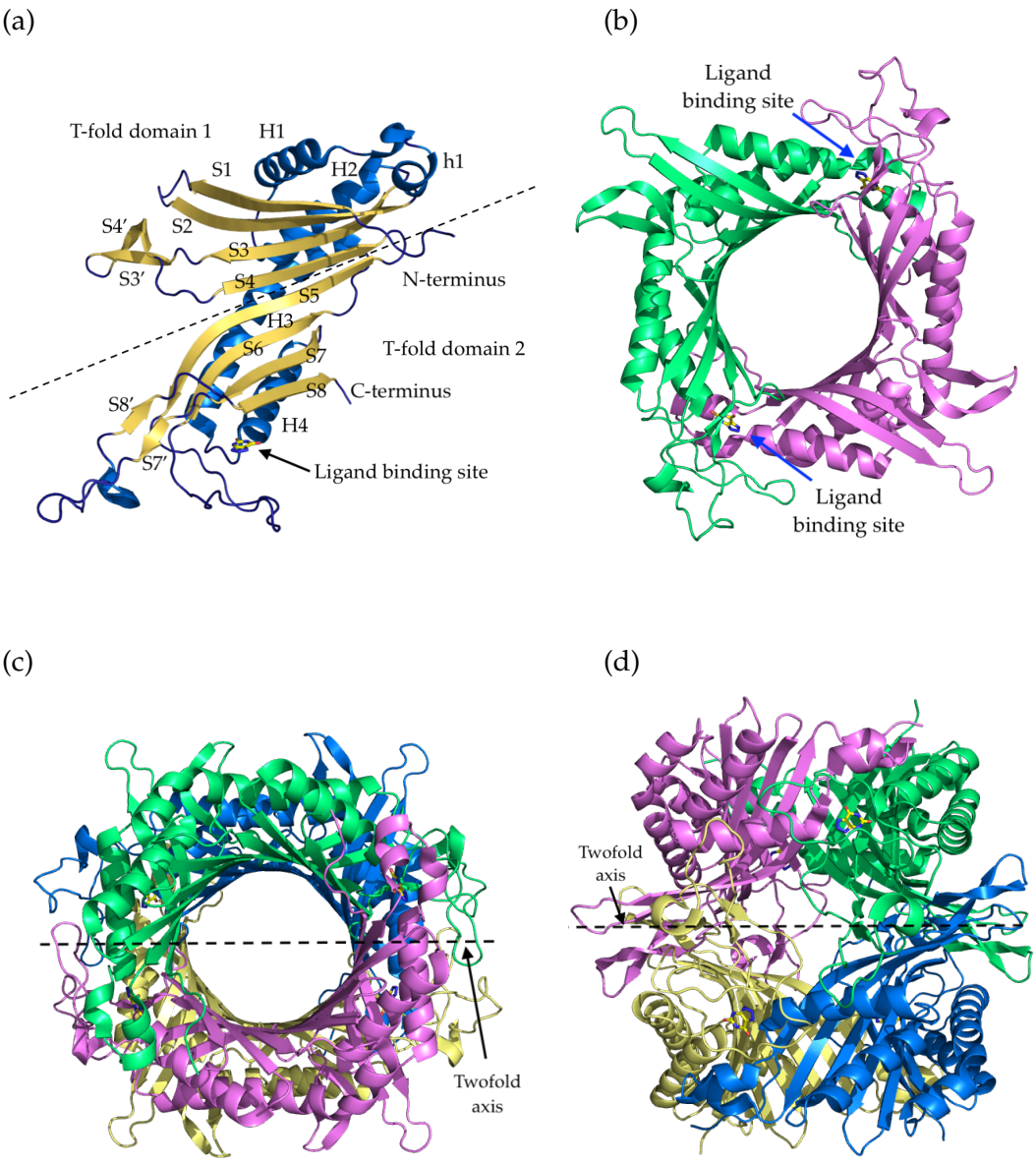

FIGURE 1.7: The overall structure of *Aspergillus flavus* Urate Oxidase (UOX) bound to inhibitor 8-azaxanthine (AZA) in PDB entry 1R51 [68]. (a) A monomer of *Af*UOX contains two successive T-folds: the dotted line shows the separation of the domains. H and S are used to represent α-helices in yellow and β-strands in blue, respectively. (b) The ligand binding site is located at the interface between two dimers. (c) The tetramer of functional UOX enzyme, forming a barrel structure with the twofold axis shown by a dotted line. (d) 90° rotation of the tetramer.

Superfamilies can have high structural similarities but vary widely in terms of function. There are currently a total of five enzymes that have been identified as possessing a T-fold structure. The list includes GTP cyclohydrolase I 10, 6-pyruvol tetrahydropterin synthase, 7,8-dihydroneopterinn aldolase and 7,8-dihydroneopterin triphosphase epimerase, in addition to UOX [66]. Enzymatic function ranges from the biosynthesis of folate and pteridines to purine degradation [69].

A common feature of T-fold enzymes is that all substrate molecules contain pyrimidine or purine rings. In addition, all ligand binding pockets are located in a deep and narrow channel at the interface between monomers, typical for the binding of small molecule substrates [66]. Another feature found in T-fold-containing enzymes is the presence of topohydrophobic regions, where sequences contain a series of strong hydrophobic residues (Val, Ile, Leu, Phe, Met, Tyr, Trp) [70]. This characteristic is seen across all members of the T-fold superfamily [66, 70]. In terms of functionality, the number of monomers required for the structure of active site varies across the superfamily, however, conserved glutamine or glutamate residues are found in the binding sites and are important for anchoring the substrate molecules [66].

T-fold enzymes have been found to have a high structural similarity. In a comparison of UOX with the other enzymes possessing the T-fold motif, it was found that they superimpose with a mean of 1.4 Å root mean square deviation (RMSD) on the common core (aligned on Cα) [66]. However, the enzymes show a wide sequence variation, exhibiting a low level of sequence identity, with a mean of 10.5% along the aligned regions [66]. It has been suggested that all proteins are descended from a limited number of ancestors and through evolution the sequence similarity has diverged, but structural aspects, such as the common fold or functional characteristics, have been retained [66, 71, 72]. This is demonstrated in the currently identified members of the T-fold superfamily where the sequence divergence is high but the T-fold motif and substrate structure show similarities [66].

1.2.4 Structure of the Active Site

In this section, a structural comparison between different UOXs is described, with reference to a sequence alignment. This alignment is used to highlight identical residues seen across a range of UOXs. These identical residues are discussed, with attention given to their role in the active site, and their possible functional capabilities.

A sequence alignment of 10 different UOX sequences with a 30-50% identity is shown in Figure 1.8: the full details of the UOX sequences included are described in Table 1.2. Residues likely to be present across the whole UOX family can be identified from this sample. In total 23 residues are conserved, indicated by a red background. There are 13 residues in close proximity to the active site and they are identified by a yellow star: the relevance of these residues is described below.

TABLE 1.2: Details of Urate Oxidase (UOX) sequences used in the sequence alignment shown in Figure 1.8

SWISS-PROT identifiers	Residues aligned	Organism
URIC_ASPFL	1 - 301	*Aspergillus flavus*
URIC_EMENI	1 - 301	*Emericella nidulans*
URIC_CYBJA	1 -303	*Cyberlindnera jadinii*
URIC_DROME	32 - 352	*Drosophila melanogaster*
URIC_DROVI	26 - 342	*Drosophila virilis*
URIC_MOUSE	1 - 302	*Mus musculus*
URIC_SOYBN	1 - 309	*Glycine max*
URIC_ARATH	1 - 309	*Arabidopsis thaliana*
PUCL_BACSU	181 - 494	*Bacillus subtilis*
PUCL_BACSB	1 - 332	*Bacillus sp.*

The structure of the UOX active site has been extensively investigated, in both the

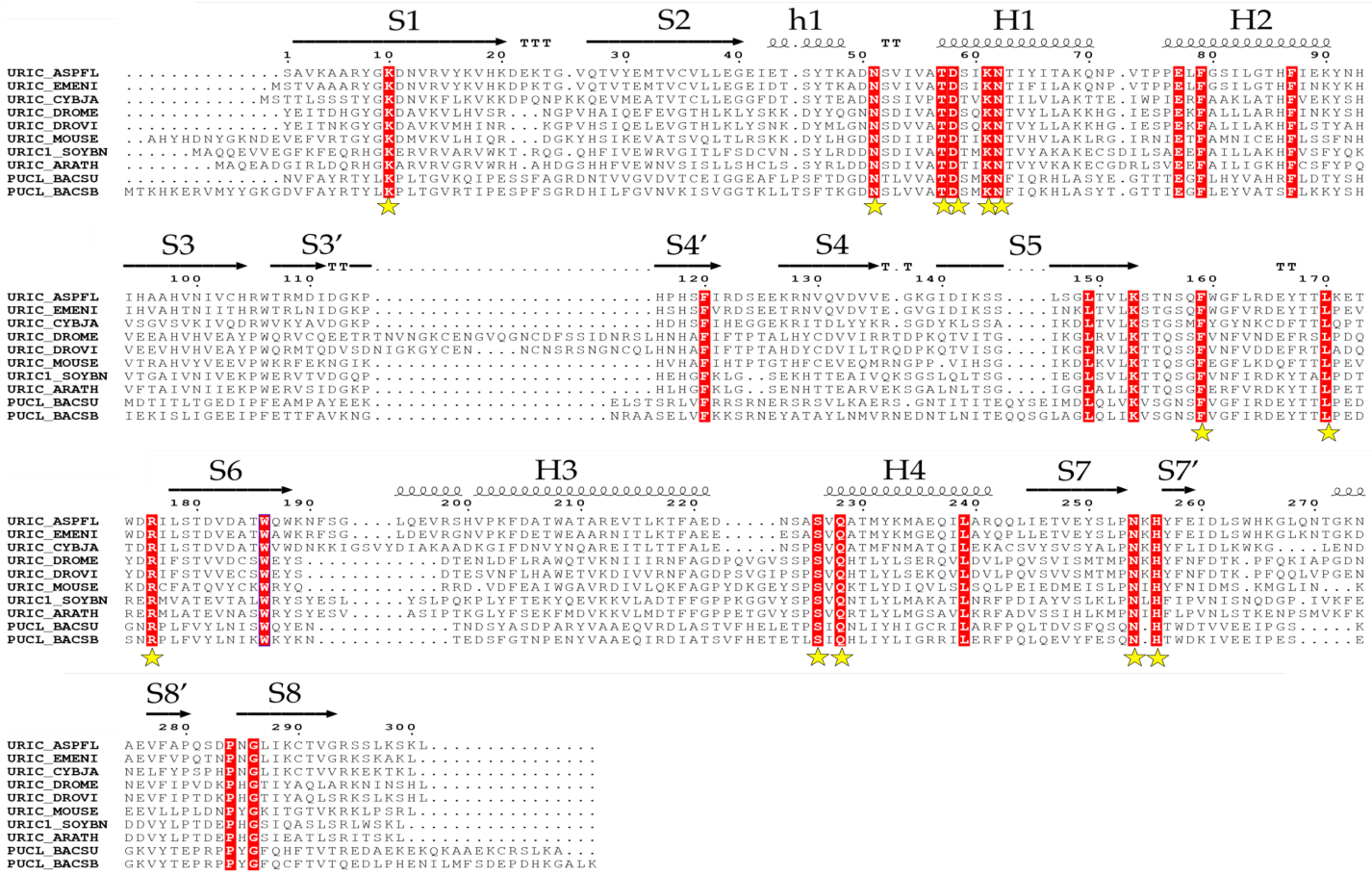

FIGURE 1.8: An alignment of 10 remote sequences of Urate Oxidase (UOX), labelled with their SWISS-PROT identifiers. There are 23 identical residues that are highlighted by a red background. Conserved residues of relevance to the active site are indicated by yellow stars. Residue numbering is in accordance with *A. flavus* UOX and α-helices and β-sheets identities are taken from [65]. Sequence identity and further details can be found in Table 1.2. Figure produced using ESPRIPT [73, 74]

presence and absence of a ligand with > 100 structures deposited in the PDB [75]. The first X-ray crystal structure from Colloch *et al.*, previously discussed in Section 1.2.3, was taken from *Aspergillus flavus* UOX and was able to provide details on the key residues in the active site (PDB entry 1UOX, no longer available). It was crystallised in complex with 8-azaxanthine (AZA) which acts as an inhibitor to the reaction as, unlike UA, it cannot be oxidised and prevents the binding of molecular O_2 [65]. A structural comparison of AZA and UA is shown in Figure 1.9. This allowed the identification of residues surrounding the active site and the interactions with the ligand under aerobic conditions. It is important to note that residues referred to in this chapter follow the *Aspergillus flavus* numbering, for consistency. The * sign is used to denote those residues participating in binding that are present on the neighbouring monomer, and continues throughout this thesis.

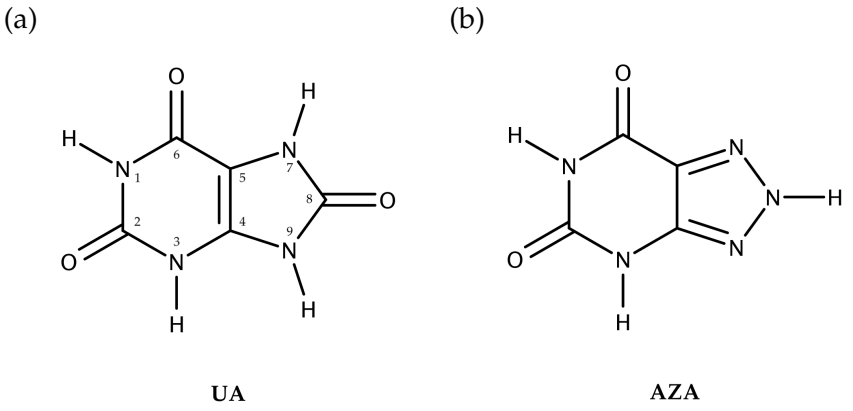

FIGURE 1.9: (a) Structure of the natural substrate uric acid (UA) in comparison with (b) inhibitor molecule 8-azaxanthine (AZA).

However, the initial binding mode of AZA, as seen in the structure by Colloch *et al.* solved to 2.05 Å [65], was corrected in a further X-ray structural study by Retailleau *et al.* at a resolution of 1.80 Å [68]. The substrate molecule is found to be rotated around the active site, changing its interactions with residues Arg176 and Gln228. The original and revised orientations are shown in Figure 1.10 [68].

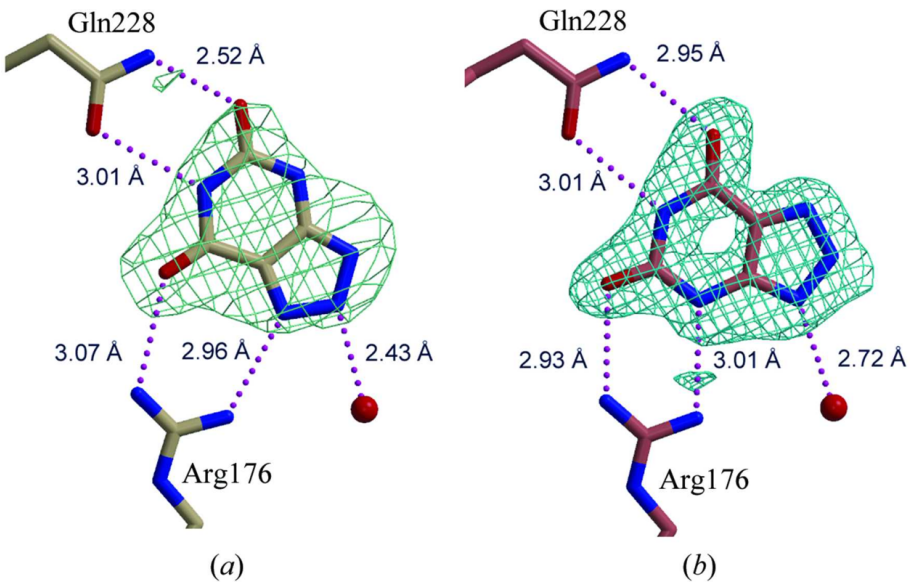

FIGURE 1.10: (a) Ligand binding mode of uric acid (UA) proposed from the first crystal structure of Urate Oxidase (UOX) in complex with 8-azaxanthine (AZA) by Colloch *et al.* [65] solved to 2.05 Å and (b) corrected ligand orientation of UOX:AZA, published by Retailleau *et al.* in an X-ray structure at a higher resolution of 1.80 Å [68]. Both $2F_o$-F_c electron density maps are contoured at 1.75 σ. Reproduced from [68] with permission of the International Union of Crystallography.

Further structural studies showed that the natural substrate UA bound to the enzyme in the same location identified in the AZA complex: this was also observed in other UOX:inhibitor complexes [68, 76, 77]. Negatively charged ions such as Cl^- and CN^- have an inhibitory effect by blocking the active site after ligand binding, preventing the binding of O_2 [78–80]. This allowed the visualisation of UA bound to the active site without being converted to the product [79, 80]. Anaerobic crystal growth in conjunction with data collection at 100 K enabled the structural investigation of UOX:UA describing the active site in an anaerobic environment, i.e., before the binding of O_2 [81]. The overall structure of the active site with UA bound is shown in Figure 1.11, and Figure 1.10 (b) shows the specific bonding interactions of UA and active site residues.

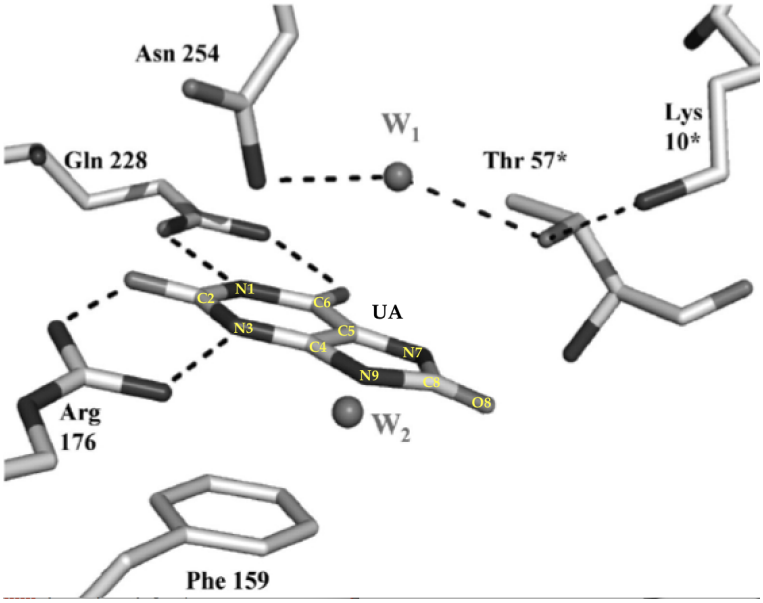

FIGURE 1.11: The active site of Urate Oxidase (UOX) with natural substrate uric acid (UA) bound under anaerobic conditions, trapping solvent molecule, W1, in the active site. The residues Gln228 and Arg176 hold the purine ring in position and Phe159 provides π stacking interactions below. Residues Asn254, Lys10*, and Thr57* encompass the peroxohole where solvent molecule W1 occupies the O_2 position prior to its binding. Solvent molecule W2 is seen hydrogen bonded to a nitrogen atom at position N9 of UA. Figure adapted from [82]. © 2011 Wiley-Liss, Inc.

Proximal residues Arg176 and Gln228, often described as "molecular tweezers", hold the substrate in the active site through hydrogen bonding interactions [77, 82, 83]. The guanidinium group of Arg176 acts as a hydrogen bond donor to both deprotonated N3 and the carbonyl group at C2, with distances of $\sim$ 3.01 Å and $\sim$ 2.89 Å respectively [68, 80, 83]. This particular residue is of interest as it one of the nonsense mutations identified in the gene silencing event, described in Section 1.2.1 [30]. The carbonyl group of Gln228 acts as a hydrogen bonding acceptor for the protonated N1 at $\sim$ 2.95 Å whilst the amine -NH_2 donates to the carbonyl at C6 at a distance of $\sim$ 3.12 Å [68, 80, 83]. A conserved glutamine or glutamate residue is found in the active site of T-fold containing enzymes and thought to be important for anchoring the substrate molecules, as discussed in Section 1.2.3: a Gln228

residue is present in the active site of UOX. The backbone amide of Thr57* is located $\sim$ 2.9 Å from N7, indicative of hydrogen bonding, where the amide is protonated and the N7 is deprotonated [80]. In addition, there is strong π-π interaction between the purine ring of the substrate and residue Phe159, located directly below the plane of the binding site. Residues Arg176, Gln228, Phe159, and Thr57* are shown in the sequence alignment to be identical across all sampled UOX sequences in Figure 1.8, indicating that the active site environment present in different UOXs is extremely similar.

Above the bound ligand is a cavity with a width of approximately 5.5 Å in the O_2-free UOX [82]. By calculating the electrostatic potential, it was shown that the cavity is positively charged [68], supported by the binding of negatively charged CN^- and Cl^- [83]. Interestingly, in several Flavin enzymes a positive charge surrounding the active site has been proposed to increase the reactivity of O_2 [19, 84]. For example, glucose oxidase possesses an electrostatically preorganised active site where a protonated histidine residue is thought to increase the rate of reaction. Identified by site-directed mutagenesis and kinetic studies, this positively charged residue is in a location to stabilise the superoxide-flavin semiquinone radical pair, important for increasing the rate of reaction in Flavoprotein enzymes with O_2 [19, 85, 86]. A histidine residue (His256) is also present in the UOX active site and is found to be identical across the sample of UOXs shown in the sequence alignment, however, if the His256 is related to the positively charged active site has not been determined.

Examination of the cavity located in the active site of the UOX:AZA structure determined using X-ray crystallography [65], identified a solvent molecule, termed W1, positioned directly above the C4-C5 bond of UA. This solvent molecule W1 is hydrogen bonded to two residues: Thr57* and Asn254 that are flexible in the ligand-free structure and become locked into a rigid position when O_2 is bound [79]. Upon binding, O_2 occupies the cavity above the bound ligand at the location

of solvent molecule W1 in the anaerobic structure. The positioning of O_2 has lead to this position being termed the 'peroxohole' [87]. Both the displacement of solvent molecule W1 and a reorganisation of solvent in the active site occur when O_2 binds [81]. This was observed in a study of X-ray structures, the anaerobic UA-anaerobic complex and the UA oxygen-bound complex, where the displacements of active site waters could be identified by comparing the two structures [81]. Due to the proximity of solvent molecule W1 to the C5 position on the ligand, it has been suggested that solvent molecule W1 is ideally positioned to hydrolyse the dehydrourate intermediate (DHU) in the formation of 5-hydroxyisourate (5-HIU) [88].

A number of water molecules surround the active site. Low B-factors indicate a well ordered, hydrogen-bonded water network that is seen to change on ligand binding [68]. A second solvent molecule (W2), is located within hydrogen bonding distance of N9 in UA, as shown in Figure 1.11. Solvent molecule W2 is shown to be central to a hydrogen bonding network of water molecules, all conserved in ligand bound complexes [68]. Due to the hydrogen bonding distances between these solvent molecules, W1-W2 have been characterised as the two end points of a low energy proton transfer system, proposed to play a key role in UOX catalysis [82, 83]. Neutron structures by Oksanen *et al.* of UOX:AZA and UOX:8-HX at room temperature investigated the nature of the bonding network between these two key waters, however, the neutron scattering density along the molecules was diffuse, giving an indication that this network has a degree of mobility, and suggested that protons are being shuffled [80]. However, this diffuse density left some ambiguity of the orientation of the individual water molecules and as a result the exact bonding interactions have not yet been determined.

Residue Asn254 forms the structure of the peroxohole, shown in Figure 1.11, where the distance between the Asn254 sidechain nitrogen atom and solvent molecule W1 is $\sim$ 3.10 Å [78]. The presence of conserved asparagine (and histidine) residues

are typically seen in heme catalase X-ray structures: both residues are thought to be important for binding H_2O and H_2O_2 [88–90]. Therefore, it has been suggested that Asn254 may be important in the binding of H_2O_2 before expulsion as a by-product [88]. Residue Asn254 is also conserved across all samples in the sequence alignment shown in Figure 1.8.

Two functionally relevant residues have been identified by site-directed mutagenesis as Thr57*, a component of the 'peroxohole' structure, and neighbouring residue Lys10* (Thr69* and Lys9* in *B. subtilis*), both located on the neighbouring protomer. The mutation of both Thr57* and Lys10* showed a large reduction in kinetic activity, V_{max}, determined by stopped-flow spectroscopic measurements [91]. Additionally, measurements of the double mutation showed that the V_{max} had only a 2-3 fold difference in activity than that of the single mutants. This reduction in kinetic activity indicated that these residues may play an important role in the reaction mechanism [91]. From these findings it was suggested that Thr57* would abstract a proton from the substrate acting as a 'general base' [91]. However, Thr57* cannot conduct this deprotonation step without activation by another residue, therefore, its close proximity of Lys10* suggested that the Lys10* residue may act to deprotonate Thr57* for activation. This would then enable proton abstraction from the substrate by Thr57*: this proposed synergystic mechanism resulted in these residues being termed a "catalytic dyad" [91]. This 'general base' proposal is discussed in more detail in the following Section 1.2.5. A catalytically relevant Lys10* in a prime position to conduct proton transfers shows similarities to some Flavin-containing oxidases where a protonated lysine is thought to be important for catalysis [92]. In the case of monomeric sarcosine oxidase, it has been suggested that a lysine residue forms a Proton Relay System (PRS) with a threonine residue and several water molecules. This PRS is thought to be involved in delivering protons to the C4a-peroxyflavin adduct [92].

Further structural studies using X-ray crystallography, observed that residue His256

was located at a critical position, hydrogen bonding distance from Lys10*, suggesting a more extensive "catalytic triad" rather than dyad [80, 82, 88, 93]. Imhoff *et al.* noted that the extension of this system to incorporate His256 follows the suggestion that the abstraction of a proton from the substrate is followed by the delivery of this proton to the solvent [91]. In addition, all three of these residues are found to be conserved across the sampled sequences in Figure 1.8. In *Bacillus* sp. His256 is in the same location but slightly displaced [94]. A catalytically important histidine has been postulated to play an important role in other enzymatic reactions involving O_2. In the case of monooxygenases TcmH and ActVA-Orf6, it is suggested that a histidine residue acts as a general base, catalysing the dehydration of the peroxide intermediate in this enzyme [95]. Interestingly, ActVA-Orf6 contains no prosthetic groups and appears to only require O_2 for reaction, similar to UOX [95]. Another role of an active site histidine residue has been proposed in flavoprotein glucose oxidase, where a conserved, protonated histidine residue is thought to facilitate the catalytic reaction by creating a polarized environment favourable for electron transfer [12, 96].

The catalytic triad seen in the active site of UOX is similar to other enzymes with different functions. In particular, the presence of a similar catalytic triad is seen in the α/β-hydrolyse fold superfamily of enzymes [97]. This family have been found to usually contain a catalytic triad consisting of a nucleophilic residue (serine, cysteine, or aspartic acid), a strictly conserved histidine, and an acidic residue acting as a charge relay system [98–100]. Two enzymes of interest are the cofactor-independent 1-*H*-3-hydroxy-4-oxoquinaldine, 2,4-dioxygenase (HOD) and 1-*H*-3-hydroxy-4-oxoquinoline, 2,4-dioxygenase (QOD) that are the only dioxygenases suggested to belong to the α/β-hydrolyse fold superfamily [97]. It has been suggested that the Thr57*-Lys10* catalytic dyad/Thr57*-Lys10*-His265 catalytic triad found in UOX may act similarly to the catalytic triad found in cofactor-free HOD/QOD, operating as a charge relay system [82].

However, due to the limited structural information available on these reactive intermediates, none of these hypotheses have been visualised directly. These mechanisms of action continue to remain elusive in the field of O_2 activation in biology.

1.2.5 The UOX Mechanism

Without typical methods of activating O_2 for reaction (Section 1.1) it is not understood how cofactor-free UOX is able to function effectively. This section will describe the current mechanistic proposals of UOX catalysis and discuss the intermediates suggested to form the UOX catalytic pathway.

A scheme representing the overall reaction mechanism of UA to allantoin is presented in Figure 1.12. Neutral UA is shown as the initial substrate, followed by the deprotonation to the N3 monoanion, 8-HX. There are then two possible pathways, Path 1 and Path 2. The deprotonation of the 8-HX to the UA dianion, followed by an electron transfer from the UA dianion to O_2 is described in Path 1. Alternatively, Path 2 shows the deprotonation of 8-HX with the concurrent transfer of an electron to O_2. Both paths result in a caged radical pair: the UA radical monoanion and superoxide. Path A shows the radical recombination of the UA radical monoanion and superoxide to form a peroxide intermediate 5-(hydro)peroxisourate (5-HPIU), before the generation of a dehydrourate (DHU), after the expulsion of H_2O_2. Path B describes a peroxide independent pathway and the direct formation of DHU. The formation of 5-hydroxyisourate (5-HIU) is shown as the final reaction step before further degradation to allantoin. UOX is shown in blue at stages of the reaction mechanism where it is proposed to play a role. The atoms from the O_2 molecule are expelled as H_2O_2, shown in red and the solvent molecule that attacks the C5 atom to form 5-HIU, is shown in green.

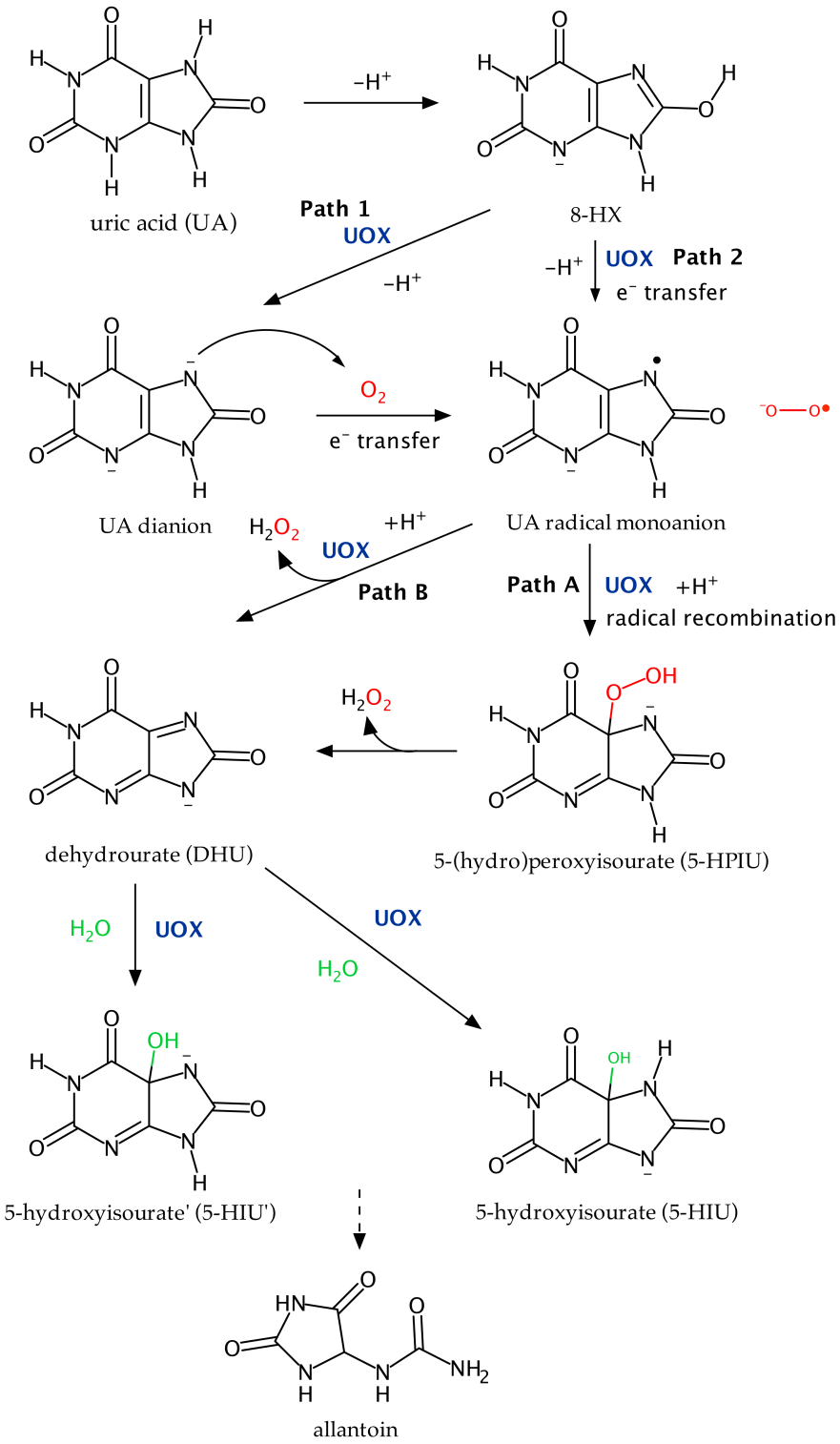

FIGURE 1.12: Reaction scheme of the Urate Oxidase (UOX) catalytic mechanism, presenting the possible steps in the reaction where UOX may play a role. UOX is shown in blue at stages of the reaction where it is suggested to play a role. Molecular O_2, expelled as H_2, is shown in red. The solvent molecule involved in the formation of 5-hydroxyisourate (5-HIU) is shown in green.

The two half redox equations, describing the overall UOX reaction are shown in Equations 1.2 and 1.3.

$$UA + HOH \rightarrow 5 - HIU + 2H^+ + 2e^- \tag{1.2}$$

$$O_2 + 2e^- + 2H^+ \rightarrow H_2O_2 \tag{1.3}$$

The protonation state of UA

The optimum pH for UOX activity is under basic conditions, between pH 8 - 10 [101], however, the enzyme is still largely active at physiological pH [64, 102]. The UA molecule has two pK_a sites, approximately 5.4 and 9.8, shown in Figure 1.13 (b) [42, 63]. The preference for basic conditions for catalytic activity, implies that UA binds to the enzyme as a monoanion, deprotonated at the N3 position, Figure 1.13 (c) [42, 103–106]. In addition, the N3-deprotonated tautomer was found to be present in the sodium salt of urate [107]. The N9 anion is also present at pH 7, identified by both NMR and theoretical calculations. In fact, the N3N9 dianionic species was found to be most prevalent in solution above pH 10, with N3N7 and N1N9 as minor anionic species [106]. The different UA species are detailed in Figure 1.13.

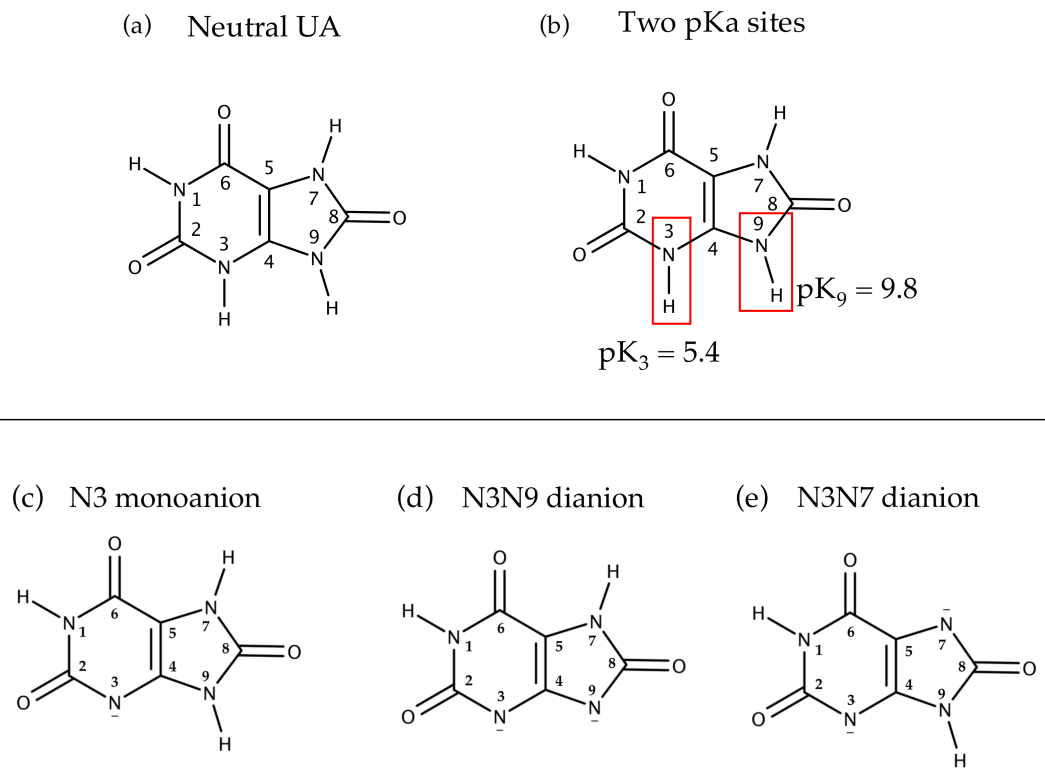

FIGURE 1.13: (a) Neutral uric acid (UA) is shown with atoms numbered as referred to in the text. (b) The two main pKa sites are shown as position N3 and N9 with values taken from [106]. The structure of the N3 monoanion (c) and two dianions, (d) N3N9 and (e) N3N7, are also shown for reference.

The first crystal structure of UOX in complex with ligand 8-azaxanthine by Colloch *et al.* suggested that the bound substrate molecule is the N3N9 dianion [65]. This N3N9 dianion has been identified as the major species present in solution, shown in Figure 1.13 (e). However, this UOX-bound species was later corrected to the N3N7 dianion by Retailleau *et al.*, as previously shown in Section 1.2.4, Figure 1.10 [68, 76, 88]. The proposal that the bound species was the N3N7 dianion was concluded due to the proximity of hydrogen atoms from residues Arg176 and Thr57* to the substrate, shown in Figure 1.13 (e) [68]. In particular, the distance between N7 atom and the main chain nitrogen atom of Thr57* was reported to be $\sim$ 2.9 Å, allowing room for only one hydrogen atom. It was considered more likely that this hydrogen belongs to the peptide bond, implying that the N7 atom is deprotonated [68].

In addition, UOX in complex with inhibitor 9-methyl uric acid (9-MUA), where a methyl group replaces the hydrogen at N9, confirms that the protonation state of the N9 position is not important for binding [81, 106]. The N3N7 dianion is represented in Figure 1.12 following the deprotonation of 8-HX, the N3 monoanion. Colloch *et al.* proposed that the main function of UOX is to create an environment where the reactants are positioned for reaction, acting more as a scaffold than an active participant [65].

Investigation into a general base mechanism

However, there are also other suggestions in which UOX is central to the chemistry of UA oxidation. Researchers Tipton and colleagues had suggested that the dianionic UA species was the first reactive intermediate in the UOX mechanism [64, 106]. Therefore, as UA was found to exist as a monoanion in solution, it was considered that the role of UOX was to abstract a proton from the N3 monoanion (8-HX) to form the reactive dianion followed by an electron transfer to O_2 [64, 91, 108]. The N3N7 dianion was found to be the most reducing available UA species [108] which would then undergo oxidation, followed by hydration, to form the product 5-HIU [64, 105]. The formation of the reactive N3N7 dianion is shown in Figure 1.12, Path 1. The negative ionisation potential implies that the dianion can spontaneously transfer electrons to the O_2 molecule more easily than neutral UA and the UA monoanion [108]. This led to the suggestion by Imhoff *et al.* that UOX must contain a 'general base' system in close proximity of the active site, capable of a deprotonation [91]. A similar method of substrate activation by proton abstraction, before reaction with O_2, has been reported both in metallo-oxygenase enzymes and several cofactor-independent oxygenases [3, 22, 109].

In addition to the 'general base' system, it was suggested that UOX also needed the capability to store and stabilise electrons, or monoelectron species [82]. EPR spectroscopic measurements observed a radical species during the UOX reaction [110],

leading to suggestions that the activated state of UA was the N3 radical monoanion, shown in Figure 1.12, Path 2 [82]. The formation of this radical species would circumvent the spin-forbidden reaction of singlet UA with triplet O_2 and allow the transfer of electrons to O_2 by the activated substrate.

Neutron studies by Oksanen *et al.* investigated the structures of hydrogenated UOX (HUOX) in complex with AZA and UA, employing the inhibitory nature of Cl^- in the active site by conducting crystal growth in halogenated conditions [80, 111]. The HUOX:UA complex, referred to as HUOX:8-HX, identified the bound urate species in the active site as the 8-hydroxyxanthine monoanion (8-HX) at the N3 atom instead of the reactive dianion species. The structural difference between the N3 monoanion and the N3N7 dianion is shown in Figure 1.12 [80]. The presence of a deuterium atom attached to the oxygen atom at O8, confirmed this enol tautomer as the species bound to HUOX in the presence of Cl^-. The neutron density map from the published HUOX:8-HX structure is shown in Figure 1.14. From these results, a mechanism involving this enol tautomer was proposed. Oksanen *et al.* suggested that a general base is still required for deprotonation of the 8-HX monoanion, removing the proton observed at the O8 position in the monoanionic species. However, it was also postulated that this was concomitant with an electron transfer to an electron acceptor within the protein, shown as Path 2 in Figure 1.12 [80]. This was in contrast to the proposals made by Tipton and colleagues. The exact location of the general base proposed by Imhoff *et al.* and whether the electron transfer step is direct from the substrate or mediated by UOX was not determined from this study.

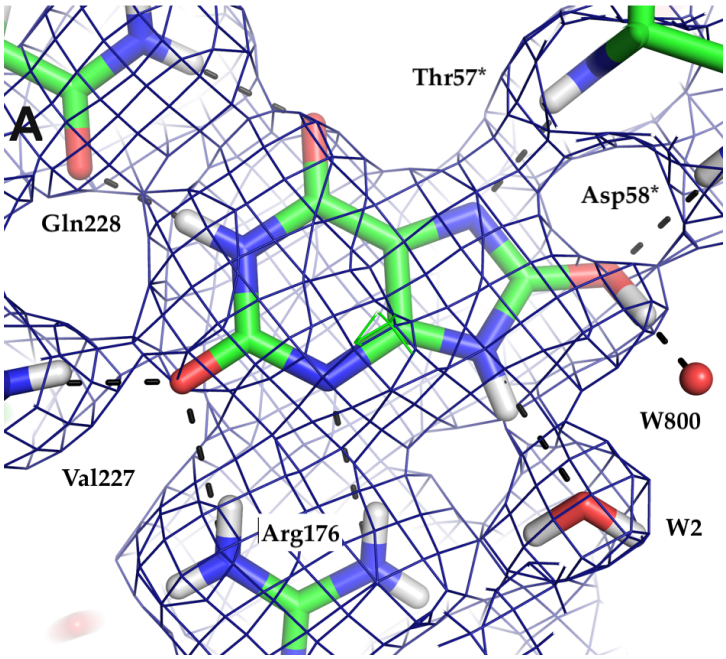

FIGURE 1.14: $2mF_o$-DF_c neutron density map contoured at 1.0 σ showing the presence of the 8-hydroxyxanthine monoanion (8-HX) in the Hydrogenated Urate Oxidase (HUOX) active site [80]. Adapted from [111] © 2014 Oksanen et al. Distributed under CC-BY 4.0.

In support of the mechanism proposed by Oksanen *et al.*, a purely computational study by Wei *et al.*, based on the HUOX:8-HX neutron structure [80], suggested that the N3N7 dianion species did not exist [80, 112]. This is represented by Path 2 in Figure 1.12. Instead, it was suggested that the more feasible mechanism would proceed via a deprotonation-electron transfer with both steps mediated by UOX [80, 112]. In this mechanism, it was proposed that the Lys10* residue acted as the 'general base', deprotonating the proton at position O8, assisted by the hydroxyl group of Thr57*, shown in Figure 1.15 (a) and (b) [112]. In addition, an electron transfer occurs simultaneously from the substrate to the O_2 molecule, creating a radical substrate and radical O_2 in the active site, Figure 1.15 (b) and (c) [112]. A second proton transfer from the positively charged Lys10* group to the O_2 radical, Figure 1.15 (d), before a radical recombination reaction, forming the 5-(hydro)peroxide intermediate, Figure 1.15 (e) and (f). This is then followed by the expulsion of H_2O_2.

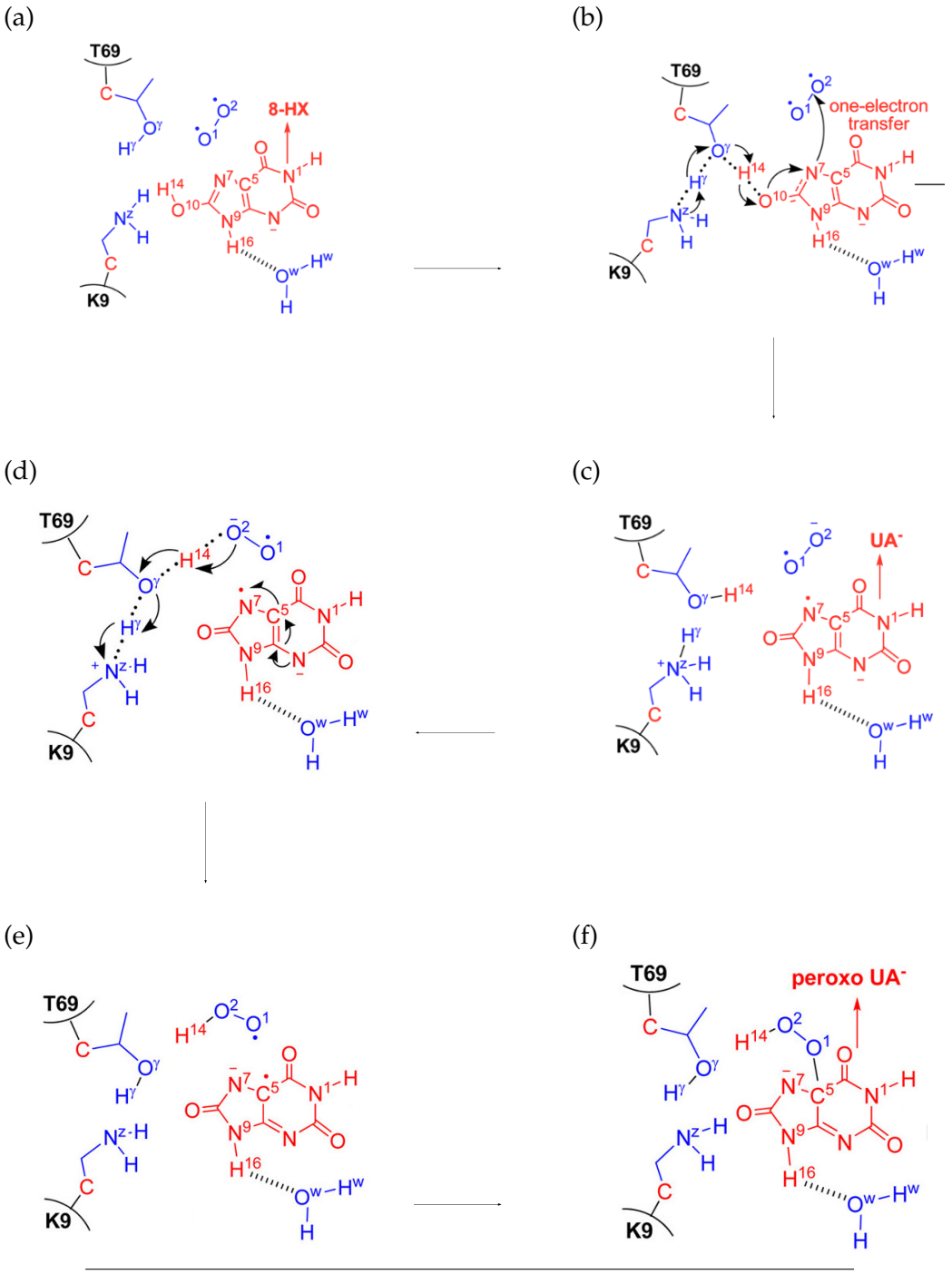

FIGURE 1.15: The UOX reaction mechanism, proposed by Wei *et al.*, showing the deprotonation of the 8-hydroxyxanthine (8-HX) monoanion by active site residues. The formation of the 5-(hydro)peroxyisourate intermediate is also described. In this study K9 and T69 refer to Lys10* and T57* in *Aspergillus flavus*, respectively. Adapted with permission from [112]. Copyright 2017 American Chemical Society.

Determination of a Peroxide-dependent Pathway

A study by Altarsha *et al.* presented theoretical calculations that proposed that UA oxidation proceeded independently of a peroxide intermediate [108]. Instead, it was suggested that a dehydrourate (DHU) intermediate was formed directly from the energetically favoured N3N7 dianion [108]. This is shown by Path B in Figure 1.12. However, the suggestion that the electron transfer from UA to O_2, followed by the immediate attack of the DHU by solvent to form 5-HIU, was termed an unlikely mechanism [65, 108, 113]. In addition, the transfer of two electrons from the singlet state UA dianion to the triplet state O_2 would violate the spin conversion rule, previously described in detail in Section 1.1 [113, 114].

Mechanistic studies had proposed a peroxide-dependent pathway for UOX catalysis, however were unable to provide structural evidence of a peroxide intermediate, Path A in Figure 1.12 [106, 113, 115]. Direct evidence of a (hydro)peroxide-intermediate, 5-(hydro) peroxyisourate - 5-PIU, was presented in a structural study by Bui *et al.* [81]. Using X-ray crystallography, in conjunction with *in crystallo* Raman spectroscopy and QM/MM calculations, this study was able to unambiguously determine the presence of a 5-(hydro)peroxide-intermediate [81]. The (hydro) peroxyisourate intermediate determined in this study is shown in Figure 1.16, and the formation of the 5-(hydro)peroxyisourate intermediate is described as Path A in Figure 1.12.

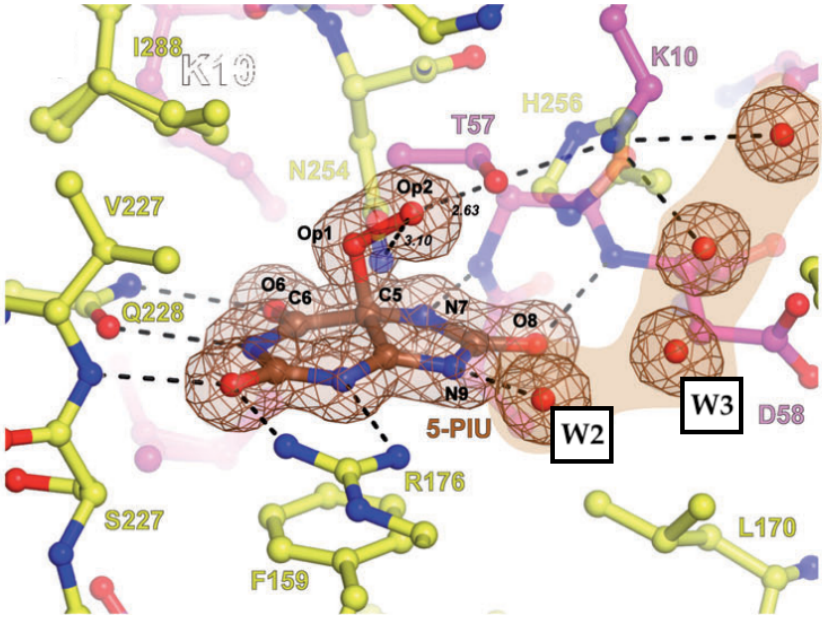

FIGURE 1.16: Direct evidence of a 5-(hydro)peroxyisourate intermediate determined by X-ray crystallographic studies conducted by Bui *et al.* [81]. The $2mF_o$-DF_c electron density map, contoured at 1σ, clearly shows the bond formed between the C5 atom of uric acid (UA) and the O_2 molecule. Figure adapted from [81] © 2014 The Authors. Published by Wiley-VCH Verlag GmbH & Co. KGaA.

The identification of this key 5-PIU intermediate was essential in furthering the understanding of cofactor-free mechanisms. In fact, peroxide intermediates are commonly proposed for other systems where reaction with O_2 would result in a violation of the spin conversion rule [2, 114]. However, these related reactions commonly involve a cofactor or metallic centre. Flavin and Pterin reactions are thought to proceed via a similar (hydro)peroxide intermediate. Several Flavin-dependent monooxygenases have been shown to operate via a semiquinone-superoxide pair, resulting in the formation of a C4a-(hydro)peroxyflavin intermediate, described in Section 1.1 [14, 116]. The Flavin C4a-hydroperoxide acts as an electrophile and substrates containing activating groups such as hydroxyl act as nucleophiles [16, 17]. The mechanism is similar to UOX and UA: the HPIU forms DHU then undergoes attack by a solvent molecule to form 5-HIU [64, 106]. Interestingly, a

peroxide-dependent mechanism has also been proposed for families of cofactor-free monooxygenases and dioxygenases, further support for the suggestion that cofactor-free reactions proceed in a Flavin-like manner [97, 117, 118]. For the dioxygenases HOD, QOD, and DpgC, it is proposed that the substrates transfer a single electron to O_2. This generates a radical pair that can collapse to a peroxide species after a radical recombination. [97, 119]. These intermediates have only been determined spectroscopically, meaning there is little structural evidence to support these claims. However, understanding the mechanism of UOX may also shed some light on these enzymes if the intermediates are believed to be similar.

Formation of 5-hydroxyisourate and allantoin

The final product of the UOX-mediated UA degradation pathway is allantoin. It was initially thought that allantoin was the product of UOX catalysis, however, the expulsion of CO_2 was delayed in comparison to the O_2 uptake [120], giving an indication other intermediates were present after UA. As a result, the true reaction product of the UOX catalytic process was identified as 5-hydroxyisourate (5-HIU) [106, 121, 122]. This metastable species has been shown to degrade to allantoin either enzymatically or naturally [59, 106, 115, 121, 123, 124]. Isotopic labelling studies showed the hydroxyl group present on at the C5 position of 5-HIU is derived from a solvent H_2O molecule and the O_2 atoms involved in the reaction are expelled as H_2O_2 [64, 106, 123]. The H_2O_2 by-product is proposed to take one proton from UA and one from a solvent molecule [108]. The expulsion of the atoms of O_2 as H_2O_2 and the addition of hydroxyl group at C5 from the solvent, forming 5-HIU, are shown in Figure 1.12. Spectrophotometric assays showed that there is an ordered mechanism of substrate addition with UA binding to UOX before O_2 and the chirality of the reaction 5-HIU infers that the hydroxylation takes place in the active site [62, 106]. Hydrolysis of 5-HIU occurs at the N1-C6 bond, followed by the migration of the carboxylate group to C4. The production of allantoin follows decarboxylation where CO_2 is derived from the C6 of UA [106, 123].

1.3 Aim and Motivation

There is limited structural information on reactive intermediates in the UOX catalytic pathway. As a result, the method by which UOX facilitates the oxidation of UA remains elusive. The exact protonation states of important active site residues in reactive intermediates are also undetermined. In addition, the structurally conserved water network surrounding the active site and its importance in catalysis is also not confirmed.

Building on previous X-ray and neutron studies, the purpose of this study was to further investigate two structures in the UOX catalytic pathway. Complexes of perdeuterated Urate Oxidase (DUOX) with 8-azaxanthine (AZA) and 9-methyl uric acid (9-MUA) are presented in this thesis. The AZA inhibitor binds to the UOX active site and preserves solvent molecule W1 *in situ* by preventing O_2 binding. The 9-MUA ligand forms the 9-methyl-5-peroxyisourate intermediate (5-PMUA), trapping the peroxide before the expulsion of H_2O_2.

Neutron crystallography, in conjunction with deuterium labelling, enables the determination of protonation states, hydrogen positions, and water networks. This thesis provides a structural analysis of these two complexes in two different environments: one where O_2 cannot bind, and one where it is bound, trapped in an intermediate species. The examination of the protonation states of catalytic residues, and identifying important solvent molecules, provides information typically unattainable using other techniques. The aim is that these findings further our understanding on the functionality of cofactor-free enzymes and how they achieve their reaction with O_2.

Chapter 2

Experimental Methods

Abstract

This chapter covers the laboratory and experimental techniques employed in this research project. Molecular biology and techniques of particular interest to the purification of UOX are presented and analysed. The process by which proteins are deuterated and the associated challenges are also discussed.

Introduction to crystallographic theory and its applications in structural biology are described herein. Topics including crystal growth, data collection, and analysis and structural refinement are also presented.

Finally, the technique of neutron protein crystallography is explored and how it provides complementary information on hydrogen positions and biological mechanisms compared with other techniques.

2.1 Molecular Biology

2.1.1 Cell Growth and Protein Expression

Commercial pET vectors are widely used in the production of recombinant proteins. A particular gene of interest can be cloned into the pET vector, which is then strictly controlled under the T7 transcription and regulatory system. A map of the expression vector pET-24b+ describing its key components is shown in Figure 2.1. This particular construct is used in the recombinant expression of UOX.

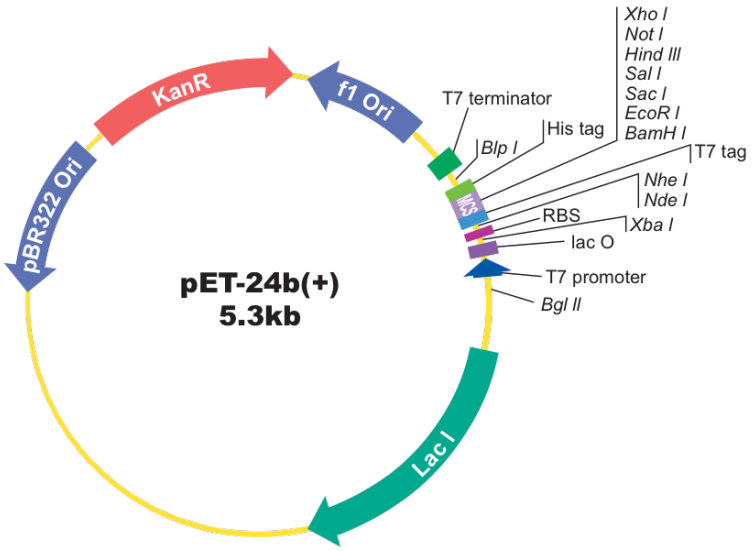

FIGURE 2.1: The pET-24b+ vector map showing the presence of the kanamycin resistance marker and the T7/*lac* promotor system that can be used for the expression of recombinant proteins. Figure taken from the Genscript website (https://www.genscript.com/gsfiles/vector-map/bacteria/pET-24b.pdf).

Expression vectors typically contain the following components:

- Antibiotic resistance gene - cells containing the expression plasmid of interest can be selectively grown. Common antibiotics include kanamycin (kan^R) or

ampicillin (amp^R). Kan^R is an aminoglycoside antibiotic and binds to the bacterial 30S ribosomal subunit, resulting in the midreading of t-RNA and preventing the bacteria from synthesising proteins essential for growth.

- Promotor - this is recognised by RNA polymerase and begins the transcription of the gene. Gene expression can be controlled using molecular biology reagents causing induction or repression. In this case, the T7*lac* promotor is employed and can be induced in the presence of isopropyl θ-D-1-thiogalatopyranoside (IPTG).

- Terminator - also recognised by RNA polymerase and stops transcription.

Bacterial transformation is the process of introducing recombinant DNA into a host cell. This method can be employed in order to selectively overexpress a protein of interest. 'Competent' cells are used, meaning that they are more able to readily uptake foreign DNA. The transformation process contains an important heat shock step [125, 126]. Cells are briefly exposed to a temperature of $\sim$ 42 °C, which encourages the forming of pores that allow the plasmid of interest to enter the cell. The cells are returned to room temperature to allow the cell walls to self-heal, the addition of a nutrient-rich medium, such as SOC, can aid the recovery.

Escherichia coli cells, or *E. coli*, are widely used in conjunction with commercial pET vectors. *E. coli* is a suitable host in the expression of recombinant proteins. The in-depth knowledge of the genome and its controllability make it a popular choice for the production of proteins in large quantities [127]. Another reason that *E. coli* is commonly chosen as a useful host for the expression of recombinant proteins is that it has extremely fast growth kinetics, with cell doubling time of about 20 minutes in an optimal environment [128].

Monitoring the growth of bacterial cells is also essential for optimising and subsequently maximising the production of a target protein. The optical density (OD_{600}) is used to assess the turbidity of the solution and thus give an indication of the

quantity of cells. This is because the cells present in the solution scatter the light away from the photovoltaic cell, giving a lower electrical signal than seen for an empty cuvette. A wavelength of 600 nm is chosen for analysis in comparison to UV light as it minimises damage to the cells. This important feature allows the monitoring of cell growth and gives an indication of when the log phase is reached and therefore when to induce the overexpression.

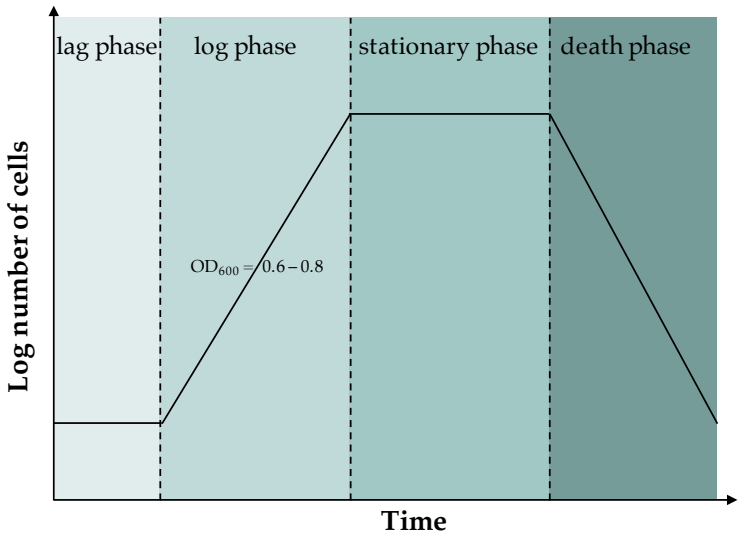

FIGURE 2.2: The main stages of bacterial cell growth. The lag phase indicates initial growth is slow before exponential growth during the log phase. The stationary phase follows before the death phase where cells die faster than multiply. Figure adapted from [129, 130].

Bacterial cell growth occurs in four stages as shown in Figure 2.2. The first stage is known as the lag phase - during this stage cell growth is slow, allowing the cells to adapt to their new growth environment. The following stage, the log phase, is the optimal stage for cell production with an increase in the rate of cell division. Cell growth begins to stagnate during the stationary phase before finally the death phase. Cell death results from a lack of growth media, and an excess of waste products, and overcrowding meaning cells begin to die quicker than divide. It is considered ideal to induce overexpression of the target protein during the log phase whilst the culture is fast growing to maximise protein production and to harvest the

cells during the stationary phase. This is typically done at OD_{600} levels of 0.6 - 0.8.

A selective marker for an antibiotic is included in the pET vector, as discussed above. Ampicillin is commonly used as an antibiotic in this process, however, in the presence of deuterated media, it can cause *leaky expression*. This describes plasmid instability and leakage of the foreign DNA out of the cell under the stressful deuterated conditions. This leads to cell multiplication without the incorporation of the inserted DNA and significant reduction in the production of the desired protein. Alternatively, there can be leakage of β-lactamase into the medium. The β-lactamase is responsible for the hydrolysis of the β-lactam ring of ampicillin, rendering the antibiotic ineffective. As a solution, kanamycin is used instead of ampicillin where the enzyme kanamycin acetyl-transferase is not as prone to leakage. As a result, vectors are recloned to amend the antibiotic resistance before expression under deuterated High Cell Density Culture (HCDC) conditions [131].

2.2 Production of Deuterated Biomolecules

The production of deuterated biomolecules can contribute to the success of many neutron scattering experiments. Hydrogen accounts for $\sim$ 50% of atoms in a protein, however, replacing the hydrogen atoms with its isotope deuterium can be beneficial: this is explained in further detail in Section 2.6. The substitution of hydrogen (^{1}H) for deuterium (^{2}H or D) is not a straightforward process due to the relative toxicity associated with ^{2}H [131]. There are two possible ways of incorporating deuterium into a protein structure. The simplest method is to exchange only the labile hydrogens, including O-H, N-H, and S-H positions. This can be done by changing hydrogenated protein solution into deuterated solution using dialysis, a series of concentration/dilution steps, or after crystal growth. However, the labile hydrogen atoms only account for $\sim$ 25% of protein hydrogens, and methods

of soaking exchange solvent-accessible groups describes 15-20 % of the protein hydrogen content [132]. A significant number of non-exchangeable hydrogens in the protein remain, for example, -CH_3 groups. The unwanted effects that this can cause is explained in Section 2.6. A more rigorous method, perdeuteration, involves the complete replacement of all hydrogen positions in a protein with deuterium - both non-exchangeable and labile positions [131]. Carbon-bound hydrogens can only be incorporated into the protein structure via protein biosynthesis.

Luria broth, or LB, is commonly used as a growth medium in the production of cell cultures, however, a deuterated equivalent is not commercially available. The Life Sciences Group based at the ILL, Grenoble have developed the following protocol for the production of recombinant proteins in deuterated conditions. In the absence of deuterated LB, a deuterated minimal media (D-Enfors) is used, containing mineral salts with components essential for bacterial growth (eg, $AsSO_4$ as a source of nitrogen) and d_8-glycerol as the carbon source. However, use of minimal media can result in slow cell growth and a low yield of recombinant proteins. As deuterium is toxic in high concentrations, it has been found to be more effective to introduce deuterium into the cell growth process gradually. This can be done through a process called *adaptation*. The *E. coli* strain BL21 (DE3) is commonly used in the expression of perdeuterated recombinant proteins as it adapts to the presence of D_2O more easily than other strains [131]. *E. coli* BL21 (DE3) cells are first grown in a hydrogenated minimal medium (H-Enfors). This allows the cells to first adapt to the minimal media growth environment. Repeats of this process are conducted using 1:10 dilution of overnight culture in fresh hydrogenated minimal medium, until the growth rate increased and the cell generation time has reduced. This is then repeated with deuterated minimal medium. The adaptation process is described in Figure 2.3. After this stage, cells can be recovered and stored on cryobeads for future use, or scaled up in preparation for fermentation.

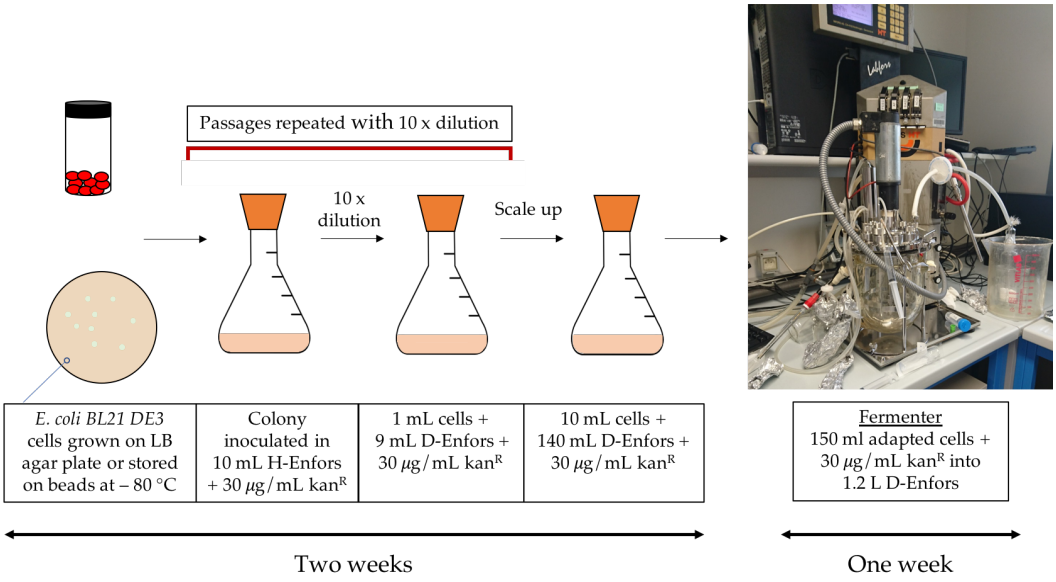

FIGURE 2.3: Preparation of adapted cells for growth in deuterated medium. *E. coli* BL21 (DE3) cells are grown on an LB agar plate with antibiotic or taken from storage at - 80 °C. The cells are grown first in minimal hydrogenated media (H-Enfors) before further growth in minimal deuterated media (D-Enfors). This culture is then scaled up in preparation for inoculation in the fermenter. Figure adapted from [131].

Fermentation is the process used for producing perdeuterated recombinant proteins in high cell density cultures (HCDC). The process is convenient for producing HCDCs as it important to encourage growth in challenging conditions and to maximise cell growth when working with expensive deuterated medium. Numerous variable parameters allow closer control of the optimum conditions for cell growth than for cultures produced in flasks.

- Base - In the aerobic multiplication of cells there is the generation of acidic by-products. By adding a deuterated base, 1 M NaOD, the pH can be maintained at an optimal level pH 6.9 and prevent cell death due to toxicity from the build up of acidic by-products.

- Stirrer Speed - One method of monitoring the growth of cells is by the variation in pO_2 level, reducing as it is consumed by the respiring and dividing cells. The level is maintained at $\sim$ 30 %. If the level reduces, the stirrer speed

is altered to increase the O_2 flow and compensate for the increased O_2 demand by cells.

- Feeding - deuterated glycerol, d_8-glycerol, is used as the carbon source and is initially added as 5 g/L during the batch phase. As this is consumed and is indicated by the sharp increase in pO_2, the process enters the fed-batch phase in which supplemental 120 g/L d_8-glycerol is fed into the medium (total mass $\sim$ 50 g).

The closed system by which the fermenter operates also limits the contamination of H_2 from the atmosphere into the growth medium and subsequently the target protein.

The fermentation is composed of two stages, the batch phase and the fed-batch phase. The batch phase occurs in the initial stages of cell production where the cells consume the d_8-glycerol supply in the deuterated minimal medium. The cell culture is then supplemented by a fresh feeding solution of 120 g/L d_8-glycerol. This controlled feeding of the culture is dependent of the cell generation time and increases exponentially during the fermentation process [131]. This is continued until there is a suitable level of biomass for induction: cells are typically induced with 1 mM IPTG at an OD_{600} of $\sim$ 15 and cells are harvested when cells reach an OD_{600} of $\sim$ 20 [131].

However there are some limitations associated with producing deuterated biomolecules. It has been noted that in comparison to typical hydrogenated biomolecules, the yield tends to be lower [133, 134]. This can lead to a lengthier and costly process to achieve masses of biomolecules needed for material heavy techniques, such as spectroscopy or dynamic studies.

The use of deuterium/hydrogen substitution is commonplace in neutron studies. However, doubling the mass of the atom from ^1H to ^2H can have changes on bonding and interactions. For example, in methyl groups, C-D bond lengths have lower

vibrational amplitudes and frequencies compared to C-H, indicating shorter and stronger bonds. This has implications in secondary and tertiary structure as fully deuterated sidechains tend to be more compact, reducing the strength of intermolecular and intramolecular interactions of non-polar side chains [135]. Properties such as oligomerisation rate [135] and exchange rate [136] were found to be different between hydrogenated and deuterated proteins. Deuterated proteins were also found to have an increased susceptibility to heat denaturation compared to their hydrogenated counterparts [134, 137, 138]. These differences are related to the kinetic properties of the proteins rather than structural effects. It has also been observed that aggregation properties have been affected in some proteins [139, 140].

Many studies have found there to be no significant changes between the structures of deuterated and hydrogenated proteins [141–144]. Overall, it is accepted that each deuterated protein must be characterised using complementary techniques or high resolution X-ray crystallography in order to identify any possible discrepancies between the samples prior to neutron studies [139, 145].

2.3 Purification Techniques

2.3.1 Cell Lysis and Protein Extraction

The initial step of protein purification aims to isolate the target protein from the cells in which it was expressed. The method used is dependent on whether the protein is cytosolic or secreted. UOX is a cytosolic protein therefore cells must be broken, or lysed, to extract the protein. This can be done either mechanically or enzymatically, or a combination of techniques can be employed to optimise the protein extraction step.

The purification of UOX employs both mechanical and enzymatic techniques in the extraction of the protein from cells. The mechanical technique used is sonication. It acts by generating sonic waves to break open cells, causing them to release their contents into solution. A sonicator is typically used and contains a probe that can be placed directly into a homogenous solution containing cells resuspended in a lysis buffer. The sonicator generates sound energy electronically which is delivered into the solution by a probe. This is subsequently converted into mechanical energy and results in the formation of small bubbles which implode. This implosion is also known as 'cavitation' and causes the disruption of the cell wall and, ultimately, its rupture. The sonication step should be conducted whilst the protein solution is kept on ice, preventing the proteolysis or aggregation of the protein due to overheating. In addition to sonication, lysozyme is added to the resuspended cells to break down the cell walls, enzymatically assisting the extraction of UOX.

Additives can also be employed in the extraction of the target protein. After cell breakage, DNA and RNA molecules released into the solution, causing an increase in viscosity. Endonucleases, such as benzonase, are commonly added to the resuspended cells to breakdown these molecules, substantially reducing the viscosity and aiding the next stages of the purification process. Protease inhibitor cocktails are also used to block the activity of proteases and prevent the possible digestion of the target protein. However, many common protease inhibitor tablets contain EDTA which can inhibit the activity of benzonase at even low concentrations, so EDTA-free protease inhibitor tablets are preferred.

2.3.2 Dialysis

Dialysis is a commonly used purification technique that involves the exchange of small molecules, such as salts, by diffusion though a semi-permeable membrane in solution. A solution containing the protein is placed inside a membrane which is

then inserted into a large volume of buffer, known as the dialysate. A concentration gradient is formed between the regions of high and low concentration of the unwanted molecules or salts. Once equilibrium is reached between the two regions, the dialysate can be changed to a new solution in order to create another concentration gradient, allowing further diffusion. The dialysis membrane tubing used is carefully selected with consideration to the size of the pores. The pore size, or molecular weight cutoff (MWCO), must permit the diffusion of molecules smaller than the protein, whilst retaining the protein within the tubing.

2.3.3 Ammonium Sulfate Precipitation

The differences in the solubilities of proteins can be exploited during purification as this varies widely depending on the protein structure. Ammonium sulfate precipitation (ASP) is used as a basic, yet effective, technique that separates proteins this way. This technique is suitable for many proteins and is tag-independant so is widely applicable.

At high salt concentrations, the solubility of a protein is reduced leading to precipitation and a process called 'salting out' [146]. Ammonium sulfate dissociates into the ions NH_4^+ and SO_4^{2-}, both of which are early members of the the cation and anion Hofmeister series respectively, shown in Figure 2.4. These ions increase solvent surface tension and increase the hydrophobic interaction between the protein and water whilst decreasing the solubility of non-polar molecules [147].

These ions interact with the negative and positive regions in a protein. This reduces the contact with H_2O molecules whilst maintaining the core hydration layer, aiding the preservation of the proteins natural conformation. The protein reacts to a highly polar environment by limiting its contact with the solvent through compacting and self-associating [148]. This process becomes energetically favourable as it results in the additional bound water molecules becoming free, subsequently increasing

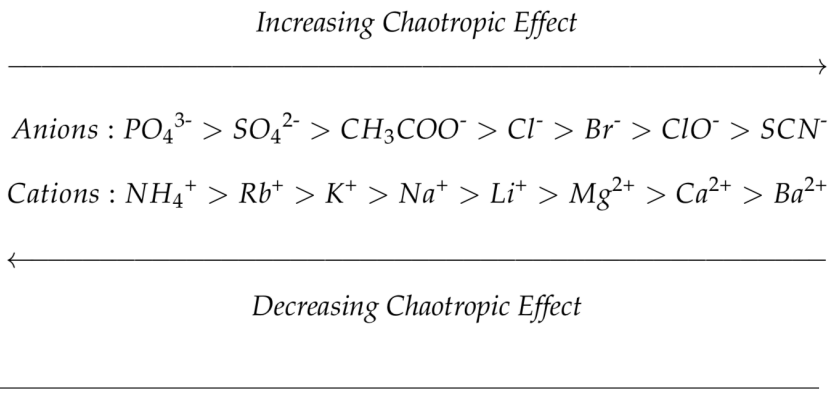

FIGURE 2.4: The Hofmeister series describes the increasing/decreasing chaotropic effect of both anions and cations.

the entropy of the system and making the process thermodynamically favourable. By precipitating stepwise fractions of different salt concentrations, it is possible to isolate proteins of different solubility and remove impurities that aggregate easily. Published tables can be consulted in order to determine the weight of ammonium sulfate, or the volume of concentration of ammonium sulfate, needed to obtain the desired concentration [149].

2.3.4 Ion Exchange Chromatography

Ion Exchange Chromatography (IEC) is based on the fundamental attraction of oppositely charged moieties. Depending on the pH of the environment and the isoelectric point (pI) of the protein, proteins carry a charge. This property can be exploited in IEC by utilising charged ligands attached to resins to bind oppositely charged proteins. There are two general types of ion-exchangers: cations and anions. Cations exchangers carry a negative charge and bind positively charged proteins, whereas anion exchangers carry a positive charge and so bind negatively charged proteins.

Weak anion exchangers are classified as a weak base that easily loses charge at a high pH due to deprotonation. Conversely, a strong exchanger consists of charged

groups that act as a strong base.

Selection of a buffer species is dependant on the isoelectic point (pI) of the protein. Binding of proteins is achieved at low salt concentrations and elution typically occurs with the introduction of a high salt concentration. The window for isocratic elution is very small so a linear salt concentration gradient is used, giving a higher resolution. The process of ion exchange chromatography is detailed in Figure 2.5.

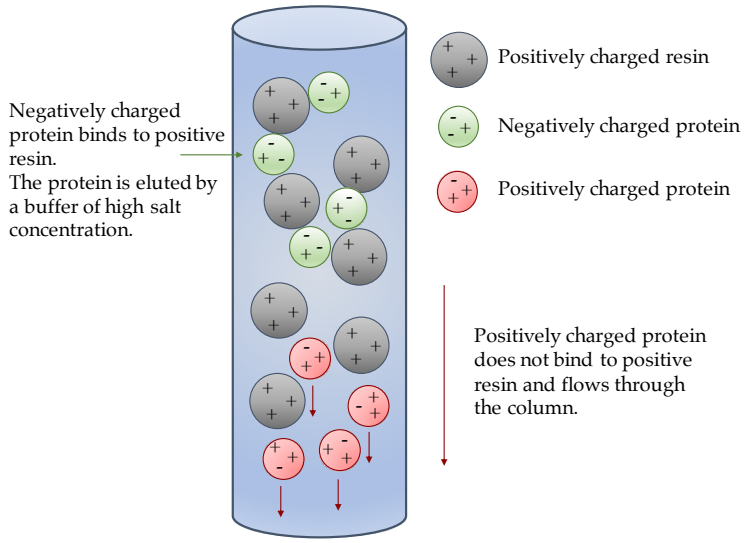

FIGURE 2.5: The process of ion exchange chromatography. Positively charged resins are used in anion exchange chromatography. Positively charged proteins pass through the column without binding to the resin whereas negatively charged proteins are bound. The charge of the protein depends on the pI and on the buffer used. Typically negatively charged proteins can be eluted by increasing salt concentration in the buffer.

Diethylaminoethyl-sepharose (DEAE) is a positively charged resin and acts as a weak anion exchanger, binding negatively charged proteins. The positive charge on the molecule arises from the protonated amine group. This amine group has a pKa of 10 so it is essential that for the protonation to occur, the pH of the buffer must be at least 2 pH units lower. Q-Sepharose is a strong anion exchanger which also binds negatively charged proteins. It is classified as a strong exchanger due to the fact that it is a quaternary resin so cannot be deprotonated, even at high pHs. The anion exchange ligands DEAE and Q-Sepharose are shown in Figure 2.6.

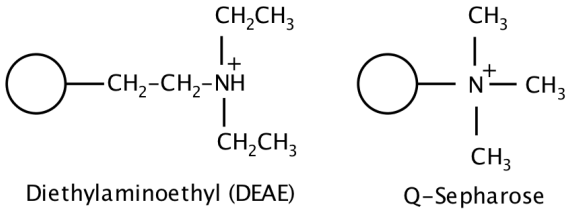

FIGURE 2.6: Both DEAE and Q-Sepharose are anion exchanger ligands, binding negatively charged proteins. DEAE is classed as a weak exchanger as it can be deprotonated above pH 10. Q-Sepharose is a quaternary amine so cannot be deprotonated and is classed as a strong exchanger.

2.3.5 Hydrophobic Interaction Chromatography

Protein hydrophobicity is dependent on several factors: the number of polar or non-polar residues in the amino acid sequence, and the proteins tertiary and quaternary structure in a given solution. The technique of hydrophobic exchange chromatography (HIC) exploits the hydrophobic regions present on proteins, and encourages binding to hydrophobic ligands. A common environment used in this process to encourage hydrophobic interactions is an aqueous solution with a high salt content. In a low salt environment, water molecules adopt an ordered arrangement around the hydrophobic areas of the protein. Increasing salt concentration can cause the protein molecules to interact with the ligand, driven by a net increase in entropy from the reorganisation of the water network. In this process, the overall surface area of the hydrophobic sites of the protein exposed to the polar solvent is decreased. This results in a less structured, higher entropy environment, and is the favoured thermodynamic state.

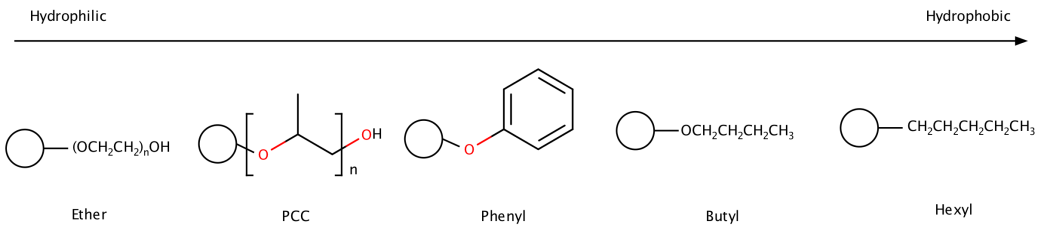

FIGURE 2.7: Common ligands used in HIC are typically carbon based molecules to promote hydrophobic interaction with protein molecules in the presence of high salt. Hydrophobicity increases with aliphatic chain length and molecule size.

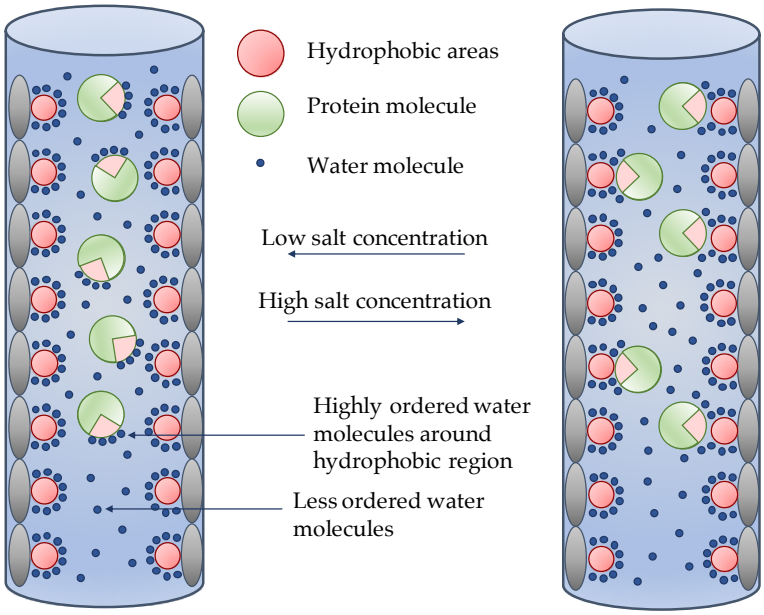

FIGURE 2.8: The process of hydrophobic interaction chromatography. In a low salt environment, ordered water exists around the hydrophobic residues on both the protein molecule and the ligand. In a high salt concentration, the ions interact with water molecules, decreasing the number of ordered molecules surrounding the hydrophobic areas and encouraging the interaction between the protein and the ligand.

As a general rule, hydrophobic interactions will increase with aliphatic chain length. The use of aromatic rings such as phenyl groups can also strengthen hydrophobic interactions with absorbed compounds through π-π stacking with aromatic sidechains. Several sidechains used in HIC are shown in Figure 2.7.

Elution of protein molecules is achieved by the addition of a low salt concentration buffer which decreases the strength of the hydrophobic interactions, leading to the desorbtion of protein molecules and subsequent elution, shown in Figure 2.8. Protein elution is dependent on the strength of hydrophobic interaction with the ligand and how quickly it is desorbed.

2.3.6 Gel Filtration Chromatography

Gel filtration/size exclusion chromatography can be used as a preparative method and separate protein molecules based on their size and shape, or hydrodynamic volume. The hydrodynamic volume is described as the volume a protein molecule creates when the molecule is tumbling rapidly in solution. Size exclusion columns contain a resin with porous holes in the beads, this gives rise to a number of paths that molecules can travel through. These pores, known as the stationary phase, are of a certain size and allow only smaller molecules to pass through. This results in smaller protein molecules taking a longer time to elute from the column. In comparison, larger molecules are excluded form these pores only passing through the solvent, mobile phase, and so have the shortest path and are eluted first. The order of elution of molecules can be described as the inverse of their hydrodynamic volume. The process of gel filtration is described in Figure 2.9.

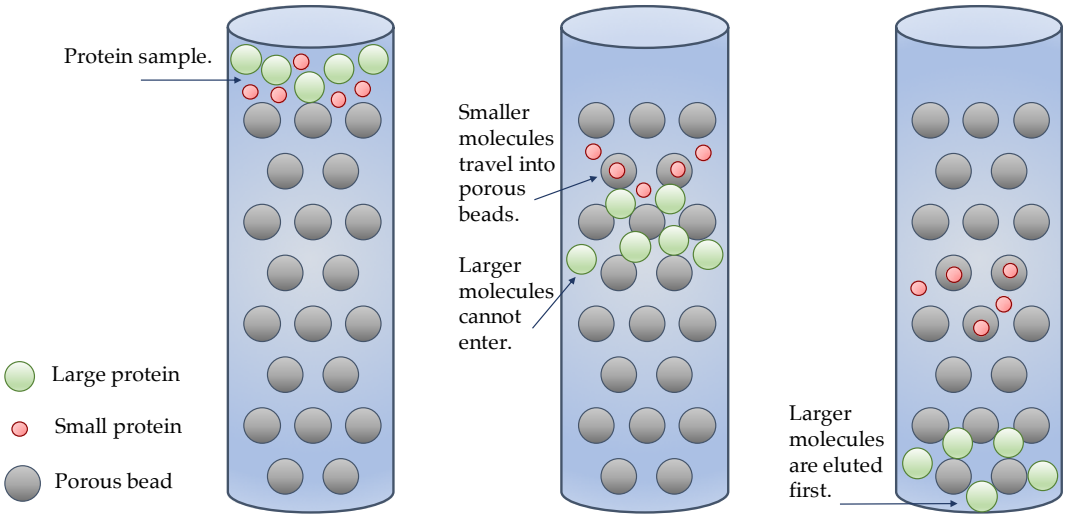

FIGURE 2.9: The process of gel filtration. A protein solution is loaded onto the column, composed of a mixture of different sizes of proteins. The beads present in the column are porous and smaller proteins can pass into these, resulting in a longer elution time. Larger proteins do not pass into the beads and so follow the shortest path and are eluted first.

There is no intentional binding interaction present in the method of size exclusion chromatography which has the additional benefit that fragile proteins are not damaged, but electrostatic and van der Waals interactions are unavoidable in many cases. Also, in the absence of binding, the resolution that can be obtained is limited.

This technique is effective in the latter stages in the purification process when the protein is mostly pure, due to the risk of large levels of contaminants damaging the column.

2.4 Crystallisation

The crystallisation of proteins for use in crystallography and subsequent structure solution has been an invaluable technique for scientists to elucidate the structure and function of biological macromolecules. Crystals are formed by the directional

and ordered self-association of protein molecules to form a periodically repeating 3-dimensional crystal lattice. The growth of good-quality crystals is essential for successful X-ray diffraction experiments. An additional challenge for neutron diffraction is the controlled growth of large crystals, often in deuterated conditions [150].

One important aspect in the formation of highly diffracting protein crystals is the purity of the protein sample. Any impurities remaining in the protein solution after the purification process can interfere with nucleation and crystal growth. They may also be incorporated into the crystal structure, affecting diffraction quality [151]. Therefore it is extremely important to have an efficient purification process where the final purity of the sample is analysed by SDS-PAGE, or mass spectrometry.

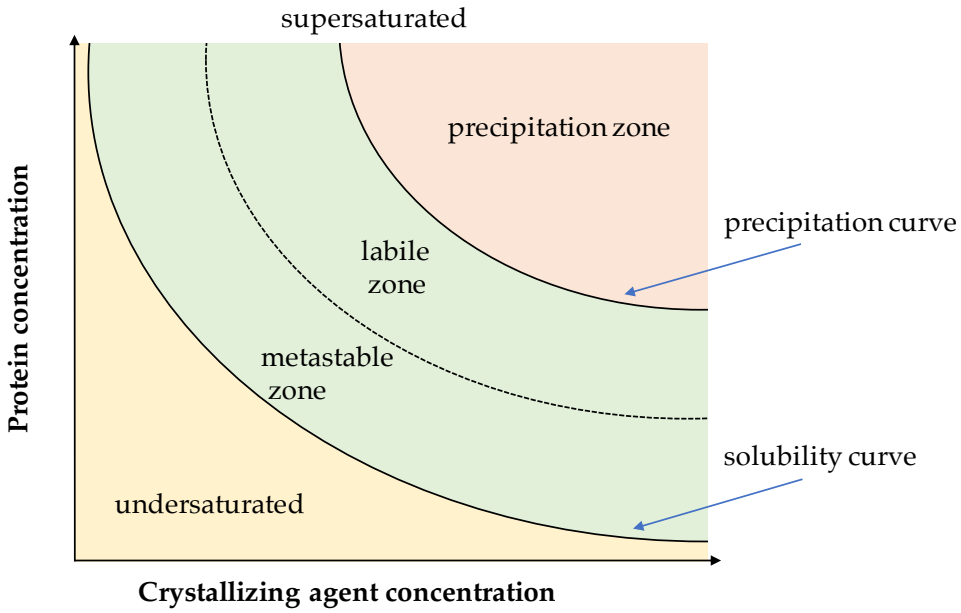

FIGURE 2.10: Graphical representation of the relationship between increasing protein concentration and increasing precipitant concentration. From the solubility diagram it is possible to identify the optimum zone for crystal growth. At low concentrations, the protein remains undersaturated and nuclei will not form. However, at very high concentrations, precipitation will occur due to the aggregation of excess of protein molecules. Nucleation occurs in the upper metastable zone, where the solution is supersaturated. This leads to the concentration of protein to decrease and crystal growth.

The phase diagram provides a pictorial representation of the crystallisation process,

shown in Figure 2.10. It shows the relationship between protein concentration and the temperature, pH, or in this case crystallisation agent concentration. Knowledge of the phase diagram specific to the target protein is valuable for the identification of the supersaturation zone, increasing the chances of crystal growth. Supersaturation is defined as when the protein concentration is higher than its solubility. On the diagram, there are four important areas in the phase diagram that relate to the likelihood of achieving crystallisation: the undersaturated region, the supersaturated region consisting of the metastable zone and the labile zone, and the precipitation zone [152].

There are two separate steps that are involved in the production of protein crystals: nucleation and growth, both driven by supersaturation [153]. Supersaturation can be achieved through manipulating the temperature, ionic strength, and pH, as well as the addition of precipitating agents [154–156]. Nucleation is a first order phase transition where the protein molecules pass from a disordered state to an ordered state [156, 157]. The formation of a nucleus involves overcoming an energy barrier and is the rate determining step in this process [152]. The rate of nuclei formation is directly related to the number and quality of the crystals produced and occurs in the labile zone. No production of nucleation is seen in the metastable zone however it governs crystal growth. Ideal crystallisation conditions initiate nucleation before leading to growth in the metastable zone, before other nucleates have time to form [157]. Therefore the optimum location for this on the phase diagram is close to the border between the metastable and labile zone. Conversely, nuclei close to the precipitation zone border tend to grow quickly and contain defects. In the precipitation zone, aggregates can form faster than nuclei if the protein concentration is too high [152].

The batch crystallisation method is a straightforward technique which involves mixing the protein solution with the appropriate precipitant solution in a closed vessel, with no additional reservoir solution [158]. A pictorial representation of the

batch method is shown in Figure 2.11. This technique involves no exploration of the phase diagram as the initial conditions achieve supersaturation directly and remain stable for several weeks. Well diffracting crystals can be produced in these conditions by ensuring that nucleation occurs when the protein and crystallisation solution are initial contact, reaching the metastable zone as the solutions are mixed [155].

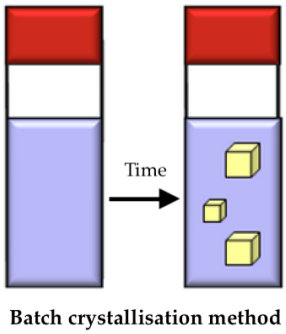

FIGURE 2.11: Batch crystallisation method. Small vials, or wells, containing protein and precipitant solutions at supersaturated conditions are sealed and left undisturbed during crystal growth. Figure adapted from [155].

2.5 Crystallography

2.5.1 Crystal Structure

The most popular way of obtaining structural information at the atomic level on biological structures is X-ray crystallography. Protein molecules are ordered into a crystal in the x, y and z dimensions, where a crystal can be considered as an infinitely repeating *lattice*. A lattice is a set of points in space where the environment of each point can be considered identical.

The simplest building block of a crystal is the unit cell, defined by lengths a, b and c and angles α, β, γ. The unit cell is generated from a motif, also referred to as the asymmetric unit, via symmetry operations. This motif can be rotated, reflected,

inverted and translated from one lattice point to another and can partially or fully occupy the unit cell. The full list of symmetry operations required to generate the unit cell from the asymmetric unit is called the space group. A space group is related to the point group but is more flexible in definition, where the point group requires operation around a defined point, the space group however allows translations and glide planes.

Unit cells can be characterised based on the number and locations of the lattice points in the following manner: primitive (P), body-centred (I), face-centred (F) and side-centred (C). When combined with the 7 crystal systems, 14 Bravais lattices can be described detailing the individual characteristics of both the unit cell and symmetry, shown in Table 2.1.

TABLE 2.1: The seven crystal classes.

Lattice system	**Axial lengths and angles**	**Bravais lattices**
Cubic	a = b = c $\alpha = \beta = \gamma = 90°$C	P, I, F
Tetragonal	a = b $\neq$ c $\alpha = \beta = \gamma = 90°$C	P, I
Orthorhombic	a $\neq$ b $\neq$ c $\alpha = \beta = \gamma = 90°$C	P, I, F, C
Hexagonal	a = b $\neq$ c $\alpha = \beta = 90°$C, $\gamma = 120°$C	P
Trigonal	a = b = c $\alpha = \beta = \gamma \neq 90°$C	P
Monoclinic	a $\neq$ b $\neq$ c $\alpha = \beta = 90°$C, $\gamma = 120°$C	P, C
Triclinic	a $\neq$ b $\neq$ $\alpha \neq \beta \neq \gamma \neq 90°$C	P

In combination with the number of Bravais lattices, a total of 230 space groups are possible including 32 point groups. However, mirror planes and centres of inversion are excluded for biological molecules. These are examples of improper symmetry where an object is transformed onto a mirror image however it is not possible in this case as amino acids possess a chiral centre [159]. This leaves a total

of 11 point groups that can exist for biological molecules. The point group is what defines the morphology of the crystal.

The unit cell is repeated by translations throughout the crystal in all directions to give a highly ordered structure [160].

2.5.2 The Scattering of Waves

Elastic scattering is seen when an incident wave is scattered by an object, for example an atom, changing the direction of the wave but conserving its momentum. An example of elastic scattering is diffraction. Scattering from one atom is extremely weak so multiple atoms are needed to amplify the intensity of the scattered wave. In the case of crystalline material, a series of ordered atoms lie on planes at defined distances apart forming the crystal lattice. Bragg's Law, Equation 2.1, defines the conditions in which diffraction is possible. It relates the wavelength of radiation λ, the scattering angle θ between the incoming wave and plane and the distances between atoms on planes d_{hkl} [161].

$$n\lambda = 2dsin\theta \tag{2.1}$$

In order to examine atomic structures, a probe that has a wavelength of the same order as atomic spacings is required. X-rays with a wavelength of Angstroms (Å) are a common and highly used probe as they are relatively cheap to produce in comparison to other sources. It is also possible to produce X-rays with a high flux which allows the examination of small and complex structures in a short timeframe. Neutrons also have a number of advantages as an atomic probe. Both X-rays and neutrons can be produced with varying wavelengths.

Bragg planes are represented by three Miller indicies *h*, *k*, *l*. These values relate the planes to the unit cell. The *hkl* value represents the number of times that the Bragg plane cuts the *a*, *b* and *c* axes of the unit cell respectively. For example (*h*, *k*, *l*) = (3,2,1) cuts the *a* axis 3 times, *b* axis two times and the *c* axis once. If there is a value of 0 this indicates that the plane does not cross a particular axis.

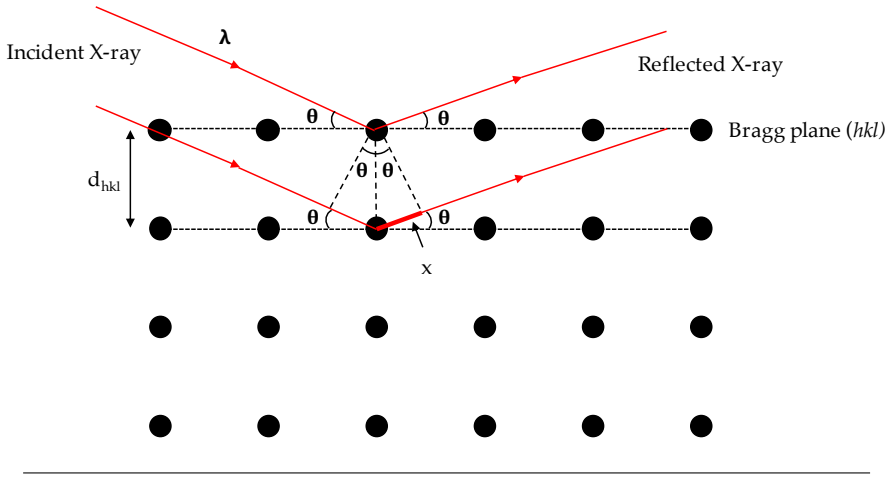

FIGURE 2.12: Two incident, in phase, X-rays are reflected by planes defined by *hkl*, separated by an interplaner distance, d. The second wave has to travel extra distance *n*, equal to an integer number of wavelengths to remain in phase. The angle of incidence is denoted as θ and is the same as the angle of reflection. The relationship $n\lambda = 2dsin\theta$ defines the conditions that satisfy Bragg's Law.

There are two types of scattering: coherent and incoherent. Coherent scattering is seen where the pathlengths of waves are different by $n\lambda$ representing an integer number of wavelengths. This means that the waves remain 'in phase' and interfere constructively with the addition of their amplitudes. Incoherent scattering is where these criteria are not met and the amplitudes of the 'out of phase' waves cancel. A representation of Bragg's Law with respect to atomic positions is shown in Figure 2.12.

Reciprocal space is an important concept in crystallography. In addition to the real space lattice, a reciprocal lattice also exists. This reciprocal lattice is seen on the *diffraction pattern*. The diffraction pattern is measured from the constructively scattered waves that fulfil Bragg's Law. Each spot on a diffraction pattern, known

as a reflection, corresponds to a lattice point in reciprocal space with coordinates *hkl* and a set of planes in the real space crystal.

The real space lattice is defined by the dimensions a, b and c however it is necessary to consider a reciprocal lattice defined in the Equation 2.2. Any point on the reciprocal lattice can be calculated by summing unit translations (a_*, b_*, c_*) of the reciprocal lattice with any integer (h, k, l), as defined in Equation 2.2.

$$s = ha^* + kb^* + lc^* \tag{2.2}$$

2.5.3 The Ewald Sphere

Monochromatic Data Collection

The Ewald sphere gives a pictorial representation of Bragg's Law and what conditions are required in a diffraction experiment [162]. It is a geometrical construction of a sphere with the real crystal and what can be considered as the real space origin in the centre. When a reciprocal lattice point, representing the real space Bragg planes, lies exactly on the edge of the sphere, Bragg's Law is satisfied and diffraction is seen. The sphere has a radius of $1/\lambda$, representing the wavelength λ in reciprocal space and the diffracted beam is represented by S, the scattered wave. In addition, there is a limiting sphere within the construction, shown in Figure 2.13. The radius of $2/\lambda$ defines the maximum resolution that can be obtained from a diffraction experiment: if there are lattice points that fall outwith the limiting sphere, it will not be possible to record these reflections during the experiment. Reducing the wavelength results in a larger Ewald sphere and more measurable reflections. Larger unit cell dimensions have smaller reciprocal lattices, resulting more reflections but also in closer recorded diffraction spots. The Ewald sphere construction is independent from the contents of the unit cell and relates to both

the unit cell dimensions and wavelength of radiation.

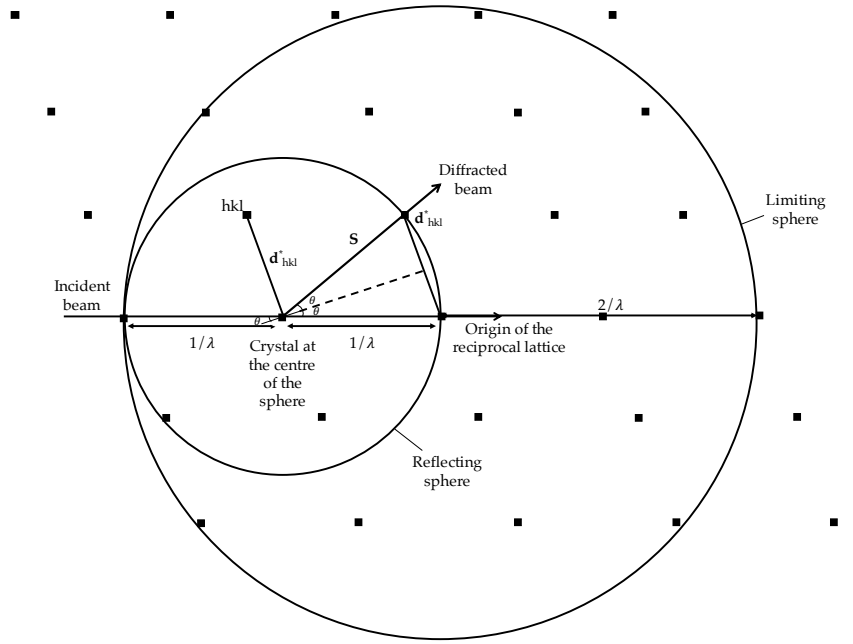

FIGURE 2.13: The Ewald construction in the monochromatic case. The Ewald, or reflecting, sphere has a radius of $1/\lambda$ with the crystal located at the centre. Lattice points located on the edge of the sphere indicate the conditions in which Bragg's Law is satisfied and give rise to diffraction. The limiting sphere indicates the maximum resolution that can be obtained from this experiment.

There are two ways that Bragg's Law can be satisfied experimentally as there are two possible variables, λ and θ, whilst the d_{hkl} values stay fixed. The most common data collection method uses a *monochromatic* beam, where the value for λ is fixed and the angle of incidence, θ, is varied. Rotating the real crystal around an axis also rotates the reciprocal lattice. This rotation translates the reciprocal lattice points through the stationary Ewald sphere, achieving the diffraction of multiple lattice points from the multiple Bragg planes. Monochromatic data collection involves taking multiple adjacent frames to increase the data completeness and in order to collect full reflections that are usually spread across a selection of images. This is known as the *rotation* or *oscillation* method [163].

Quasi-Laue Data Collection

In Laue, or Quasi-Laue, diffraction experiments, the other variable in Bragg's Law is changed, λ. Laue data collection uses the full range of wavelengths, or white beam, whereas Quasi-Laue uses a range of wavelengths between a bandpass of λ_{min} and a λ_{max}, considered as a pink beam. The Ewald construction is different for Laue diffraction when representing what conditions fulfil Bragg's Law. Due to the range of wavelengths, there are two spheres representing the λ_{min} and the λ_{min} used. Each reciprocal lattice point that lies in between these two spheres is recorded as a diffraction spot, shown in Figure 2.14. This allows a broader range of reciprocal space, i.e., more reciprocal lattice points, to be measured in a single frame.

This method can be exploited in neutron diffraction experiments. Due to the typically low flux of neutrons, a Laue or Quasi-Laue data collection technique can increase both the number of reflections and the flux relative to the monochromatic method [164]. However, spatial overlap can become a problem when using the Quasi-Laue data collection strategy. This issue arises when protein crystals have large unit cell dimensions or display a high degree of mosaicity. Not only are these common problems in macromolecules but the need for larger protein crystals in neutron macromolecular crystallography also leads to an increased risk of higher mosaicity. To reduce this effect, the bandpass can be narrowed resulting in fewer reflections or alternatively the sample to detector distance can be increased to spread out reflections, preventing overlap [165]. Harmonic overlaps are also problematic with Quasi-Laue data collection: where Bragg's law is satisfied by multiple wavelengths and reflections are superimposed on the detector [166]. However using a longer λ can reduce the effect by separating the Bragg peaks [166].

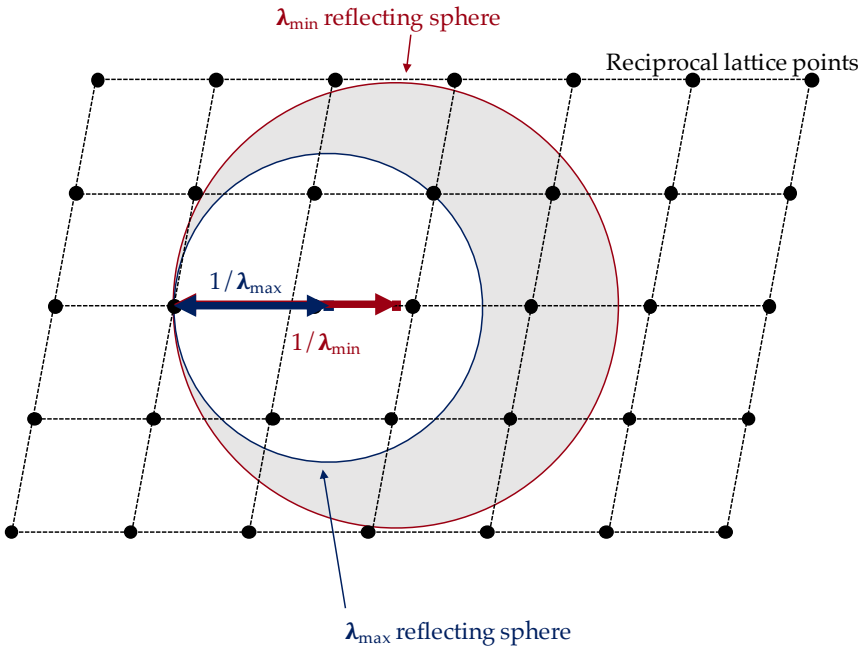

FIGURE 2.14: A range of wavelengths are used in Quasi-Laue data collection between λ_{min} and λ_{max}, defined by the two circles. Points on the reciprocal lattice give rise to diffraction if located inside the two circles, covering a larger area of reciprocal space than in monochromatic mode.

TABLE 2.2: Neutron coherent scattering lengths and incoherent cross sections for common elements found in macromolecular structures. The X-ray scattering factors are also included for direct comparison.

Isotope	**Atomic number**	**Neutron coherent scattering length (10^{-12} cm)**	**Neutron incoherent cross section (Barn = 10^{-28} m^2)**	**X-ray scattering factors (10^{-12} cm)**
^{1}H	1	-0.374	80.27	0.28
^{2}H	1	0.667	2.05	0.28
^{12}C	6	0.665	0.00	1.69
^{14}N	7	0.973	0.50	1.97
^{16}O	8	0.580	0.00	2.25
^{32}S	16	0.280	0.00	4.50

2.5.4 X-ray and Neutron Scattering Factors

In X-ray diffraction, the X-rays are scattered by electron clouds with the intensity proportional to the number of electrons squared, $I \propto z^2$. Each atom has a different scattering factor, which increases with the number of electrons. Common elements such as carbon and oxygen have form factors of 1.69 x 10^{-12} cm and 2.25 x 10^{-12} cm whereas lighter elements have a much lower form factor value such as of 0.28 x 10^{-12} cm for hydrogen. In addition, the scattering factor decreases with increasing scattering angle $\sin\theta/\lambda$ due to the similar size of the electron cloud and the wavelength of the X-ray beam. Table 2.2 details the X-ray scattering factors for elements commonly found in macromolecules.

Neutrons do not follow the same trend as they interact with the nucleus, not the electron cloud. The coherent scattering length b_c, is equivalent to the X-ray scattering factor however it has no dependency on the scattering angle and the magnitude of b_c is indicative of the strength of the interaction. This can be explained by the smaller size of the nucleus in comparison to the neutron beam. The b_c value can also be positive or negative, unlike X-ray scattering factors which are always positive. Whether the sign is positive or negative is associated with a shift in phase

between the incident and scattered neutron waves. Interestingly, the neutron scattering power shows no clear pattern across the periodic table. This is detailed Table 2.2.

Neutron coherent scattering lengths are also isotope specific, meaning that there can be different values for nuclei of non-zero spin. We can consider two isotopes of hydrogen: ^{1}H and ^{2}H, or deuterium. Both ^{1}H and ^{2}D have different nuclear compositions leading to very different scattering lengths. The average scattering length for a ^{1}H nucleus is b = -0.374 x 10^{-12} cm whereas the average value for a ^{2}H nucleus is b = 0.668 x 10^{-12} cm (Table 2.2).

There is also an incoherent cross-section to consider, measured in Barns; 1 Barn = 10^{-24} cm^2. The incoherent cross-section is most significant in elements containing unpaired nuclear spins. This contributes to the overall background measurement, which can mask the strength of the coherent scattering by decreasing the signal to noise ratio (Table 2.2).

2.5.5 Structure Factors and Electron Density

Reciprocal space and real space are mathematically related via a Fourier transform and this relates the diffraction pattern to the diffracting object, as previously described. Any given reflection *(hkl)* can be represented as a structure factor containing an amplitude and a phase, F_{hkl}. The structure factor is a summation of the scattering contributions from all atoms on the plane *hkl*, each with a corresponding structure factor f_{hkl}.

Structure factors for X-rays can be described as shown in Equation 2.3. This represents the scattering from any given singular atom i corresponding to plane *hkl* resulting in f_i contributing to the amplitude of the reflection. The second term $e^{2\pi i(hx_n + ky_n + lz_n)}$ represents the phase of the wave.

$$f_{hkl} = f_i e^{2\pi i(hx_n + ky_n + lz_n)} \tag{2.3}$$

Amplitudes are obtained experimentally by measuring the intensity of the diffraction spots. All atoms contribute to each reflection in the diffraction pattern with each atomic scattering factor contributing to the measured amplitude. The total scattering in a reflection can be represented by summing all scattering factors f_{hkl} and phases for each atom, shown in Equation 2.4.

$$F_{hkl} = \sum_{n=1}^{n=N} f_n e^{2\pi i(hx_n + ky_n + lz_n)} \tag{2.4}$$

Another description of F_{hkl} involves the integration of the electron density, ρ, at the given position x, y, z, as described in Equation 2.5. This relationship is important as it relates the measured amplitudes to the electronic structure of the object under investigation.

$$F_{hkl} = \int_h \int_k \int_l \rho(x, y, z) e^{2\pi i(hx_n + ky_n + lz_n)} dxdydz \tag{2.5}$$

However crystals are not immobile objects, with atomic vibrations affecting the quality of the diffraction. An additional factor must be taken into account when calculating the structure factors, known as the Debye-Waller factor, or B factor, defined in Equation 2.6.

$$B_j = 8\pi^2 U_j^2 \tag{2.6}$$

This additional term has units Å^2 and where U is the measurement the mean-square displacement of atom j. As the U parameter increases, the overall B-factor increases and reduces the scattering contribution from the atom. The vibration of

the atoms can result in the electron density becoming spread out as a result of the disorder. The true equation relating the structure factor and the electron density considering this additional term is shown in Equation 2.7.

$$F_{hkl} = \int_h \int_k \int_l \rho(x, y, z) e^{2\pi i(hx_n + ky_n + lz_n)} e^{-B_j sin^2\theta/\lambda^2} \tag{2.7}$$

As previously described, when expressed as a Fourier transform the structure factors (F_{hkl}) can be calculated using the electron density, *ρ(x,y,z)*. Fourier transforms can be reversed, therefore it is possible to calculate the electron density *ρ(x,y,z)* from the structure factors F_{hkl}. This reverse Fourier transform is shown in Equation 2.8, where the volume of the unit cell is represented by V.

$$\rho_{x,y,z} = \frac{1}{V} \sum_h \sum_k \sum_l |F(h,k,l)| e^{2\pi i(hx_n + ky_n + lz_n)} \tag{2.8}$$

Each F_{hkl} contains the information on all of the atoms in a given plane *hkl*. It represents a wave, consisting of an amplitude, a frequency, and a phase. Amplitudes are measured and λ is known from the X-ray source. The variable that is lost during the diffraction experiment is the phase information. As this is needed in order to calculate the electron density this poses a problem, known as the *phase problem*. Methods developed for solving this phase problem include Patterson Methods, SAD and MAD Phasing, and Molecular Replacement. There is also the method of protein structure prediction which uses the amino acid sequence to predict the secondary and tertiary structure of the protein.

2.5.6 Data Collection and Processing

The first step from diffraction images towards structure solution is indexing the diffraction patterns from the images collected during the experiment. The aim of

indexing is to obtain a list of *hkl* indicies for each recorded reflection. Indexing the data once the diffraction images have been collected provides the approximations of the unit cell dimensions, the crystal orientation and an estimate of the Bravais lattice. These are used in conjunction with knowledge of the instrument parameters such as crystal-detector distance and wavelength.

Indexing can also be conducted using only a few images in order to devise a data collection strategy most suitable for the crystal. Knowledge of the Bravais lattice indicates any symmetry elements and this knowledge can be useful to ensure the collection of a complete dataset. It is also possible to estimate the most likely space group from the symmetry-related intensities. These symmetry elements can then be exploited to minimise the exposure to the beam, which is especially important for radiation sensitive samples. As neutrons show no obvious damage from exposure to the beam, this is less of a problem.

To obtain the intensities (I) related to the *hkl* values from the diffraction pattern, the diffraction spots must be integrated. It is also necessary to obtain the errors associated with the intensities or, standard uncertainties (σ). This process involves predicting the position of each Bragg reflection on each image and measuring the intensity and error estimate, after background subtraction. There are two methods that can be employed: summation integration and profile fitting [167]. In summation integration, the number of pixels and their values are added together, background pixels are also summed and subtracted from the total pixels value. This is most useful for strong diffraction spots. The profile fitting method provides a more accurate estimate of the integrated intensity for weaker reflections. It assumes either a 2D or 3D shape is known for each spot and the intensity is calculated when a best fit is seen between the known spot profile and the observed spot profile [168].

Indexing and integration programs that are commonly used are XDS [169], Mosflm [168], HKL2000 [170] and DIALS [171] for monochromatic data and *LAUEGEN* [172] for Laue diffraction.

After indexing and integration, an *mtz* file is generated that contains all of the unmerged reflections. Scaling and merging steps are required in order to equate all the observations on a common scale. The data are not on a common scale due to a number of experimental parameters including, but not limited to: radiation damage, fluctuations in incident beam, absorbance in the crystal as a result of non-uniform morphology.

Quasi-Laue neutron data collection has an additional stage. As a range of wavelengths are used, an additional step known as *wavelength normalisation* must be conducted. This can be done using the program *LSCALE* [173]. This is done to equate the measured intensities from different wavelengths onto a common scale prior to scaling.

2.5.7 Data Quality Indicators

There are numerous indicators that are available for crystallographers to use when evaluating the quality of the data. There are indicators for both merged and unmerged data. The difference between the per image B-factor, R_{factor}, and/or Deiderichs R_d factor [174] of the unmerged data can be used to estimate the amount of radiation damage a sample receives, important for biological molecules. There are also indicators that can calculate the precision of merged data which are more important for downstream processes.

$$I/\sigma(I) \tag{2.9}$$

Historically, the signal to noise ratio has been used to decide a high resolution cut-off before scaling. Below that level the diffraction spots can be excluded from the data used in refinement. The universally accepted cut-off level was $\sim$ 2 - 3.

Other metrics include R_{merge} and $R_{p.i.m}$.

$$R_{merge} = \frac{\sum_{(h,k,l)} \sum_{i=1}^{n} |I_i(h,k,l) - I(h,k,l)|}{\sum_{(h,k,l)} \sum_{i=1}^{n} I_i(h,k,l)} \tag{2.10}$$

R_{merge} calculates the agreement between multiple measurements of a reflection around the average. However, this value tends to increase with an increased number of observations (multiplicity) and is now commonly replaced with other statistical indicators [167, 175, 176].

$$R_{p.i.m.} = \frac{\sum_{(hkl)} \sqrt{1/n-1} \sum_{(h,k,l)} |I_i(h,k,l) - I(h,k,l)|}{\sum_{(h,k,l)} \sum_{i=1}^{n} I_i(h,k,l)} \tag{2.11}$$

$R_{p.i.m.}$ (precision-indicating merging R_{factor}) is used to calculate the precision of merged data. It describes the precision of the averaged intensity measurements and details the standard error of the mean. This statistic is related to R_{merge} with an additional term that removes the relationship with multiplicity. It is therefore a more appropriate choice than R_{merge} for deciding a high resolution cutoff [176, 177].

$$CC_{1/2} = \frac{\sum (x - \langle x \rangle)(y - \langle y \rangle)}{[\sum (x - \langle x \rangle)^2 \sum (y - \langle y \rangle)^2]^{1/2}} \tag{2.12}$$

For $CC_{1/2}$, the dataset is randomly split into two halves and within each dataset the average intensity is calculated for each unique reflection. Plotting this correlation coefficient (CC) against resolution measures the internal consistency of the dataset. The range of $CC_{1/2}$ is from 1.0: total correlation and 0.0: no correlation. The value of $CC_{1/2}$ tends to 0 with the decrease in the signal to noise ratio. It is the primary indicator for selecting a high resolution cutoff [176]. An example of a recommended resolution cutoff is given in software package xia2, where the default cutoff value of $CC_{1/2} > 0.5$ [178]. However, it has also been observed that including data up to a value of $CC_{1/2} \sim 0.1$ - 0.2 resulted in improved the quality of the difference maps and led to an improved refined model [179].

2.5.8 Structure Refinement and Model Building

After data collection and reduction is completed and phases are obtained, it is necessary to refine a model against the data collected. The model is typically in the form of a PDB, a file which contains information on the protein sequence, atomic coordinates, B-factors (isotropic or anisotropic), and occupancies. This process in the context of this thesis is covered in Chapter 4, Section 4.5 and Chapter 5, Section 5.5.

Structural refinement is the optimisation of a series of model parameters in order to give the best model fit against a set of observations [180]. This iterative process is carried out which aims to build a molecular model that will best fit the data collected.

Key aspects of structural refinement are 'observations' and 'parameters of a model'. Observations include everything known about the model prior to refinement: unit cell parameters, structure factor amplitudes, phase information and stereochemical knowledge [180]. Parameters of a model are commonly detailed in a PDB format [181], and include the atomic coordinates, atomic displacement parameters, and occupancies. Refinement quality is improved when there is a larger ratio of observations to parameters.

Restraints and constraints can be used in order to aid the refinement process. A restraint prevents specific individual/independent parameters from diverging too far from target values. This is done using accepted knowledge of the structure such as bond angles or bond lengths [182, 183]. Knowledge from a higher resolution similar structure, or a reference model, can also be used as external restraints. This involves using distance restraints between nearby atoms from the reference model to aid the refinement. Mathematically, restraints can be considered as additional experimental observations, by restricting the possible values of the parameters in question [184]. A constraint forces specific parameters to be refined together, for

example, a rigid body refinement or fixing an atomic position. This imposes a restriction onto the refinement calculation and improves the ratio of observations to parameters.

The model and electron or neutron density maps can be visualised using molecular graphics packages, such as Coot [185]. The observed structure factor amplitudes are described as F_o and the structure factor amplitudes calculated from the model are described as F_c. Two electron or neutron density maps are consulted during structural refinement. The $2F_o$-F_c, or a Sigma-A weighted map $2mF_o$-DF_c, is a representation of the electron density around the model. The F_o-F_c/mF_o-DF_c map, or 'difference map', can indicate errors in the model. If there are atoms missing then these appear as positive density whereas when there are incorrectly placed atoms in the model, the difference map shows negative density. This map gives an indication of how close the model is to the experimental data with peaks above 3.0 σ deemed significant. This map can also provide useful information when used in calculating an *omit map*, where parts of the structure such as small molecules and mutated sidechains are removed. If truly present in the structure, these atoms are clearly visible in the difference map. As the model is amended as per the indications of the F_o-F_c, the phases systematically improve.

2.5.9 Joint Refinement

X-ray data provides information on the distribution of electrons within a sample. As this is intrinsically related to the mass of the atom, X-ray data can provide information on C, N, O, S atoms within proteins. In comparison, neutrons provide information on the nuclear positions as they are scattered by nuclei, including ^{1}H and ^{2}D atoms. Therefore it is possible to use the complementary X-ray and neutron data together using a joint refinement strategy to solve the structure. This can be conducted using programs such as *phenix.refine* [186].

Refinement should be conducted on datasets ideally taken from the same crystal, or at least an isomorphous sample, for example, under the same crystallisation conditions and experimental temperature [186]. Including ^{1}H and ^{2}H atoms in the model leads to a substantial increase in the number of refinement parameters, however, this problem is offset by the increase in experimental data available to use in a joint structural refinement [186]. Furthermore, the addition of the extra information from the X-ray data aids the low completeness and resolution commonly seen in neutron datasets.

2.5.10 Model Validation and Statistical Indicators

The progress of refinement can be monitored concurrently by the global statistical indicator the R-value, or R_{work}/R_{factor}, which measures the discrepancies between the observed structure amplitudes and those calculated from the model [187]. The lower the value of this R-factor indicates the increase in correlation between the data and model. However it is possible to overfit the data, interpreting information as significant when this is not the case, which can artificially reduce the R_{work} [187, 188]. To counteract this problem, an additional cross validation metric known as R_{free} is also monitored during refinement. This involves excluding a small percentage of the reflections from the refinement process and calculating an R_{factor} from these reflections independently from the refinement. This is a method of reducing bias as there is no effect from the refinement to these reflections. A clear indication of overinterpretation of the data is when the values of R_{free} and R_{work} diverge to over a 10% difference.

$$R_{factor} = \frac{\sum_{(h,k,l) \notin \{testset\}} ||F_{obs}(h,k,l) - F_{calc}(h,k,l)||}{\sum_{(h,k,l) \notin \{testset\}} |F_{obs}(h,k,l)|} \tag{2.13}$$

$$R_{free} = \frac{\sum_{(h,k,l)\in\{testset\}} ||F_{obs}(h,k,l)| - |F_{calc}(h,k,l)||}{\sum_{(h,k,l)\in\{testset\}} |F_{obs}(h,k,l)|} \tag{2.14}$$

Another method of model validation is the Ramachandran Plot [189, 190]. This uses prior knowledge of stereochemical restraints and is essential to the structure determination of macromolecules [191]. It has a pictorial representation of the stereochemical information, plotting the torsion angles ϕ and ψ of all amino acids contained in the macromolecule. Plotting the possible combinations of angles, establish what angle combinations are not possible due to steric hinderance. It plots individual residues into 'fully allowed', 'partially allowed' and 'forbidden' depending on identified clashes between atoms within the residues. This information can be consulted during and after the model building process in order to assess the likelihood of amino acid conformations, pointing towards a feasible model.

2.5.11 Radiation Damage

X-rays provide an ideal probe for examining protein structure at the atomic level, however, radiation-induced degradation, or radiation damage, can occur during data collection, particularly those conducted at 'brighter' light sources. At a wavelength of 1A, around 10% of the interacting X-ray photons are elastically scattered (diffraction) [192]. Approximately 90% of interacting photons will deposit their energy into the crystal via the photoelectric effect, resulting in excitation processes [193], and through Compton inelastic scattering.

The excitation events caused by the photoelectric effect can cause structural damage to the protein molecules and overall crystal lattice. The photoelectric effect describes the ejection of a tightly bound electron from the inner shell of an atom, following the absorption of a high energy X-ray photon, and leads to radiation damage [194]. The ejected electron will produce 500 additional ionisations within

a few micrometers of the initial ionisation site [195, 196]. Radiation damage can be divided into primary and secondary radiation damage. Primary radiation damage is a result of the X-ray photons interacting with an atomic electron within the crystal. This leads to the absorption of energy, where this energy is either dissipated through heat (thermal vibration of the molecule), or results in the generation of high energy photoelectrons, lower energy Auger electrons, and other radical species [197, 198] and is dose dependent. Secondary radiation damage arises when the species produced in the primary event cause damage to the sample through the generation of additional free radicals. Secondary radiation damage is both time and temperature dependant. Both primary and secondary radiation damage can be further classed as direct or indirect events. Direct events involve the generation of radicals from the atoms in the protein molecule whereas indirect events are produced from non-protein atoms, e.g., the destruction of solvent molecules where hydroxyl and hydrogen radicals are produced [197, 198].

These reactive species lead to a series of chemical reactions which can alter the structure of the sample and can cause both global and specific effects. Global radiation damage appears by a loss of resolution of the data, an increase in Wilson B-factors and mosaicity, and can alter unit cell parameters [192, 199]. Experimental factors that can be consulted to assess radiation damage include per-image R_{merge}, per-image B-factor, and Diederichs R_{factor} (Rd) [174]. Specific damage as a result of irradiation includes modification of individual residues, causing local changes before the overall diffraction of the crystal is affected. For example, disulphide bonds can be reduced causing bond breakage, and decarboxylation of acidic residues can occur, resulting in the generation of CO2 [199–202]. In the case of extensive radiation damage, these effects can be observed in the electron density maps. Active sites have been found to be particularly vulnerable to radiation damage [201, 203]. Redox proteins and those containing metal atoms can be easily reduced during irradiation, leading to important changes in the structure during the data collection [203], with Beitlich and colleagues [204] specifically referring to heme proteins as

ṽacuum cleaners, describing their ability to suck up electrons. This is due to the likelihood that an atom will interact with an X-ray photon increases with atomic number [196]. As a result it may not be possible to distinguish structural features attributed to radiation damage from the results of mechanistic reactions, questioning the reliability of the results obtained using this technique, and creating difficulties in obtaining high resolution data [198, 205]. However, there are cases where radiation damage has been used in experiments as an asset. Phasing methods utilising structural damage inflicted by X-rays, radiation damage-induced phasing (RIP), have been shown to be successful in several cases where datasets have been collected at high brilliance sources [206–208]. Investigations into catalytic mechanisms have also used radiation damage to their advantage [81, 209]. In order to mitigate the effects of radiation damage, crystals can be cooled to cryogenic temperatures of between 80-100 K before and during data collection. This process of cryo-cooling does not prevent primary radiation damage [210, 211], but can reduce the effect of secondary radiation damage by 70 fold [212] as the diffusion of free radicals is reduced. As a result, it is now estimated that over 90% of protein structures have been determined at cryo-temperatures [213]. Alternatively, the use of radical scavengers has been suggested to reduce the detrimental effects of free radicals caused by irradiation [195]. However, there are problems when proteins complexes containing radical scavengers as they can increase the susceptibility of the active site to radiation damage, as is the case for UOX studies where the substrate UA is a free radical scavenger [81]. Serial X-ray crystallography involving multiple crystals can alleviate the effects of radiation damage and complementary techniques can also be utilised in order to monitor any radiation induced changes, such as microspectrophotometry, Raman, and EXAFS [81, 194, 214].

While X-ray crystallography remains the most popular technique in structural biology, other methods can be used to investigate radiation-sensitive structures. Studies involving X-ray Free Electron Lasers have been proved to be advantageous in such cases [215]. The use of a very intense X-ray beam allows for a large X-ray dose

to be deposited at ambient temperatures, with pulses on the femtosecond timescale, leading to measurable diffraction before the complete ionisation of the structure destroys the lattice [216]. Alternatively, the use of neutrons as a non-destructive probe can also be valuable in samples susceptible to radiation damage [164, 217]. As neutrons do not cause any observable radiation damage, it is possible to study protein samples at RT without any unwanted destructive effects and under more physiological conditions. The technique of neutron macromolecular crystallography is covered in more detail in Section 2.6.

2.6 Neutron Macromolecular Crystallography

X-ray crystallography accounts for $\sim$ 138,000 structures in the PDB and gives information on the structures of biomacromolecules at the atomic level, namely the heavier atoms (C, N, O, S) [75]. Due to the short data collection times and small sample requirements, it is the probe of choice for structural biology. Notably, only $\sim$ 900 structures have been determined to a resolution of < 1.0 Å, the resolution at which it is possible to visualise hydrogen atoms. Additional factors such as high levels of thermal motion or bond polarity may also have an effect on the ability to locate hydrogen positions, meaning that even at high resolution, confidently identifying their locations remains challenging [218]. In the context of macromolecules where around 50% of atoms are hydrogen, the knowledge of these positions is important to fully understanding both function and structure. Many biological processes centre around hydrogen bonding networks, protonation states of residues and substrates, and proton transfer pathways.

Neutron macromolecular crystallography (NMX) is a complementary structural technique to X-ray macromolecular crystallography. NMX is responsible for $\sim$ 150 PDB depositions, with > 50% of these in the last 5 years [75]. Many aspects of enzymatic mechanisms involve hydrogen atoms and, from NMX studies, it is possible

to locate hydrogen positions in macromolecules. This allows the elucidation of protonation states of amino acid residues, hydrogen bonding networks, and water orientations, information previously unattainable from other techniques. However, drawbacks from this is that neutron production is expensive, interaction is relatively weak and the flux of neutrons is very low. This leads to long data collection time and the need for large samples to amplify the scattering signal.

The scattering power of hydrogen is of the same order of magnitude as carbon when using neutrons as the diffraction probe compared to using X-rays which is dependant on the number of electrons, hydrogen only having one (Section 2.5.4, Table 2.2). However, the coherent scattering length of ^{1}H is negative. This results in unwanted cancellation effects seen in neutron scattering density maps. For example, in common groups, such as -CH_2 and -CH_3, the negative scattering of the ^{1}H, -0.374 x 10^{-12} cm, cancels the signal from the positively scattered C atom, 0.665 x 10^{-12} cm. In addition, the large incoherent cross-section of ^{1}H contributes to a large background on the detector during experimental measurements. This results in a decreased signal to noise ratio and subsequently limits the resolution of the data.

The ^{2}H isotope of hydrogen, deuterium, plays a key role in neutron experiments. As previously mentioned, neutron scattering power varies according to nuclear composition, therefore deuterium has different properties to ^{1}H. Deuterium has a positive coherent scattering length value of 0.667 x 10^{-12} cm, similar to that of ^{12}C and ^{16}O, shown in Table 2.2. This positive value does not result in cancellation effects that are seen with ^{1}H. In addition, the incoherent scattering cross-section is $\sim$ 40 times lower for ^{2}D than ^{1}H (2.05 Barn vs 80.27 Barn). This vastly reduces the contribution to the background and increases the signal to noise ratio. Replacing hydrogen atoms for deuterium is commonplace in neutron studies to increase the quality of the neutron density maps. Hydrogens can be replaced by buffer exchange or by protein expression under deuterated conditions. The deuteration methods of macromolecules are covered in more detail in Section 2.2.

2.6.1 LADI-III Diffractometer at ILL

Producing protein crystals suitable for diffraction studies has been the bottleneck for biological structural analysis for decades. In NMX there is the added difficulty that ideally hydrogen should be replaced by deuterium as discussed above. In addition, weak flux can lead to lengthy data collection times. Developments in instrumentation have enabled the use of smaller samples and shorter data collection times [164].

LADI-III (LAue DIffractometer) has been operational at the ILL (Institut Laue-Langevin) since 2008 and is used for the study of biological macromolecular crystals. A schematic layout of the LADI-III instrument is shown in Figure 2.15. The instrument is located on the H143 neutron guide which produces cold neutrons of wavelength up to 0.025 eV. A Ni/Ti multilayer band-pass filter is used to select a range of wavelengths [219, 220] and has the possible ranges $\sim$ 2.9 - 3.9 Å, 3.6 - 4.7 Å, 4.1 - 5.3 Å. For example, $\sim$ 2.9 - 3.9 Å could be selected to collect data to high resolution. Using a range of wavelengths allows multiple Bragg reflections to be collected simultaneously thus shortening data collection times and also reduces the problem of overlapping higher order reflections [221].

The instrument uses a Neutron Image Plate (NIP) which consists of a photostimulable material (BaFBr doped with Eu^{2+} ions) mounted on a flexible plastic sheet, surrounding the sample [223–225]. Gadolinium acts as a neutron scintillator and Gd_2O_3 is mixed with the photostimulable material to make the image plate sensitive to neutrons [164, 226]. The image plate lines the inside of the cylindrical drum allowing a large coverage of reciprocal space and multiple reflections to be measured at once. Both of these aspects help to reduce the data collection times needed [164].

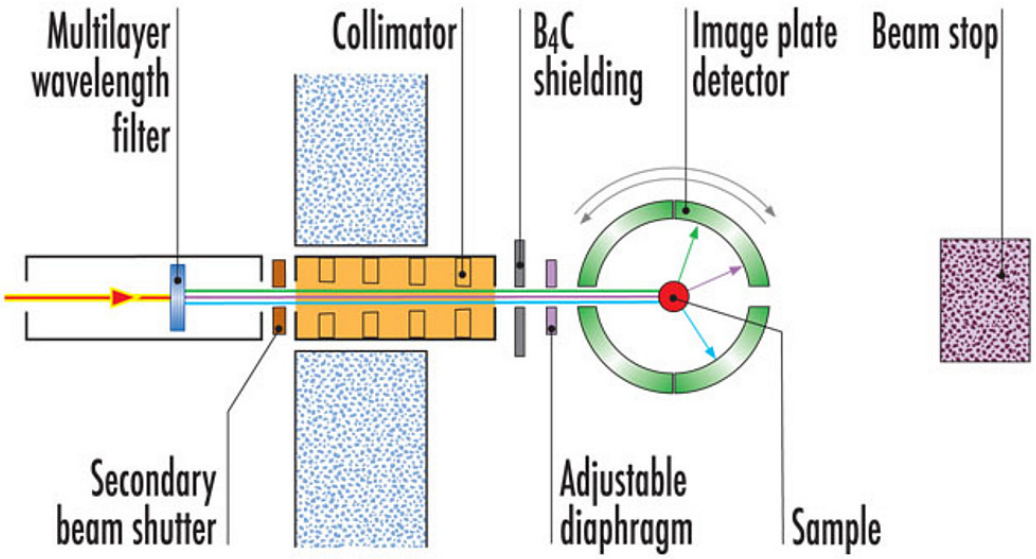

FIGURE 2.15: Schematic of the LADI-III instrument set-up at the ILL, Grenoble. The multilayer wavelength filter allows the extraction of a wavelength band most suitable to the sample. The cylindrical detector allows for a wider coverage of reciprocal space in comparison to flat detectors [164]. Image taken from [222].

2.7 Mass Spectrometry

Mass spectrometry can be used for both the qualitative and quantitative analysis of proteins. This technique can be used to rapidly and accurately determine the mass of a molecule using a small quantity of sample. There are three sections to a mass spectrometer: an ion source, a mass analyser and a detector [227]. The ionisation source is responsible for the generation of an assortment of positive and negative charged molecules in the gas phase. After ionisation, the molecules pass though a mass analyser, and are recorded on the detector at different times, directly related to their mass and charge (m/z, the mass to charge ratio). The detector counts the

number of ions and measures the relative abundance. A mass spectrum is generated plotting *m/z* versus the intensities. This technique can be used alongside time-of-flight (TOF).

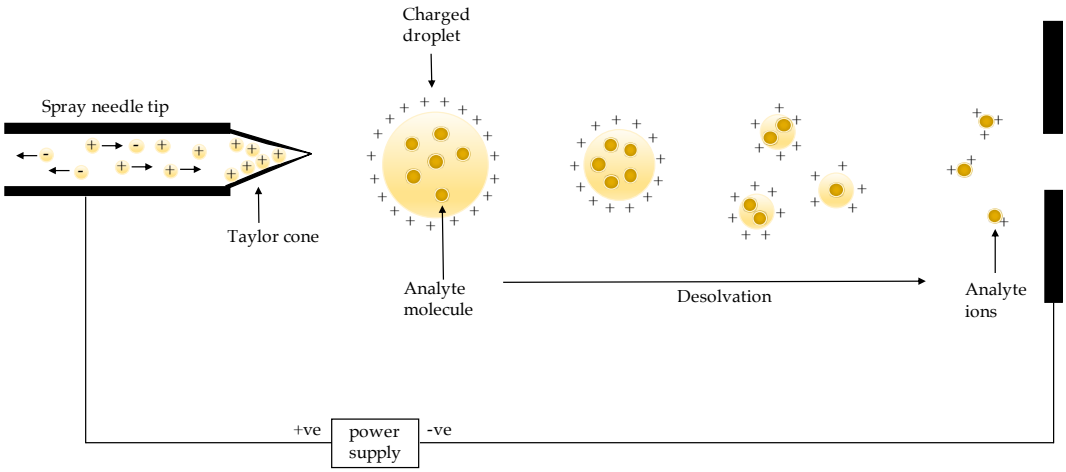

FIGURE 2.16: ESI-MS: the generation of positive charges in the Taylor cone results in the appearance of a charged droplet. Desolvation occurs until each droplet contains a single molecule of analyte, which is then measured on a detector which identifies the *m/z* ratio.

Electrospray ionisation is most commonly used for biological molecules and is shown in Figure 2.16 [228]. The sample is dissolved in a volatile solution, loaded into a conductive capillary where a voltage is applied. This electric field encourages a build-up of charges to form on the surface of the droplet at the tip of the capillary. Once the charges have accumulated to a high level the droplet bursts forming many smaller highly charged droplets. These droplets desolvate through high pressure and potential differences until each droplet contains a singular molecule of analyte.

From the resulting data, a mass spectrum is generated by plotting the different *m/z* ratios. This results in a Gaussian distribution. The value of m does not change whilst neighbouring peaks have a charge difference given as $z_1 = z_2$-1. For the determination of the m of the protein of interest, the *m/z* of two neighbouring peaks is determined experimentally as x and y. By forming two equations as ($m/z_1 = x$ and $m/z_2 = y$), simultaneous equations can be used to calculate the values for m, z_1 and z_2.

Mass spectrometry is a useful technique to evaluate the level of deuteration achieved from the perdeuteration process. With knowledge of the amino acid sequence and by measuring the masses of the perdeuterated and hydrogenated samples, it is possible to calculate the level of deuteration. It is essential to assess this to ensure a high percentage of deuteration has been reached. It is commonplace to conduct such experiments before neutron experiments in order to validate deuteration level [141, 142, 144, 229–236].

2.8 Thermal Shift Assay

The thermal stability of a protein can be determined using a Thermal Shift Assay (TSA). Also known as Differential Scanning Fluorimetry (DSF), or a ThermoFluor Assay, this technique identifies the melting temperature (T_m) of proteins upon thermal denaturation [237]. The T_m value is taken from the midpoint of the unfolding transition [238]. In contrast to Differential Scanning Calorimetry (DSC), which has historically been the method of choice for assessing the stabilities of proteins, TSA has a high-throughput and is a much cheaper method of analysis.

The use of fluorescent dyes is commonplace in TSA measurements. For example, the SYPRO Orange dye [239] is used by the HTX Platform (Platform for Structural Biology, Grenoble). The fluorescence of this dye is quenched in a polar environment, but increases in a non-polar environment [240]. With increasing temperature, the protein unfolds, exposing the hydrophobic core: this increases the fluorescence signal of the dye until the protein is completely unfolded [240, 241].

The assessment of a proteins T_m in a range of solutions can identify conditions that enhance the proteins stability [237]. This is beneficial for proteins that aggregate during storage and, therefore, require the addition of stabilising buffers or ligands [237]. In addition, it has been reported that increased stability closely

correlates with the likelihood of crystallisation of recombinant proteins, so TSA measurements can be used to identify optimal crystallisation conditions [237, 242].

TSA experiments have been conducted to investigate the effect of hydrogen and deuterium on protein stability [135, 138, 144, 243, 244]. When hydrogenated proteins are exchanged against deuterated buffers, the labile hydrogen positions are replaced with deuterium atoms. This affects hydrogen bonding interactions and has been termed the primary deuterium isotope effect [135]. The addition of deuterium into the hydrogen bonding network is thought to increase the strength of the hydrogen bonds and, subsequently, increases the T_m [135]. The replacement of non-exchangeable hydrogen atoms with deuterium affects the hydrophobic interactions in the protein, termed the secondary deuterium isotope effect [135]. It has been proposed that the replacement of hydrogen with deuterium weakens the hydrophobic interactions in the protein and, as a result, reduces the T_m. Therefore, a reduction in thermal stability is expected for perdeuterated proteins, and this effect has been observed in previous studies [138, 243, 244]. However, despite this difference in thermal stability, limited structural and functional differences have been reported.

Chapter 3

Production of Perdeuterated Urate Oxidase (DUOX) and Biophysical Characterisation

Abstract

Deuterium labelling can be an asset to neutron crystallographic experiments. The perdeuteration of proteins involves the substitution of non-exchangeable hydrogens, in addition to those located at labile positions, with deuterium. The biosynthesis of UOX in deuterated conditions requires the optimisation of the expression system in order to maximise the mass of deuterated protein, DUOX, produced. This chapter presents the optimisation of the UOX expression system and the production of DUOX using High Cell Density Culture (HCDC) in fermentation. The purification of DUOX is described, detailing the qualitative analysis of the sample at each stage of the process. Additional characterisation techniques, such as mass spectrometry and thermofluor assays are also described in this chapter. Mass spectrometry was employed to evaluate the level of perdeuteration achieved by

fermentation and a thermofluor assay was conducted to ascertain any differences in stability between hydrogenated UOX (HUOX) and DUOX.

3.1 Expression and Optimisation of DUOX

3.1.1 Bacterial Transformation

The untagged UOX wild type (UOX_{wt}) protein from *Aspergillus flavus* consists of 301 amino acids (Appendix A). The codon optimised synthetic cDNA (Genscript) was inserted into a pET24b vector (Novagen) carrying kanamycin (kan^R) resistance. The vector was kindly supplied by colleagues in the Steiner Research Group. Vector amplification was conducted using *E. coli* JM109 cells before plasmid DNA isolation and transformation into *E. coli* BL21 (DE3) competent cells. These *E. coli* cells were selected as the expression system for the production of DUOX. Cell transformation was carried out by adding 5 ng DNA to 25 μL thawed competent cells on ice for 30 minutes. This sample was then heat shocked at 42 °C for 30 seconds to allow the DNA to enter the cells, then incubated on ice for 2 minutes after mixing the solution. 100 μL SOC medium was added to the solution and incubated at 37 °C at 150 RPM for 1 hour. After incubation, the cells were spread onto an LB agar plate containing kan^R. Colony growth was seen after incubation at 37 °C, overnight (O/N).

3.1.2 Expression and Solubility Testing

The perdeuteration process requires a minimal deuterated medium and a deuterated carbon source. The expression and solubility of UOX in LB, minimal hydrogenated media, and deuterated minimal media were compared. Minimal media is used as common media such as LB are not commercially available in a deuterated

form. The contents of the minimal media (Enfors) are described in Appendix A. This section will discuss the following:

- Comparison of the expression and solubility of the protein in hydrogenated minimal media (H-Enfors) with LB
- Comparison of the expression and solubility of the protein in deuterated minimal media (D-Enfors) with LB and H-Enfors

This enabled the identification of the best conditions for the production of the protein in deuterated conditions by fermentation.

Expression and Solubility Testing in Hydrogenated Minimal Media

A hydrogenated minimal medium, H-Enfors, was first tested to establish the effect of minimal medium in comparison to nutrient rich LB medium. Solubility and expression tests were conducted on two different overexpression times at 30 °C: 5 hours and overnight. This temperature was selected as it is consistent with the fermenters optimal operational temperature.

After transformation, 50 mL of LB with kan^R was inoculated with several colonies and incubated overnight at 37 °C. 2 mL of this starter culture was used to inoculate 3 flasks of 15 mL LB and 3 flasks of 15 mL H-Enfors. All cultures were incubated at 30 °C. Once each of the flasks reached an OD_{600} of $\sim$ 0.8, a sample of 500 μL was removed to record the level of expression Before Induction (BI). Each flask was then induced with 2 mM IPTG. After each expression time, an aliquot from each sample was also taken to measure UOX expression After Induction (AI).

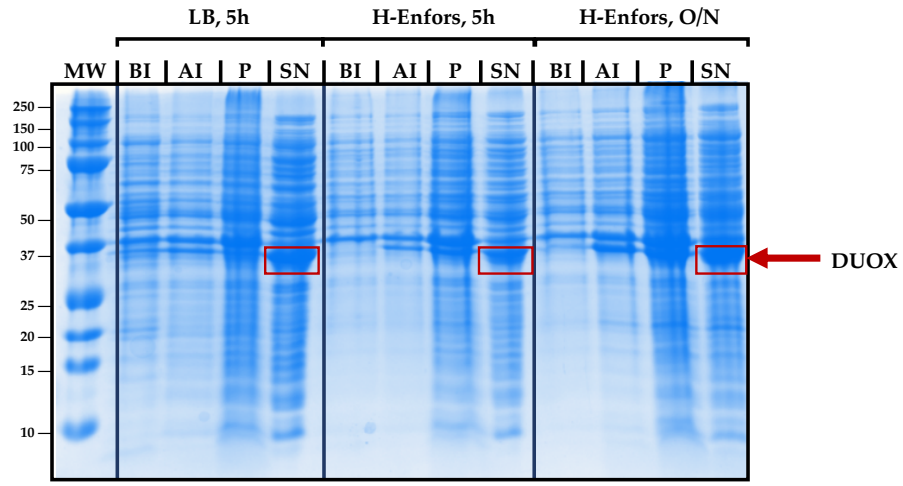

FIGURE 3.1: SDS-PAGE showing the expression and solubility of HUOX in H-Enfors, a hydrogenated minimal medium with comparison to expression in LB. The MW (kDa) lanes represent a molecular weight marker. Expression was conducted at 30 °C in both LB and H-Enfors. The different expression times are separated by a solid black line. Before Induction (BI) and After Induction (AI) samples show the level of protein expression. The level of insoluble vs soluble protein is evaluated by comparing the Pellet (P) sample with the Supernatant (SN). After visual inspection of the SDS-PAGE gel, it was concluded that the addition of minimal media shows little effect on the level of expression when compared directly to LB media. However the quantity of soluble HUOX is higher in the overnight expression time than in the 5 hours culture.

The samples before induction and after induction were analysed to investigate the effect of minimal media on the expression of HUOX. Cells were pelleted from all before induction and after induction samples by centrifugation at 10,000 RPM for 5 minutes at 4 °C. The excess supernatant was removed and 100 μL of sample buffer added and mixed.

The pellet (P) and supernatant (SN) samples were evaluated for the level of both soluble and insoluble HUOX expressed in each condition. Testing the solubility of the expressed protein required 15 mL of each of the final cultures. Cells were collected by centrifugation at 5,000 RPM for 8 minutes at 4 °C. Each cell pellet was then resuspended in 2 mL of lysis buffer (50 mM Tris-acetate pH 8.0). Cell lysis was carried out using glass beads: 0.5 mL of glass beads were added to 1 mL of the resuspended pellet. All samples were placed in the disruptor for 5 minutes at

4 °C. 3 μL of sample buffer added to 15 μL of the supernatant and set aside for the analysis of soluble protein. 50 μL of sample buffer was added directly to the pelleted cells and heat shocked at 100 °C for 10 minutes for the analysis of insoluble protein presence.

Equivalent quantities of cells from each sample were loaded onto an SDS-PAGE gel, shown in Figure 3.1. The results from minimal media were directly compared with HUOX in LB at 30°C after 5 hours expression time. A band $\sim$ 34 kDa consistent with the MW of the HUOX monomer is seen on the SDS-PAGE gel. The level of expression seen in the H-Enfors samples, at both 5 hours and overnight expression times, show a similar quantity of soluble protein to that observed in LB medium at 30 °C. This indicates that there is very little effect of minimal medium on the expression of HUOX. After visual inspection, the solubility test results between the 5 hour and overnight expression times show that there is a larger quantity of soluble protein present in the overnight expression time. This suggested that a longer expression time is the preferred condition for the expression of HUOX in minimal media.

Expression and Solubility Testing in Deuterated Minimal Media

For the production of perdeuterated protein, 100% of the components in the growth medium must be deuterated. This is to prevent the inclusion of any hydrogen that may be incorporated into the protein during expression. Prior to the fermentation process, a further test of the expression and solubility of UOX in D-Enfors was also conducted to assess the effect of deuterated minimal medium. The same parameters as the H-Enfors tests were repeated and compared to LB expressed at 30 °C. Visual inspection of the SDS-PAGE shown in Figure 3.2 shows that level of expression is higher in the D-Enfors overnight sample when compared to the 5 hour sample. The quantity of soluble protein is also higher in the overnight sample and is similar to that obtained from LB 30 °C with 5 hours expression time. This result is consistent with what was observed in the H-Enfors expression and solubility tests. It was

concluded that the expression conditions for the fermentation process should be 30 °C, with overnight expression to obtain the largest quantity of DUOX. The results from the tests of D-Enfors are described in Figure 3.2. Comparison of the expression and solubility of HUOX in LB media at different expression temperatures and times can be found in Appendix A, Figure A.2 for reference.

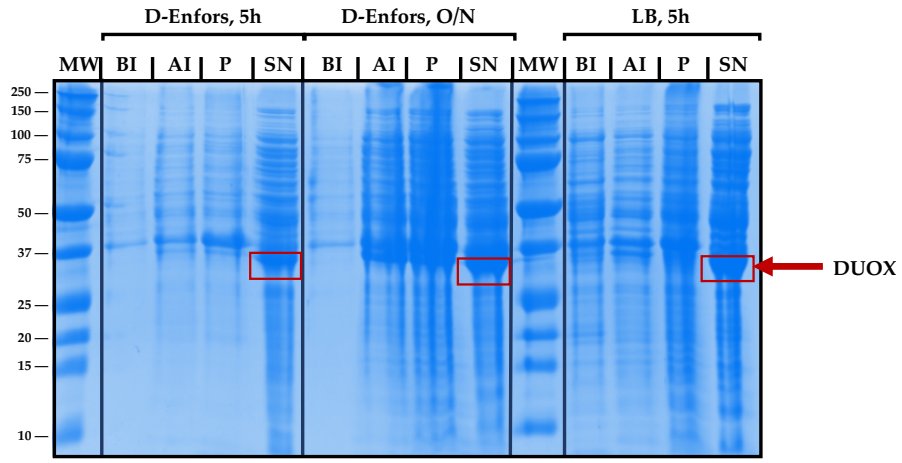

FIGURE 3.2: SDS-PAGE showing the expression and solubility of DUOX in D-Enfors, a deuterated minimal medium and compared to expression in LB. The MW (kDa) lanes represent a molecular weight marker. Expression was conducted at 30 °C and different expression times are separated by a solid black line. The level of overnight (O/N) expression was more significant than in the sample that was overexpressed for 5 hours from both the After Induction (AI) and supernatant (SN) samples. From these results it was concluded that the most suitable conditions for DUOX expression in the fermenter was 30 °C overnight.

3.2 The Production of Perdeuterated UOX (DUOX)

The process of fermentation is commonly used to produce High Cell Density Cultures (HCDC). The HCDC allows the production of large amounts of biomass in a minimal volume. This type of culture is ideal for deuterated conditions because the cost of D_2O and deuterated (d_8) glycerol are high [131]. For example, it costs 380 EUR per litre of D_2O: one fermentation typically uses $\sim$ 2 L in total. In addition,

it costs 20 EUR per gram of d_8-glycerol: one fermentation typically uses $\sim$ 50 g of d_8-glycerol in total.

Fermentation was chosen to produce perdeuterated UOX for 100% hydrogen to deuterium replacement. The details of the fermentation process for the production of perdeuterated protein are detailed in Chapter 2, Section 2.2.

3.2.1 Cell Adaptation for Growth in Deuterated Media

To enhance the growth of bacteria in deuterated media, an adaptation phase is needed. This adaptation involves diluting a small culture of 10 mL each day for $\sim$ 10 times. Chapter 2 describes the adaptation protocol in more detail.

Adapted cells can be used in the fermentation process immediately, or can be stored on cryo-beads at -80 °C until required. During this study, both of these methods were employed. To awaken the cells, several cryo-beads are removed and placed in 10 mL D-Enfors with 30 μg/mL kan^R and grown at 37 °C overnight. After overnight growth, 1 mL of culture is inoculated into 10 mL fresh D-Enfors and the process is repeated a minimum of three times before transferring to the fermenter starter culture. The expression of these awoken cells was tested and results are detailed in Figure 3.3, showing that the storage on cryo-beads had no effect on the ability of the cells to express protein.

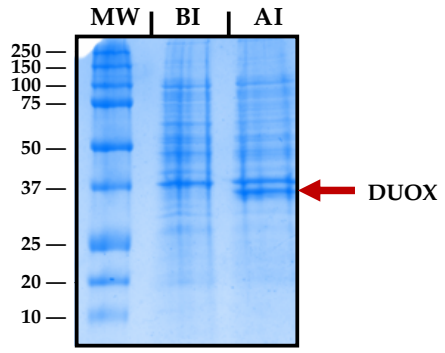

FIGURE 3.3: SDS-PAGE displaying the expression test on cells awoken after storage on cryo-beads after adaptation. The band in the After Induction (AI) lane is identified as DUOX when compared with the Before Induction (BI) sample and a MW standard (kDa), confirming the ability of cells to express DUOX after storage on cryo-beads.

3.2.2 Fermentation of DUOX

150 mL of starting culture is required to inoculate 1.2 L of D-Enfors in the fermenter. This starting culture contains D-Enfors and 30 μg/mL kan^R.

The advantage of the fermentation process is the control of important parameters such as mass flow (d_8-glycerol), pO_2, pH, and stirrer speed. The OD_{600} is measured by manually extracting small samples of the culture at regulated intervals in order to monitor cell growth. The air flow of O_2 (pO_2) also gives an indication of cell respiration. The value decreases from 100% as the cells utilise the O_2 until a sharp drop to 30%. At this point, the stirrer speed is adjusted to increase the O_2 flow to the system, answering the demand for O_2 from the multiplying cells. A base solution of 1 M NaOD is added to the fermenter culture to compensate for the increasing acidity from the cellular byproducts, maintaining the pH at 6.9.

The fermentation consists of three phases: the batch phase, the fed-batch phase and the induction phase. The batch phase is the primary phase in the growth of deuterated cells, where the cells use the starting quantity of d_8-glycerol present in the fermenter (5 g/L). The fed-batch phase begins once this d_8-glycerol has been

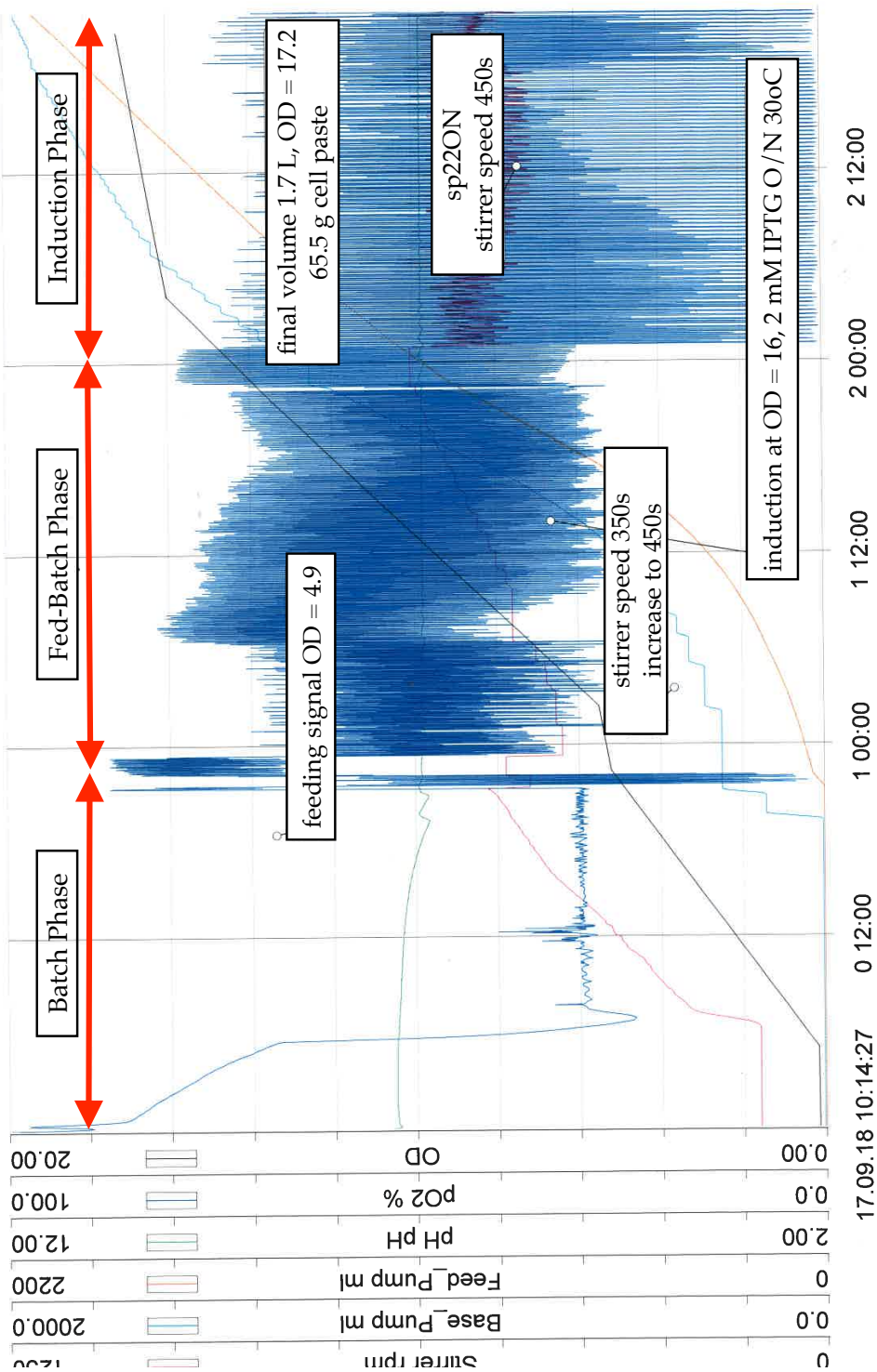

FIGURE 3.4: Fermenter profile with time in hours on the x axis and monitored parameters on the y axis: stirrer speed, base, feed, pH, pO_2 and OD.

consumed in the growth of the cells and has to be supplemented by the 120 g/L feeding solution. The beginning of this phase was observed by the drop of the pO_2 to 30%, indicating the lack of a carbon source. The feeding solution is added exponentially until a sufficient amount of biomass has been produced. The last phase is the induction phase. The induction was carried out at OD_{600} = 16 with 2 mM IPTG dissolved in D_2O, with expression at 30°C overnight. After 16 hours overexpression the cells were collected by centrifugation at 8000 RPM at 4°C for 25 minutes and stored at - 20 °C. The fermenter was stopped at an OD of 17.2 and 65.5 g of cells paste was obtained from 1.7 L of media. The fermenter profile is shown in Figure 3.4 and details the parameters monitored during the fermentation process.

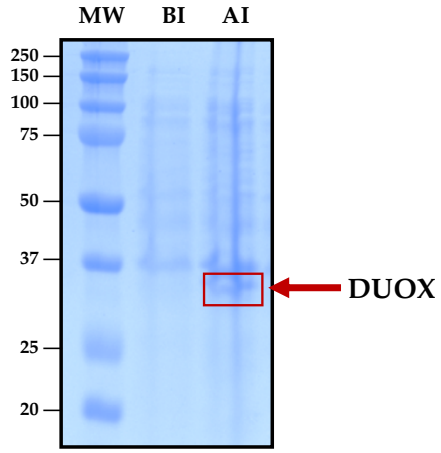

FIGURE 3.5: SDS-PAGE analysis of the samples Before Induction (BI) and After Induction (AI). With reference to the Molecular Weight marker (MW), a band at ∼34 kDa after induction confirms the successful over expression of UOX in controlled and fully deuterated conditions.

The level of expression before and after induction was examined using the same protocol as described in Section 3.1.2. As shown in Figure 3.5, a band located around ∼34 kDa after induction confirms the overexpression of DUOX under the controlled conditions of the fermenter. The band on the gel is weaker than previously seen in the expression of HUOX. However from the large mass of cell paste obtained, it was expected that a sufficient mass of DUOX was expressed. This is discussed in Section 3.3.1.

3.3 Protein Purification of DUOX

The purification protocol for HUOX was an established protocol, employed by the Steiner Research Group. An overview of the steps involved in this purification protocol is given in Figure 3.6. During this research project, the purification of HUOX was conducted to verify all steps. This protocol was then repeated with DUOX. The following section discusses the purification of DUOX only.

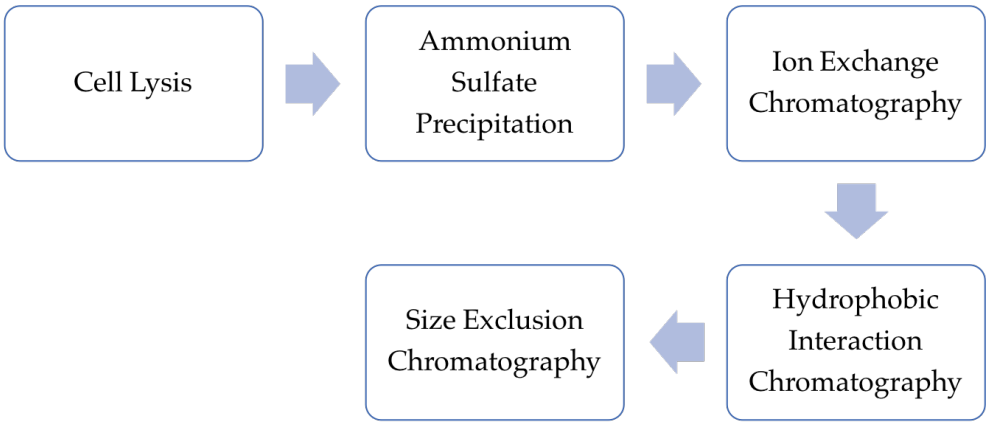

FIGURE 3.6: The overview of the DUOX purification protocol. The individual steps and results will be discussed in the following paragraphs.

Cell Lysis

Each DUOX purification was conducted with approximately 8 - 10 g pelleted cells. This frozen pellet was thawed and resuspended in lysis buffer (50 mM Tris-HCl 5 mM KCl pH 8.0 - 5 mL/g of cell paste) at 4°C, supplemented with an EDTA-free protease inhibitor cocktail, benzonase, and lyzozyme. The resuspended cells were sonicated for $\sim$ 22 minutes on ice, with sequential breaks to prevent overheating

that can damage the protein. Cell debris was removed by centrifugation at 19500 RPM at 4°C for 40 minutes and the supernatant recovered.

Ammonium Sulfate Fractionation

Ammonium sulfate fractionation was conducted on the protein solution, separating into protein:salt pellets at concentrations of 25 %, 40 %, and 55% of ammonium sulfate at 4°C. The quantity of ammonium sulfate needed for fractionation was calculated by consulting the published tables [149, 245]. Solid ammonium sulfate was added to the protein solution to the required concentration and equilibrated over 2 hours. Each salt pellet was recovered by centrifugation at 19500 RPM at 4 °C. The differing percentages were analysed using SDS-PAGE to identify the fraction with the highest concentration of DUOX for further purification, as shown in Figure 3.7. Typically 25% and 40% fractions were seen to remove contaminants and DUOX was isolated in the 55% fraction.

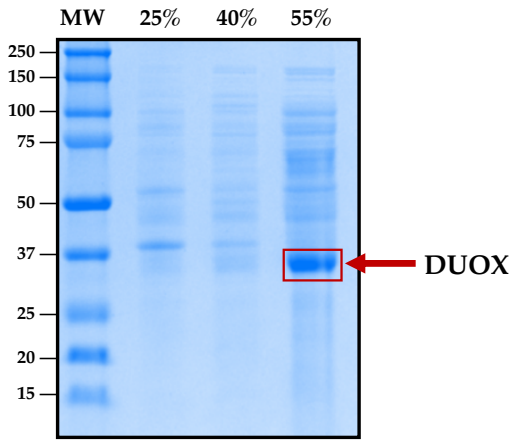

FIGURE 3.7: SDS-PAGE examining the protein content of different ammonium sulfate fractions at 25%, 40% and 55%, where the 55% fraction shows the largest amount of DUOX and is chosen for further purification.

SDS-PAGE analysis in Figure 3.7 confirmed that the 55% pellet contained the highest quantity of DUOX. This pellet was further purified by resuspending in 50 mM Tris-HCl, pH 8.0 and dialysed against 2 x 2 L of 50 mM Tris-HCl pH 8.0. The dialysed supernatant was collected and centrifuged at 19500 RPM, 4 °C for 40 minutes

in order to remove any precipitation.

DEAE and Q Sepharose Ion Exchange Chromatography

The protein solution was loaded onto a GE Healthcare HiTrap DEAE Sepharose FastFlow column pre-equilibrated in 50 mM Tris-HCl, 5 mM KCl pH 8.0. The elution of the protein was followed at 280 nm and recorded on the chromatogram, see Figure 3.8. Contaminants were then eluted at by 50 mM Tris-HCl, 600 mM KCl pH 8.0 and discarded. The fractions corresponding to the first peak observed on the chromatogram were pooled and immediately loaded onto a GE Healthcare Q-Sepharose FastFlow column. The elution of the protein was again followed at 280 nm and recorded on the chromatogram, see Figure 3.8. Additional contaminants were eluted using 50 mM Tris-HCl, 600 mM KCl pH 8 and discarded. Protein-containing fractions were recorded by chromatogram and analysed by SDS-PAGE. Fractions containing DUOX, confirmed by SDS-PAGE, were pooled together. Chromatograms from both DEAE and Q Sepharose ion exchange columns and the SDS-PAGE analysis from the Q Sepharose column are shown in Figures 3.8 and 3.9.

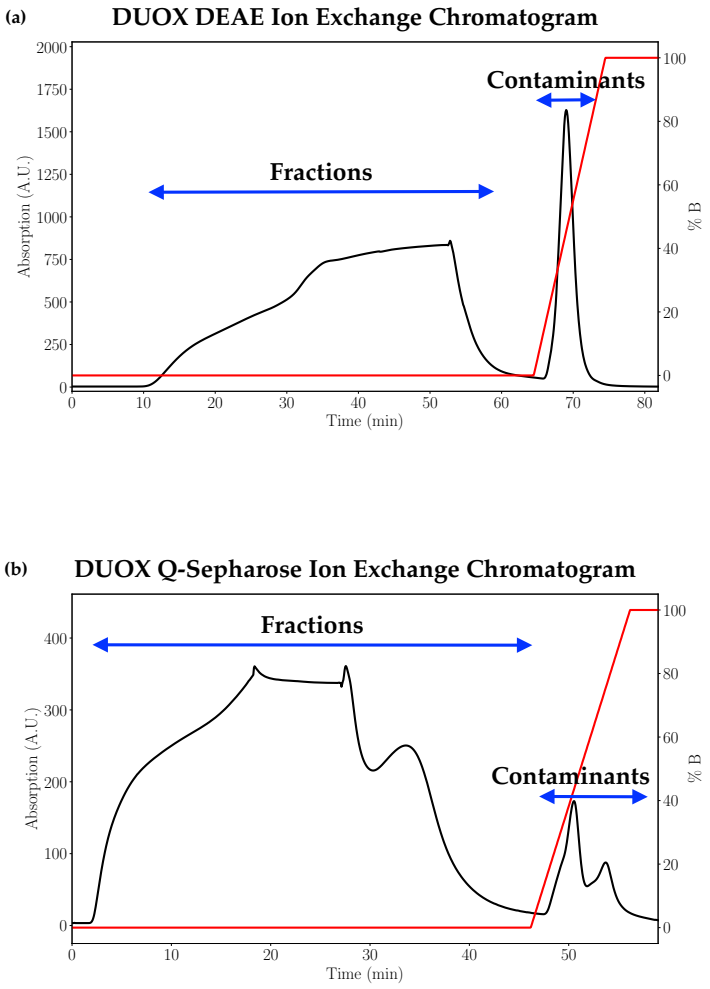

FIGURE 3.8: (a) Chromatogram from DEAE Ion Exchange column follows the elution of DUOX. The elution of DUOX is indicated by the wide peak between Time 10 - 65 mins. Contaminants recorded by the secondary peak were discarded. These fractions were pooled and immediately loaded onto the Q Sepharose column. (b) Q Sepharose chromatogram shows a peak between 3 - 48 mins indicating the elution of DUOX.

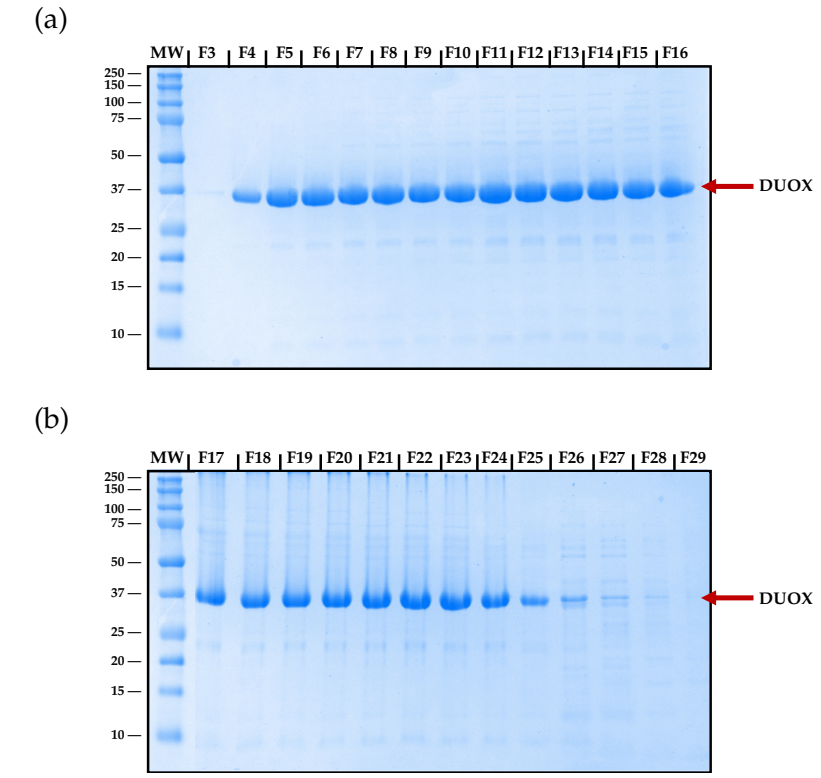

FIGURE 3.9: (a) and (b), Flowthrough fractions from the Q-Sepharose column were analysed using SDS-PAGE and compared with a molecular weight standard (MW, kDa).

Phenyl Sepharose Hydrophobic Interaction Chromatography

Solid ammonium sulfate was then added gradually to the protein solution to a total concentration of 1 M. The equilibrated solution was loaded onto a GE Healthcare HiLoad 16/10 Phenyl Sepharose column pre-equilibrated in 1 M $(NH_4)_2SO_4$, 30 mM KP_i pH 8.0. The protein was eluted using a gradient of 30 mM KP_i pH 8.0 and fractions were analysed using SDS-PAGE to assess purity. Chromatogram and SDS-PAGE gel are described in Figure 3.10.

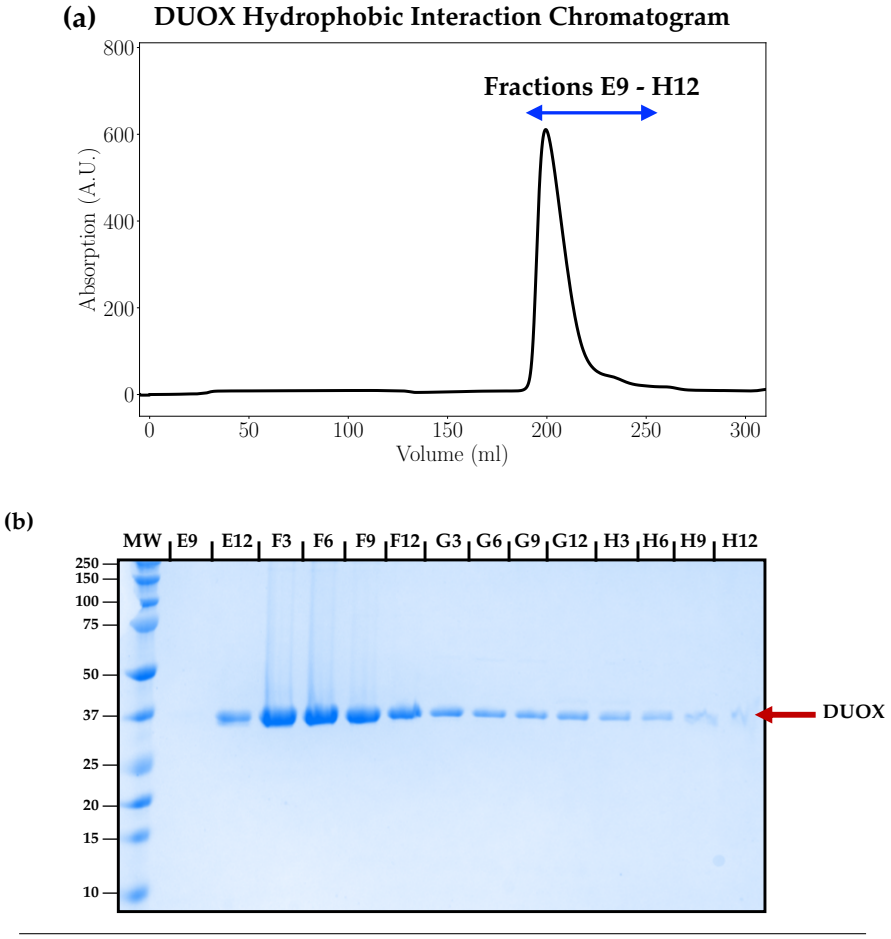

FIGURE 3.10: (a) Chromatogram from Hydrophobic Interaction Chromatography. Peak indicating the elution of DUOX is seen from 185 mL - 250 mL. (b) Eluted fractions were compared against a molecular weight standard (MW, kDa) and pure DUOX fractions were identified for use in the subsequent size exclusion step.

Size Exclusion Chromatography s75

Purest fractions were pooled and concentrated to < 5.0 mL before loading onto a GE Healthcare HiLoad 16/60 Superdex75 prep grade Size Exclusion column pre-equilibrated in 50 mM Tris-acetate pH 8.0. Fractions at an elution peak at $\sim$ 50 mL, seen on the chromatogram, were analysed on SDS-PAGE: chromatogram and SDS-PAGE are shown in Figure 3.11. The purest fractions were combined and used for further experiments.

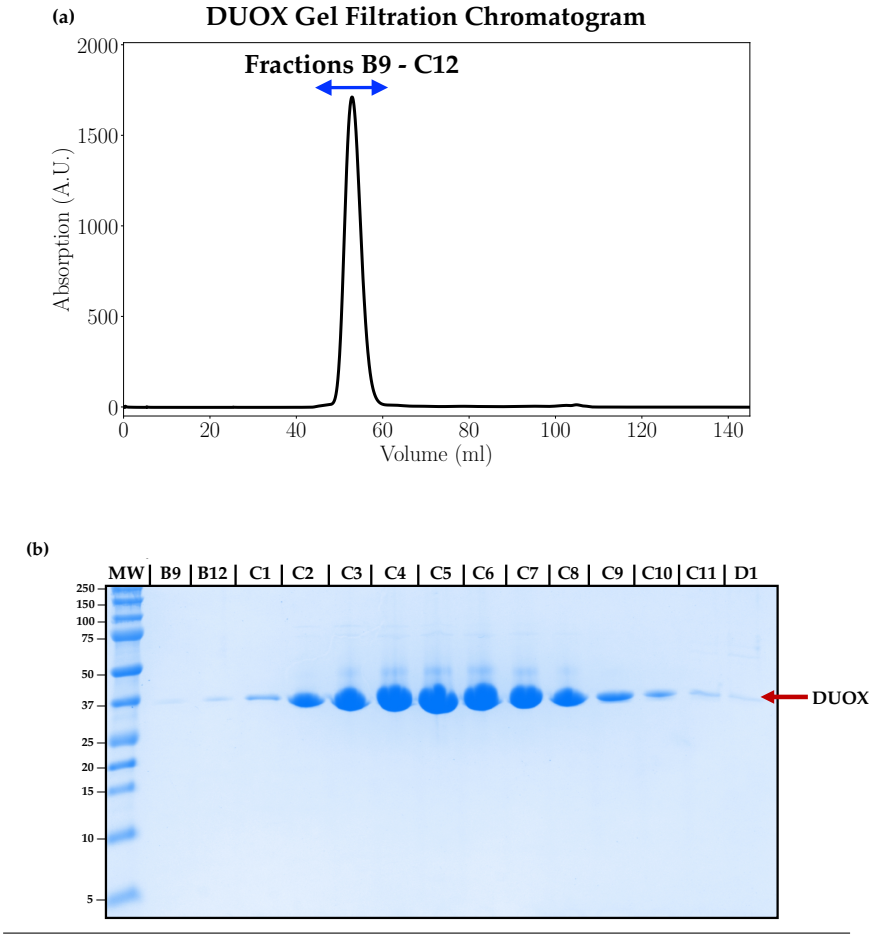

FIGURE 3.11: (a) Size Exclusion chromatogram. Peak between 40 - 60 mL shows the elution of DUOX. (b) Eluted fractions were compared against a molecular weight standard (MW, kDa) and pure DUOX fractions pooled for exchange/concentration steps in preparation for crystallisation experiments.

3.3.1 Comparison of HUOX and DUOX Expression

It was possible to probe the efficiency of the fermenter in producing DUOX by comparing the results from both HUOX and DUOX purifications. These statistics are detailed in Table 3.1. Comparison of the respective yields of HUOX and DUOX produced per gram of cell paste as 4.20 mg and 1.8 mg, indicates that the HUOX is produced in greater quantities. However, directly comparing the mass of UOX

TABLE 3.1: Statistics from HUOX and DUOX purifications. By comparing values obtained between the two purifications, it is possible to evaluate the efficiency of the fermenter and calculate the mass of protein expected from each expression: HUOX in flasks and DUOX from the fermenter. It is important to take into account the mass of materials used in each process.* indicates protein yield before concentration for crystallisation.

	HUOX in LB	**DUOX in D-Enfors**
Cell paste mass used in purification	10 g	10 g
Yield of UOX	42 mg*	18 mg*
mg protein/g cell paste	4.20 mg/g	1.8 mg/g
Volume of media	4 L	1.7 L
g of cell paste/ L of media	4.5 g/L	39 g/L
Estimated total UOX	75.6 mg	119.34 mg

obtained from one purification, does not accurately represent the results of the fermenter. Extrapolation of these values to consider the total UOX produced shows that the fermenter produces a higher quantity of cell paste relative to the volume of media used 4.5 g/L of cell paste in LB compared to 39 g/L cell paste in the fermenter. From the information obtained from the purification, the calculations show that the total yield of DUOX is higher than that calculated for HUOX. For HUOX, the total is 75.6 mg per flask expression (of 4 L in total) vs DUOX, where the total is 119.34 mg for one fermenter (1.7 L). As previously described, deuterated materials are costly, so maximising the expression of the protein of interest whilst keeping the quantity of material to a minimum is desirable. Therefore, we can conclude that whilst the level of overexpression is not clear from SDS-PAGE analysis, quantifying the level of protein produced proves that under fermenter conditions DUOX has been overexpressed to a substantial level in comparison to typical HUOX expression.

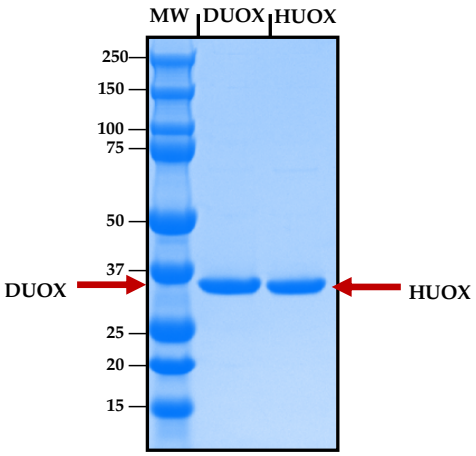

FIGURE 3.12: SDS-PAGE gel showing pure fractions of DUOX and HUOX. The molecular weight (MW) difference is observed visually by a slight displacement in the band position, indicating that the MW of DUOX is higher than that of HUOX.

The difference in molecular weight between HUOX and DUOX was calculated to be approximately 1,820 Da (as described in Section 3.4). A pure sample of both HUOX and DUOX protein was analysed using SDS-PAGE, as shown in Figure 3.12. The effect of perdeuteration on the mass of the protein is seen in differing migration distances between the two samples.

The entire purification process is conducted in hydrogenated buffers, therefore the perdeuterated protein contains only deuterium in the non-exchangable atoms of the protein at this stage. After the purification procedure is completed the protein is buffer exchanged into deuterated buffer to replace all the labile hydrogen positions with deuteriums. This is done through a repetition of concentration:dilution steps. A Merck KGaA 10 kDa millipore centrifugal unit was used to concentrate the pure protein solution < 10 % starting volume. This was then diluted 10 fold using 50 mM Tris-acetate, 30 mM NaAc, pD 7.59, with the addition of salt to increase the solubility of the protein. This process was repeated a minimum of 2 times before finally concentrating the protein to > 20 mg/mL.

3.4 Mass Spectrometry

The mass spectrometry measurements were conducted using Mass Spectrometry Platform as part of the Partnership for Structural Biology, Grenoble. Mass spectrometry can be used assess the level of deuteration of proteins produced through fermentation. Comparing measured masses to calculated values can establish the number of hydrogens successfully substituted by deuteriums into non-exchangeable positions in the protein. Both the masses of HUOX and DUOX were recorded and compared. In the case of HUOX, the sample was concentrated to 2 mg/mL and analysed in 50 mM Tris-acetate pH 8.0. For DUOX, the sample was concentrated to 2 mg/mL and analysed in 50 mM Tris-HCl pH 8.0, due to the increased solubility of DUOX in halogenated buffers. For both of the samples, hydrogenated buffer was used for instrumental reasons.

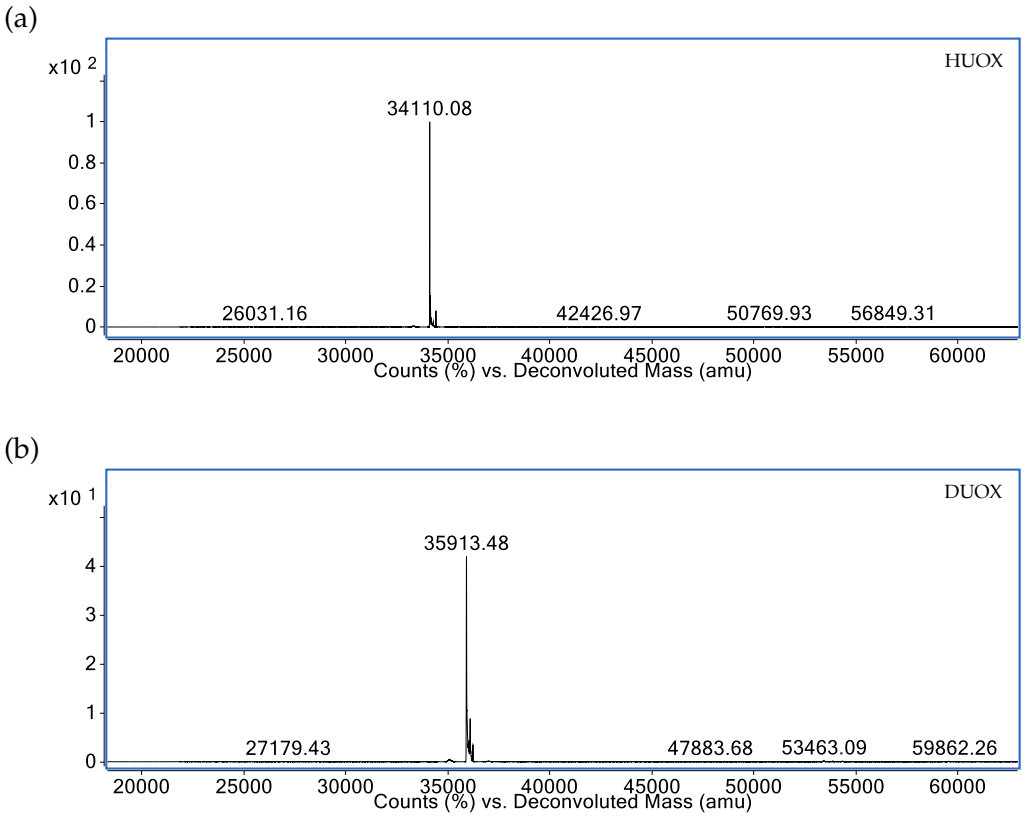

FIGURE 3.13: The deconvoluted spectra of both HUOX (a) and DUOX (b) giving the measured molecular weights in kDa for the two isotopically different proteins.

The expected molecular weights (MW) of both the hydrogenated and perdeuterated protein can be calculated from the amino acid sequence in the protein: the UOX sequence obtained from ProtParam is given in Appendix A, Figure A.1. Using an excel table and the amino acid sequence of UOX, it was possible to evaluate the number of non-exchangeable hydrogen positions in the protein, and calculate the overall expected mass. The table and calculated values are shown in Appendix A, Table A.3 for reference. The MW of HUOX and DUOX was calculated to be 34,098 Da and 35,918 Da, respectively.

The deconvoluted spectra that were provided by Dr Luca Signor, IBS Grenoble, show the experimentally measured mass of HUOX as 34,110 Da and of DUOX as 35,913 Da (Figure 3.13). Examination of the number of non-exchangeable sites and their MW calculates that there should be a mass difference of 1,820 Da between the HUOX and DUOX samples if all the sites are successfully replaced with deuterium during protein biosynthesis. The MW difference between the experimentally measured masses of HUOX and DUOX is 1,803 Da. Calculating this as a percentage of available sites is >99%, confirming the success of the fermentation process at achieving high levels of deuteration. This is consistent with the level of perdeuteration recorded in other projects that follow the protocol established by the Life Sciences Group at the Institut Laue-Langevin (ILL) [131, 231, 235, 246, 247].

3.5 Thermofluor Assay

The thermal stabilities of HUOX and DUOX were compared using a Thermofluor Assay. Thermofluor Assay experiments were conducted using the HTX Platform, as part of the Partnership for Structural Biology, Grenoble. Both samples were measured in hydrogenated buffers containing 50 mM Tris-HCl at pH 8.0. Concentrations of 0.8 mg/ml and 1.0 mg/ml were used for the HUOX and DUOX samples

respectively. Normalised curves showing the fluorescence and melting point (T_m) of the two proteins are shown in Figure 3.14.

The graphs show similar profiles with two features: in both cases there is a small increase in fluorescence between 40 °C and 50 °C. This may be due to the dissociation of tetramer however, the amplitude of the peak is not substantial enough to draw this conclusion. Further analysis may confirm a relationship between temperature and multimer dissociation. The typical sigmoidal curve is shown for both samples between 50 °C and 75 °C. The melting temperature (T_m) is calculated as the midpoint of the sigmoidal curve, values for HUOX and DUOX are shown in Table 3.2. It is observed that the T_m of DUOX is approximately 4 °C lower than that of HUOX indicating a reduced stability.

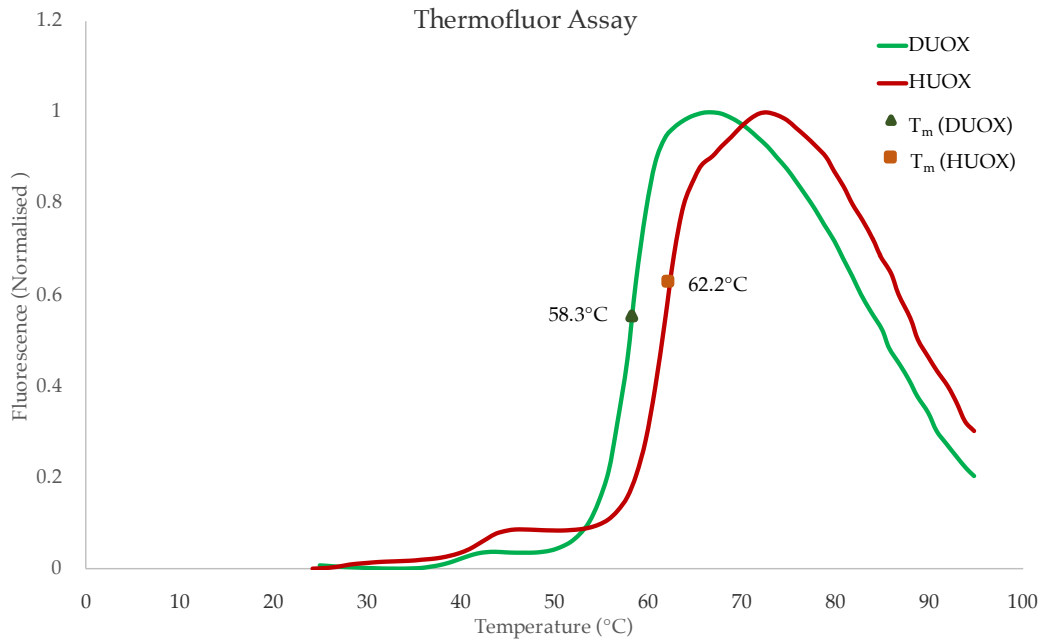

FIGURE 3.14: Normalised fluorescence data from thermofluor assay, identifying the T_m of both HUOX and DUOX samples. With increasing temperature, an increase in fluorescence is seen due to the unfolding of the protein and the binding of the fluorescent dye. The green curve shows the profile for DUOX and the red curve shows the profile for HUOX. The T_m for each protein is indicated in the legend.

TABLE 3.2: T_m values for HUOX and DUOX, calculated from Thermofluor Assay data.

	HUOX	**DUOX**
T_m value (°C)	62.2	58.3

This difference in T_m has been noted in other examples in literature suggesting that deuterated proteins are commonly less stable to heat denaturation than the hydrogenated counterparts [138, 243, 244]. For example, the deuterated Enzyme I^{Ntr} showed a reduction in thermal stability of $\sim$ 4 °C, in addition to enhanced oligomerization propensity and an increased sensitivity to proteolysis *in vivo* [243]. Studies into the thermal stability of perdeuterated glutathione *S*-transferase and P450cam also showed similar results with a reduced thermal stability of $\sim$ 3.8 °C and $\sim$ 4 °C, respectively [138, 244]. It has been suggested that a reason for this reduced thermal stability may be that by substituting backbone hydrogen atoms with deuteriums, the activation barrier for unfolding is lowered. The C-D bond has a decreased vibrational amplitude in comparison to C-H, as a result, this weakens the strength of hydrophobic interactions and lowers the T_m [138].

Chapter 4

Joint Refinement of Perdeuterated Urate Oxidase (DUOX) complexed with 8-azaxanthine (AZA)

Abstract

This chapter presents the structural investigation of perdeuterated Urate Oxidase (DUOX) complexed with the inhibitor 8-azaxanthine (AZA). The purpose of this research was to examine the chemical environment and solvent structure in the active site of the DUOX:AZA complex using neutron crystallography (NMX).

Previous X-ray studies have identified a solvent molecule (termed W1) that occupies the cavity above the ligand binding site (the peroxohole) [65]. This solvent molecule W1 has been observed in UOX complexes with the natural substrate uric acid (UA), 9-methyl uric acid (9-MUA), and inhibitor AZA [65, 81, 82]. It is displaced upon O_2 binding in the oxidation reaction of UA. The proximity of the W1 solvent molecule to the C5 position of UA is thought to be important in the hydration reaction that forms 5-hydroxyisourate [68].

The charge and bonding interactions of this W1 solvent molecule with active site residues, Thr57* and Asn254, in the DUOX:AZA complex, are determined in this study. The protonation states of active site residues, suggested to form a catalytic triad consisting of Thr57*-Lys10*-His256, are also determined. These are then compared with the results obtained with previous neutron studies by Oksanen *et al.* of hydrogenated Urate Oxidase (HUOX) in complex with AZA and UA, inhibited by a chlorine atom [80].

Key features in the experimental design, such as ligand choice and buffer composition, enabled this dataset to be collected at 298 K. Both neutron and X-ray datasets were collected at this temperature on the same crystal. The two datasets were used to perform joint refinement of DUOX:AZA complex. The experimental details and results are given in this chapter. The analysis of these results in a mechanistic context are also discussed herein.

4.1 Introduction

Urate Oxidase (UOX) is a widely studied enzyme and both its structure and function have been investigated using a wide range of techniques. X-ray crystallography has been invaluable in providing insight into the structure of UOX with > 100 number of structures deposited in the PDB [75]. The first X-ray structure of *Apergillus flavus* UOX by Colloch *et al*. studied UOX in complex with inhibitor 8-azaxanthine (AZA) [65]. The structural differences between AZA and the natural substrate uric acid (UA) are shown in Figure 4.1. In comparison to UA which contains a carbonyl group at position C8, the AZA molecule contains an amide group. The AZA inhibitor also cannot be oxidised and prevents the binding of O_2 to the active site.

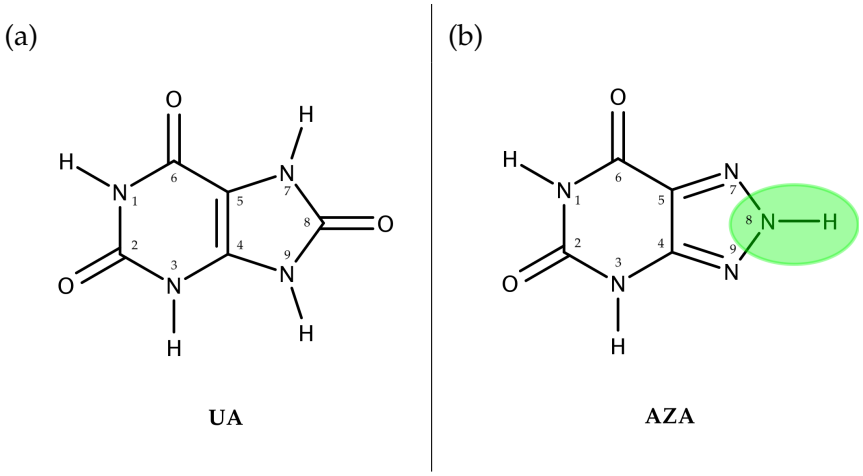

FIGURE 4.1: (a) The structure of the natural substrate uric acid (UA). (b) The structure of inhibitor 8-azaxanthine (AZA). The carbonyl group at position 8 on the purine ring in UA is replaced with an amide group in AZA.

Other studies of UOX in complex with natural substrate UA have been conducted using X-ray crystallography [81, 82]. Samples were prepared under O_2-free conditions (anaerobic) and successfully trapped a solvent molecule, commonly referred to as W1 in literature [65, 80, 81], located above the substrate in the initial stage of the reaction as shown in Figure 4.2. This W1 solvent molecule is then displaced as O_2 binds to the same location. However, the proximity of this W1 solvent molecule is thought to be important in the hydration reaction to form 5-hydroxyisourate (5-HIU) [68]. However, due to the limitations of X-ray crystallography, previously described in Chapter 2 (Sections 2.5.4 and 2.6), these studies did not provide any information on the charge of this water molecule and the exact details of its bonding interactions with active site residues.

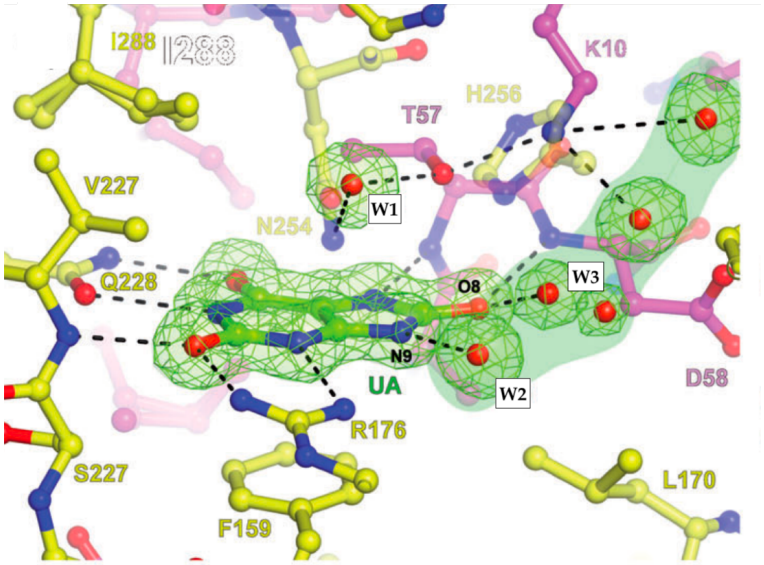

FIGURE 4.2: The natural substrate uric acid (UA) bound to hydrogenated Urate Oxidase (HUOX) under anaerobic conditions before the binding of O_2. A solvent molecule (W1) occupies the peroxohole above UA and several conserved water molecules are detailed with hydrogen bonding distances to active site residues. $2mF_o$-DF_c electron density (green) contoured to 1 σ. Figure adapted from [81] © 2014 The Authors. Published by Wiley-VCH Verlag GmbH & Co. KGaA.

Neutron macromolecular crystallography (NMX) is a powerful technique that can be used to locate hydrogen positions. A review of the NMX technique is described in Chapter 2, Section 2.6. Previous neutron studies by Oksanen *et al.* [80] have been conducted on hydrogenated UOX (HUOX) complexes. These included HUOX complexed with inhibitor AZA (HUOX:AZA) and the natural substrate UA (HUOX:UA), soaked in deuterated buffer [80]. The HUOX:UA complex suggested that UA binds to UOX as the N3 deprotonated monoanion, before being rapidly tautomerised to form 8-hydroxyxanthine (8-HX), therefore referred to as the HUOX:8-HX complex. The HUOX:AZA complex showed that AZA also binds as the N3 monoanion. In this case, halogenated crystallisation conditions had an inhibitory effect on the reaction as a Cl^- atom binds to the location of the W1 solvent molecule/O_2 [65, 78, 80, 82]. The bonded negatively charged Cl^- atom displaces the W1 solvent molecule and prevents the binding of O_2. Catalytic residues had previously been identified

as Lys10*-Thr57* [91], although subsequent research suggested extending this proposal to a catalytic triad involving the residues Lys10*-Thr57*-His256 [77]. Oksanen *et al.* identified the protonation states of this triad in both the HUOX:AZA and HUOX:8-HX complexes, however, the complexes showed several important differences. The catalytic triad in the HUOX:8-HX complex was found to contain the following protonation states: the deuterated hydroxyl group on Thr57* points towards the active site; Thr57* accepts a hydrogen bond from the positively charged $-NH_3^+$ group present on Lys10*; neighbouring His256 is neutral, unprotonated in the Nϵ position, also accepting a hydrogen bond from the positively charged Lys10* $-NH_3^+$. This is shown in Figure 4.3 (a) and (b) [80]. In contrast, the protonation states in the HUOX:AZA complex were found to be the following: the hydroxyl group on Thr57* is deuterated and points towards the lone pair on the $-ND_2$ group on Lys10*; the neighbouring His256 is neutral and unprotonated in the Nϵ position acting as a hydrogen bond acceptor for the Lys10* $-ND_2$. This different bonding network is described in Figure 4.3 (c) and (d) [80]. However, Oksanen *et al.* also suggested that a similar bonding network to the HUOX:8-HX complex was also present in the HUOX:AZA complex, however, the resolution of the data collected was considered insufficient to allow the refinement of both conformations [80]. It also was noted that the use of hydrogenated protein and subsequent effect from the incoherent scattering complicated the interpretation of the neutron density maps [80].

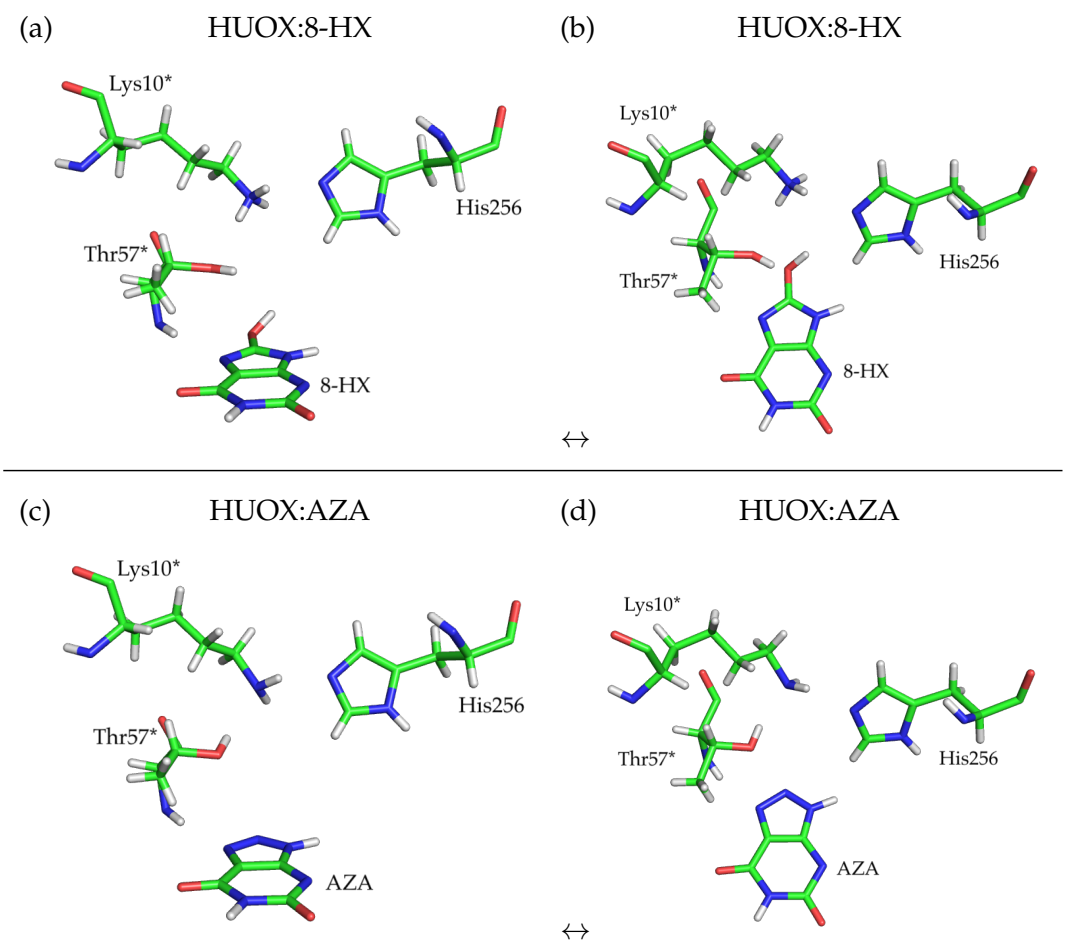

FIGURE 4.3: Protonation states of reactive site residues described in previous neutron studies. (a) and (b) The protonation states of the Thr57*-Lys10*-His156 catalytic triad in hydrogenated Urate Oxidase:8-hydroxyxanthine complex (HUOX:8-HX). The 8-hydroxyxanthine (8-HX) monoanion is also shown. (c) and (d) Different protonation states of the Thr57*-Lys10*-His156 catalytic triad in the hydrogenated Urate Oxidase:8-azaxanthine complex (HUOX:AZA). Adapted from [111] © 2014 Oksanen et al. Distributed under CC-BY 4.0.

Presented in this chapter is the crystallisation, neutron and X-ray data collection, and structure solution of perdeuterated UOX (DUOX) in complex with the inhibitor AZA. The use of perdeuterated protein reduces the problems associated with hydrogenation, allows shorter NMX data collection times, and tends to enhance the resolution of the data for well-diffracting samples [248, 249]. Protein perdeuteration also facilitates data collection for smaller crystal volumes [143, 233, 234, 250].

In addition, halogen-free crystallisation conditions enabled the conservation of the W1 molecule [65]. The W1 molecule has been identified as an oxygen atom using X-ray crystallography, however, its charged state had not been identified prior to this study.

This study aims to identify the charged state of the W1 solvent molecule using neutron crystallography, given that this technique is able to distinguish between D_2O, D_3O^+, and OD^- molecules. We also consider whether the molecule located above the AZA ligand affects the protonation states of active site residues, with comparison to previous studies involving inhibition by chlorine [80]. The bonding networks of functionally relevant amino acids and active site water molecules are described in detail and discussed in the context of previously published structures.

4.2 Crystallisation of DUOX:AZA

The expression and purification of DUOX is described in Chapter 3. The preparation of the protein solution for crystallisation experiments is also described in Chapter 3.

The batch crystallisation method was employed for the growth of DUOX:AZA crystals. A mixture of 30 μL total volume with protein solution and crystallisation buffer in a 2:1 ratio was prepared. The crystallisation buffer consisted of 50 mM Tris-acetate, 8% PEG 8000, pD 7.59 in D_2O. The DUOX:AZA crystals were produced by co-crystallisation as the AZA ligand was added to the crystallisation buffer to a concentration of 13mM. The ligand was added into the crystallisation solution by agitating the solution on a bench-top shaker until visibly dissolved.

Sitting Drop plates (Hampton Research) were used for the crystallisation set-up and sealed using crystallisation tape. The protein and buffer solution (30 μL) were

mixed in the concave sitting drop post and the reservoir was left empty. The crystallisation set-up for this experiment is shown in Figure 4.4 (a). These solutions were left to crystallise at 18 °C. After ∼ 5 days nucleation was observed with crystals reaching full size after ∼ 10 days.

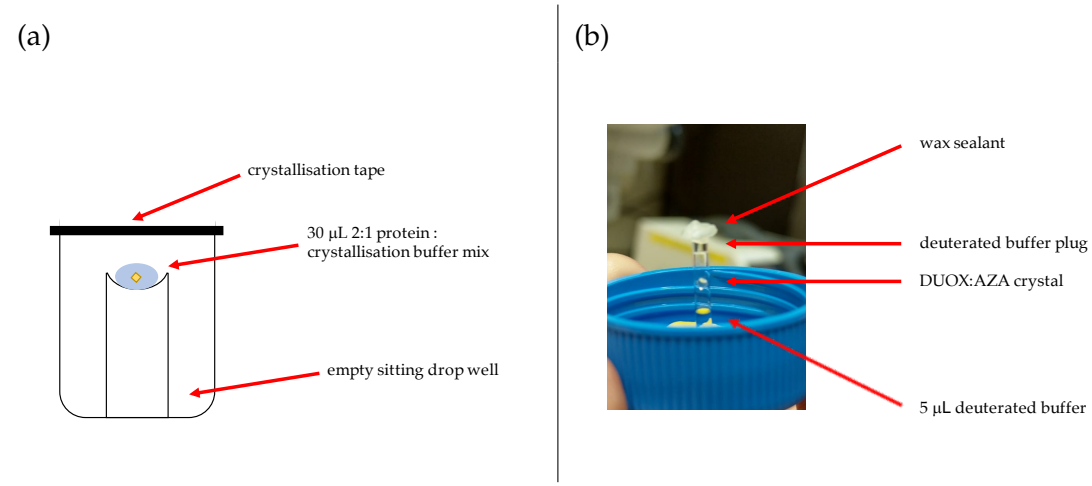

FIGURE 4.4: (a) Batch crystallisation set-up for producing perdeuterated Urate Oxidase:8-azaxanthine (DUOX:AZA) crystals. A 30μL mixture containing 2:1 protein to crystallisation buffer was prepared using Sitting Drop plates (Hampton Research) with an empty reservoir, sealed with crystallisation tape. (b) DUOX:AZA crystal mounted in a 3 mm diameter quartz capillary for data collection.

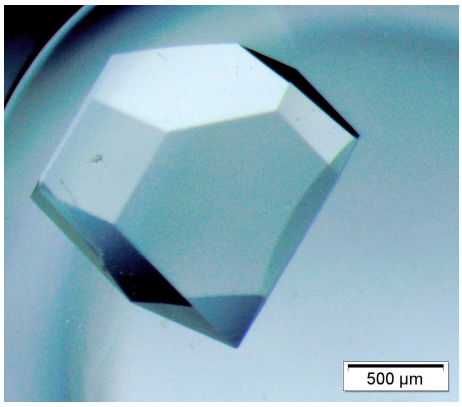

FIGURE 4.5: A perdeuterated Urate Oxidase:8-azaxanthine (DUOX:AZA) crystal with a volume of 1.5 mm^3 was used for neutron data collection and subsequent X-ray data collection.

A fully deuterated single crystal of approximate volume 1.5 mm^3 (1.4 mm x 1.2 mm

x 0.9 mm) was selected for data collection and mounted in a quartz capillary with an internal width of 3 mm, shown in Figures 4.4 (b) and 4.5. Mother liquor ($\sim$ 5 μL) was added to the base of the capillary in order to keep the crystal hydrated during data collection. Excess mother liquor surrounding the crystal was removed to reduce the effect of the solvent on the scattering and to prevent crystal movement during data collection. This capillary was then sealed with wax to prevent any exchange with air and to prevent the dehydration of the crystal.

4.3 Quasi-Laue Data Collection on LADI-III

The DUOX:AZA crystal was mounted into the sample position of the LADI-III beamline at the Insitut Laue-Langevin (ILL), Grenoble [164]. LADI-III is equipped with a large cylindrical detector which surrounds the sample and is composed of neutron-sensitive image-plates (diameter: 400 mm, height: 450mm) [164]. Quasi-Laue neutron diffraction data was collected to 2.1 Å using a wavelength range of 3.12 - 4.2 Å, centered at 3.68 Å. The crystal was held in a stationary position during data collection, with the angle of rotation changed by 10° between each image. The crystal was rotated through a total of 100° and a total of 11 images were collected with an exposure of 1.5 hours per image. This crystal was then recovered and subsequently used for X-ray data collection. One neutron Laue diffraction image with an exposure time of 1.5 h is shown in Figure 4.6.

The program *LAUEGEN* [172] was used in the reduction of the neutron data, followed by wavelength normalisation using *LSCALE* [173]. All reflections were then scaled and merged using *SCALA* [251] and converted to structure factors using the program *TRUNCATE* [252, 253]. Neutron data acquisition statistics are detailed in Table 4.1.

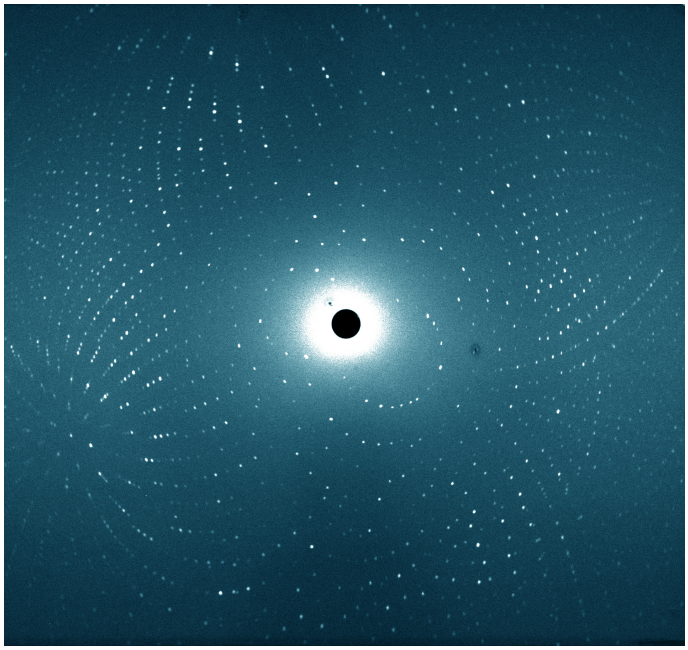

FIGURE 4.6: A Quasi-Laue neutron diffraction pattern of the perdeuterated Urate Oxidase:8-azaxanthine (DUOX:AZA) crystal with 1.5 h exposure time.

4.4 X-ray Data Collection on FIP

Protein crystals do not suffer from radiation damage during neutron data collection, therefore, it was possible to collect an X-ray dataset on the same DUOX:AZA crystal. It is important to collect datasets on homologous crystals as the unit cell parameters should be as similar as possible to facilitate the joint refinement of the structure (see Section 2.5.9 in Chapter 2). The sample was measured at 293 K using the FIP beamline at the ESRF at λ = 0.9800. A total of 240 images of 1° oscillation with 5 *s* of exposure per image were recorded on an ADSC Q315 detector. The intensities were indexed and integrated using the *XDS* package [169], and were then merged and scaled using the CCP4 program *AIMLESS* [254]. The X-ray data acquisition statistics are detailed in Table 4.1.

TABLE 4.1: Neutron and X-ray data collection statistics for perdeuterated Urate Oxidase:8-azaxanthine (DUOX:AZA) crystal at 293 K.

	Neutron data LADI, ILL	X-ray data FIP, ESRF
Space group	*I* 2 2 2	*I* 2 2 2
Unit cell parameters		
a b c (Å)	80.63, 96.13, 105.40	80.63, 96.13, 105.40
$\alpha\ \beta\ \gamma$ (°)	90 90 90	90 90 90
Wavelength (Å)	3.12 - 4.2	0.9800
No. of images	11	240
Angle between images (°)	10	1
Average exposure time	1.5 *h*	5 *s*
Resolution (Å)	40.0-2.1 (2.21-2.1)	48.06-1.34 (1.36-1.34)
No. of observations	64599 (7846)	855056 (25098)
No. unique reflections	19234 (2357)	91676 (4447)
Completeness (%)	80.2 (68.1)	100 (98.7)
Multiplicity	3.4 (3.3)	9.3 (5.6)
$\langle I/\sigma I \rangle$	5.8 (2.9)	22.1 (1.4)
R_{merge}	0.14 (0.38)	0.045 (1.120)
$R_{p.i.m.}$	0.079 (0.215)	0.015 (0.550)
$CC_{1/2}$	98.7 (82.6)	100.0 (53.3)

Values in parentheses are for the highest resolution shell.

4.5 Joint Neutron and X-ray Refinement

Structural refinement of DUOX:AZA was performed using PDB structure 1R51 as a starting model. This model was modified in preparation for refinement by the removal of all solvent molecules, ligand, and alternative conformers of residues using *PDB TOOLS* [255]. In addition, all atoms were randomly shifted by 0.1 Å in order to reduce any model bias. The N-terminus acylated serine residue was also mutated to a serine residue.

Refinement of the model was conducted using the *PHENIX* suite and model building was carried out using the *Coot* program [185, 186]. Structure refinement and model building were firstly conducted using the X-ray structure factors alone at a resolution of 1.34 Å. Using this information, it was possible to locate the positions of heavier atoms in the protein (C, N, O, S). In the first step of the refinement process a rigid body refinement was conducted, followed by multiple refinements of the atomic coordinate positions, individual occupancies, and B-factors. In this process the B-factor of all atoms were refined anisotropically. The AZA ligand was modelled and refined using the geometry restraints generated using *eLBOW* [256].

In preparation for joint refinement using both the neutron data and X-ray data (previously used for this structure refinement), a single file containing X-ray and neutron structure factors was generated using *PHENIX.refine*. A total of 10% and 5% of reflections were assigned as R_{free} flags from the X-ray and neutron datasets respectively. Joint refinement identified the location of all atoms in the protein, the ligand protonation state and the orientation of waters. As the protein was perdeuterated and the crystal was grown under fully deuterated conditions, deuterium atoms were added to all hydrogen atom positions on the protein using *READYSET*. The ligand was deuterated accordingly, refined using deuterated geometry restraints generated using *eLBOW*, and its occupancy refined as 1.0. The structure of the deuterated AZA ligand is described in Figure 4.7.

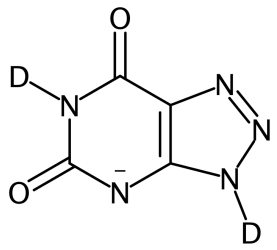

AZA monoanion

FIGURE 4.7: The protonation state of 8-azaxanthine (AZA) bound to perdeuterated Urate Oxidase (DUOX), the same as was reported in previous neutron studies [80].

All solvent molecules fitted using the X-ray-only refinement were removed and D_2O molecules were added to positive peaks visible in both X-ray and neutron mF_o-DF_c density maps with a value of $\sigma > 3$. These molecules were manually orientated in *Coot* using the X-ray data to anchor the oxygen atom position and the additional information from the neutron data to orientate the direction of the deuterium atoms, respecting hydrogen bonding partners. In several of the D_2O molecules that were manually fitted to satisfy a sensible hydrogen bonding network had their positions fixed during refinement. However, it was observed that this resulted in a large increase in the RMSD of the bond angles, therefore, it was decided that unrestrained refinement was more suitable for these D_2O molecules, leading to slightly different hydrogen bond geometry from expected values. Additional water molecules that could be identified from the X-ray data only were modelled as oxygen atoms, as there was no further information provided from the neutron data. A total of 259 D_2O molecules were fitted with an additional 87 modelled as oxygen atoms only.

All side chains containing labile hydrogen positions were individually examined and deuterated accordingly: deuterium atoms were added to positions showing positive peaks in the mF_o-DF_c neutron density map $\sigma > 3$ and removed from negative peaks in the mF_o-DF_c neutron density map $\sigma > -3$. It was assumed that there

was no contamination from hydrogen in the sample due to the perdeuteration of the protein and the use of deuterated buffers.

The final structure had X-ray R_{work}/R_{free} values of 10.42% and 12.28% respectively, and neutron R_{work}/R_{free} values of 21.75% and 24.19% respectively. Full refinement statistics are detailed in Table 4.2.

TABLE 4.2: Model-refinement statistics for the joint refinement of DUOX:AZA.

Resolution(Å) X-ray	48.07 - 1.40
Resolution(Å) neutron	32.21 - 2.10
Number of reflections neutron	19083
Number of reflections X-ray	80589
Completeness (%) X-ray	99.95 (100.00)
Completeness (%) neutron	78.66 (67.00)
R_{work} X-ray	0.1042
R_{work} neutron	0.2175
R_{free} X-ray	0.1128
R_{free} neutron	0.2419
B factors (Å^2)	
Protein	25.24
Ligand	17.37
Solvent	48.28
R.M.S Deviations	
Bond lengths (Å^2)	0.013
Bond angles (Å)	1.390
No. of Waters (D_2O, O)	259, 87

4.6 Joint Refinement Results

Neutron and X-ray data were collected at RT on the same crystal at resolutions of 2.1 Å and 1.34 Å, respectively. The crystal space group was *I* 2 2 2, which is typically seen in structures of UOX complexes deposited in the PDB [75].

4.6.1 UOX:AZA Bonding Interactions

In the ligand binding pocket, omit maps were calculated and a significant positive peak in both the mF_o-DF_c electron density and neutron density maps was observed in the active site. Omit maps were calculated in the absence of AZA using both the X-ray data and X-ray/neutron data separately. The AZA molecule was modelled with an occupancy of 1.0. The information on protonation states obtained from the neutron data in the joint refinement was used to deuterate the ligand molecule. The positive peak in the mF_o-DF_c neutron density map is shown in Figure 4.8.

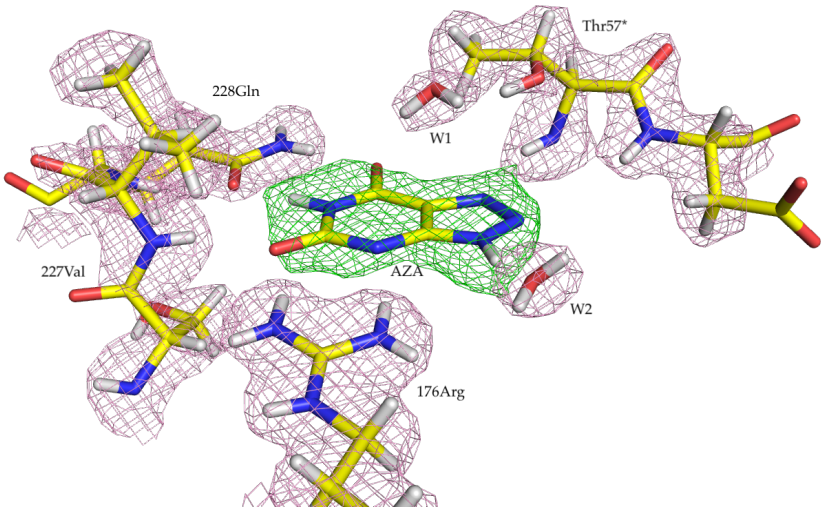

FIGURE 4.8: Neutron omit map calculated in the absence of 8-azaxanthine (AZA), identifying a clear positive peak in the mF_o-DF_c neutron density map contoured at 3.0 σ (green). The 2mF_o-DF_c neutron density map is contoured at 1.5 σ (pink).

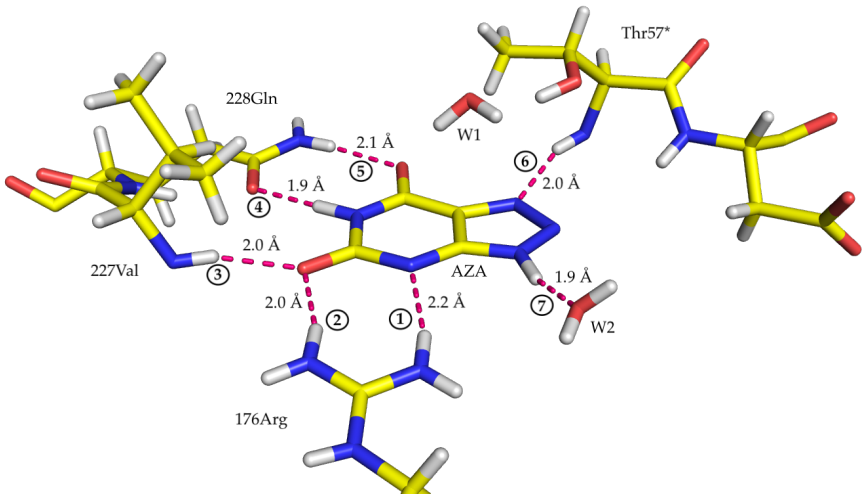

FIGURE 4.9: Hydrogen bonding partners between active site residues and AZA, hydrogen bonds are indicated by pink dashed lines. Hydrogen bond angles are numbered and detailed in Table 4.3.

TABLE 4.3: DUOX:AZA active site residues and hydrogen bond angles.

Hydrogen Bond (Donor – Hydrogen ····· Acceptor)									Bond Angle
①	Arg176	N	–	Arg176	D	–	AZA	N3	167°
②	Arg176	N	–	Arg176	D	–	AZA	O6	164°
③	Val227	N	–	Val227	D	–	AZA	O2	165°
④	Gln228	O	–	AZA	D1	–	AZA	N1	175°
⑤	Gln228	N	–	Gln228	D	–	AZA	O6	176°
⑥	Thr57*	N	–	Thr57*	D	–	AZA	N7	155°
⑦	AZA	N9	–	AZA	D9	–	W2	O	164°

Hydrogen bonding pairs are seen between several residues and the inhibitor molecule. The oxygen of Gln228 acts as a hydrogen bond acceptor to the deuterated N1 atom of AZA, and the -NH_2 group donates a hydrogen bond to the O6 of AZA. The guanidinium of Arg176 is positively charged, donating two hydrogen bonds to the N3 and O2 atoms of AZA. In addition, the deuterated backbone amide of Thr57*

acts as a hydrogen bond donor to the N7 position of AZA. These three residues are clearly identified as hydrogen bonding partners enabling the binding of the inhibitor molecule. Similar to the anaerobic UOX:UA structure, W2 is shown to hydrogen bond to the deuterated N9 position. The distance between the hydrogen atom on N9 and the oxygen atom of the W2 solvent molecule is 1.9 Å. Bonding partners and distances between AZA and UOX are shown in Figure 4.9 and hydrogen bond angles are detailed in Table 4.3.

4.6.2 The Solvent Molecule, W1

The X-ray data implied that the atom present above the inhibitor molecule is most likely an oxygen atom. The neutron data were used to determine the exact charge of this molecule and its orientation. In an omit map modelling only the oxygen atom, a large positive peak was observed in the mF_o-DF_c neutron density maps at 3.0 σ and spread across the W1 molecule, suggesting the presence of two deuterium atoms. This is shown in Figure 4.10 (a). Individually calculating omit maps on both D1 and D2 atoms, also presented strong evidence that the molecule was indeed a D_2O molecule, with localised positive peaks in the mF_o-DF_c neutron density maps at 3.0 σ, at each side of the oxygen atom. These omit maps are also shown in Figure 4.10 (c) and (d). When deuterium atoms are added, the $2mF_o$-DF_c neutron density map shows a defined orientation of the W1 water molecule, as shown in Figure 4.10 (b). The W1 molecule adopts a perpendicular orientation above the C4-C5 bond of AZA. The distance between oxygen atom of the W1 molecule and C5 atom of AZA is 3.5 Å.

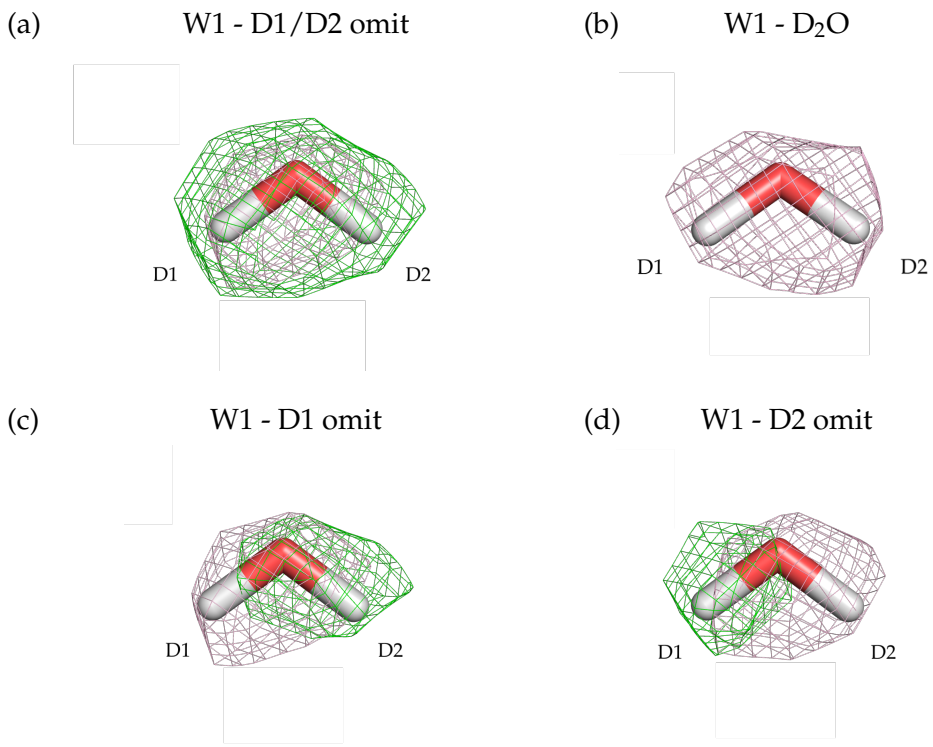

FIGURE 4.10: (a) Omit map in the absence of both deuterium atoms from the D_2O molecule, (b) Both deuterium atoms and oxygen atom of this D_2O molecule modelled, (c) Omit map in the absence of the D1 atom, (d) Omit map in the absence of the D2 atom. The $2mF_o$-DF_c neutron density map is contoured at 2.0 σ (pink) and mF_o-DF_c neutron density map is contoured at 3.0 σ (green).

4.6.3 Catalytic Residues

The residues surrounding the active site are described in Figure 4.11, and Tables 4.4 and 4.5. The protonation states of the residues containing labile hydrogen sites were determined by calculating omit maps.

The W1 solvent molecule is located above the AZA molecule in the active site, forming hydrogen bonds with residues Thr57* and Asn254 [65, 68].

Upon closer examination of Asn254, and neighbouring residues, it was observed that the residues Pro253-Asn254-Lys255 form an alternate conformation. Positive

peaks in both the mF_o-DF_c electron density map and mF_o-DF_c neutron density map at 3.0 σ was seen along the backbone of all three residues. This is shown in Figure 4.11 (a) and (b). This suggested that this chain of residues formed an alternate conformation. The two conformations are described in Figure 4.11 (c) and (d). The major conformation has an occupancy of 0.66 and is shown in yellow, and the minor alternate conformation has an occupancy of 0.33 and is shown in pink (Figure 4.11 (c) and (d)).

Using the X-ray data alone, it was not possible to resolve the orientation of the Asn254 polar sidechain, however, positive peaks in the mF_o-DF_c neutron density map identified that the -ND_2 points into the peroxohole, towards the W1 solvent molecule, forming hydrogen bonds in both conformations. The distance between the deuterium atom of Asn254 and the oxygen atom of the W1 solvent molecule in the major conformation is 2.2 Å. In the minor conformation the hydrogen bonding distance between the -ND_2 group of Asn254 to the oxygen atom of W1 is 2.3 Å. The hydrogen bonding distances between Asn254 and W1 are shown in Figure 4.12.

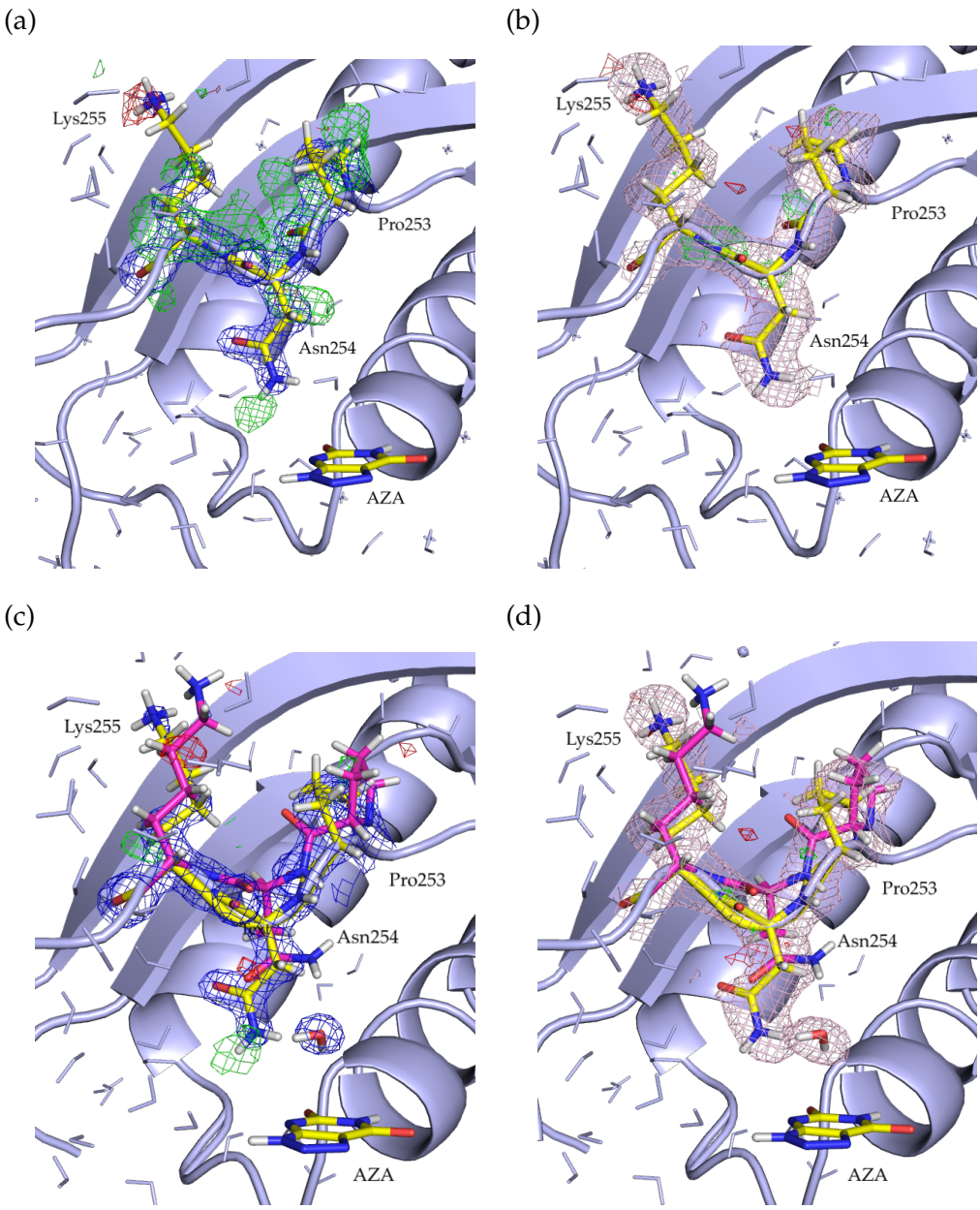

FIGURE 4.11: (a) The mF_o-DF_c electron density map, contoured at 3.0 σ (green), shows positive peaks surrounding residues Pro253, Asn254 and Lys255. This suggested that these three residues formed an alternate conformation. (b) The mF_o-DF_c neutron density map, contoured at 3.0 σ (green), also shows some positive peaks on the backbone of these residues. (c) It was chosen to model residues Pro253, Asn254 and Lys255 in an alternate conformation in the active site. (d) The major conformation has an occupancy of 0.66 (in yellow) and the minor conformation has an occupancy of 0.33 (in pink). The $2mF_o$-DF_c electron density map is contoured at 2.0 σ (blue) and the $2mF_o$-DF_c neutron density map is contoured at 1.0 σ (pink).

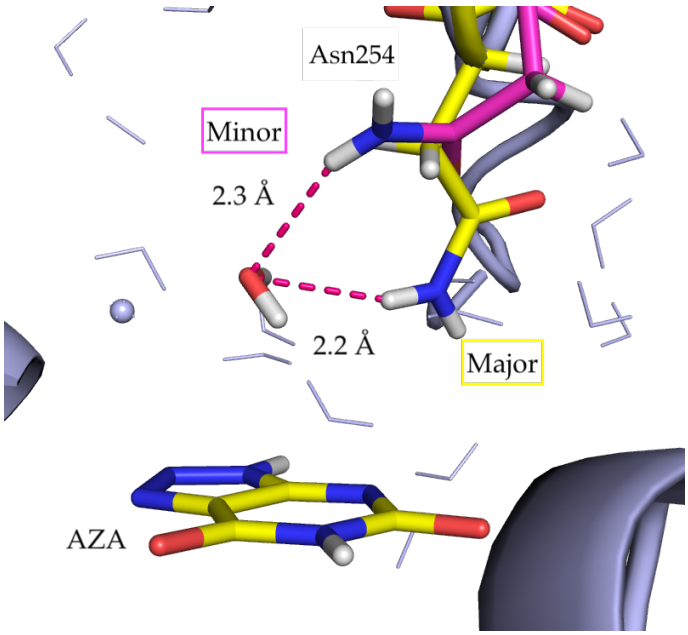

FIGURE 4.12: The -ND_2 group of the Asn254 sidechain forms hydrogen bonds with the oxygen atom of W1 in both major and minor conformations. The hydrogen bonds are indicated by pink dashed lines.

Residue Thr57* has been found to play a role in the catalytic function of UOX [91], and its hydroxyl sidechain is located next to the W1 solvent molecule/O_2 binding site. After calculating an omit map in the absence of the deuterium on the sidechain hydroxyl group of Thr57*, no positive peak was seen in the mF_o-DF_c neutron density map at 3.0 σ. This is shown in Table 4.4 (a). The value of 3.0 σ was used as it was the average level in which deuterium atoms could be seen on other threonine residues in the protein. Reducing the contour level to 2.5 σ resulted in no significant positive peaks in the mF_o-DF_c neutron density map next to the oxygen atom of the Thr57* hydroxyl group, shown in Table 4.4 (b). However, a further reduction in contour level to 2.0 σ showed a positive peak in the mF_o-DF_c neutron density map attached to oxygen atom of the Thr57* hydroxyl group, as shown in Table 4.4 (c). This is in addition to other positive peaks in the mF_o-DF_c neutron density map on the carbon atoms of the sidechain, attributed to noise. Therefore, from our data we are unable to provide convincing evidence that the Thr57* is deuterated. However,

it is likely that Thr57* is indeed deuterated as threonine residues commonly have neutral sidechains. At the resolution of this neutron data (2.1 Å), it has been possible to determine other important protonation states of the residues surrounding the active site, therefore it can be suggested that the Thr57* sidechain is deuterated and this deuterium atom is highly mobile. When the Thr57* is modelled with a deuterium atom on the hydroxyl group and the occupancy refined, it shows a peak in the $2mF_o$-DF_c neutron density map at 1.5 σ and with an occupancy of 0.58. It was chosen to model the deuterated hydroxyl group, with consideration to the most likely chemical state. The final model is shown in Table 4.4 (d).

Residue Lys10* is also involved in UOX catalysis [91]. Calculating an omit map of Lys10* in the absence of the three deuterium atoms on the sidechain nitrogen atom, showed a positive peak in the mF_o-DF_c neutron density map at 3.0 σ, shown in Table 4.4 (e). A positive peak located at the sidechain nitrogen atom was visible at all three contour levels (3.0, 2.5, and 2.0 σ), shown in Table 4.4 (e), (f), and (g). This provided evidence to suggest that this residue contains a charged ammonium group -NH_3^+. Therefore, it was chosen to model three deuterium atoms on this sidechain nitrogen atom: the final model is shown in Table 4.4 (h).

Neutron Omit mF_o-DF_c Map and Test Model (3.0 σ)	Neutron Omit mF_o-DF_c Map and Test Model (2.5 σ)	Neutron Omit mF_o-DF_c Map and Test Model (2.0 σ)	Neutron $2mF_o$-DF_c Map and Final Model (1.0 σ)
(a) Thr57*	(b) Thr57*	(c) Thr57*	(d) Thr57*
(e) Lys10*	(f) Lys10*	(g) Lys10*	(h) Lys10*

TABLE 4.4: Omit maps and final models for active site residues Thr57* and Lys10*. Omit maps involved the removal of -**OD** from Thr57*, (a)-(c), and -$\mathbf{ND_3}^+$ in Lys10*, (e)-(g). The protonation states of these residues were investigated by altering the σ level from 2 σ to 3 σ in the mF_o-DF_c neutron density map (green). The protonation states in the final models for Thr57* and Lys10* are shown in (d) and (h), respectively. The $2mF_o$-DF_c neutron density map is contoured at 1.0 σ (pink).

Residue His256 also lies in the proximity of the active site and is proposed to play a role in catalysis [77, 91]. When a deuterium atom bonded to His256 nearest Lys10*, Nϵ2 was modelled, no peak was observed in the mF_o-DF_c neutron density map at 3.0 σ, shown in Table 4.5 (a). However, changing the contour level 2.5 σ resulted in a negative peak in the mF_o-DF_c neutron density map at the deuterium atom bonded to Nϵ2, described in Table 4.5 (b). This negative peak was also seen at contour level 2.0 σ, in addition to the appearance of positive peaks on the carbon atoms of the histidine sidechain, shown in Table 4.5 (c). However, considering the negative peak seen at 2.5 σ, and the proximity to the positively charged Lys10* -ND_3^+ group, it was chosen to model this histidine residue as neutral. The final model is described in Table 4.5 (d).

An additional observation was that the deuterium atom modelled at the Cδ2 position of His256 showed no density in the 2mF_o-DF_c neutron density map of the final model, shown in Table 4.5 (d). It is expected that this deuterium atom would be seen in the 2mF_o-DF_c neutron density map as the protein is perdeuterated and the high level of deuterium incorporation has previously been determined (Chapter 2, Section 3.4) and found to be > 99%. Therefore, this lack of density is unlikely to come from hydrogen incorporation in the sample, however, may be explained by the level of completeness of the neutron data ($\sim$ 80%).

Neutron mF_o-DF_c Map and Test Model (3.0 σ)	Neutron mF_o-DF_c Map and Test Model (2.5 σ)
(a)	(b)
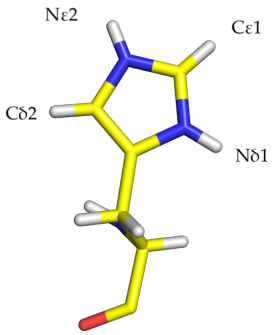	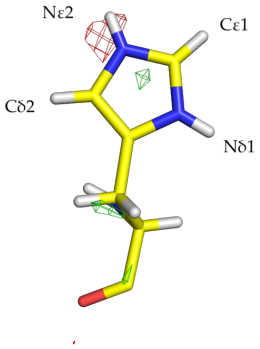
His256	His256
Neutron mF_o-DF_c Map and Test Model (2.0 σ)	**Neutron $2mF_o$-DF_c Map and Final Model (1.0 σ)**
(c)	(d)
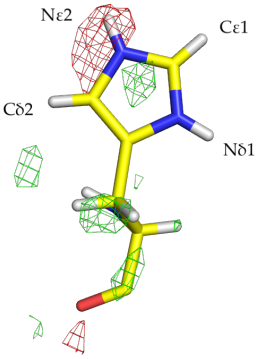	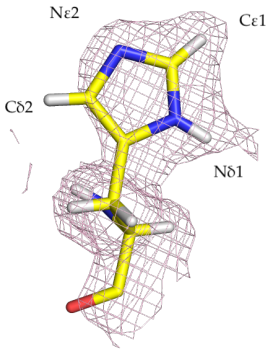
His256	His256

TABLE 4.5: A model containing a positively charged His256 shows no peak in the mF_o-DF_c neutron density map at 3.0 σ (green). However, there is a negative peak in the mF_o-DF_c neutron density map on the deuterium atom attached to -Nϵ2. This peak, shown at 2.5 σ and 2.0 σ (red), indicates an incorrectly modelled atom. Positive peaks in the mF_o-DF_c neutron density map were also observed (green). The final model of a neutral His256 is shown in (d). The $2mF_o$-DF_c neutron density map is contoured at 1.0 σ (pink).

Using the information from the omit maps calculated for each residue proposed to play a role in catalytic activity, we present the following hydrogen bonding network. Residue Thr57* is deuterated at the hydroxyl position -OD. This donates a hydrogen bond to the oxygen atom of the W1 solvent molecule in the active site with a hydrogen bond distance of 2.1 Å. Lys10* neighbours Thr57* and has a positively charged sidechain: $-ND_3^+$. This charged nitrogen atom donates a hydrogen bond to the lone pair of the hydroxyl oxygen atom of Thr57* at a distance of 2.0 Å. Furthermore, Lys10* donates a second hydrogen bond to the neutral His256: the unprotonated nitrogen atom of His256 acts as a hydrogen bond acceptor to the positively charged group of Lys10*, at a distance of 2.2 Å. This hydrogen bonding network is shown in Figure 4.13 with associated hydrogen bond angles detailed in Table 4.6. The overall structure of the protonation states in the active site and the $2mF_o$-DF_c neutron density maps are shown in Figure 4.14.

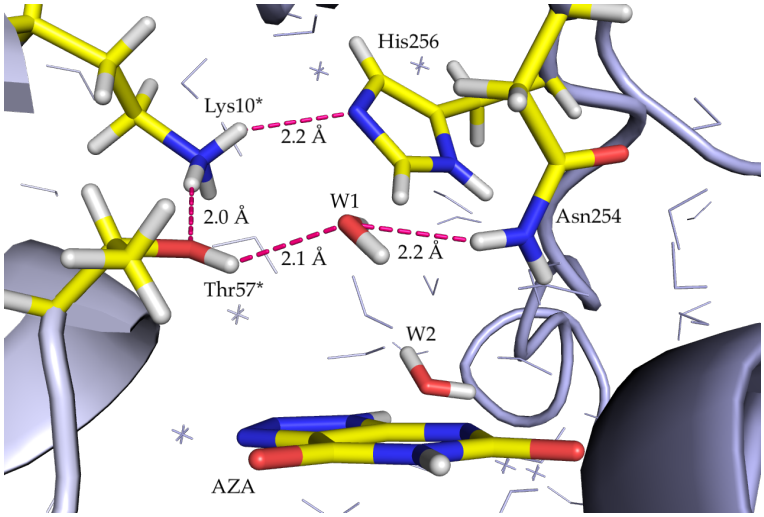

FIGURE 4.13: Hydrogen bonding network of active site residues. The relationship between proposed catalytic residues Thr57*:Lys10*:His256 are shown in relation to the W1 molecule. The distance between the major conformation of Asn254 and the W1 molecule is also shown. Hydrogen bonding distances are shown by pink dashed lines.

TABLE 4.6: DUOX:AZA active site residues and hydrogen bond angles (Donor – Hydrogen ····· Acceptor).

Hydrogen Bond (Donor – Hydrogen ····· Acceptor)								Bond Angle
Lys10*	N	–	Lys10*	D	·····	His256	N	145°
Lys10*	N	–	Lys10*	D	·····	Thr57*	D	167°
Thr57*	O	–	Thr57*	D	·····	W1	O	126°
Asn254	N	–	Asn254	D	·····	W1	O	153°

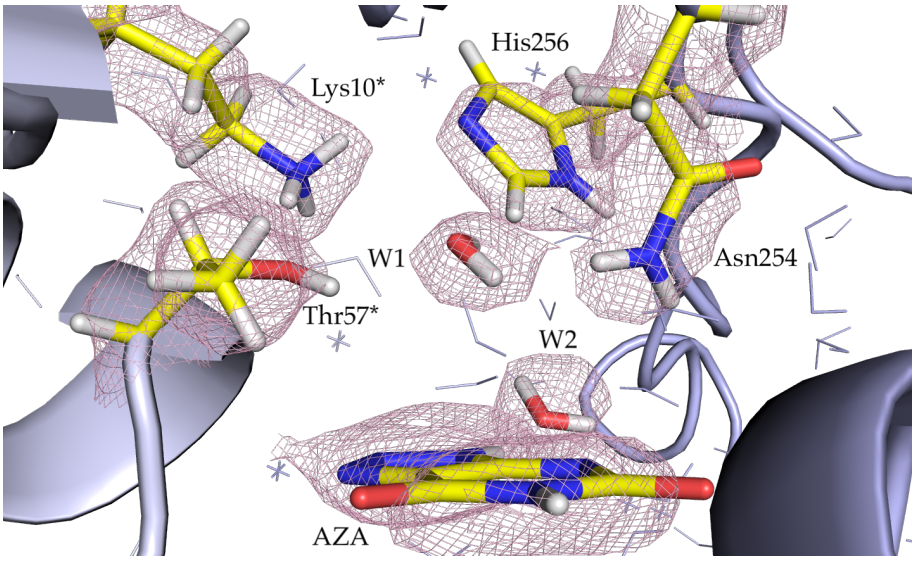

FIGURE 4.14: The determined protonation states in the active site of DUOX:AZA. The $2mF_o$-DF_c neutron density map is contoured at 1.0 σ (pink).

4.6.4 Active Site Water Network

As previously described, catalytically important solvent molecule W2 is hydrogen bonded to the deuterated N9 atom of AZA. A chain of water molecules is seen to provide a link between Lys10* and W2. One deuterium atom of -NH_3^+ on Lys10* hydrogen bonds to solvent molecule W102 at a distance of 2.1 Å. The W102 has an occupancy of 0.83 and hydrogen bonds to W64, occupancy 1.0, with a distance

of 2.2 Å. It is solvent molecule W64 that is shown to hydrogen bond to the W2 molecule with a distance of 2.0 Å. This bonding network is described in Figure 4.15 and associated hydrogen bond angles are detailed in Table 4.7.

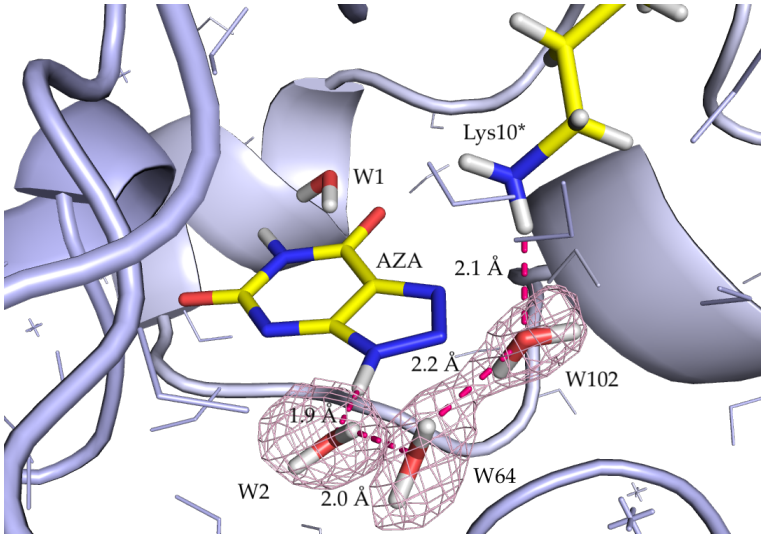

FIGURE 4.15: Hydrogen bonding network of D_2O molecules surrounding the active site. A clear network of three D_2O molecules link the Lys10* residue and the deuterated N9 atom of the bound 8-azaxanthine (AZA) ligand. Dashed pink lines show hydrogen bonding distances. The $2mF_o$-DF_c neutron density map is contoured at 1.0 σ (pink).

TABLE 4.7: Hydrogen bond angles for the W2 ····· Lys10* water network (Donor – Hydrogen ····· Acceptor).

Hydrogen Bond (Donor – Hydrogen ····· Acceptor)								Bond Angle
AZA	N9	–	AZA	D9	·····	W2	O	164°
W2	O	–	W2	D1	·····	W64	O	151°
W64	O	–	W64	D1	·····	W102	O	112°
Lys10*	N	–	Lys10*	D	·····	W102	O	166°

An additional water network is seen connecting W2 and His256, through W43. One deuterium atom of W2 forms a hydrogen bond with the oxygen atom of W43 with a distance of 2.5 Å. In addition, the oxygen atom also forms a hydrogen bond

with NϵD2 of His256 at a distance of 2.1 Å. A pictorial description of this alternative hydrogen bonding network involving catalytically important W2 and His256 is shown in Figure 4.16 with details of hydrogen bond angles in Table 4.8.

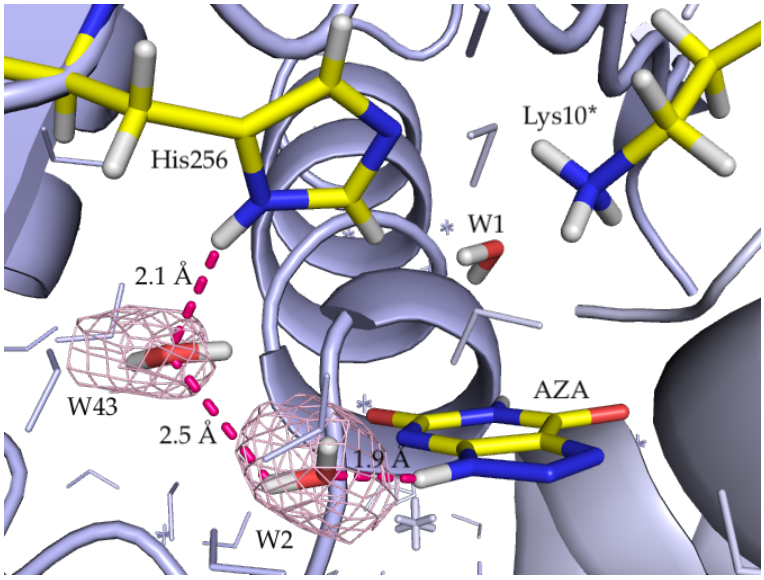

FIGURE 4.16: Hydrogen bonding network of D_2O molecules surrounding the active site. In addition to the network connecting Lys10* and the deuterated N9 atom of 8-azaxanthine (AZA), another network of D_2O molecules is seen to connect His256 and the deuterated N9 atom of AZA. Dashed pink lines show hydrogen bonding distances. The $2mF_o$-DF_c neutron density map is contoured at 1.0 σ (pink).

TABLE 4.8: Hydrogen bond angles for the W2 ····· His256 water network (Donor – Hydrogen ····· Acceptor).

Hydrogen Bond (Donor – Hydrogen ····· Acceptor)								Bond Angle
AZA	N9	–	AZA	D9	·····	W2	O	165°
W2	O	–	W2	D2	·····	W43	O	151°
His256	N	–	His256	D	·····	W43	O	112°

4.7 Discussion

Examination of the neutron structure of perdeuterated Urate Oxidase (DUOX) in complex with 8-azaxanthine (AZA) has allowed the identification of the protonation states of the residues in the active site when the AZA ligand is bound. The UOX:UA complex has previously been found to possess a solvent molecule termed W1 in the active site, as identified by X-ray experiments [81]. This W1 solvent molecule is seen to occupy the cavity above the ligand binding site, peroxohole, before its expulsion upon the binding of O_2 [65]. However, from X-ray data alone, the charge of the W1 solvent molecule and its interactions with surrounding residues remains elusive. Whether the W1 solvent molecule exists as H_2O, H_3O^+, or OH^- has not been seen using other techniques. The use of perdeuteration, and deuterated buffers, remove the problems associated with hydrogenation such as the negative coherent scattering length and large incoherent cross section. Therefore, it has been possible to determine the charged state of the W1 molecule and visualise key water networks surrounding the AZA inhibitor molecule.

The ligand binding position has been identified from previous X-ray structures and is the same for both the natural substrate and other inhibitor molecules [68, 76, 78, 80]. Our data have confirmed all bonding interactions between AZA and active site residues and that AZA binds as an N3 monoanion, described in previous studies [76, 77, 80, 82, 83].

The X-ray and neutron data were able to confirm the presence of the W1 molecule in the peroxohole located above the active site, as seen in other X-ray structures [65, 81, 82]. In our structure, the X-ray data show that the distance between the oxygen atom of the W1 molecule and C5 of AZA is 3.5 Å. This distance is slightly longer than previously reported values in X-ray structures of UOX:AZA where the distance is 3.3 Å [68] and in UOX:UA anaerobic complexes distances were shown as 3.26 Å [82] and 3.19 Å [81], respectively. This may be due to the difference in

temperature of data collection: 100K for the previously reported structures and room temperature for the structures reported in this thesis.

The residues Thr57* and Asn254 both form hydrogen bonds with the W1 molecule, holding it in position above the ligand or substrate molecule [68]. Our data strongly suggests that residues 253-255 form alternate conformations. The Asn254 involved in bonding adopts two visible positions; in both positions the amide -ND_2 group of Asn254 hydrogen bond to the oxygen atom of the W1 solvent molecule. The major and minor conformations have hydrogen bonding distances of 2.2 Å and 2.3 Å, respectively. With this information we suggest that there is an enhanced mobility of this region compared to that observed in previous cryo-cooled structures.

Catalytically important Thr57* forms a hydrogen bond with the oxygen atom of the W1 molecule. At the average threshold used to visualise the presence of deuterium atoms of other threonine sidechains (3.0 σ in the mF_o-DF_c neutron density map), there was no evidence for a deuterium atom on the hydroxyl group of Thr57*. By altering the contour level to 2 σ in the mF_o-DF_c neutron density map, a positive peak appears next to the oxygen atom of the Thr57* hydroxyl group. However, at this threshold, additional positive peaks are observed on the carbon atoms of the Thr57* sidechain. Therefore, the positive peak seen at the oxygen atom cannot be considered as unambiguous evidence of a deuterium atom and, instead, may be considered as noise. However, chemical knowledge suggests that a unprotonated Thr57* sidechain is extremely unlikely. With this consideration, it was chosen to model the Thr57* sidechain with a deuterium atom, forming a hydrogen bond with the oxygen atom of the W1 solvent molecule at a distance of 2.1 Å.

It was determined that the sidechain of Lys10* contained a positively charged -ND_3^+. An omit map showed a positive peak in the neutron mF_o-DF_c neutron density map surrounding the sidechain nitrogen atom. Modelling three deuterium atoms showed agreement in the $2mF_o$-DF_c neutron density map. Therefore, we

propose the positively charged Lys10*-ND_3^+ group donates a hydrogen bond to the lone pair of Thr57* with a bonding distance of 2.0 Å.

Neighbouring His256 was found to be in a neutral state. The charge of His256 was investigated by modelling both a neutral and positive residue. A negative peak in the mF_o-DF_c neutron density map was seen at the deuterium atom attached to the Nϵ2 atom, located at bonding distance to Lys10*. From this information, also considering the positively charged Lys10*, it was chosen to model His156 as neutral.

We compared the protonation states of the active site residues in our structure to those in previously published neutron structures [80]. These studies identified the protonation states of active site residues with hydrogenated UOX (HUOX) in complex with inhibitor AZA, HUOX:AZA, and natural substrate UA, forming HUOX:8-HX. Both complexes were inhibited by the presence of a chloride atom, occupying the binding site of the W1 solvent molecule/O_2. Interestingly, the protonation states of the catalytic triad Thr57*-Lys10*-His256 in HUOX:AZA differed from those of the HUOX:8-HX complex. This is described in more detail in section 4.1, Figure 4.3. However, the study suggested that it is likely that the triad in HUOX:AZA exists in two conformations: the one presented in the published model containing a Lys10* -ND_2 accepting a hydrogen bond from Thr57*, and a conformation identical to that seen in HUOX:8-HX where Lys10* is positively charged -ND_3^+ and the deuterated Thr57* hydroxyl group points towards the Cl^- in the active site. It states that due to the limited resolution of the neutron data, they were unable to refine both conformations. In our structure DUOX:AZA, we have found that the protonation states of the catalytic triad are different to those in the HUOX:AZA complex. In fact, the protonation states of Thr57*-Lys10*-His256 that we have determined are identical to those seen in HUOX:8-HX [80].

An extensive network of conserved water molecules surrounds the active site in

many UOX complexes, as identified by X-ray studies [68, 76, 77, 81, 83]. In particular, the W1 and W2 solvent molecules have been proposed to be ideal candidates as acid-base system terminators [78]. However, previous studies have been unable to identify the relationship between this water network, including the W1 solvent molecule, and surrounding active site residues [78, 80, 81]. The W2 solvent molecule positioned close to the deuterated N9 atom of AZA is shown to be catalytically relevant as its absence in MUA complexes inhibits the reaction [81, 106, 257]. These positions are shown in both other UOX:AZA structures [80] and also UOX:UA anaerobic structures [81]. This forms an ordered hydrogen bonding network from the active site along Thr57*-Lys10*-His256, previously suggested to have relationship in catalytic activity [77].

4.8 Conclusion

DUOX in complex with its inhibitor AZA has been crystallised and neutron data collected to a resolution of 2.1 Å. In addition, X-ray data was collected on the same crystal to a resolution of 1.34 Å. The structure of this complex has been solved using the method of joint refinement. By employing the technique of neutron crystallography, coupled with perdeuteration, hydrogen positions, and hydrogen bonding networks have been identified.

In this DUOX:AZA complex, it has been possible to determine the charge of the W1 solvent molecule. Our data shows that the W1 solvent molecule exists as an D_2O in the AZA-bound active site, and not as D_3O^+ or OD^-. It is held in the peroxohole by hydrogen bonding to residues Thr57* and Asn254. The Asn254 residue forms a hydrogen bond to the oxygen atom of the W1 molecule in both its conformations in this model.

The protonation states of residues surrounding the active site have also been determined. From our data, we present the Thr57*-Lys10*-His256 'catalytic triad' with the W1 molecule *in situ*. Catalytically relevant Thr57* is shown to donate a hydrogen bond to the W1 molecule. Additionally, it accepts a hydrogen bond from Lys10* which contains a positively charged sidechain -NH_3^+. Neighbouring His256 is neutral and positioned to accept a hydrogen bond from Lys10*. The finalised protonation states of this bonding network is shown in Figure 4.17. Conserved water molecules were also investigated and hydrogen bonding networks established.

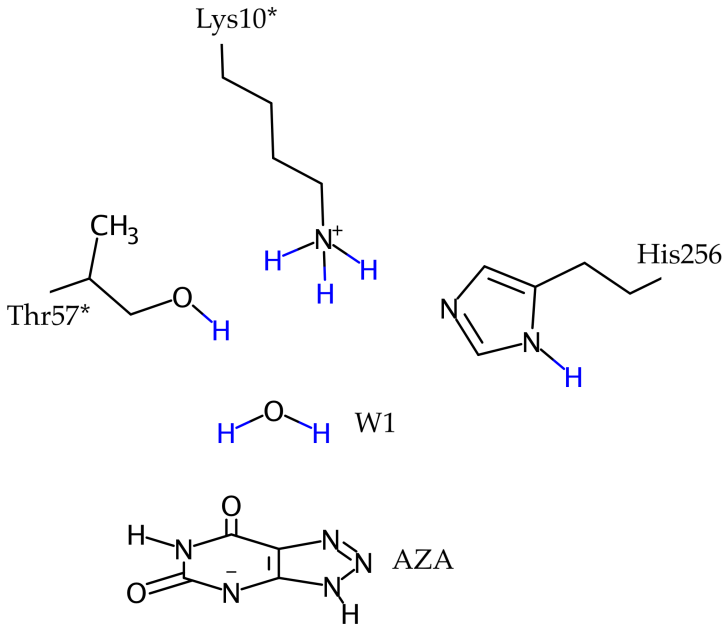

FIGURE 4.17: The perdeuterated Urate Oxidase:8-azaxanthine (DUOX:AZA) active site. Schematic of the DUOX:AZA active site and the protonation states of the catalytic triad: Thr57*-Lys10*-His256. It has been determined that the residues Thr57*, Lys10* and His256 form a hydrogen bonding network, linking to the W1 solvent molecule held in the active site in this DUOX:AZA complex.

The absence of chlorine as an inhibitor allows the preservation of the W1 solvent

molecule. Building on previous neutron studies, we have provided additional information on UOX in complex with AZA, collecting a dataset of higher completeness and neutron density maps with no cancellation effects observed from hydrogen contamination.

Chapter 5

Neutron Refinement of Perdeuterated Urate Oxidase (DUOX) complexed with 9-methyl uric acid (9-MUA)

Abstract

This chapter describes a structural study of perdeuterated Urate Oxidase (DUOX) in complex with the structural analogue of uric acid (UA), 9-methyl uric acid (9-MUA). In aerobic conditions 9-MUA reacts with O_2 and forms the 9-methyl-5-peroxyisourate intermediate (5-PMUA). This research investigated the protonation states of active site residues in the DUOX:5-PMUA complex and the structure of the peroxide intermediate. The neutron structure of this complex is important for an understanding of which active site residues are involved in the peroxide formation and stabilisation.

9-MUA has a high structural similarity to the natural substrate of UOX, UA. The

substitution of a hydrogen atom with a methyl group at the N9 atom position of the purine ring enables the trapping of the peroxide intermediate by preventing the expulsion of the H_2O_2 by-product. Neutron and X-ray datasets were collected on the same crystal at 298 K. X-ray refinement, joint refinement, and neutron refinement were performed using these datasets. Experimental details and results are described within this chapter. Further analysis of the implications of the results presented are also discussed in the context of UOX reactivity.

5.1 Introduction

The structure of reactive intermediates in the UOX reaction pathway have been widely investigated using a variety of techniques, as described in detail in Chapter 1 of this thesis [80, 81, 91, 104, 108, 115, 122, 123]. One particular area of interest was the proposal of two different UOX catalytic pathways involving the reaction of UA and O_2. The presence of a peroxide intermediate, 5-(hydro)peroxyisourate (5-PIU), had been suggested by Tipton and colleagues [106, 113, 115], generated from the radical recombination reaction of the UA radical and a superoxide anion [81, 112]. In contrast, Altarsha *et al.* suggested the reaction mechanism was peroxide independent, instead a dehydrourate intermediate (DHU) would form directly from the N3N7 reactive dianion [108]. A mechanism, based on the results of neutron studies by Oksanen *et al.*, also suggested a peroxide-independent pathway, where the O_2 molecule accepts two electrons: one from the UA radical anion and one from an unidentified intermediate acceptor contained within the protein [80].

Bui *et al* used X-ray crystallography, in conjunction with *in-crystallo* Raman spectroscopy and quantum mechanics/molecular mechanics (QM/MM) calculations, to unambiguously determine that the reaction proceeded via a peroxide intermediate [81]. In this study, two crystal structures were presented: UOX in complex with 9-MUA, and UOX in complex with the natural substrate, UA. For clarity in

the following discussion, these structures will be referred to as containing hydrogenated UOX (HUOX). Bui *et al.* reasoned that the replacement of a labile hydrogen atom with a methyl group at position N9 in 9-MUA could stabilise any peroxide intermediate: it had been proposed that this hydrogen atom is abstracted during the expulsion of H_2O_2 [81]. A structural comparison of 9-MUA and UA is shown in Figure 5.1.

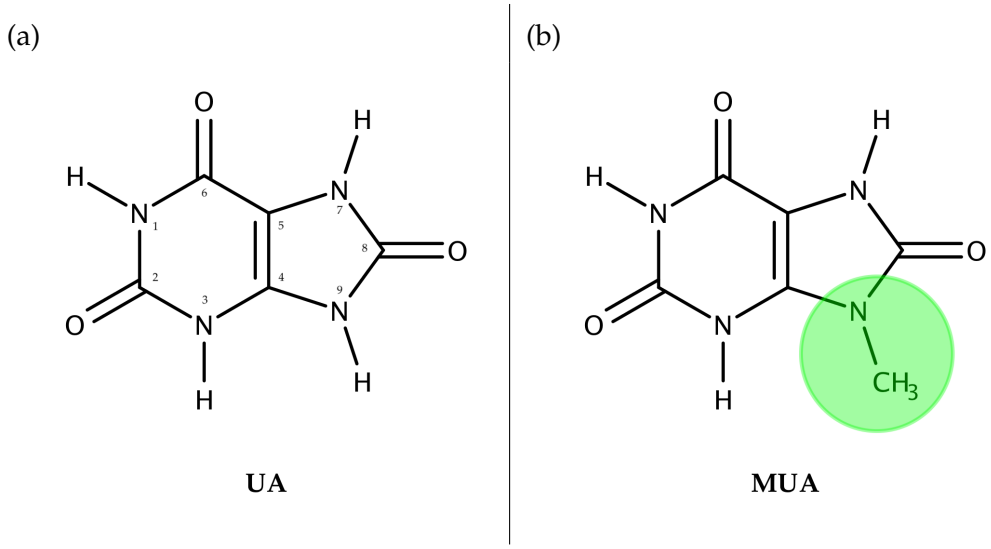

FIGURE 5.1: Natural substrate uric acid (UA) (a) is shown in comparison to structural analogue 9-methyl uric acid (9-MUA) (b). The 9-MUA molecule is structurally different in the N9 position where the labile hydrogen is replaced with a methyl group -CH_3, this is highlighted in green.

X-ray data was collected on a HUOX crystal complexed with 9-MUA, after exposure to air/O_2. The resultant electron density maps clearly showed that the 9-MUA ligand converts to the 9-methyl-5-(hydro)peroxyisourate intermediate (5-PMUA) as shown in Figure 5.2 [81]. The C5 atom of 9-MUA forms a bond with an oxygen atom of O_2 (Op1). QM/MM calculations suggested that the experimentally determined distance of the C5-Op1 of the 5-PMUA bond was consistent with that of a hydroperoxide monoanion [81]. An additional structure consisting of HUOX in complex with UA also showed the presence of a peroxide intermediate,

5-(hydro)peroxyisourate (5-PIU), thus confirming that the UOX catalytic pathway proceeded via a peroxide-dependant mechanism [81].

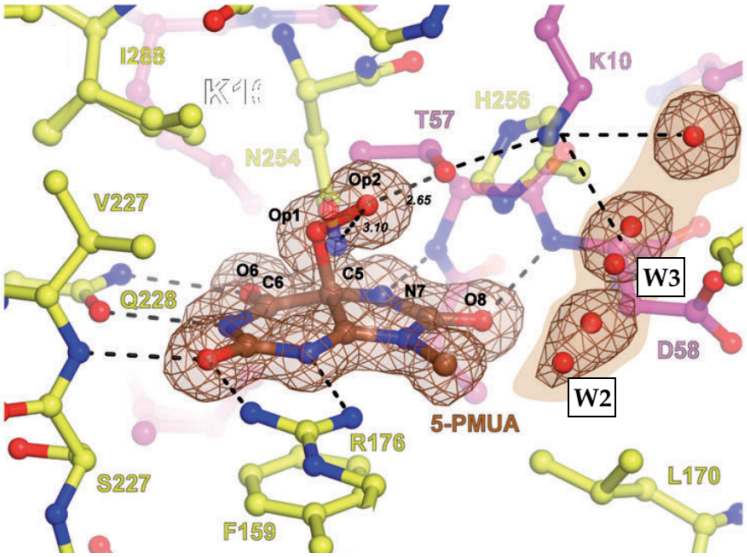

FIGURE 5.2: The 9-methyl-5-(hydro)peroxyisourate (5-PMUA) ligand bound to hydrogenated Urate Oxidase (HUOX) as determined by X-ray crystallographic studies. The C5 atom bonds to Op1 atom of O_2. $2mF_o$-DF_c electron density map is contoured at 1.0 σ in brown. Figure adapted from [81]

By comparing the structures of HUOX:5-PMUA and HUOX:5-PIU, differences in the water network surrounding the active site were observed. The substitution of a -CH_3 group at position N9, disrupts the hydrogen bond between a hydrogen atom on UA and the oxygen atom of the solvent molecule, W2. This solvent molecule is central to a hydrogen bonding network of water molecules in the active site and has been characterised as an end point of a low energy proton transfer pathway, also involving solvent molecule W1, which is proposed to be involved in the UOX catalytic activity [82, 83].

Bui *et al.* also found that the C5-Op1 bond was susceptible to radiolysis at low X-ray doses [81]. It was proposed that a one-electron reduction, induced by X-rays, caused the peroxide bond rupture and is supported by additional QM/MM calculations [81]. Furthermore, the C5-Op1 bond of 5-PMUA was found to be more

sensitive to radiolysis than in 5-PIU: it was suggested that this may be due to the inductive effect of the methyl group [81].

A peroxide intermediate has also been proposed for a group of Flavin-dependent monooxygenases [14, 116]. Flavin cofactors can exist in either a one- or two- electron reduced state, meaning that these molecules can both accept and donate electrons. In reactions with O_2, a reduced Flavin moiety can deliver one electron to the O_2 molecule, resulting in the generation of a radical pair: a Flavin semiquinone and superoxide [14, 15]. These radicals can then undergo a 'spin allowed' radical recombination reaction to form a C4a-(hydro)peroxyflavin intermediate [14, 15]. This C4a-(hydro)peroxyflavin intermediate shows structural similarities to the 5-PIU intermediate observed in UOX catalysis. More details on the reactions of Flavin enzymes are given in Chapter 1 of this thesis.

Interestingly, a peroxide-dependent mechanism has also been proposed for cofactor-independent dioxygenases [97, 119]. The substrates are thought to transfer a single electron to O_2 following an initial deprotonation, generating a radical pair that can collapse to a peroxide species after a radical recombination. This has been suggested for dioxygenases of different functions: HOD, QOD, and DpgC [97, 119]. These intermediates have not been structurally determined, however, this system of deprotonation followed by peroxide formation is similar to that proposed for UOX [112].

In the case of UOX, how the peroxide intermediate observed by Bui *et al.* is formed and stabilised is still not understood [81]. The role that catalytically relevant residues play in this process has also not yet been determined. Investigation into the protonation states of these residues, particularly the catalytic triad Thr57*-Lys10*-His256, may yield answers that can further our understanding of how this mechanism proceeds and provide additional information on cofactor-free catalysis.

This chapter presents the crystallisation, neutron and X-ray data collection, and

subsequent structure solution of DUOX in complex with structural analogue 9-MUA, forming 5-PMUA intermediate. This work builds on the X-ray studies by Bui *et al.* that were able to unambiguously determine the existence of a peroxide-intermediate [81]. The examination of the protonation states of important residues in the active site may further the understanding of how this peroxide species is produced and stabilised. From this information it may be possible to try and identify the role of UOX in this catalytic step.

5.2 Crystallisation of DUOX:5-PMUA

The expression and purification of DUOX is described in Chapter 3. In addition, the process of exchanging the protein into fully deuterated conditions is also described in Chapter 3, Section 3.3. The protein was concentrated to > 20 mg/ml in fully deuterated conditions, 50 mM Tris-acetate, 30 mM NaAc at pD 7.59.

The batch crystallisation method was used for growing crystals of DUOX:5-PMUA. Crystallisation conditions were optimised and found that a mixed solution, containing both hydrogenated and deuterated buffers, produced higher quality crystals. Mixtures measuring a total of 30 μL, consisting of 20 μL protein solution (deuterated) and 10 μL crystallisation buffer (hydrogenated) were prepared. The hydrogenated crystallisation buffer consisted of 50 mM Tris-acetate, 8% PEG 8000, adjusted to pH 8.0 using 20 % acetic acid. DUOX:5-PMUA crystals were produced by co-crystallisation. 9-MUA was added to the crystallisation buffer to a concentration of 11mM and the solution was agitated overnight until fully dissolved.

Sitting Drop plates (Hampton Research) were used in the crystallisation set-up, using the concave sitting drop post for the mixture and leaving the reservoir empty, before sealing with crystallisation tape. The crystallisation set-up has previously been shown in Chapter 4, Figure 4.4. The mixtures were left to crystallise at 18 °C.

After $\sim$ 5 days nucleation was observed, with crystals reaching full size after $\sim$ 10 days. Upon reaching full size (> 1.0 mm^3) crystals were immediately mounted into a quartz capillary with an internal diameter of 3 mm in preparation for data collection.

The crystal was added to the halfway point of the capillary with deuterated mother liquor present at the bottom of the capillary. After mounting the crystal into the capillary, a neutron dataset was collected. It was observed that although the crystallisation conditions had an excess of deuterium, there was a level of hydrogen contamination still present in the crystal. Therefore, a further buffer exchange into 100% deuterated conditions was required.

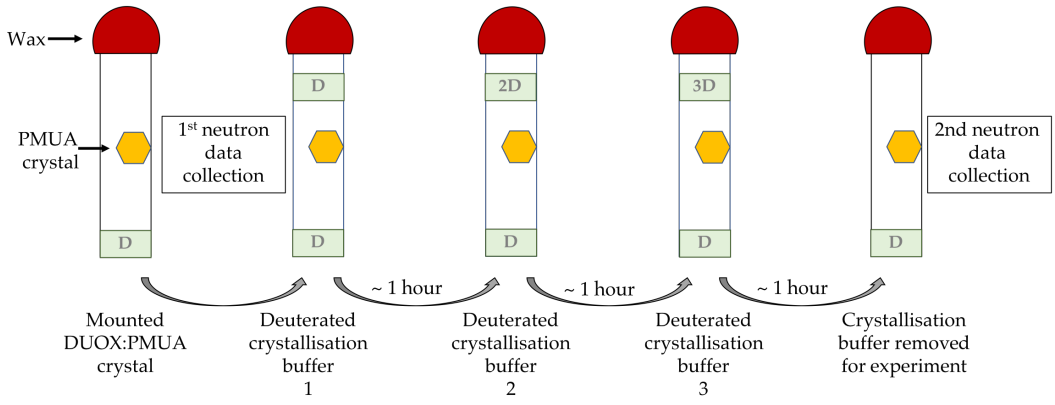

FIGURE 5.3: Method used for buffer exchanging the hydrogens incorporated into the crystal to deuterium through systematic vapour diffusion. The buffer plug was replaced after $\sim$ 1 hour diffusion times with fresh deuterated buffer, before removal for data collection.

Buffer exchange into 100% deuterated conditions was conducted within the quartz capillary in which the crystal was mounted. Approximately 5 μ L of deuterated crystallisation buffer, 50 mM Tris-acetate 8% PEG 8000, pH 7.59 with 11 mM 9-MUA, was added to the top of the capillary closest to the wax sealant. This sample was left to buffer exchange for $\sim$ 1 hour before replacement with fresh 100% deuterated buffer. This process was repeated 3 times as shown in Figure 5.3. Comparison of the data collected before and after the buffer exchange via vapour diffusion

showed clear deuterium incorporation, as explained in Section 5.6.2 of this chapter.

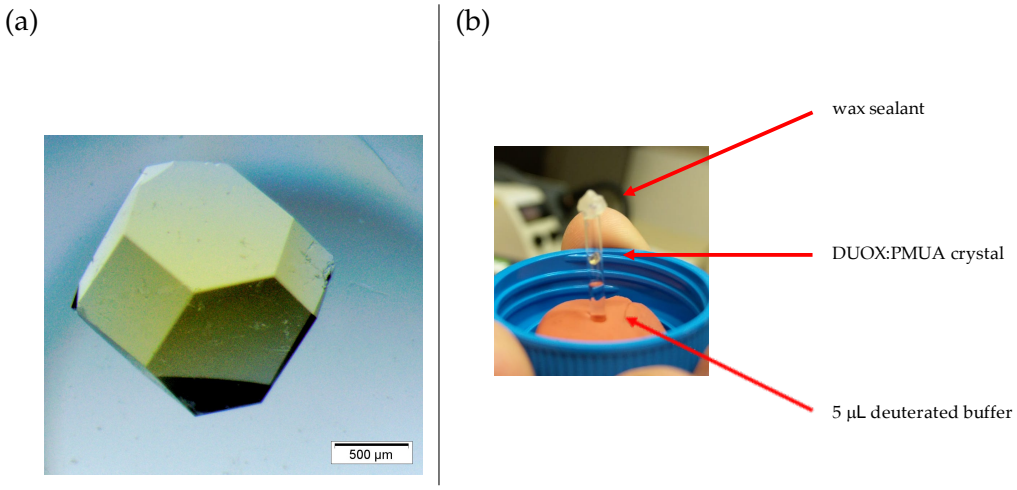

FIGURE 5.4: (a) A 1.2 mm^3 crystal of perdeuterated Urate Oxidase in complex with 9-methyl-5-peroxyisourate (DUOX:5-PMUA) was used for data collection and subsequent X-ray data collection (b) This crystal mounted in a 3 mm diameter quartz capillary for data collection.

Mother liquor above the crystal was completely removed and the capillary was sealed with wax to prevent any exchange with air and to prevent dehydration of the crystal. Other samples had suffered a problem of condensation inside the capillaries during data collection where droplets of solvent had been seen to accumulate on the walls of the quartz capillaries causing the crystal to move during data collection, and in some cases loss of diffraction. Therefore, the crystal was hydrated with buffer at one end of the capillary only. In this data collection, the crystal remained hydrated for the duration of the neutron and X-ray measurements, with no condensation problems. The DUOX:5-PMUA crystal selected for data collection and the mounted crystal set-up is shown in Figure 5.4 (a) and (b). It is important to note that the neutron data collection described in this chapter was conducted immediately after the buffer exchange process was completed.

5.3 Quasi-Laue Data Collection on LADI-III

The DUOX:5-PMUA crystal was mounted onto the sample position of the LADI-III beamline located at the Institut Laue-Langevin (ILL), Grenoble [164]. LADI-III is equipped with a large cylindrical detector which surrounds the sample and is composed of neutron-sensitive image-plates (diameter: 400 mm, height: 450mm) [164]. This beamline Quasi-Laue neutron diffraction data was collected to a resolution of 1.9 Å. A wavelength range of 3.12 - 4.2 Å, centered at 3.68 Å was used throughout the data collection. As typical for the Quasi-Laue method, the crystal was held in a stationary position for the duration of the experiment, rotating by an angle of 10° between each image. A total of 36 images were collected with an average exposure time of 2 hours, using 5 different crystal orientations to increase the completeness of the dataset. A Quasi-Laue diffraction image with an exposition time of 2 hours is shown in Figure 5.5. The crystal was recovered and used in the subsequent X-ray data collection.

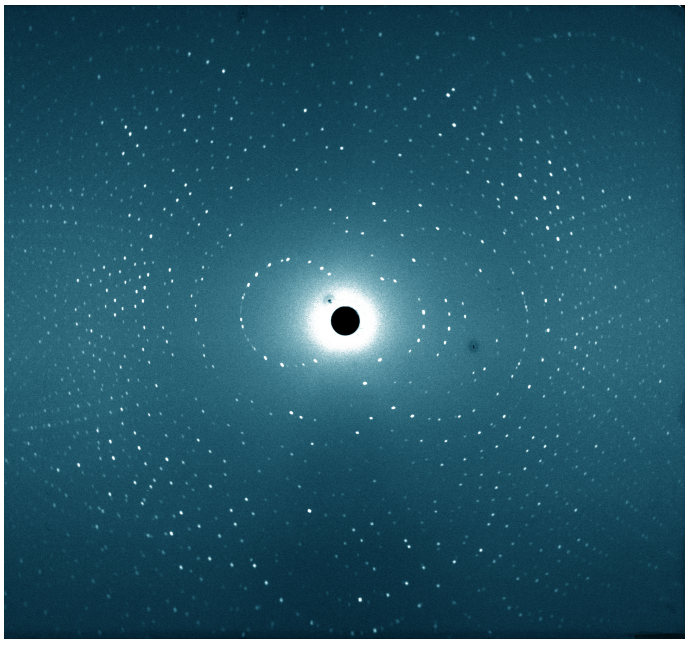

FIGURE 5.5: A Quasi-Laue neutron diffraction pattern from the crystal of perdeuterated Urate Oxidase in complex with 9-methyl-5-peroxyisourate crystal (DUOX:5-PMUA) with 2 h exposure time.

TABLE 5.1: Neutron and X-ray data collection statistics for DUOX:5-PMUA crystal at 293 K.

	Neutron data LADI, ILL	X-ray data FIP, ESRF
Space group	*I* 2 2 2	*I* 2 2 2
Unit cell parameters		
a b c (Å)	80.08, 96.15, 105.36	80.08, 96.15, 105.36
$\alpha\ \beta\ \gamma$ (°)	90 90 90	90 90 90
Wavelength (Å)	3.12 - 4.2	0.9800
No. of images	36	240
Angle between images (°)	10	1
Average exposure time	2 *h*	5 *s*
Resolution (Å)	40.0-1.90 (2.00-1.9)	40.04-1.39 (1.41-1.39)
No. of observations	195714 (17813)	598501 (28822)
No. unique reflections	29734 (3892)	81736 (3982)
Completeness (%)	92.5 (83.9)	100 (100)
Multiplicity	6.6 (4.6)	7.3 (7.2)
$\langle I/\sigma I \rangle$	9.2 (3.8)	17.2 (1.2)
R_{merge}	0.132 (0.349)	0.055 (1.925)
$R_{p.i.m.}$	0.044 (0.157)	0.022 (0.766)
$CC_{1/2}$	99.4 (98.7)	99.9 (51.1)

Values in parentheses are for the highest resolution shell.

The reduction of the neutron data was conducted by the program *LAUEGEN* [172] and followed by wavelength normalisation using *LSCALE* [173]. The scaling and merging of recorded reflections was conducted using *SCALA* [251] before using *TRUNCATE* [252, 253] to convert the intensities to structure factors. Full statistics for the neutron data collection are described in Table 5.1.

5.4 X-ray Data Collection on FIP

An X-ray dataset was collected on the same crystal that was used in the neutron data collection. The time between neutron data collection and X-ray data collection was two weeks, due to beamtime availability at the ESRF, Grenoble. It was measured at 293 K using the FIP beamline at the ESRF at λ = 0.9800. A total of

240 images of 1° oscillation and 5 *s* exposure per image were recorded on an ADSC Q315 detector. The intensities were indexed and integrated using the *XDS* package then were merged and scaled using the CCP4 program *AIMLESS*. The statistics are shown in Table 5.1.

5.5 Refinement of DUOX:5-PMUA

The model 4CW6 was taken from the PDB and used as a starting model for the refinement. Firstly, alternate conformers, waters molecules, and the ligand molecule, were removed from the model. The model was also converted to isotropic B-factors and atomic positions were shifted by 0.1 Å to reduce model bias. This model contained an acetylated serine residue that was mutated in the model to a terminal serine residue as in our sequence.

Structure refinement using X-ray data alone was conducted using the *PHENIX* suite and model building was done using the Molecular Graphics Package *Coot* [185, 186]. By first refining the model using only the higher resolution X-ray data, it was possible to locate the positions of the heavy atoms in the protein complex in preparation for joint refinement with neutron data (C, N, O, S). The primary step of refinement was to conduct a rigid body refinement. This was followed by iterations of refinements of atomic coordinate positions, individual occupancies, and B-factors. After 3 rounds of refinement, the models atomic B-factors were refined anisotropically. The 5-PMUA ligand was modelled with an occupancy fixed at 1.00 and refined using the geometry restraints generated using *eLBOW* [256].

Structure factor amplitudes from both X-ray and neutron data collections were combined in one *.mtz file* for joint refinement. The R_{free} flags consisted of 5% and 10% of the reflections from the neutron and X-ray data, respectively. The model built using the X-ray data was used as the starting model. All water molecules

modelled as oxygen atoms only were removed. Deuterium atoms were added to all hydrogen positions using the program *READYSET*, due to the use of perdeuteration and vapour diffusion exchange into deuterated buffer. However, it was observed that the X-ray and neutron data presented different features, particularly surrounding the 5-PMUA ligand, causing problems with the interpretation of the protonation states in the active site, see Sections 5.6.3 and 5.6.4. Therefore, a 'neutron-only' refinement strategy was used to finalise the model.

The jointly refined structure was used as a starting model and all 'X-ray only' features were removed. This included 'X-ray only' water molecules (oxygen atoms) and split conformers that were only visible in the electron density map. In addition, all atoms were refined isotropically. The full statistics for this finalised neutron-only structure are reported in Table 5.2. The R_{work} value for this structure was 21.39% and the R_{free} value was 25.21%. The final refinement for which statistics are reported in Table 5.2, used the best X-ray model as a *reference model* in the phenix input parameters. We reasoned that this should improve the overall model as bond lengths and angles should be better defined in the X-ray structure. We verified that this approach did not influence the final protonation states, these were consistent with and without the inclusion of the reference model. The addition of the *reference* model resulted in a slight improvement in the R_{free}, R_{factor}, and the RMSD of bonds and angles.

D_2O molecules were manually fitted into positive density in the mF_o-DF_c neutron density map at $\sigma > 3.0$. *Coot* was used to correctly orientate and model these D_2O molecules. Several mobile water molecules could be identified were modelled as oxygen atoms only as their orientations were not clearly seen in the mF_o-DF_c neutron density map.

Similarly to the method described in Chapter 4, labile hydrogen positions in side chains were systematically checked. Deuterium atoms were added to positive peaks seen in the mF_o-DF_c neutron density map and removed from negative peaks,

both at levels of $\sigma > 3.0$. In this process it was assumed that there was minimal contamination from hydrogen in the previous buffer and from atmospheric humidity.

TABLE 5.2: Model-refinement statistics for the neutron-only refinement of perdeuterated Urate Oxidase in complex with 9-methyl-5-peroxyisourate (DUOX:5-PMUA).

	Neutron only statistics
Resolution (Å)	38.39 - 1.9
Number of reflections	29360
Completeness (%)	90.61 (83.58)
R_{work}	0.2139
R_{free}	0.2521
B factors (Å^2)	
Protein	46.23
Ligand	39.51
Solvent	53.59
R.M.S Deviations	
Bond lengths (Å^2)	0.005
Bond angles (Å)	0.924
No. of Waters (D_2O, O)	190, 12

5.6 Results

5.6.1 Deuterium Incorporation

The inclusion of deuterium atoms could be evaluated by comparing the neutron density maps before and after the buffer exchange. The visualisation of D_2O molecules, and the lowering of the background scattering arising from hydrogen incoherent scattering, provided evidence that the addition of deuterium from the exchange

had been successful. A number of D_2O molecules contained hydrogen atoms in the initial dataset however after buffer exchange showed well defined $2mF_o$-DF_c neutron density. A sample of D_2O molecules are shown before and after buffer exchange in Figure 5.6. For each D_2O molecule, the neutron density before buffer exchange does not show a well-defined orientation and show negative peaks in the mF_o-DF_c neutron density maps. It is likely that these negative peaks are attributed to hydrogen contamination in the solvent. However, examining molecules in the same positions after buffer exchange shows that the D_2O molecules now adopt a well-defined orientation and show no negative peaks in the mF_o-DF_c neutron density map. In addition to the visualisation of several new D_2O molecules in the data collected after buffer exchange, the neutron density maps also showed an overall reduction in noise.

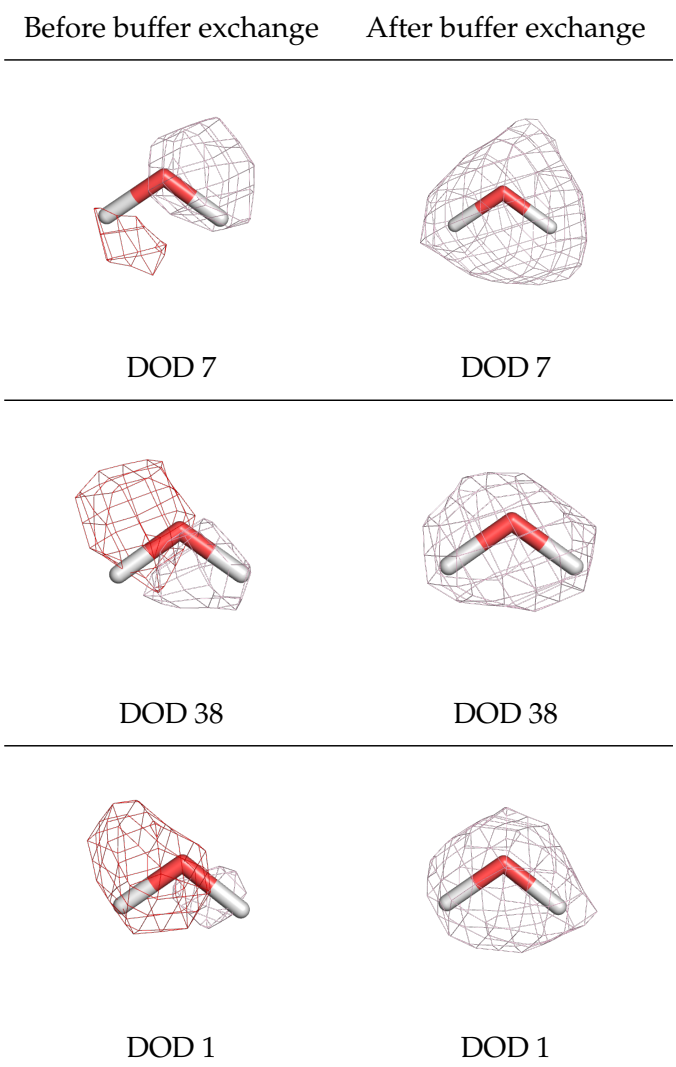

FIGURE 5.6: The left hand column shows the $2mF_o$-DF_c and mF_c-DF_c neutron density maps from the dataset collected before buffer exchange, contoured at 1.0 σ and 3.0 σ, respectively. Negative peaks in the mF_o-DF_c neutron density maps are shown in red, indicative of hydrogen atoms. In contrast, the right hand column shows the same D_2O molecules after buffer exchange. The $2mF_o$-DF_c neutron density map shows a more defined shape with no negative peaks in the mF_o-DF_c neutron density map.

To further evaluate the D:H incorporation in the structure, the number of amide hydrogen atoms present in the protein backbone was investigated. Amide atoms are usually tightly hydrogen bonded in the structure and the most difficult to exchange for deuterium in comparison to the dynamic active site. In these data, it was

seen that of the 315 backbone amide atoms in the structure, 6 showed clear negative peaks in the neutron mF_o-DF_c maps, indicative of hydrogen atoms. This represents only $\sim$ 2% of amide backbone hydrogen atoms. These backbone hydrogen atoms were distributed evenly amongst secondary structure elements: α-helices, β-sheets and loops, showing no preference for a particular region of the protein. This information, in addition to the number of well defined D_2O molecules, gives a high level of confidence that the vapour diffusion exchange method was successful.

5.6.2 Peroxide Stability

It was observed that the lifetime of the peroxide was shortened in DUOX:5-PMUA crystals grown in 100% deuterated conditions (Dr. S. Bui, personal communication, 24 September 2018). This was observed during X-ray experiments under cryo-cooled conditions using a home X-ray source. Although the intermediate is stable at 293 K, over several weeks the peroxide C5-Op1 bond is seen to break and crystals begin to deteriorate. In the case of NMX studies where data collection can be on the time scale of days, preserving the peroxide at high occupancy for the duration of the experiment was vital. In comparison, in HUOX:5-PMUA crystals the peroxide lifetime can be over 5 weeks, as reported in previous experiments involving HUOX:5-PMUA crystals in 100% hydrogenated conditions for X-ray experiments (Dr. S. Bui, personal communication, 24 September 2018) [81]. The time between RT neutron and X-ray data collection was approximately 2 weeks, however the length of time between crystallisation set-up and X-ray data collection was a total of 4 weeks. The lifetime of the crystal used in this data collection and the total timescale associated is shown in Figure 5.7. In mixed buffer solutions, such as the sample reported in this chapter, the peroxide was seen to have a longer lifetime than in 100% deuterated conditions (Dr. S. Bui, personal communication, 24 September 2018).

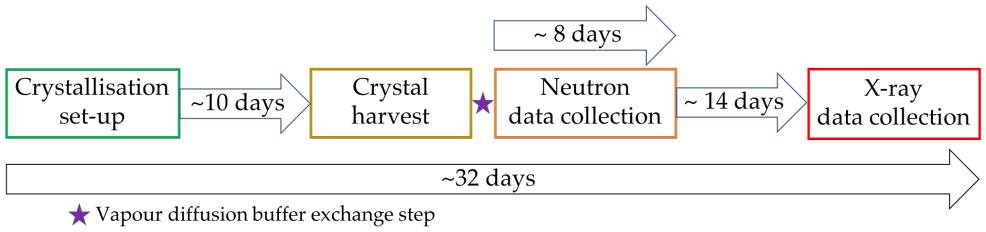

FIGURE 5.7: Timeline describing the length of time between setting-up the crystallisation of DUOX:5-PMUA to when the crystal was harvested for data collection. It also describes the length of time between crystal harvesting, the neutron data collection, and the X-ray data collection. These details must be considered, as the short lifespan of the crystal is central to our interpretation of the data collected.

In previous studies of the HUOX:5-PMUA complex, the peroxide bond (C5-Op1) has been found to be susceptible to radiolysis [81]. Even at low X-ray doses, it was observed that the C5-Op1 bond of 5-PMUA could be lysed, resulting in the regeneration of 9-MUA and O_2. Therefore, *RADDOSE-3D* [258] was used to calculate the dose received by the DUOX:5-PMUA crystal by synchrotron radiation, taking the large crystal dimensions into account. The average dose received by the whole crystal was 1.1 kGy and the average dose received by the exposed region was 5.0 kGy. This value was compared with those obtained in previous experiments monitoring the peroxide radiolysis [81]. In these studies, breakage of the peroxide bond was observed at average dose values of 19 kGy, where the occupancy of UOX:5-PMUA was calculated as 78% and liberated O_2 was present at 22%. A higher percentage of peroxide bond lysis was observed in higher doses. From the same study, an additional dataset was collected with a calculated dose of 2.5 kGy and observed that peroxide bond had an occupancy of 100% [81]. The value of 2.5 kGy can be considered as relatively similar to the value calculated from this experiment, 1.1 kGy, suggesting that the DUOX:5-PMUA intermediate should be intact.

With consideration to the calculated dose received by the DUOX:5-PMUA crystal in this experiment, and in comparison with previous recorded values, it was expected

that the peroxide would not suffer radiation-induced bond lysis and remain intact during the X-ray data collection.

5.6.3 Results from 'X-ray only' and Joint neutron/X-ray Refinement

The X-ray data alone were used to build the initial model before the addition of deuterium atoms. The 5-PMUA ligand was fitted into a positive peak in the mF_o-DF_c neutron density map. A characteristic of 5-PMUA is the pyrimidalization of the carbon atom at position C5. The C5 atom is sp^3 hybridized and adopts a tetrahedral configuration, bonding to C4, C6 and N7 of 9-MUA, and Op1 of the peroxide [81]. However, in the 'X-ray only' model where both Op1 and Op2 have occupancy 1.0, a strong negative peak in the mF_o-DF_c electron density map was observed across the C5-Op1 bond, shown in Figure 5.8 (b). This is indicative of the partial lysis of the peroxide bond in the X-ray data. An additional negative peak at 3.0 σ was seen in the mF_o-DF_c electron density map at the C5 atom, providing further evidence of a non sp^3 hybridized species at C5 and the appearance of a planar species, 9-MUA.

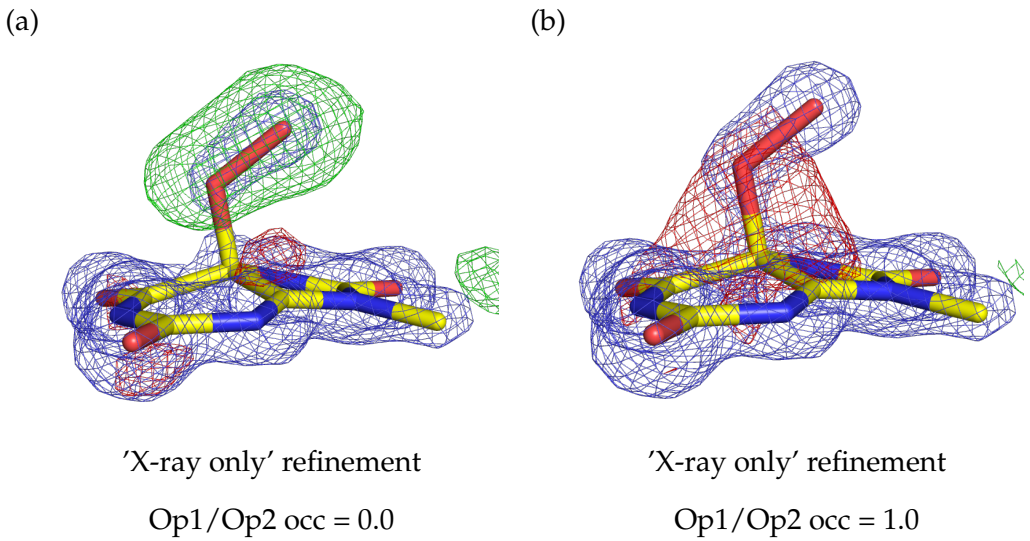

FIGURE 5.8: (a) An omit map calculated in the absence of Op1 and Op2 atoms. Positive peaks in the mF_o-DF_c electron density map at 3.0 σ, shown in green, indicates the presence of two oxygen atoms in the peroxide position. A further negative peak in the mF_o-DF_c electron density map on the C5 atom is seen in red. (b) Electron density map calculated with 5-PMUA fixed to an occupancy of 1.0. A negative peak in the mF_o-DF_c electron density map at 3.0 σ is observed between the C5-Op1 bond, indicative of partial peroxide bond lysis. The $2mF_o$-DF_c electron density maps are contoured at 2.0 σ.

An omit map excluding only the Op1 and Op2 atoms was conducted, shown in Figure 5.8 (a). A positive peak in the mF_o-DF_c electron density map showed the location of the two oxygen atoms of the peroxide. It is important to note that the omission of Op1 and Op2 did not remove an additional negative peak in the mF_o-DF_c electron density map located at the C5 position. The occupancies of each oxygen atom were refined and found to be 0.65 and 0.85 for Op1 and Op2, respectively. The occupancies, in conjunction with the strong negative peak in the mF_o-DF_c electron density map at 3.0 σ across the C5-Op1 bond indicate the loss of peroxide in the X-ray data. It has been shown in previous literature that liberated O_2 results from the C5-Op1 bond lysis, therefore it can be suggested that the X-ray structure represents a split state: DUOX:5-PMUA and DUOX:9-MUA + O_2.

A joint refinement strategy was then used to gather further information on the

DUOX:5-PMUA complex. However, as expected, similar problems were observed concerning the X-ray data. The joint refinement results are shown in Figure 5.9. Both Figure 5.9 (a) and (b) show the omit maps of Op1 and Op2 in the mF_o-DF_c electron density and neutron density maps, respectively. However, Figure 5.9 (c) and (d) shows the 5-PMUA ligand with Op1 and Op2 modelled with the occupancies fixed at 1.0. In common with the previous observation, a large negative peak in the mF_o-DF_c electron density map dominates the signal from the 5-PMUA ligand, suggesting the partial lysis of the C5-Op1 peroxide bond in the mF_o-DF_c electron density map (Figure 5.9 (c)). It is interesting to note that no negative peak is seen across the C5-Op1 bond in the mF_o-DF_c neutron density map, as shown in Figure 5.9 (d). This provides evidence that the peroxide bond is intact in the neutron dataset, whereas the C5-Op1 bonds suffers partial lysis as seen in the X-ray dataset.

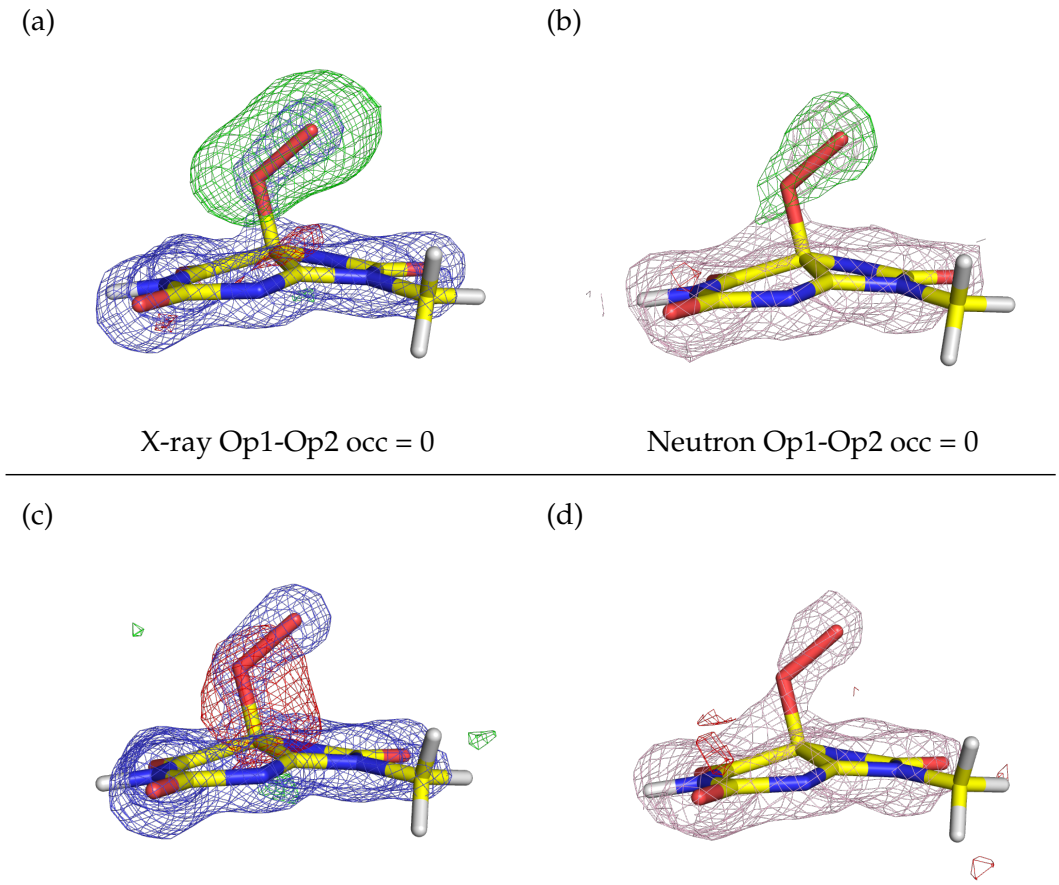

FIGURE 5.9: The structure of 5-PMUA from the joint refinement. The X-ray and neutron maps have been shown separately for clarity. The omit maps seen in (a) and (b) show positive peaks in the mF_o-DF_c electron density and neutron density maps and indicate the presence of Op1 and Op2 (in green). (c) and (d) show 5-PMUA when Op1 and Op2 were constrained to occupancies of 1.0. A negative peak in the mF_o-DF_c electron density map at 3.0 σ was observed across the peroxide bond (in red). This is absent in the mF_o-DF_c neutron density map. The $2mF_o$-DF_c electron density maps are contoured to 2.0 σ, the $2mF_o$-DF_c neutron density maps are contoured to 1.0 σ, whereas all mF_o-DF_c maps are contoured to 3.0 σ.

In the joint refinement, it was also observed that numerous D_2O molecules showed large B-factors, with values > 50 Å^2. This effect was not observed for the individual X-ray or neutron refinements. When modelled as D_2O, with occupancy values fixed at 1.0, numerous water molecules showed density in $2mF_o$-DF_c electron density and neutron density maps. However, many also showed additional strong

positive peaks in the mF_o-DF_c electron density map at the same location with large B-factors. It was often observed that the B-factors of the oxygen atoms differed significantly from the B-factors of the adjacent deuterium atoms. Several approaches were tested to rectify this problem, such as manually resetting B-factors and deleting then re-adding the D_2O molecules. Each method that was tested resulted in the continued increase in B-factors for a number of D_2O molecules after more than one round of refinement. This effect was also seen in some residues in flexible loop regions. The labile deuterium atoms on several sidechains such as asparagine, lysine and glutamine amino acids reported B-factors of > 100 Å^2. While it is expected that atoms from this flexible region would show higher B-factors than those tightly bound in secondary structure elements, these values were lower in the neutron only refinement. These positive peaks in the mF_o-DF_c electron density maps and large B-factors hampered the interpretation of the maps, and was suggestive that the X-ray and neutron datasets were reporting different features.

From this information, the following can be seen: the electron density maps show a partially lysed peroxide (5-PMUA) and the joint refinement strategy showed a conflict between the X-ray and neutron data. Since the main focus of this structural investigation is the locations of hydrogen atoms in the structure, it was considered unreasonable to try to extract information on active site hydrogen positions using these X-ray data. To prevent potential bias from the X-ray data, the structural refinement subsequently proceeded with the neutron data alone.

5.6.4 Results from Neutron-Only Refinement

The neutron dataset had a high overall completeness of 92.5%, whereas most Quasi-Laue neutron datasets are less complete, averaging around 80% completeness [259]. The initial model was taken from the last joint refinement, with X-ray derived features removed. As previously described, no negative peak in the mF_o-DF_c neutron

density map was seen at the C5-Op1 bond or localised at the C5 position from the jointly-refined model.

An omit map was calculated in the absence of Op1 and Op2 atoms using the neutron data alone. This omit map is shown in Figure 5.10 (a). A strong positive peak in the mF_o-DF_c neutron density map is shown located above the peroxide, indicating the position of the Op1 and Op2 atoms. The final model is shown in Figure 5.10 (b) with Op1 and Op2 modelled, both with occupancies fixed at 1.0. The $2mF_o$-DF_c neutron density map does not completely cover both Op1 and Op2 atoms. This could be due to the lower signal-to-noise ratio, which may arise from the relatively low fluxes of neutron beams. In addition, it is observed that the B-factors are higher for Op1 and Op2 in the 'neutron only' model than they are in both the 'X-ray only' and jointly-refined models, as detailed in Table 5.3. However, the absence of a negative peak provides strong evidence that the C5-Op1 bond is intact as derived from the neutron data. Therefore, the final model of 5-PMUA from the neutron only refinement is presented in Figure 5.10 (b). The oxygen atom occupancies and B-factors calculated for each model are detailed in Table 5.3.

TABLE 5.3: Occupancies of peroxide atoms Op1 and Op2 in X-ray, joint refinement and neutron models. *B-factors in 'X-ray only' and joint refinement structures were refined anisotropically for non D/H atoms.

Model	Op1 occupancy	Op2 occupancy
X-ray data only	0.65	0.85
Joint refinement	0.64	0.71
Neutron data only	0.69	1.00
	Op1 B-factor	Op2 B-factor
X-ray data only*		
Occupancy 1.0	25.62	27.22
Occupancy refined	20.78	22.10
Joint refinement*		
Occupancy 1.0	28.16	25.26
Occupancy refined	23.83	20.33
Neutron data only		
Occupancy 1.0	40.14	31.42
Occupancy refined	35.68	30.81

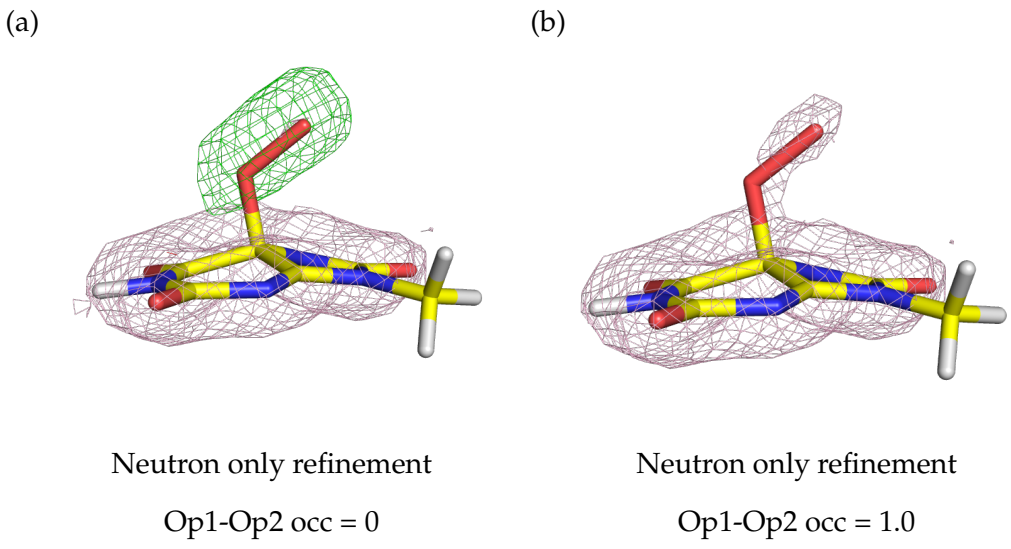

FIGURE 5.10: (a) An omit map calculated in the absence of atoms Op1 and Op2. The positive green peak in the mF_o-DF_c neutron density map is contoured to 3.0 σ. (b) Both Op1 and Op2 atoms are modelled with an occupancy fixed at 1.0 and no negative peak is seen in the mF_o-DF_c neutron density map. The $2mF_o$-DF_c neutron density maps are contoured to 1.0 σ.

The C5-Op1 bond length was found to be 1.5 Å and the Op1-Op2 bond length was found to be 1.5 Å. These measurements are similar to previously reported values for HUOX:5-PMUA [81]. All 5-PMUA bond angles involving the Op1-Op2 atoms are detailed in Table 5.4.

TABLE 5.4: Bond angles of 5-PMUA, specifically the bonds connecting the peroxide and Op1-Op2 atoms.

Bonding atoms (A – B – C)					Bond angle
C5	–	Op1	–	Op2	118°
C6	–	C5	–	Op1	94°
C4	–	C5	–	Op1	103°
N7	–	C5	–	Op1	112°

In the evaluation of the 5-PMUA structure using only the neutron data, the possibility of a deuterium atom bonded to Op2 was investigated. This would define this peroxide intermediate as a hydroperoxide species. The examination of numerous omit maps found no evidence of an Op2-bonded deuterium atom. In the omit map of Op1 and Op2 , shown in Figure 5.10 (a), a positive peak surrounds the positions of the two oxygen atoms and no additional peak is observed in the vicinity of Op2 where a deuterium atom would be expected. Additionally, a deuterium atom was modelled on Op2 and the occupancy refined to 0.16. This low value provides evidence to suggest that there is no deuterium atom on this peroxide. In the final model we present the peroxide as unprotonated, and therefore negatively charged at Op2.

5.6.5 DUOX:5-PMUA Bonding Interactions

The 5-PMUA ligand binds in the same location as the AZA ligand presented in Chapter 4. The bonding distances and angles were measured and described in Figure 5.11 and Table 5.6.

An additional interaction is seen between O8 of 5-PMUA and the backbone amide on residue Asp58* with a hydrogen bonding distance of 2.1 Å between the two atoms.

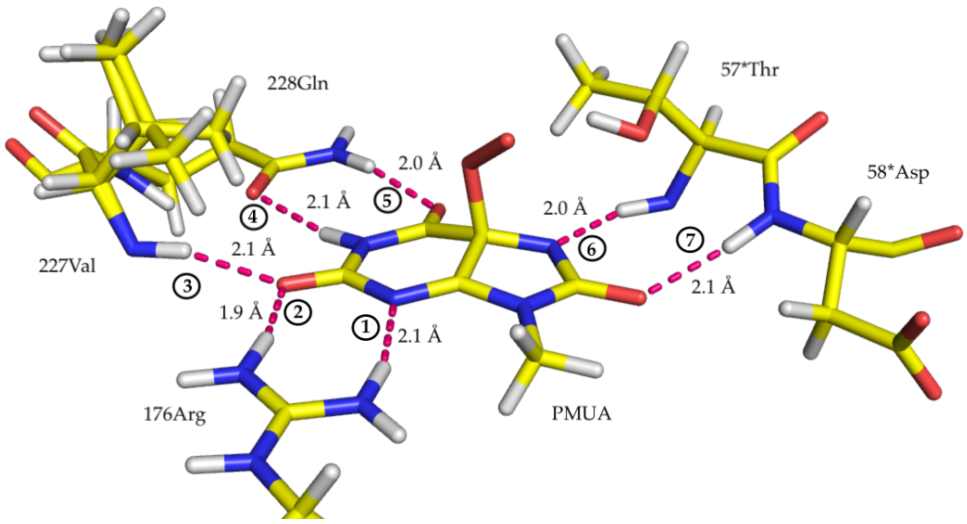

FIGURE 5.11: Hydrogen bonding partners between active site residues and 5-PMUA. The hydrogen bonds are indicated by pink dashed lines. Hydrogen bond angles are numbered and detailed in Table 5.6.

TABLE 5.5: DUOX:5-PMUA active site residues and hydrogen bond angles.

	Hydrogen Bond (Donor – Hydrogen ····· Acceptor)									Bond Angle
(1)	Arg176	N	–	Arg176	D	–	5-PMUA	N3		166°
(2)	Arg176	N	–	Arg176	D	–	5-PMUA	O6		166°
(3)	Val227	N	–	Val227	D	–	5-PMUA	O2		162°
(4)	Gln228	O	–	AZA	D1	–	5-PMUA	N1		169°
(5)	Gln228	N	–	Gln228	D	–	5-PMUA	O6		167°
(6)	Thr57*	N	–	Thr57*	D	–	5-PMUA	N7		158°
(7)	Asp58*	N	–	Asp58*	D	–	5-PMUA	O8		99°

5.6.6 Catalytic Residues

The protonation states of the residues surrounding the active site and the 5-PMUA ligand were also investigated. The protonation states of the residues that will be discussed in this section are shown in Figure 5.12, where the deuterium atoms of relevance are highlighted in red, for reference.

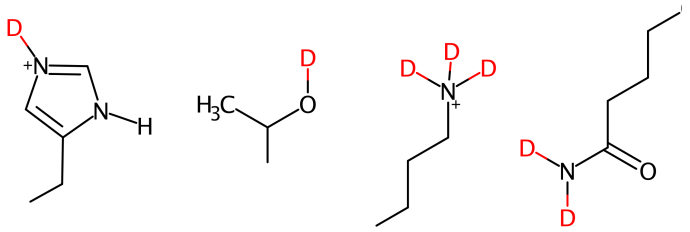

FIGURE 5.12: The protonation states of active site residues of interest. The locations of the deuterium atoms under investigation are shown in red.

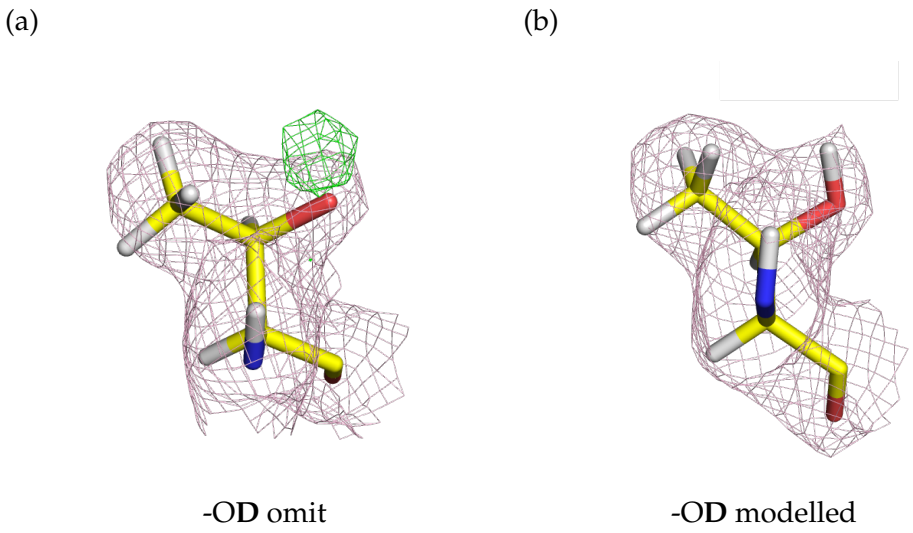

FIGURE 5.13: Omit map and final model of residue Thr57*. (a) shows the omit map calculated in the absence of the deuterium atom of the hydroxyl sidechain -O**D**. A positive peak in the mF_o-DF_c neutron density map is seen at 3.0 σ. (b) the final model shows the deuterated hydroxyl group of Thr57*. The $2mF_o$-DF_c neutron density maps are contoured to 1.0 σ.

The protonation state of catalytically important Thr57* is shown in Figure 5.13. The removal of the deuterium atom attached to the sidechain hydroxyl group resulted in a positive peak in the mF_o-DF_c neutron density map at 3.0 σ, shown in Figure 5.13 (a), providing strong evidence for the presence of a deuterium atom. Therefore the final model of Thr57*, shown in Figure 5.13 (b), includes an -OD group where the is deuterium atom is pointing towards the negatively charged Op2 atom of the peroxide, forming a hydrogen bond with a distance of 2.0 Å. The occupancy of this deuterium atom was refined as 0.84.

The neighbouring residue Lys10* is also catalytically important [91]. Modelling a singular conformation in the absence of the three deuterium atoms attached to the sidechain nitrogen atom, resulted in a large positive peak at 3.0 σ in the mF_o-DF_c neutron density map, shown in Figure 5.14 (a). However, this positive peak was also seen to extend along the aliphatic chain of Lys10*, suggesting that this residue

adopts two conformations. The X-ray data were consulted and a positive peak was also seen in the mF_o-DF_c electron density map at 3.0 σ at the same location, providing further evidence of a split. A second omit map was calculated using the model in which Lys10* is in two conformations, with the removal of the three deuterium atoms from both sidechain nitrogen atoms, as detailed in Figure 5.14 (b). A large positive peak is seen in the mF_o-DF_c neutron density map surrounding the two sidechain nitrogen atoms, however, the positive peak along the Lys10*sidechain shows a reduction in size. The distance between the two Lys10* sidechain nitrogen atoms was found to be 0.4 Å, and the occupancies were refined to 0.63 and 0.37. In order to investigate the protonation states of this residue, a number of omit maps were conducted, and different models were tested.

Both the single and alternate conformations of Lys10* were modelled to investigate the protonation state of the sidechain nitrogen: using -ND_3^+ and -ND_2 groups. The models containing -ND_3^+ groups are detailed in Figures 5.14 (c) and (d). In the singular conformation, Figure 5.14 (c), a positive peak remained in the mF_o-DF_c neutron density map at the -ND_3^+ group position. However, in the alternate conformation, Figure 5.14 (d), a negative peak appears in the mF_o-DF_c neutron density map. Interestingly, in Figures 5.14 (e) and (f), no significant positive or negative peaks are seen: this suggested that -ND_2 may be the more reasonable model for both the singular and alternate conformations. It is important to note that in Figures 5.14 (a), (b), (c), and (d), His256 is unprotonated and in Figures 5.14 (e) and (f) His265 is deuterated with a fixed occupancy of 1.0.

Singular Conformation	Alternate Conformation
(a)	(b)
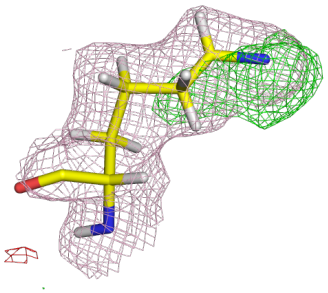	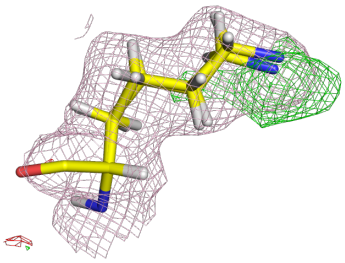
-N$\mathbf{D_3}^+$ omit	-N$\mathbf{D_3}^+$ omit
(c)	(d)
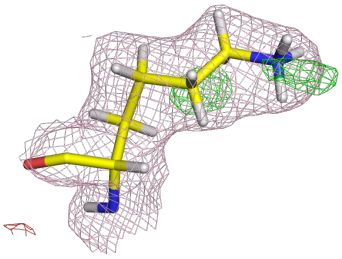	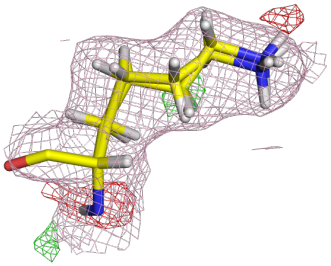
-N$\mathbf{D_3}^+$ modelled	-N$\mathbf{D_3}^+$ modelled
(e)	(f)
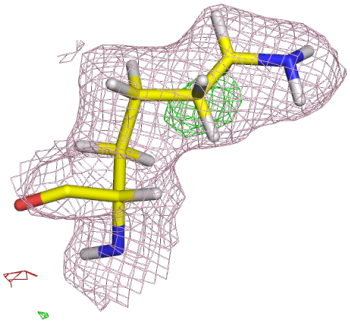	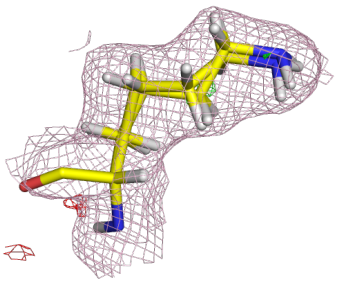
-N$\mathbf{D_2}$ modelled	-N$\mathbf{D_2}$ modelled

FIGURE 5.14: The omit maps and models of the singular and alternate conformations of Lys10*. (a) and (b) show the omit maps calculated in the absence of -N$\mathbf{D_3}^+$ atoms for singular and alternate conformations of Lys10*, respectively. (c) and (d) the -N$\mathbf{D_2}$ group is modelled on the singular and alternate conformations of Lys10*, respectively. (d) and (e) the -N$\mathbf{D_3}^+$ group is modelled on the singular and alternate conformations of Lys10* respectively. The mF_o-DF_c neutron density maps are contoured at 3.0 σ, with positive peaks represented by green and negative peaks by red. All 2mF_o-DF_c neutron density maps are contoured at 1.0 σ.

The location of the positive peak in the mF_o-DF_c neutron density map in the presence of an -ND_3^+, described in Figure 5.14 (c), was adjacent to the unprotonated His256 residue. In addition, a negative peak in the mF_o-DF_c neutron density map was seen in the presence of two -ND_3^+ groups (Figure (5.14 (d)). Therefore, we considered that a relationship may exist between the protonation states of these neighbouring residues. To probe this relationship, a further set omit maps were calculated: these are shown in Figure 5.15. However, the refinement of individual atom occupancies cannot be obtained for residues adopting more than one conformation, due to the limitations of the refinement program used. This means all atoms refine to the same occupancy as each conformer with a total occupancy of 1.0, where the total is the sum of all conformer occupancies. For example in this case, all atoms from one Lys10* conformer have the occupancy of 0.69, whereas the all atoms from the other conformer have an occupancy value of 0.31. Therefore, in order to calculate the occupancy values for the individual deuterium atoms located on the Lys10* sidechain, only the major conformation of Lys10* was included in these models.

In the omit map where all three deuterium atoms are removed from the Lys10* sidechain nitrogen atom, and His256 was also unprotonated at -NDϵ2, a positive peak in the mF_o-DF_c neutron density map was observed extending from the sidechain of Lys10* to the sidechain of His256, as shown in Figure 5.15 (a). When both -ND_2 and -ND_3^+ groups were modelled on Lys10*, an additional positive peak in the mF_o-DF_c neutron density map was seen between the Lys10* sidechain nitrogen atom and the nitrogen atom of the uncharged His256 (Figure 5.15 (b) and (c)). When modelling both a charged Lys10* and His256, this positive peak in the mF_o-DF_c neutron density map was seen to disappear (Figure 5.15 (e)). However, the occupancies of each deuterium atom refined to values of 1.00, 0.91 and 0.06: the lowest value was found on the deuterium atom nearest His256, whereas the deuterium atom on the charged His256 refined to an occupancy of 0.51 (Figure 5.15 (f)). It was not possible to conduct the same tests with the alternate conformation

of Lys10* as detailed above.

(a) Lys10*-NH_3^+
omit His256-NH
omit

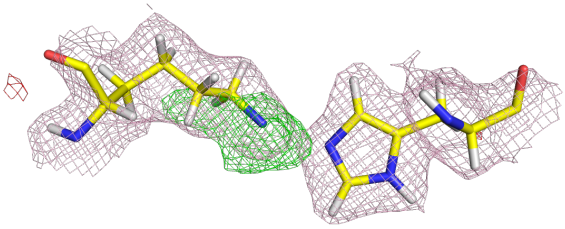

(b) Lys10*-NH_3^+
His256-NH omit

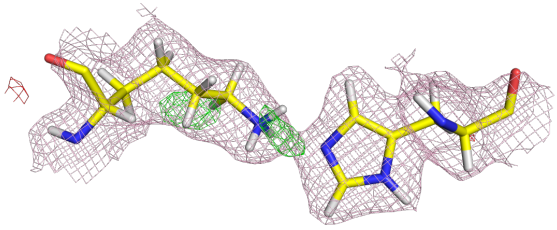

(c) Lys10*-NH_2
His256-NH omit

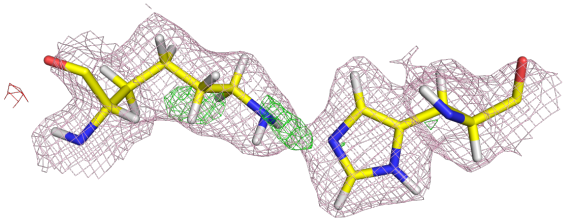

(d) Lys10*-NH_3^+
omit His256-NH

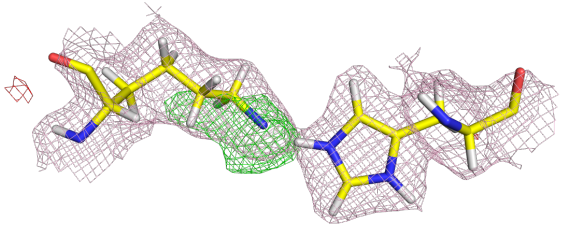

(e) Lys10*-NH_3^+
His256-NH

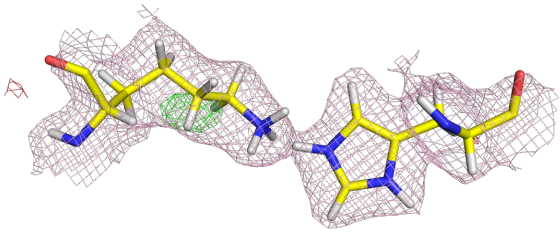

(f) Lys10*-NH_2
His256-NH

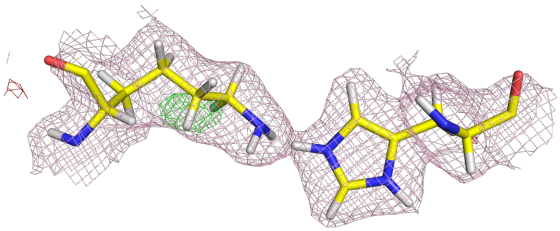

FIGURE 5.15: Investigation into the protonation states of residues Lys10* and His256, where Lys10* is in a singular conformation. The $2mF_o$-DF_c neutron density maps are contoured to 1.0 σ and the mF_o-DF_c neutron density maps contoured to 3.0 σ. Positive peaks are shown in green and negative peaks are shown in red.

(a) Lys10*-NH_3^+
His256-NH omit
90 ° rotation

(b) Lys10*-NH_2
His256-NH omit
90 ° rotation

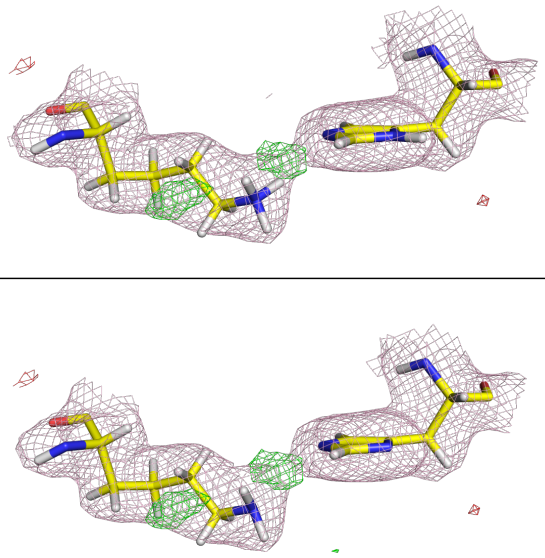

FIGURE 5.16: Investigation into the protonation states of residues Lys10* and His256, where Lys10* is in a singular conformation. The $2mF_o$-DF_c neutron density maps are contoured to 1.0 σ and the mF_o-DF_c neutron density maps contoured to 3.0 σ. Positive peaks are shown in green and negative peaks are shown in red.

The omit maps shown in Figure 5.15 suggest modelling His256 as positively charged. However, despite removing the residual density between His256 and Lys10*, the His256 -NDϵ2 only accounts for 50% of the deuterium atom. Figures 5.16 (a) and (b) show a 90 ° rotation of Figures 5.15 (b) and (c), respectively. Inspection of these maps indicates that the positive peak attributed to the His256 -NDϵ2 is not in a favourable geometric position, pointing out of the plane of the His256 residue. This result most likely indicates that the deuterium atom is in fact shared between His256 and Lys10*, however, it is not easy to model this correctly.

(a)

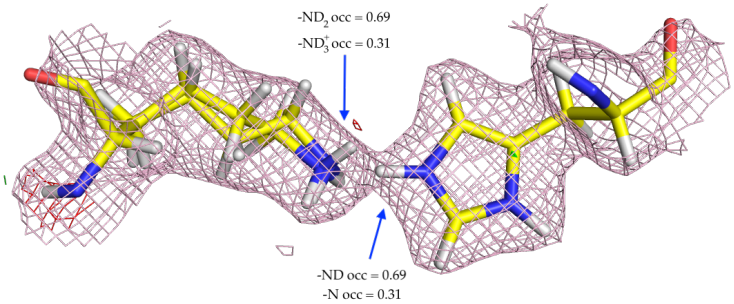

Top-down view

(b)

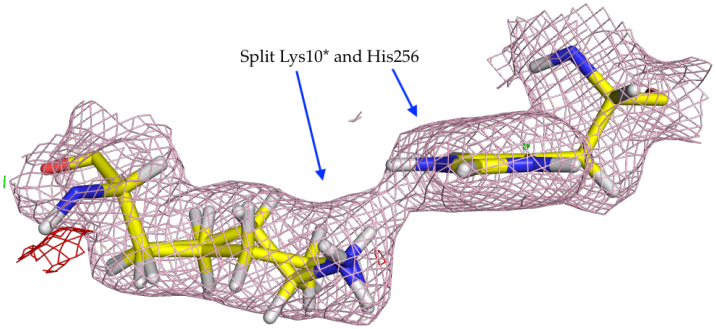

Side-on view

FIGURE 5.17: The model of residues Lys10* and His256 where the deuterium atom is present on both residues to a total occupancy of 1.0. Both residues are modelled in an alternate conformation: Lys10* with an -ND_2 group and positively charged His256 have an occupancy of 0.63 whereas Lys10* with an -ND_3^+ group and neutral His256 have an occupancy of 0.37. a) shows the top down view and (b) shows the side-on view. The $2mF_o$-DF_c neutron density map is contoured at 1.0 σ and the mF_o-DF_c neutron density map is contoured at 3.0 σ.

Another approach to investigate these residues, involved splitting the Lys10* residue to include each a -ND_3^+/-ND_2 group on either nitrogen atom, with the corresponding His256 coupled in either the absence or presence of a deuterium atom -Nϵ2. The occupancies for this were set according to the occupancies of the two alternate conformers of Lys10* (0.63 and 0.37). In Figure 5.17 (a) and (b), a model is shown

describing this conformation. In this case, the deuterium atom is located mostly on the His256, with an occupancy of 0.63. There is no residual positive peaks in the mF_o-DF_c neutron density map seen in between the two residues. The deuterium atom from His256 hydrogen bonds to the lone pair of the Lys10* -ND_2 group with a hydrogen bonding distance of 2.4 Å, conversely the deuterium atom from the Lys10* -ND_3^+ group forms a hydrogen bond with the unprotonated nitrogen atom of His256 at a distance of 2.2 Å. However, the fixing the occupancy at 0.63 artificially increases the occupancy of the -NDϵ2 atom of His256, which previously refined at 0.51.

With this in consideration, we suggest that the simplest model would involve the Lys10* residue in an alternate conformation with each nitrogen atom containing a positively charged -ND_3^+ group, leaving the His256 unprotonated, shown in Figure 5.18. This model satisfies the evidence for a split Lys10* residue and accounts for the total number of deuterium atoms between the two residues. In addition, as the density present next to His256 is not in a favourable geometry to be satisfied by modelling a deuterium atom on His256, it is chemically more likely that the deuterium atom is on the Lys10* -ND_3^+ sidechain. However, it is important to consider that this deuterium atom may have a level of mobility that is not possible to model, or may partially exist in between the two residues. The relationship between these Lys10* and His256 residues has presented challenges in determining a final model, however, may be indicative of the ability of these residues to transfer protons between each other, which may have implications in the reaction mechanism. In this model, hydrogen bonding distance between the Lys10* -ND_3^+ and Thr57* -OD was found to be 2.5 Å.

(a)

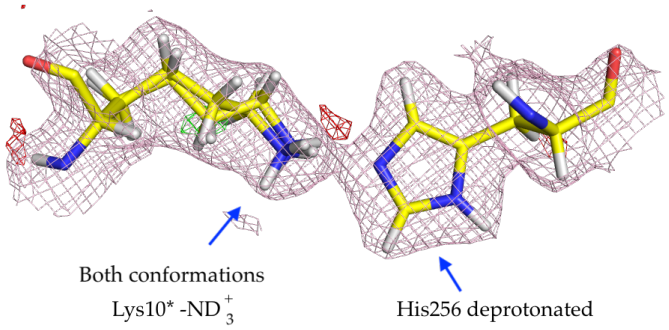

(b)

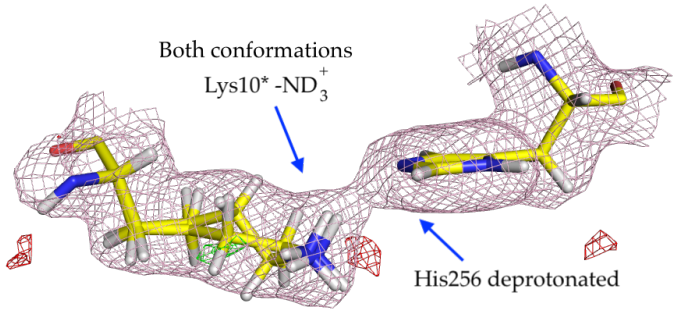

FIGURE 5.18: With consideration to the location of the positive peak in the mF_o-DF_c neutron density map, it was chosen to model the Lys10* with an -ND_3^+ group and unprotonated His256. (a) shows the top down view and (b) shows the side-on view. The $2mF_o$-DF_c neutron density map is contoured at 1.0 σ and the mF_o-DF_c neutron density map is contoured at 3.0 σ.

Residue Asn254 is within bonding distance of the 5-PMUA peroxide Op2 atom. An omit map was calculated in the absence of both the deuterium atoms on the sidechain nitrogen atom. However, this omit map showed no evidence of deuterium atom positions as no positive peaks in the mF_o-DF_c neutron density map were observed, shown in Figure 5.19 (a). To further investigate the orientation of the Asn254 sidechain, the sidechain was flipped, swapping the location of the -ND_2 and carbonyl groups. This resulted in the appearance of a positive peak in the mF_o-DF_c neutron density map next to the oxygen atom (Figure 5.19 (b)), suggesting that

this orientation is incorrect. The final model is shown in Figure 5.19 (c) with the two deuterium atoms attached to the sidechain nitrogen atom. The occupancies of each deuterium atom were also refined and found to have values of 0.20 and 0.29. The hydrogen bonding distance between the Asn254 and Op2 is measured at 2.0 Å. All bond angles from the active site residues are detailed in Table 5.6.

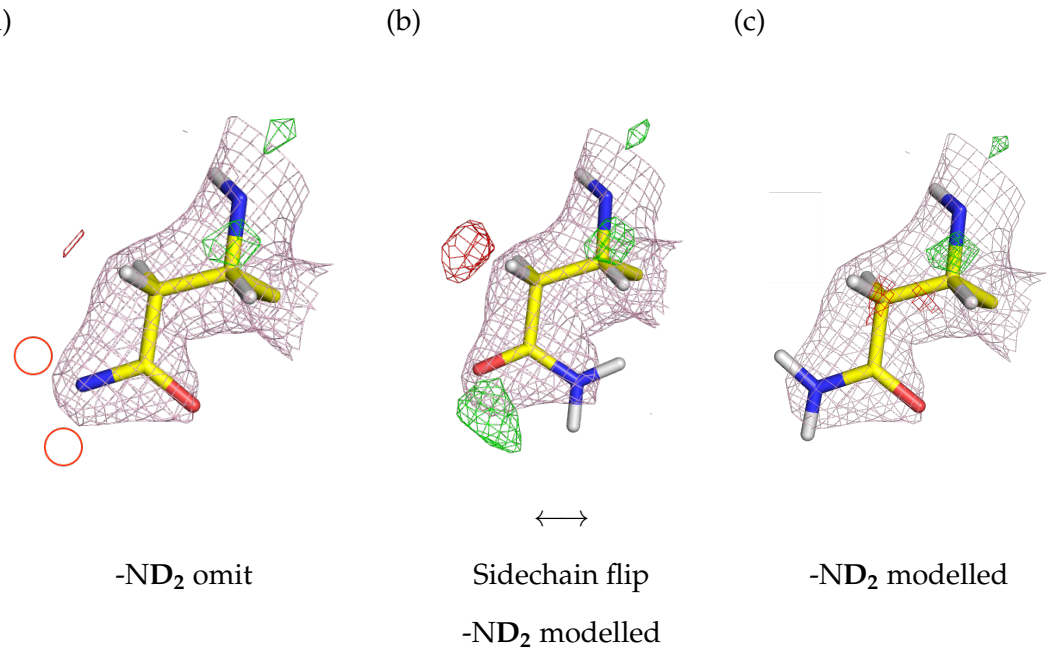

FIGURE 5.19: Investigation into the orientation of residue Asn254. (a) This omit map was calculated in the absence of both nitrogen-bound deuterium atoms (indicated by red circles). (b) Flipping the residue orientation results in a positive peak in the mF_o-DF_c neutron density map next to the sidechain oxygen atom. (c) This final model presents the -NH_2 group as shown. Positive and negative residual noise peaks are seen in both maps, shown in green and red respectively. The $2mF_o$-DF_c neutron density maps are contoured at 1.0 σ whereas the mF_o-DF_c neutron density maps are contoured to 3.0 σ.

TABLE 5.6: The hydrogen bond angles of residues in the active site.

	Hydrogen Bond (Donor – Hydrogen ····· Acceptor)								Bond Angle
(1)	Thr57*	O	–	Thr57*	D	–	5-PMUA	Op2	143°
(2)	Lys10*	N	–	Lys10*	D	–	Thr57*	O	134°
(3)	His256	N	–	His256	D	–	Lys10*	N	124°
(4)	Lys10*	N	–	Lys10*	D	–	His256	N	136°
(5)	Asn254	N	–	Asn254	D	–	5-PMUA	Op2	143°

5.6.7 Active Site Water Network

A comparison was made between the X-ray and neutron data and it was found that there were a higher number of water molecules observed in the X-ray data.

Surrounding the active site there are several water molecules, observed as oxygen atoms in the X-ray data. However, the positive peaks in the mF_o-DF_c electron density maps are not well defined, indicating a degree of mobility. In the mF_o-DF_c neutron density map, the same D_2O positions showed very weak peaks. It was not possible from this information to determine the orientation of the D_2O molecules. Hence these D_2O molecules were modelled as oxygen atoms only. As as result, it was not possible to draw any reliable conclusions on the nature of this hydrogen bonding network and the relationship between these molecules and the catalytic residues in the active site.

The -CH_3 group attached to the N9 position of 5-PMUA shows no density in the 2mF_o-DF_c neutron density map, as expected due to the cancellation effects caused by the covalently bonded hydrogens (see Table 2.2 and Section 2.6 in Chapter 2). Solvent molecule W2 does not form a hydrogen bond with NH9 of the ligand as is the case in the DUOX:AZA complex, due to the N9-CH_3 of 9-MUA. From the

neutron data presented, it has not been possible to identify the location of solvent molecule W2.

5.6.8 Final Structure of the DUOX:5-PMUA Active Site

Figure 5.20 shows the final structure of the DUOX:5-PMUA active site. The unprotonated 5-PMUA molecule is surrounded by the active site residues that have been discussed within this chapter. Residue Thr57* donates a hydrogen bond to the negatively charged Op2 atom and accepts a hydrogen bond from the Lys10* -ND_3^+. Residue His256 also accepts a hydrogen bond from the Lys10*. The Asn254 residue also donates a hydrogen bond to the Op2 atom of the 5-PMUA, however, the positions of the two deuterium atoms are not well defined in the $2mF_o$-DF_c neutron density map.

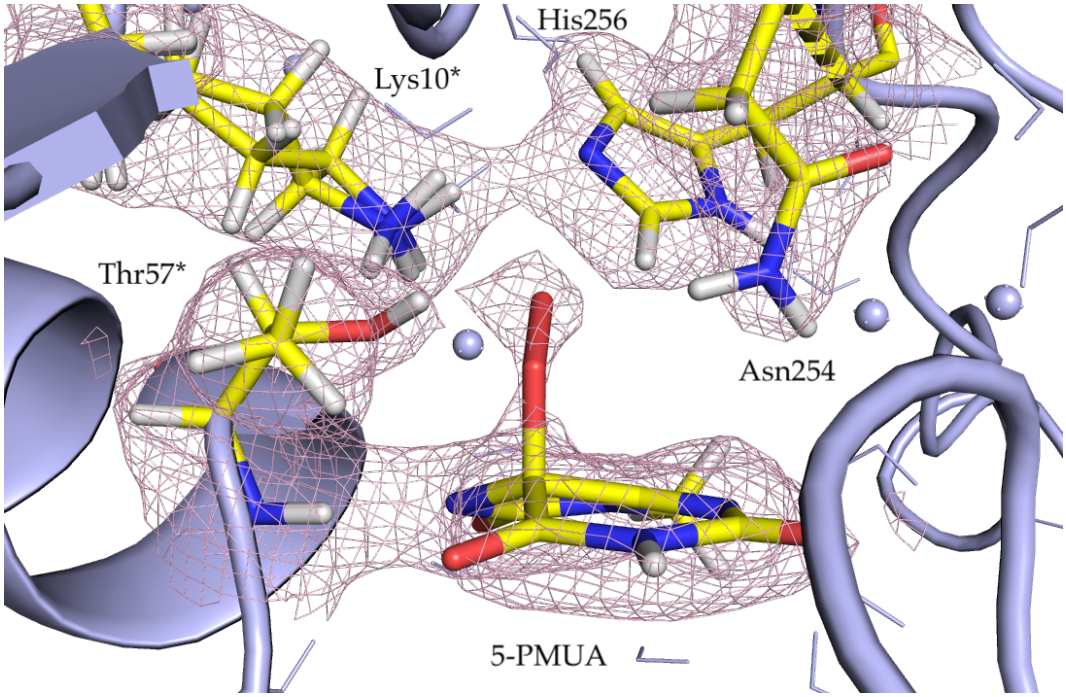

FIGURE 5.20: The final structure of the DUOX:5-PMUA active site. The protonation states of the active site residues surrounding the 5-PMUA ligand are shown. The $2mF_o$-DF_c neutron density map is contoured to 1.0 σ.

5.7 Discussion

The crystallisation of DUOX in complex with 9-MUA enabled the trapping of the peroxide intermediate 5-PMUA. Examination of the neutron structure allowed the investigation into the protonation states of residues surrounding the active site and the peroxide. The purpose of this study was to try to understand the formation and the stabilisation of the peroxide and investigate what role UOX plays in this process by looking at the hydrogen positions.

The structural analogue 9-MUA differs from the natural substrate UA as it has a methyl group attached to position N9 instead of a labile hydrogen atom. Previous studies had shown that this substitution resulted in trapping the peroxide intermediate and resulted in the suggestion that this labile hydrogen atom is abstracted during the expulsion of H_2O_2 and the formation of DHU intermediate [81]. Therefore, it was possible to produce the crystals under aerobic conditions and conduct neutron data collection at RT.

The crystal selected for data collection was grown in a mixed buffer solution with a 2:1 ratio of D:H. This excess of deuterium is due to the fact that the protein was initially fully exchanged against 100% D_2O, with only the crystallisation solution in hydrogenated conditions. It was reported that 100% deuterated crystallisation conditions shortened the lifetime of the peroxide and resulted in partial lysis of the C5-Op1 bond. It was also observed that the size of crystals grown in 100% deuterated conditions was significantly smaller. However, mixed H/D conditions were shown to extend the lifetime of the peroxide and resulted in larger crystals.

Following an initial data collection, a visible level of hydrogen contamination was observed in the crystal structure, complicating the interpretation of the neutron density maps. Therefore, further buffer exchange against a 100% deuterated solution was conducted by vapour diffusion inside the capillary where the crystal was

mounted. The use of vapour diffusion may not be as effective for deuterium incorporation as initial crystal growth in 100% D_2O, but it is a gentler method of buffer exchange for crystals grown in non-deuterated conditions [260]. A typical method for buffer exchange involves transferring the crystals into deuterated crystallisation buffer, however, this was not possible in this case as the crystal had already been mounted.

The use of vapour diffusion for buffer exchange after crystal mounting has been successfully conducted in previous neutron experiments [261–263]. In all of these cases the crystals were produced in 100% hydrogenated conditions and exchange times were on the order of weeks. For the sample presented in this chapter, buffer exchange over the course of weeks was not possible. Reasons for this include beamtime availability and the short peroxide lifetime, previously discussed. The buffer exchange strategy adopted in this case involved exchanging the deuterated buffer plug multiple times within the capillary to encourage diffusion, rather than allowing for long diffusion times. The ability to collect a dataset before and after the vapour diffusion gave a unique insight into the efficacy of this exchange process. The appearance of numerous water molecules and increased quality of the neutron density maps showed evidence that the buffer exchange process had been successful.

Both neutron and X-ray datasets were collected on the same crystal at RT. The use of two complementary datasets has numerous benefits when used together in a joint refinement. For example, there is a substantial increase in the number of observations, typically compensating for the increased number of parameters as a result of including hydrogen and deuterium atoms in the refinement [186]. Joint refinement also compensates for the lower completeness and the more limited resolution typically seen for neutron data [186]. Furthermore, it can also aid the anisotropic refinement of C, N, O and S atoms in the structure. However, in this DUOX:5-PMUA structure, it has been observed that the X-ray data shows notable differences to the

neutron data. This is seen in the partial lysis of the C5-Op1 bond, as observed by a large negative peak in the mF_o-DF_c electron density map, however, this feature was not observed in the mF_o-DF_c neutron density map. We reasoned that the loss of 5-PMUA may cause perturbations in the true protonation states of the peroxide-bound complex. It has previously been reported that the breakdown of the peroxide results in a reorganisation of solvent in the active site, with the appearance of a water molecule within hydrogen bonding distance to O8 [81]. Therefore, the possibility that the partial lysis of the C5-Op1 bond augments the proton arrangement in the active site cannot be disregarded. The partial C5-Op1 bond lysis, seen only in the X-ray data, led to a 'neutron only' refinement strategy being conducted. This removed any bias that may have been included from the split nature of 5-PMUA in the X-ray data. A neutron only refinement was also considered possible due to the high level of completeness of the neutron data collected (92.5%).

The true cause of the partial C5-Op1 bond lysis has not been identified in this study, however, is it important to consider the following possibilities. In comparison to HUOX, the perdeuteration of DUOX and the presence of deuterated buffer may have had an effect on the lifetime of the peroxide bond. By collecting datasets of DUOX:5-PMUA complexes on a home source at 100 K, it was observed that partial C5-Op1 bond lysis was seen to occur more rapidly than previously reported for HUOX:DUOX. However, it is also possible that even the low dose of X-rays calculated may have had an effect unlike that seen for HUOX. As a result, the perdeuterated DUOX:5-PMUA complex may be more sensitive to radiation damage. The lack of cryo-cooling of the DUOX sample reported in this chapter is also likely to increase the susceptibility to radiation damage in comparison to cryo-cooled HUOX. Hence, the *RADDOSE-3D* values that were used to evaluate the dose received by the crystal may not be directly comparable to the previous published values for HUOX complexes [81].

The X-ray and neutron data confirmed that the binding mode of 5-PMUA in this

complex is similar to those described previously [76, 77, 80–83] and in Chapter 4. The neutron data confirms the presence of the trapped peroxide intermediate, showing a bond between the C5 position of the 9-MUA substrate and the oxygen molecule, previously seen in X-ray studies [81]. No evidence was found in the data to suggest the presence of a deuterium atom on the peroxide Op2 atom, therefore, the 5-PMUA intermediate that is presented in this chapter was determined as unprotonated, with Op2 as negatively charged.

By comparing the DUOX:5-PMUA and HUOX:5-PMUA previously published, it was found that the C5-Op1 and Op1-Op2 bond lengths are very similar, only differing by 0.01 Å [81]. Interestingly, QM/MM calculations conducted by Bui *et al.* based on the HUOX:5-PMUA structure reported that these bond lengths are consistent with the 5-PMUA hydroperoxide monoanion species [81]. However, the experimentally determined structure that we present is the 5-PMUA dianion. A structural comparison of the 5-PMUA peroxide dianion and the 5-PMUA hydroperoxide monoanion is shown in Figure 5.21.

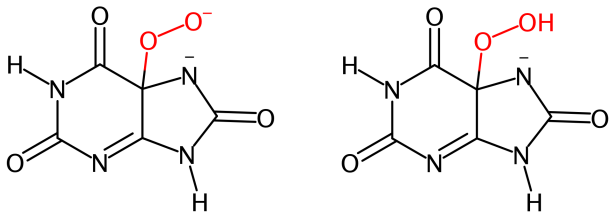

FIGURE 5.21: Structural comparison of 5-PMUA peroxide dianion and 5-PMUA hydroperoxide.

The neutron data provided unambiguous evidence that the hydroxyl group of residue Thr57* was present as -OD. This deuterium atom forms a hydrogen bond with the negatively charged Op2 atom of the peroxide, at a bonding distance of 2.0 Å. The close proximity of this residue to Op2 suggests that the proton located on Thr57* may be important for stabilising the 5-PMUA species. In addition, to form H_2O_2

the Op2 must become protonated, and the Thr57* hydroxyl deuterium atom is in an ideal location to facilitate this. As this is not seen in this structure, we suggest that this protonation of Op2 is likely to occur during the abstraction of the hydrogen atom at N9 of UA. This proton abstraction and resultant peroxide protonation may involve the solvent network and residues Lys10* and His256, forming a proton transfer system, connected via hydrogen bonds.

The protonation states of residues Lys10* and His256 were extensively investigated, with a variety of possible states probed. There was strong evidence that the Lys10* residue adopted an alternate conformation in both the X-ray and neutron data. Many models were used to probe the exact protonation states of these residues. From the information obtained from our tests, the most sensible model showed the Lys10* in an alternate conformation, with a charged -ND_3^+ sidechain in both conformations. While there is some evidence that the deuterium atom that was under investigation exists between the two residues, we reasoned that the chemically sensible model would be with the deuterium atom present on the Lys10* sidechain. However, from our observations, we suggest that there is a link between these protonation states in this intermediate. The appearance of the shared proton between Lys10* and His256, would result in a partial positively charged His256. This may suggest that a proton transfer between these residues can occur in this intermediate. This may be have relevance to the proton transfer mechanism needed for the deprotonation of N9, and formation of H_2O_2, previously described. However, further experiments would need to be conducted to verify this hypothesis.

The protonation states presented in the DUOX:5-PMUA complex are similar to those determined in previous NMX studies [80]. In both HUOX:8-HX and the DUOX:AZA structure presented in Chapter 4 of this thesis, the His256 residue is neutral, neighbouring a positively charged Lys10*.

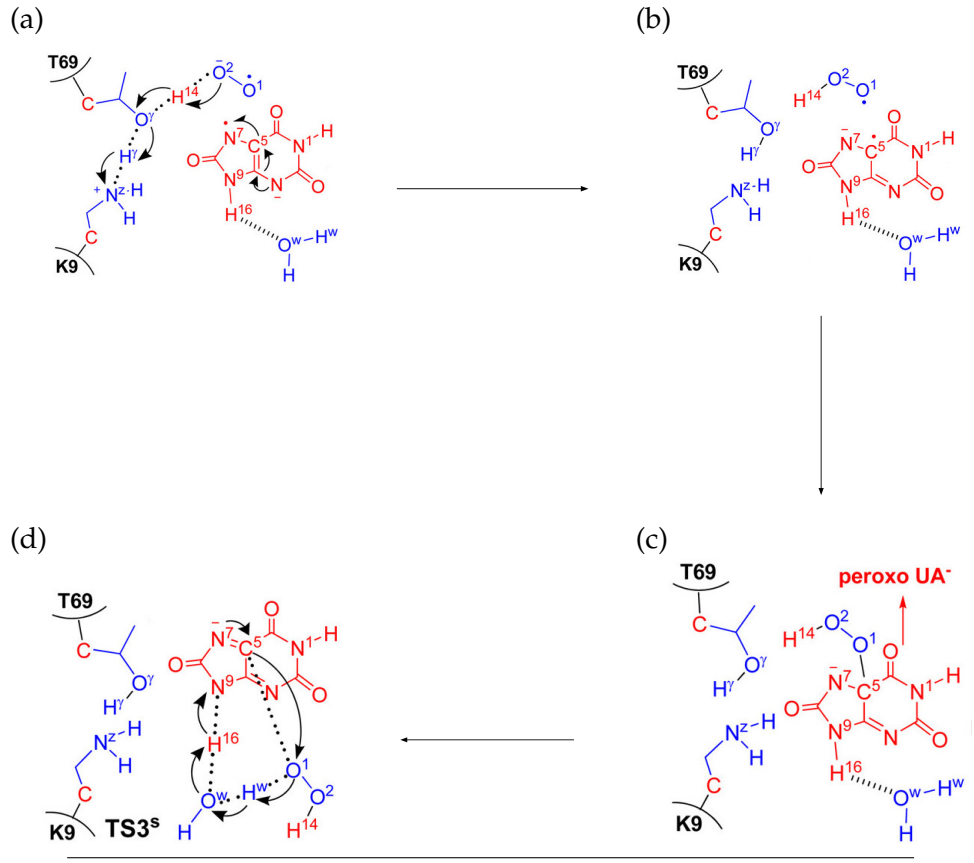

FIGURE 5.22: Proposed mechanism by Wei et al describing the protonation of the peroxide species. This mechanism suggests that the protonation of the peroxide occurs before the radical recombination reaction to form 5-peroxyisourate. Adapted with permission from [112]. Copyright 2017 American Chemical Society

In the theoretical paper by Wei et al., a mechanism was proposed using the UOX:8-HX neutron structure by Oksanen et al as the substrate [112]. The detailed mechanism taken from Wei *et al.* involving the radical recombination resulting in the formation of the peroxide is shown in Figure 5.22. The results of the QM/MM calculations proposed that the superoxide becomes protonated prior to the radical recombination with the substrate. As shown in Figure 5.22, it is proposed that the positively charged Lys9* (Lys10* in *Aspergillus flavus*) delivers a proton to the superoxide via Thr56* (Thr57* in *Aspergillus flavus*), shown in Figure 5.22 (a). This protonated superoxide then undergoes a radical recombination to form 5-(hydro)peroxyisourate, shown in Figures 5.22 (b) and (c).

In this mechanism, the expulsion of H_2O_2 is facilitated by the abstraction of a hydrogen atom from solvent by the peroxide species, resulting in the deprotonation of N9, described in shown in Figure 5.22 (d). However, from the data that we present, the peroxide is negatively charged and it is clear that Thr57* sidechain is -OD, is pointing towards the 5-PMUA ligand. Therefore, we suggest that the protonation of the peroxide does not occur before the radical recombination reaction, and is facilitated by Thr57* after the peroxide intermediate has formed. This theoretical model also does not consider the role of His256 in this process. It is possible that His256 may play a role in either the stabilisation of 5-PMUA or in the next step involving H_2O_2 expulsion.

Within this study it has not been possible to determine the nature of the water network that surrounds the active site. These conserved water molecules have been identified in previous UOX X-ray structures, with and without ligands, and at both 100 K and RT [68, 76, 77, 81, 83]. It has been suggested that water molecules W1 and W2 form two ends of a low energy proton transfer system [78, 82] however, this has not been experimentally confirmed. It is interesting to note that the X-ray structure of HUOX:5-PMUA conducted at 100 K reported that several of these active site waters adopted an alternate conformation [81]. Therefore, it is reasonable to suggest that even under cryo-cooled conditions, these waters are mobile and this explains the difficulty that we had in locating these molecules in our neutron data at RT.

5.8 Conclusion

The neutron structure that is presented within this chapter, builds on the information obtained in the X-ray structure of HUOX:5-PMUA determined by Bui *et al.* [81]. It has been possible to trap the 5-PMUA species in complex with DUOX and collect a neutron dataset at 298 K. The 5-PMUA intermediate has been determined

as unprotonated and, therefore, negatively charged at the Op2 atom. Due to the hydrogen bonding distance between residue Thr57* and the negatively charged Op2 atom of 5-PMUA, we suggest that this residue plays a role in stabilising this peroxide species. It is also likely that this proton is transferred to Op2 before H_2O_2 expulsion.

In addition, we have observed that there is a close relationship in the protonation states of residues Lys10* and His256. After extensive testing, the most sensible model presented in this chapter has a positively charged Lys10* and a neutral His256. However, it is reasonable to suggest that a proton may be partially shared. The ability of these residues to exchange protons may indicate that a proton transfer mechanism is possible, and this may have implications in the abstraction of the hydrogen at N9 of UA and the protonation of the peroxide by Thr57*, involving the solvent network connecting the two positions, in the true catalytic process.

A schematic of the protonation states is shown in Figure 5.23. We present the first structure to determine the protonation states of catalytic residues in a reactive intermediate in the UOX catalytic pathway.

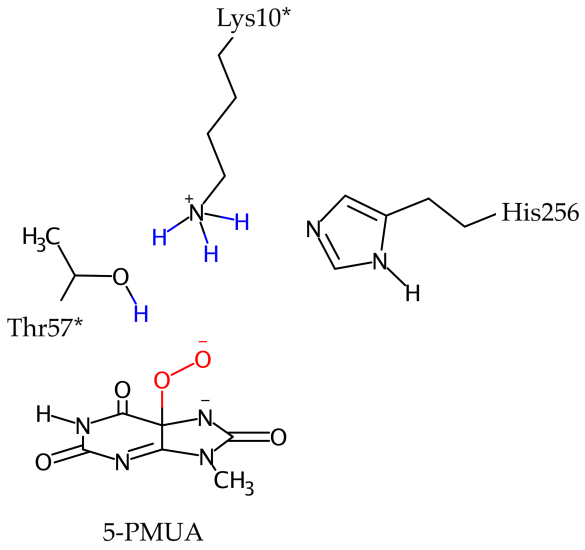

FIGURE 5.23: The final structure of the DUOX:5-PMUA active site, showing the protonation states of the catalytic triad Thr57*-Lys10*-His256 and the unprotonated 5-PMUA intermediate.

Chapter 6

Concluding Remarks and Future Perspectives

In this thesis, a structural study of the cofactor-free enzyme Urate Oxidase, (UOX), is presented. The aim of this work was to investigate how this enzyme is able to facilitate the reaction of uric acid (UA) with O_2, in the absence of redox-active metals or organic cofactors. This research was focused on understanding the role that protons play in the catalytic process, and how the protein is able to form and stabilise the structure of reactive intermediates.

6.1 Perdeuteration of UOX and Characterisation

The main focus of this work was to locate hydrogen positions in the active site and, therefore, identify hydrogen-related interactions, including hydrogen bonding and solvent networks. This information can be obtained using neutron macromolecular crystallography (NMX). To maximise the quality of the data that can be collected via this technique, UOX was perdeuterated (DUOX), i.e., both non-exchangeable and exchangeable hydrogen positions are substituted with deuterium. The benefits

associated with the deuterium labelling of macromolecules is discussed in more detail in Chapter 2.

Chapter 3 describes the perdeuteration protocol for DUOX, in addition to the biophysical characterisation. Mass spectrometry was employed to assess of the level of perdeuteration achieved by this process. These results showed that the deuterium content of DUOX was > 99%. An assessment into the thermal stability of DUOX found that the perdeuterated protein was more susceptible to heat denaturation than the hydrogenated counterpart. This observation has been reported in other studies comparing the stabilities of hydrogenated and deuterated proteins. Further studies could be conducted to identify any differences in reactivity between HUOX and DUOX. This may prove interesting when investigating the comparison between hydrogenated and deuterated macromolecules.

6.2 DUOX in complex with AZA

The structural study of DUOX in complex with 8-azaxanthine (AZA) is presented in Chapter 4. AZA acts as an inhibitor by binding to the location of the natural substrate, where it cannot be oxidised. Previous NMX studies used halogenated crystallisation conditions, resulting in the addition of a chloride atom to the active site. Our study involved the use of non-halogenated crystallisation conditions and allowed the visualisation of solvent molecule W1, in the DUOX:AZA active site. It was determined that solvent molecule W1 exists as D_2O molecule in the presence of AZA, rather than a charged species. The orientation of solvent molecule W1 and hydrogen bonding interactions involving residues Asn254 and Thr57* were identified.

Our work focused on the residues known to be catalytically relevant, dyad Thr57*-Lys10*, also residue His256, suggested to extend this network to a catalytic triad.

It was not possible to unambiguously determine the protonation state of Thr57*, due to the lack of definitive evidence from the neutron density maps. However, by employing intrinsic chemical knowledge, it was chosen to model deuterated hydroxyl group pointing towards the active site, forming a hydrogen bond with solvent molecule W1. The neighbouring residue Lys10* was found to contain a positively charged -NH_3, whereas the His256 residue was found to be neutral, unprotonated at the nitrogen atom position adjacent to Lys10*. These protonation states form a network of hydrogen donors: acceptors, connecting His256 to the solvent molecule W1.

This structure builds on information obtained in previous NMX studies conducted by Oksanen *et al.*, where HUOX was complexed with AZA in the presence of a chloride anion, as previously mentioned [80]. The DUOX:AZA dataset discussed in this thesis was collected to a slightly lower resolution (2.1 Åvs 1.9 Å) but is more complete (80.2% vs 73.2%), and does not suffer the effects from the hydrogen contribution as noted in the previous study [80]. The protonation states of HUOX:AZA were found to be different to those presented in our structure, DUOX:AZA. The hydroxyl sidechain of Thr57* donates a hydrogen bond to the neutral Lys10* sidechain, contrasting with the DUOX:AZA structure. The residue His256 was found to be neutral, similarly to that observed in DUOX:AZA. The authors suggested that a configuration identical to our findings also existed, however, the resolution of the previous neutron data meant that the two conformations were unable to be refined [80]. The protonation states in DUOX:AZA were found to be similar to those presented in another structure by Oksanen *et al.*: HUOX in complex with UA using the same chloride inhibitory method, forming HUOX:8-HX.

6.3 DUOX in complex with 9-PMUA

When DUOX is complexed with 9-methyl uric acid (9-MUA) under aerobic conditions, 9-MUA rapidly converts to the 9-methyl-5-peroxyisourate intermediate (5-PMUA). The DUOX:5-PMUA structure was able to provide information on the protonation states surrounding the active site with the peroxide intermediate *in situ*. In Chapter 5, the challenges surrounding sample preparation of DUOX:5-PMUA for NMX studies is described in detail. The lifetime of the peroxide species, coupled with longer data collection times typical in NMX studies, needed carefully timed crystal growth followed by buffer exchange. This was done using the gentler method of vapour diffusion and it was possible to visualise the efficiency of this process directly by comparing neutron density maps before and after buffer exchange.

The susceptibility of the 5-PMUA peroxide bond to selective radiolysis by low X-ray doses had been observed in previous X-ray studies of HUOX:5-PMUA [81]. This effect was observed in the case of DUOX:5-PMUA, after an X-ray dataset was collected for use in joint refinement. It was not possible to identify the true cause of this partial lysis, however, contributing factors are thought to include radiation damage, exacerbated by RT data collection, and/or an undetermined effect of deuteration. The partial lysis of the peroxide bond was not observed in the neutron data, therefore, this structure was solved using a 'neutron-only' refinement.

This research was able to determine that the 5-PMUA species bound to the active site was unprotonated, with a negative charge located on the Op2 atom. Examination of the protonation states in the active site, showed strong evidence for a deuterated Thr57* sidechain forming a hydrogen bond with the Op2 atom, suggesting that this residue plays a role in stabilising the peroxide. In addition, the proximity of this deuterium atom to the negative charge of Op2, makes Thr57* an ideal candidate to transfer a hydrogen atom to the peroxide in the formation of

H_2O_2. We suggest that this may occur concurrently with the deprotonation of the N9 hydrogen atom in UA, creating a proton relay system involving the solvent and residues Lys10* and His256.

The protonation states of residues Lys10* and His256 were shown to be strongly related. After extensive testing, the protonation states of these residues were determined as a positively charged Lys10* and a neutral His256, as this was deemed the most chemically sensible model. However, it cannot be discounted that there may be a level of mobility in this region, and that this proton transfer may have mechanistic implications. QM/MM calculations could be employed to verify this relationship.

6.4 Future Work

The NMX structures of DUOX:AZA and DUOX:5-PMUA present previously unattainable information on the protonation states of active site residues in UOX. In future work, methods for the further validation of the results presented could be conducted. Quantum mechanics/molecular mechanics (QM/MM) calculations have proven useful in supporting results from previous structural investigations into UOX [80, 81]. Therefore, this technique could be employed to confirm the protonation states determined experimentally, and can explore possible enzymatic mechanisms using the structures described in this thesis as a starting model, as previously conducted by Wei *et al.* [112].

The structures presented in this thesis also provide a solid foundation for further neutron studies into the protonation states of reactive intermediates in UOX catalysis. In order to relate the results we have determined to the true structure of the reactive intermediates, it is important to conduct additional experiments with DUOX

in complex with the natural substrate UA. The methodology used to trap the anaerobic HUOX:UA and HUOX:PIU complexes, reported in the X-ray study by Bui *et al.*, would allow direct visualisation of the protonation states of the reactive intermediates in complex with UA [81]. The study could be repeated exploiting the neutron crystallographic technique with data collection at 100K. Trapping the UA in complex with UOX in anaerobic conditions, would give an insight into the protonation state of UA in the primary reactive intermediate. This structure may yield information on if an active site residue acts as a 'general base' as previously proposed. It would also clarify if solvent molecule W1 is involved in the same bonding interactions with active site residues that are presented in this thesis and if its charge is affected by UA, in contrast to AZA. A further study could be conducted on the ligand-free UOX structure, to identify the protonation states of active site residues and solvent molecules in the absence of any ligand. This may provide an interesting structure for comparison to the primary reactive intermediate structure, to identify which residues change protonation states upon UA binding. In addition, the DUOX:PIU structure, could visualise the 5-peroxyisourate intermediate and discern whether the peroxide is indeed unprotonated in complex with the natural substrate, as is presented in this thesis. Data collection of this sample at 100K may circumvent the radiation-damage observed in the DUOX:5-PMUA structure presented in this thesis. It would also increase the length of time that the peroxide is stable for: this would also reduce the possibility that the length of the data collection time resulted in the degradation of the peroxide seen in the X-ray data.

6.5 Conclusion

NMX, coupled with deuterium labelling, has allowed the examination of the protonation states of DUOX in two different complexes: with an inhibitor, AZA, and with 9-MUA, forming the 5-PMUA peroxide intermediate.

The DUOX:AZA structure showed the AZA inhibitor-bound structure in the absence of O_2. It was possible to draw comparisons between the DUOX:AZA structure and the HUOX:8-HX structure previously published as they showed the same protonation states of active site residues [80]. The neutron dataset that is presented in this thesis is of higher completeness than the HUOX:AZA neutron structure previously published, and has provided further details on the relationship between active site solvent networks.

The neutron structure of DUOX:5-PMUA gave an insight into the active site structure in the peroxide-bound intermediate. This complex has revealed that 5-PMUA intermediate is unprotonated when bound, and is stabilised by hydrogen bonding to a catalytically relevant residue. In addition, the protonation states of other active site residues were probed, and results have suggested some proton mobility. These studies provide an interesting basis for further studies into the structure of reactive intermediates in cofactor-free UOX catalysis.

Appendix A

Supplementary Information for Chapter 3

```
        10         20         30         40         50         60
SAVKAARYGK DNVRVYKVHK DEKTGVQTVY EMTVCVLLEG EIETSYTKAD NSVIVATDSI

        70         80         90        100        110        120
KNTIYITAKQ NPVTPPELFG SILGTHFIEK YNHIHAAHVN IVCHRWTRMD IDGKPHPHSF

       130        140        150        160        170        180
IRDSEEKRNV QVDVVEGKGI DIKSSLSGLT VLKSTNSQFW GFLRDEYTTL KETWDRILST

       190        200        210        220        230        240
DVDATWQWKN FSGLQEVRSH VPKFDATWAT AREVTLKTFA EDNSASVQAT MYKMAEQILA

       250        260        270        280        290        300
RQQLIETVEY SLPNKHYFEI DLSWHKGLQN TGKNAEVFAP QSDPNGLIKC TVGRSSLKSK

L
```

FIGURE A.1: *Aspergillus flavus* UOX amino acid sequence obtained using ProtParam [264].

TABLE A.1: Minimal media ingredients and masses. For H-Enfors the ingredients are made up to 2 L of total media using $_dH_2O$ and for D-Enfors using D_2O.

$(NH_4)_2SO_4$	13.72 g
KH_2PO_4	3.12 g
Na_2HPO_4	12.02 g
$(NH_4)_2$-H-citrate	0.98 g
d_8-glycerol	10 g
1 M $MgSO_4$	0.46 g
metal salts	2 mL

*metal salts composition: 0.5g/l $CaCl_2.2H_2O$, 16.7 g/l $FeCl_3.6H_2O$, 0.18 g/l $ZnSO_4.7H_2O$, 0.16 g/l $CuSO_4.5H_2O$, 0.15 g/l $MnSO_4.4H_2O$, 0.18 g/l $CoCl_2.6H_2O$, 20.1 g/l Na-EDTA.

TABLE A.2: Details of buffers used during the DUOX purification process.

Lysis Buffer	50 mM Tris-HCl, pH 8.0 or 50 mM Tris-acetate, pH 8.0
Dialysis Buffer	50 mM Tris-HCl, pH 8.0
Ion Exchange Chromatography	
Buffer A	50 mM Tris-HCl, 5 mM KCl, pH 8.0
Buffer B	50 mM Tris-HCl, 0.6 M KCl, pH 8.0
Hydrophobic Interaction Chromatography	
Buffer C	20 mM KP_i, 1 M $(NH_4)_2SO_2$, pH 8.0
Buffer D	20 mM KP_i, pH 8.0
Gel Filtration	
Buffer E	50 mM Tris-HCl, pH 8.0 or 50 mM Tris-acetate, pH 8.0

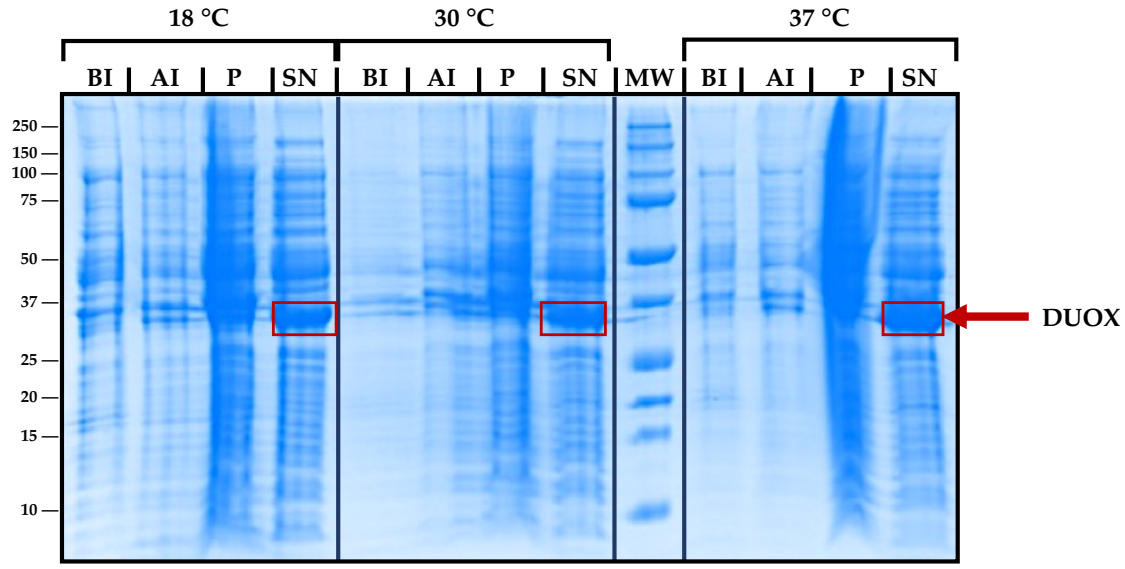

FIGURE A.2: SDS-PAGE showing the expression and solubility of HUOX in LB medium. The MW (kDa) lanes represent a molecular weight marker. The different temperatures and expression times are separated by solid black lines. The temperatures and expression times were as follows: 18 °C and overnight; 30 °C and 5 hours; 37 °C and 3 hours. The before induction and after induction samples across all temperatures show similar levels of overexpression. The SN 37 °C lane shows the largest quantity of soluble HUOX, indicating the most favourable condition.

TABLE A.3: Calculation of expected hydrogenated mass from the number of amino acids and their respective molecular weights and of expected deuterated mass from the number of amino acids and their respective molecular weights including the number of non-exchangeable deuteriums incorporated into the backbone.

Amino Acid	**Number of AA**	**hAA MW**	**hAA MW x Nb**	**Number of non-exchangeable D**	**MW of non-exchangeable D per AA**	**dAA MW**	**dAA Mw x Nb**
Ala A	19	71.079	1350.50	4	76	75.08	1426.50
Arg R	12	156.19	1874.25	7	84	163.19	1958.25
Asn N	14	114.10	1597.45	3	42	117.10	1639.45
Asp D	17	115.09	1956.51	3	51	118.09	2007.51
Cys C	3	103.15	309.44	3	9	106.15	318.43
Glu E	12	129.12	1549.39	5	100	134.12	1609.39
Gln Q	20	128.13	2562.62	5	60	133.13	2662.62
Gly G	15	57.05	855.78	2	30	59.05	885.78
His H	11	137.14	1508.55	5	55	142.14	1563.55
Ile I	18	113.16	2036.87	10	180	123.16	2216.87
Leu L	20	113.16	2263.19	10	200	123.16	2463.19
Lys K	25	128.17	3204.36	9	225	137.17	3429.36
Met	4	131.20	524.79	8	32	139.20	556.79
Phe F	10	147.18	1471.77	8	80	155.18	1551.77
Pro P	9	97.12	874.05	7	63	104.12	937.05
Ser S	23	87.08	2002.80	3	69	90.08	2071.80
Thr T	26	101.11	2628.73	5	130	106.11	2758.73
Trp W	7	186.21	1303.49	8	56	194.21	1359.49
Tyr Y	10	163.18	1631.76	7	70	170.18	1701.76
Val V	26	99.00	2574.00	8	208	107.00	2782.00
			Total: 34,098 kDa		Total: 1,820 kDa	Total: 35,918 kDa	

Bibliography

(1) In *Encycl. Ref. Genomics Proteomics Mol. Med.* Springer Berlin Heidelberg: Berlin, Heidelberg, 2006, p 408.

(2) Bugg, T. D. Dioxygenase enzymes: Catalytic mechanisms and chemical models. *Tetrahedron* **2003**, *59*, 7075–7101.

(3) Fetzner, S. Oxygenases without requirement for cofactors or metal ions. *Appl. Microbiol. Biotechnol.* **2002**, *60*, 243–257.

(4) Whittaker, J. W. Oxygen reactions of the copper oxidases. *Essays Biochem.* **1999**, *34*, 155–172.

(5) *Active oxygen in chemistry*, 1st; Foote, C. S., Selverstone Valentine, J., Greenberg, A., Liebman, J. F., Eds.; Blakie Academic and Professional: Bishopbriggs, Glasgow, 1996.

(6) *Active oxygen in biochemistry*, 1st; S., V. J., Foote, C. S., Greenberg, A., Liebman, J. F., Eds.; Springer Science and Business Media: Hong Kong, 1995, p 463.

(7) Sawyer, D. T., *Oxygen Chemistry*, 1st; Oxford University Press: New York, 1991, p 240.

(8) Jones, R. D.; Summerville, D. A.; Basolo, F. Synthetic oxygen carriers related to biological systems. *Chem. Rev.* **1979**, *79*, 139–179.

(9) *Heme Peroxidases*; Raven, E., Dunford, B., Eds.; Metallobiology; The Royal Society of Chemistry: 2016, P001–366.

(10) Stephens, P. J.; Jollie, D. R.; Warshel, A. Protein control of redox potentials of iron-sulfur proteins. *Chem. Rev.* **1996**, *96*, 2491–2513.

(11) Pau, M. Y.; Lipscomb, J. D.; Solomon, E. I. Substrate activation for O2 reactions by oxidized metal centers in biology. *Proc Natl Acad Sci U S A* **2007**, *104*, 18355–18362.

(12) Frerichs-Deeken, U.; Ranguelova, K.; Kappl, R.; Hüttermann, J.; Fetzner, S. Dioxygenases without requirement for cofactors and their chemical model reaction: Compulsory order ternary complex mechanism of 1H-3-hydroxy-4- oxoquinaldine 2,4-dioxygenase involving general base catalysis by histidine 251 and single-electron oxidation o. *Biochemistry* **2004**, *43*, 14485–14499.

(13) Palfey, B. A.; Ballou, D. P.; Massey, V. Oxygen Activation by Flavins and Pterins. *Act. Oxyg. Biochem.* **1995**, 37–83.

(14) Massay, V. Activation Of Molecular Oxygen By Flavins And Flavoproteins. *J. Biol. Chem.* **1994**, *269*, 22459–22462.

(15) Bruice, T. C. Oxygen-Flavin Chemistry. *Isreal J. Chem.* **1984**, *24*, 54–61.

(16) Huijbers, M. M.; Montersino, S.; Westphal, A. H.; Tischler, D.; Van Berkel, W. J. Flavin dependent monooxygenases. *Arch. Biochem. Biophys.* **2014**, *544*, 2–17.

(17) Van Berkel, W. J.; Kamerbeek, N. M.; Fraaije, M. W. Flavoprotein monooxygenases, a diverse class of oxidative biocatalysts. *J. Biotechnol.* **2006**, *124*, 670–689.

(18) Entsch, B.; Van Berkel, W. J. H. Structure and mechanism of para-hydroxybenzoate hydroxylase. *FASEB J.* **1995**, *9*, 476–483.

(19) Mattevi, A. To be or not to be an oxidase: challenging the oxygen reactivity of flavoenzymes. *Trends Biochem. Sci.* **2006**, *31*, 276–283.

(20) Colette Daubner, S.; Lanzas, R. O. In *Ref. Modul. Biomed. Sci.* Elsevier: 2018.

(21) *Biological Oxidation Systems*; Reddy, C. C., Hamilton, G, A., Madyastha, K. M., Eds.; Academic Press Inc.: San Diego, USA, 1990, p 545.

(22) Fetzner, S.; Steiner, R. A. Cofactor-independent oxidases and oxygenases. *Appl. Microbiol. Biotechnol.* **2010**, *86*, 791–804.

(23) Christopherson, R. I. In *Encycl. Ref. Genomics Proteomics Mol. Med.* Springer Berlin Heidelberg: Berlin, Heidelberg, 2006, pp 1333–1337.

(24) Maiuolo, J.; Oppedisano, F.; Gratteri, S.; Muscoli, C.; Mollace, V. Regulation of uric acid metabolism and excretion. *Int. J. Cardiol.* **2016**, *213*, 8–14.

(25) Keilin, J. The biological significance of uric acid. *Biol. Rev.* **1958**, *34*, 265–294.

(26) Yeldandi, A. V.; Yeldandi, V.; Kumar, S.; Narasimha Murthy, C. V.; Wang, X.; Keith, A.; Sambasiva Rao, M.; Reddy, J. K. Molecular evolution of the urate oxidase-encoding gene in hominoid primates: nonsense mutations. *Gene* **1991**, *109*, 281–284.

(27) Oda, M.; Satta, Y.; Takenaka, O.; Takahata, N. Loss of urate oxidase activity in hominoids and its evolutionary implications. *Mol. Biol. Evol.* **2002**, *19*, 640–653.

(28) Christen, P.; Peacock, W. C.; Christen, A. E.; Wacker, W. E. Urate Oxidase in Primate Phylogenesis. *Eur. J. Biochem.* **1970**, *12*, 3–5.

(29) Friedman, T. B.; Polanco, G. E.; Appold, J. C.; Maylet, J. E. On The Loss Of Uricolytic Activity During Primate Evolution - I. Silencing Of Urate Oxidase In A Homonoid Ancestor. *Comp. Biochem. Physiol.* **1985**, *81B*, 653–659.

(30) Wu, X. W.; Lee, C. C.; Muzny, D. M.; Caskey, C. T. Urate oxidase: primary structure and evolutionary implications. *Proc. Natl. Acad. Sci. U. S. A.* **1989**, *86*, 9412–9416.

(31) Yeldandi, A. V.; Wang, X.; Alvares, K.; Kumar, S.; Rao, M. S.; Reddy, J. K. Human Urate Oxidase Gene: Cloning and Partial Sequence Analysis Reveal A Stop Codon Within The Fifth Exon. *Biochem. Biophys. Res. Commun.* **1990**, *171*, 641–646.

(32) Orowan, E. The Origin Of Man. *Nature* **1955**, *175*, 683–684.

(33) Ames, B. N.; Cathcart, R.; Schwiers, E.; Hochstein, P. Uric acid provides an antioxidant defense in humans against oxidant- and radical-caused aging and cancer: a hypothesis. *Proc. Natl. Acad. Sci.* **1981**, *78*, 6858–6862.

(34) Johnson, R. J.; Titte, S.; Cade, J. R.; Rideout, B. A.; Oliver, W. J. Uric acid, evolution and primitive cultures. *Semin. Nephrol.* **2005**, *25*, 3–8.

(35) Kratzer, J. T.; Lanaspa, M. A.; Murphy, M. N.; Cicerchi, C.; Graves, C. L.; Tipton, P. A.; Ortlund, E. A.; Johnson, R. J.; Gaucher, E. A. Evolutionary history and metabolic insights of ancient mammalian uricases. *PNAS* **2014**, *111*, 3763–3768.

(36) Wu, X.; Wakamiya, M.; Vaishnav, S.; Geske, R.; Montgomery, C.; Jones, P.; Bradley, A.; Caskey, C. T. Hyperuricemia and urate nephropathy in urate oxidase-deficient mice. *Proc. Natl. Acad. Sci. U. S. A.* **1994**, *91*, 742–746.

(37) Marchetti, M.; Liuzzi, A.; Fermi, B.; Corsini, R.; Folli, C.; Speranzini, V.; Gandolfi, F.; Bettati, S.; Ronda, L.; Cendron, L.; Berni, R.; Zanotti, G.; Percudani, R. Catalysis and Structure of Zebrafish Urate Oxidase Provide Insights into the Origin of Hyperuricemia in Hominoids. *Sci. Rep.* **2016**, *6*, 1–13.

(38) Schrader, M.; Fahimi, H. D. Peroxisomes and oxidative stress. *Biochim. Biophys. Acta - Mol. Cell Res.* **2006**, *1763*, 1755–1766.

(39) Terlecky, S. R.; Koepke, J. I.; Walton, P. A. Peroxisomes and aging. *Biochim. Biophys. Acta - Mol. Cell Res.* **2006**, *1763*, 1749–1754.

(40) Proctor, P. Similar Functions of Uric Acid and Ascorbate in Man? *Nature* **1970**, *228*, 868.

(41) Waring, W. Uric acid: an important antioxidant in acute ischaemic stroke. *Q J Med An Int. J. Med.* **2002**, *95*, 691–693.

(42) Simic, M. G.; Jovanovic, S. V. Antioxidation mechanisms of uric acid. *J. Am. Chem. Soc.* **1989**, *111*, 5778–5782.

(43) Becker, B. F. Towards the physiological function of uric acid. *Free Radic. Biol. Med.* **1993**, *14*, 615–631.

(44) Howell, R. R.; Wyngaarden, J. B. On the mechanism of peroxidation of uric acids by hemoproteins. *J. Biol. Chem.* **1960**, *235*, 3544–3550.

(45) Maples, K. R.; Mason, R. P. Free radical metabolite of uric acid. *J. Biol. Chem.* **1988**, *263*, 1709–1712.

(46) Mazzali, M.; Watanabe, S.; Johnson, R. J.; Rodriguez-Iturbe, B.; Feig, D.; Kang, D.-H.; Kanellis, J.; Herrera-Acosta, J.; Kivlighn, S.; Tuttle, K. R. Is There a Pathogenetic Role for Uric Acid in Hypertension and Cardiovascular and Renal Disease? *Hypertension* **2003**, *41*, 1183–1190.

(47) Nimse, S. B.; Pal, D. Free radicals, natural antioxidants, and their reaction mechanisms. *RSC Adv.* **2015**, *5*, 27986–28006.

(48) Skinner, K. A.; Parks, D. A.; Khoo, N. H. Uric Acid Metabolism. *Encycl. Life Sci.* **2006**, DOI: 10.1038/npg.els.0003910.

(49) Ragab, G.; Elshahaly, M.; Bardin, T. Gout: An old disease in new perspective – A review. *J. Adv. Res.* **2017**, *8*, 495–511.

(50) Howard, S. C.; Jones, D. P.; Piu, C.-H. The tumor lysis syndrome [3]. *N Engl J Med.* **2011**, *364*, 1844–1854.

(51) Wilson, F. P.; Berns, J. S. Tumor Lysis Syndrome: New Challenges and Recent Advances. *Adv Chronic Kidney Dis. 2014* **2014**, *21*, 18–26.

(52) Legoux, R.; Delpech, B.; Dumont, X.; Guillemot, J. C.; Ramond, P.; Shire, D.; Caput, D.; Ferrara, P.; Loison, G. Cloning and expression in Escherichia coli of the gene encoding Aspergillus flavus urate oxidase. *J. Biol. Chem.* **1992**, *267*, 8565–8570.

(53) Leplatois, P.; Le Douarin, B.; Loison, G. High-level production of a peroxisomal enzyme: Aspergillus flavus uricase accumulates intracellularly and is active in Saccharomyces cerevisiae. *Gene* **1992**, *122*, 139–145.

(54) Hochberg, J.; Cairo, M. S. Rasburicase: future directions in tumor lysis management. *Expert Opin. Biol. Ther.* **2008**, *8*, 1595–1604.

(55) Pacher, P.; Nivorozhkin, A.; Szabo, C. Therapeutic effecrs of xanthine oxidase inhibitors: renaissance half a century after the discovery of allopurinol. *Pharmacol. Rev.* **2008**, *58*, 87–114.

(56) Doniselli, N.; Monzeglio, E.; Dal Palù, A.; Merli, A.; Percudani, R. The identification of an integral membrane, cytochrome c urate oxidase completes the catalytic repertoire of a therapeutic enzyme. *Sci. Rep.* **2015**, *5*, 1–12.

(57) Hicks, K. A.; O'Leary, S. E.; Begley, T. P.; Ealick, S. E. Structural and Mechanistic Studies of HpxO, a Novel FAD- dependent Urate Oxidase from Klebsiella pneumoniae. *Biochemistry* **2013**, *52*, 477–487.

(58) Michiel, M.; Perchat, N.; Perret, A.; Tricot, S.; Papeil, A.; Besnard, M.; De Berardinis, V.; Salanoubat, M.; Fischer, C. Microbial urate catabolism: Characterization of HpyO, a non-homologous isofunctional isoform of the flavoprotein urate hydroxylase HpxO. *Environ. Microbiol. Rep.* **2012**, *4*, 642–647.

(59) Bongaerts, G. P. A.; Vogels, G. D. Mechanism of uricase action. *BBA - Enzymol.* **1979**, *567*, 295–308.

(60) Mahler, H. R.; Hubscher, G.; Baum, H. Studies on Uricase I. Preparation, Purification and Properties of a Cuproprotein. *J. Biol. Chem.* **1955**, *216*, 625–642.

(61) Nishimura, H.; Matsushima, A.; Yoshida, K.; Inada, Y. Physicochemical of Uricase from Properties Candida and States utilis of Sulfhydryl Groups of uric with molecular oxygen serving as the electron acceptor , was first found in bovine by Schittenhelm properties literature as to the metal ions and the role of. **1982**, *91*, 41–48.

(62) Conley, T. G.; Priest, D. G. Non-classical inhibition of uricase by cyanide. *Biochem. J.* **1980**, *187*, 733–738.

(63) Bergmann, H.; Preddie, E.; Verma, D. Nodulin-35: a subunit of specific uricase (uricase II) induced and localized in the uninfected cells of soybean nodules. *EMBO J.* **1983**, *2*, 2333–2339.

(64) Kahn, K; Tipton, P. A. Kinetic mechanism and cofactor of soybean root nodule urate oxidase. *Biochemistry* **1997**, *36*, 4731–4738.

(65) Colloc'h, N.; El Hajji, M.; Bachet, B.; L'Hermite, G.; Schiltz, M.; Prangé, T.; Castro, B.; Mornon, J. P. Crystal structure of the protein drug urate oxidase-inhibitor complex at 2.05 Å resolution. *Nat. Struct. Biol.* **1997**, *4*, 947–952.

(66) Colloc'h, N.; Poupon, A.; Mornon, J. P. Sequence and structural features of the T-fold, an original tunnelling building unit. *Proteins Struct. Funct. Genet.* **2000**, *39*, 142–154.

(67) https://www.ncbi.nlm.nih.gov/Structure/cdd/cl00263.

(68) Retailleau, P.; Colloc, N.; Vivare Ás, D.; Ëoise Bonnete Â, F.; Castro, B.; El Hajji, M.; Mornon, J.-P.; Ârald Monard, G.; Prange Â, T. Complexed and ligand-free high-resolution structures of urate oxidase (Uox) from Aspergillus flavus: a reassignment of the active-site binding mode. *Acta Cryst* **2004**, *60*, 453–462.

(69) Wang, Y.; Li, Y.; Yan, H. Mechanism of dihydroneopterin aldolase: Functional roles of the conserved active site glutamate and lysine residues. *Biochemistry* **2006**, *45*, 15232–15239.

(70) Poupon, A.; Mornon, J. P. "Topohydrophobic positions" as key markers of globular protein folds. *Theor. Chem. Acc.* **1999**, *101*, 2–8.

(71) Murzin, A. G.; Bateman, A. Distant Homology Recognition Using Structural. *Proteins Struct. Funct. Genet.* **1997**, *112*, 105–112.

(72) Orengo, C. A.; Jones, D. T.; Janet, B. Protein superfamilies and domain superfolds. *Nature* **1994**, *372*, 2–5.

(73) Gouet, P.; Courcelle, E.; Stuart, D. I.; Métoz, F. ESPript: Analysis of multiple sequence alignments in PostScript. *Bioinformatics* **1999**, *15*, 305–308.

(74) Robert, X.; Gouet, P. Deciphering key features in protein structures with the new ENDscript server. *Nucleic Acids Res.* **2014**, *42*, 320–324.

(75) Berman, H. M.; Westbrook, J.; Feng, Z.; Gilliland, G.; Bhat, T. N.; Weissig, H.; Shindyalov, I. N.; Bourne, P. E. The protein data bank. *Nucleic Acids Res.* **2000**, *28*, 235–242.

(76) Retailleau, P.; Colloc'h, N.; Vivarès, D.; Bonneté, F.; Castro, B.; El Hajji, M.; Prangé, T. Urate oxidase from Aspergillus flavus: New crystal-packing contacts in relation to the content of the active site. *Acta Crystallogr. Sect. D Biol. Crystallogr.* **2005**, *61*, 218–229.

(77) Gabison, L.; Chiadmi, M.; Colloc'h, N.; Castro, B.; El Hajji, M.; Prangé, T. Recapture of [S]-allantoin, the product of the two-step degradation of uric acid, by urate oxidase. *FEBS Lett.* **2006**, *580*, 2087–2091.

(78) Gabison, L.; Chiadmi, M.; El Hajji, M.; Castro, B.; Colloch, N.; Prangé, T. Near-atomic resolution structures of urate oxidase complexed with its substrate and analogues: The protonation state of the ligand. *Acta Crystallogr. Sect. D Biol. Crystallogr.* **2010**, *66*, 714–724.

(79) Gabison, L.; Colloc'h, N.; Prangé, T. Azide inhibition of urate oxidase. *Acta Crystallogr. Sect. FStructural Biol. Commun.* **2014**, *70*, 896–902.

(80) Oksanen, E.; Blakeley, M. P.; El-Hajji, M.; Ryde, U.; Budayova-Spano, M. The neutron structure of urate oxidase resolves a long-standing mechanistic conundrum and reveals unexpected changes in protonation. *PLoS One* **2014**, *9*, 1–10.

(81) Bui, S.; Von Stetten, D.; Jambrina, P. G.; Prangé, T.; Colloc'h, N.; De Sanctis, D.; Royant, A.; Rosta, E.; Steiner, R. A. Direct evidence for a peroxide intermediate and a reactive enzyme-substrate-dioxygen configuration in a cofactor-free oxidase. *Angew. Chemie - Int. Ed.* **2014**, *53*, 13710–13714.

(82) Gabison, L.; Chopard, C.; Colloc'h, N.; Peyrot, F.; Castro, B.; Hajji, M. E.; Altarsha, M.; Monard, G.; Chiadmi, M.; Prangé, T. X-ray, ESR, and quantum mechanics studies unravel a spin well in the cofactor-less urate oxidase. *Proteins Struct. Funct. Bioinforma.* **2011**, *79*, 1964–1976.

(83) Gabison, L.; Prangé, T.; Colloc'h, N.; El Hajji, M.; Castro, B.; Chiadmi, M. Structural analysis of urate oxidase in complex with its natural substrate inhibited by cyanide: Mechanistic implications. *BMC Struct. Biol.* **2008**, *8*, 1–8.

(84) Gadda, G. Oxygen activation in flavoprotein oxidases: The importance of being positive. *Biochemistry* **2012**, *51*, 2662–2669.

(85) Roth, J. P.; Wincek, R.; Nodet, G.; Edmondson, D. E.; McIntire, W. S.; Klinman, J. P. Oxygen isotope effects on electron transfer to O2 probed using

chemically modified flavins bound to glucose oxidase. *J. Am. Chem. Soc.* **2004**, *126*, 15120–15131.

(86) Klinman, J. P. How Do Enzymes Activate Oxygen without Inactivating Themselves ? *Acc. Chem. Res.* **2007**, *40*, 325–333.

(87) Colloc'h, N.; Prangé, T. Functional relevance of the internal hydrophobic cavity of urate oxidase. *FEBS Lett.* **2014**, *588*, 1715–1719.

(88) Colloc'h, N.; Gabison, L.; Monard, G.; Altarsha, M.; Chiadmi, M.; Marassio, G.; Sopkova-de Oliveira Santos, J.; El Hajji, M.; Castro, B.; Abraini, J. H.; Prangé, T. Oxygen Pressurized X-Ray Crystallography: Probing the Dioxygen Binding Site in Cofactorless Urate Oxidase and Implications for Its Catalytic Mechanism. *Biophys. J.* **2008**, *95*, 2415–2422.

(89) Gouet, P.; Jouve, H. M.; Dideberg, O. Crystal structure of Proteus mirabilis PR catalase with and without bound NADPH. *J. Mol. Biol.* **1995**, *249*, 933–954.

(90) Putnam, C. D.; Arvai, A. S.; Bourne, Y.; Tainer, J. A. Active and inhibited human catalase structures: ligand and NADPH binding and catalytic mechanism. *J. Mol. Biol.* **2000**, *296*, 295–309.

(91) Imhoff, R. D.; Power, N. P.; Borrok, M. J.; Tipton, P. A. General base catalysis in the urate oxidase reaction: Evidence for a novel Thr-Lys catalytic diad. *Biochemistry* **2003**, *42*, 4094–4100.

(92) Trickey, P.; Wagner, M. A.; Jorns, M. S.; Mathews, F. S. Monomeric sarcosine oxidase : structure of a covalently flavinylated amine oxidizing enzyme. *Structure* **1999**, *315*, 331–345.

(93) Juan, E. C. M.; Hoque, M. M.; Shimizu, S.; Hossain, M. T.; Yamamoto, T.; Imamura, S.; Suzuki, K.; Tsunoda, M.; Amano, H.; Sekiguchi, T.; Takénaka, A. Structures of Arthrobacter globiformis urate oxidase-ligand complexes. *Acta Crystallogr. Sect. D Biol. Crystallogr.* **2008**, *64*, 815–822.

(94) Hibi, T.; Nago, T.; Nishiya, Y.; Oda, J. Crystal structure of urate oxidase from Bacillus sp. TB-90 co-crystallized with 8-azaxanthine., DOI 10.2210/pdb1j2g/pdb.

(95) Kendrew, S. G.; Hopwood, D. A. Identification of a Monooxygenase from Streptomyces coelicolor A3 (2) Involved in Biosynthesis of Actinorhodin : Purification and Characterization of the Recombinant Enzyme. *J. Bacteriol.* **1997**, *179*, 4305–4310.

(96) Roth, J. P.; Klinman, J. P. Catalysis of electron transfer during activation of O 2 by the flavoprotein glucose oxidase. **2003**, *100*, 2–7.

(97) Steiner, R. A.; Janssen, H. J.; Roversi, P.; Oakley, A. J.; Fetzner, S. Structural basis for cofactor-independent dioxygenation of N-heteroaromatic compounds at the alpha/beta-hydrolase fold. *Proc. Natl. Acad. Sci. U. S. A.* **2010**, *107*, 657–62.

(98) Bugg, T. D. Diverse catalytic activities in the $\alpha\beta$-hydrolase family of enzymes: Activation of H2O, HCN, H2O2, and O2. *Bioorg. Chem.* **2004**, *32*, 367–375.

(99) Nardini, M.; Dijkstra, B. W. α/β hydrolase fold enzymes: The family keeps growing. *Curr. Opin. Struct. Biol.* **1999**, *9*, 732–737.

(100) Rauwerdink, A.; Kazlauskas, R. J. How the Same Core Catalytic Machinery Catalyzes 17 Different Reactions: The Serine-Histidine-Aspartate Catalytic Triad of alpha/beta-Hydrolase Fold Enzymes. *ACS Catal.* **2015**, *5*, 6153–6176.

(101) Keilin, D; Hartree, E. F. Uricase, Amino Acid Oxidase, and Xanthine Oxidase. *Proc. R. Soc. London. Ser. B - Biol. Sci.* **1936**, *119*, 114–140.

(102) Laboureur, P; Langlois, C Urate oxidase of Aspergillus flavus. II. Metabolism, inhibition, specificity. *Bull. Soc. Chim. Biol. (Paris).* **1968**, *50*, 827–41.

(103) Bergmann, F.; Dikstein, S. The Relationship between Spectral Shifts and Structural Changes in Uric Acids and Related Compounds. *J. Am. Chem. Soc.* **1955**, *77*, 691–696.

(104) Pfleiderer, W Synthese, Struktur und Eigenschaften der Harnsäure sowie ihrer N-Methylderivate. *Liebigs Ann. Chem.* **1974**, 2030–2045.

(105) Goyal, R. N.; Mittal, A.; Agarwal, D. Electrochemical oxidation and kinetics of the decay of UV-absorbing intermediate of uric acid oxidation at pyrolytic graphite electrodes. *Can. J. Chem.* **1994**, *72*, 1668–1674.

(106) Kahn, K.; Serfozo, P.; Tipton, P. A. Identification of the true product of the urate oxidase reaction. *J. Am. Chem. Soc.* **1997**, *119*, 5435–5442.

(107) Mandel, N. S.; Mandel, G. S. Monosodium Urate Monohydrate, the Gout Culprit. *J. Am. Chem. Soc.* **1976**, *98*, 2319–2323.

(108) Altarsha, M.; Castro, B.; Monard, G. Intrinsic reactivity of uric acid with dioxygen: Towards the elucidation of the catalytic mechanism of urate oxidase. *Bioorg. Chem.* **2009**, *37*, 111–125.

(109) Glickman, M. H.; Klinman, J. P. Lipoxygenase reaction mechanism: Demonstration that hydrogen abstraction from substrate precedes dioxygen binding during catalytic turnover. *Biochemistry* **1996**, *35*, 12882–12892.

(110) Busi, E.; Terzuoli, L.; Basosi, R.; Porcelli, B.; Marinello, E. EPR spin trapping of a radical intermediate in the urate oxidase reaction. *Nucleosides, Nucleotides and Nucleic Acids* **2004**, *23*, 1131–1134.

(111) Oksanen, E; Blakeley, M. P.; Bonnete, F.; Dauvergne, M. T.; Dauvergne, F; Budayova-Spano, M Large crystal growth by thermal control allows combined X-ray and neutron crystallographic studies to elucidate the protonation states in Aspergillus flavus urate oxidase. *J. R. Soc. Interface* **2009**, *6*, S599–S610.

(112) Wei, D.; Huang, X.; Qiao, Y.; Rao, J.; Wang, L.; Liao, F.; Zhan, C. G. Catalytic Mechanisms for Cofactor-Free Oxidase-Catalyzed Reactions: Reaction Pathways of Uricase-Catalyzed Oxidation and Hydration of Uric Acid. *ACS Catal.* **2017**, *7*, 4623–4636.

(113) Kahn, K.; Tipton, P. A. Spectroscopic characterization of intermediates in the urate oxidase reaction. *Biochemistry* **1998**, *37*, 11651–11659.

(114) Hamilton, G, A. In *Mol. Mech. Oxyg. Act.* Hayaishi, O., Ed.; Academic Press: New York, 1974, pp 405–451.

(115) Sarma, A. D.; Tipton, P. A. Evidence for urate hydroperoxide as an intermediate in the urate oxidase reaction. *J. Am. Chem. Soc.* **2000**, *122*, 11252–11253.

(116) Chaiyen, P.; Fraaije, M. W.; Mattevi, A. The enigmatic reaction of flavins with oxygen. *Trends Biochem. Sci.* **2012**, *37*, 373–380.

(117) Thierbach, S.; Bui, N.; Zapp, J.; Chhabra, S. R.; Kappl, R.; Fetzner, S. Substrate-assisted O2 activation in a cofactor-independent dioxygenase. *Chem. Biol.* **2014**, *21*, 217–225.

(118) Machovina, M. M.; Usselman, R. J.; Du Bois, J. L. Monooxygenase substrates mimic flavin to catalyze cofactorless oxygenations. *J. Biol. Chem.* **2016**, *291*, 17816–17828.

(119) Widboom, P. F.; Fielding, E. N.; Liu, Y.; Bruner, S. D. Structural basis for cofactor-independent dioxygenation in vancomycin biosynthesis. *Nature* **2007**, *447*, 342–345.

(120) Felix, F.; Scheel, F.; Schuler, W. Die urikolyse. *Hoppe-Seyl Z* **1929**, *180*, 90–106.

(121) Modrić, N.; Derome, A. E.; Ashcroft, S. J.; Poje, M. Tracing and identification of uricase. Reaction intermediates. A direct 13C-NMR/isotope-labelling evidence. *Tetrahedron Lett.* **1992**, *33*, 6691–6694.

(122) Goyal, R. N.; Brajter-Toth, A.; Dryhurst, G. Futher insights into the electrochemical oxidation of uric acid. *J. Electroanal. Chem.* **1982**, *131*, 181–202.

(123) Bentley, R; Neuberger, A The mechanism of the action of uricase. *Biochem. J.* **1952**, *52*, 694.

(124) Tipton, P. A. Urate to allantoin, specifically (S)-allantoin. *Nat. Chem. Biol.* **2006**, *2*, 124–125.

(125) Bergmans, H. E. N.; Van Die, I. M.; Hoekstra, W. P. M. Transformation in Escherichia coli: stages in the process. *J. Bacteriol.* **1981**, *146*, 564–570.

(126) Froger, A.; Hall, J. E. Transformation of Plasmid DNA into E. Coli using the heat shock method. *J. Vis. Exp.* **2007**, 2007.

(127) Jeong, H. et al. Genome Sequences of Escherichia coli B strains REL606 and BL21(DE3). *J. Mol. Biol.* **2009**, *394*, 644–652.

(128) Baneyx, F. Recombinant protein expression in Escherichia coli. *Curr. Opin. Biotechnol.* **1999**, *10*, 411–421.

(129) https://www.moleculardevices.com/sites /default/files/en/assets/app-note/br/measu long-term-cell-growth-using-a -discontinuous-kinetic-reading.pdf.

(130) Fujikawa, H.; Kai, A.; Morozumi, S. A new logistic model for Escherichia coli growth at constant and dynamic temperatures. *Food Microbiol.* **2004**, *21*, 501–509.

(131) Haertlein, M.; Moulin, M.; Devos, J. M.; Laux, V.; Dunne, O.; Forsyth, V. T. Biomolecular Deuteration for Neutron Structural Biology and Dynamics. *Methods Enzymol.* **2016**, *566*, 113–157.

(132) Myles, D. A. Neutron protein crystallography: current status and a brighter future. *Curr. Opin. Struct. Biol.* **2006**, *16*, 630–637.

(133) Liu, X.; Hanson, B. L.; Langan, P.; Viola, R. E. The effect of deuteration on protein structure: A high-resolution comparison of hydrogenous and perdeuterated haloalkane dehalogenase. *Acta Crystallogr. Sect. D Biol. Crystallogr.* **2007**, *63*, 1000–1008.

(134) Meilleur, F.; Contzen, J.; Myles, D. A. A.; Jung, C. Structural stability and dynamics of hydrogenated and perdeuterated cytochrome P450cam (CYP101). *Biochemistry* **2004**, *43*, 8744–8753.

(135) Hattori, A.; Crespi, H. L.; Katz, J. J. Effect of Side-Chain Deuteration on Protein Stability. *Biochemistry* **1965**, *4*, 1213–1225.

(136) Yee, A. W.; Moulin, M.; Breteau, N.; Haertlein, M.; Mitchell, E. P.; Cooper, J. B.; Boeri Erba, E.; Forsyth, V. T. Impact of Deuteration on the Assembly Kinetics of Transthyretin Monitored by Native Mass Spectrometry and Implications for Amyloidoses. *Angew. Chemie - Int. Ed.* **2016**, *55*, 9292–9296.

(137) Piszczek, G.; Lee, J. C.; Tjandra, N.; Lee, C. R.; Seok, Y. J.; Levine, R. L.; Peterkofsky, A. Deuteration of Escherichia coli Enzyme INtr alters its stability. *Arch. Biochem. Biophys.* **2011**, *507*, 332–342.

(138) Brockwell, D. Physicochemical consequences of the perdeuteriation of glutathione S-transferase from S. japonicum. *Protein Sci.* **2001**, *10*, 572–580.

(139) Liu, X.; Hanson, B. L.; Langan, P.; Viola, R. E. The effect of deuteration on protein structure: A high-resolution comparison of hydrogenous and perdeuterated haloalkane dehalogenase. *Acta Crystallogr. Sect. D Biol. Crystallogr.* **2007**, *63*, 1000–1008.

(140) White, J.; Heß, D.; Raynes, J.; Laux, V.; Haertlein, M.; Forsyth, V. T.; Jeyasingham, A. The aggregation of "native" human serum albumin. *Eur. Biophys. J.* **2015**, *44*, 367–371.

(141) Gamble, T. R.; Clauser, K. R.; Kossiakoff, A. A. The production and X-ray structure determination of perdeuterated Staphylococcal nuclease. *Biophys. Chem.* **1994**, *53*, 15–25.

(142) Cooper, S. J.; Brockwell, D.; Raftery, J.; Attwood, D.; Barber, J.; Helliwell, J. R. The X-ray crystal structures of perdeuteriated and protiated enzyme elongation factor Tu are very similar. *Chem. Commun.* **1998**, 1063–1064.

(143) Blakeley, M. P.; Langan, P.; Niimura, N.; Podjarny, A. Neutron crystallography: opportunities, challenges, and limitations. *Curr. Opin. Struct. Biol.* **2008**, *18*, 593–600.

(144) Golden, E.; Attwood, P. V.; Duff, A. P.; Meilleur, F.; Vrielink, A. Production and characterization of recombinant perdeuterated cholesterol oxidase. *Anal. Biochem.* **2015**, *485*, 102–108.

(145) Fisher, S. J.; Helliwell, J. R. An investigation into structural changes due to deuteration. *Acta Crystallogr. Sect. A Found. Crystallogr.* **2008**, *64*, 359–367.

(146) Green, A. A.; Hughes, W. L. Protein fractionation on the basis of solubility in aqueous solutions of salts and organic solvents. *Methods Enzymol.* **1955**, *1*, 67–90.

(147) Duong-Ly, K. C.; Gabelli, S. B. Salting out of proteins using ammonium sulfate precipitation. *Methods Enzymol.* **2014**, *541*, 85–94.

(148) Wingfield, P. T. Protein Precipitation Using Ammonium Sulfate HHS Public Access. *Curr Protoc Protein Sci* **1994**, *3*, 3.

(149) Wood, W. I. Tables for the preparation of ammonium sulfate solutions. *Anal. Biochem.* **1976**, *73*, 250–257.

(150) Budayova-Spano, M.; Dauvergne, F.; Audiffren, M.; Bactivelane, T.; Cusack, S. A methodology and an instrument for the temperature-controlled optimization of crystal growth. *Acta Crystallogr. Sect. D Biol. Crystallogr.* **2007**, *63*, 339–347.

(151) *Protein Crystallisation*, 2nd; Begfors, T. M., Ed.; International University Line: La Jolla, California, 2009.

(152) Asherie, N. Protein crystallization and phase diagrams. *Methods* **2004**, *34*, 266–272.

(153) Nanev, C. N. On some aspects of crystallization process energetics, logistic new phase nucleation kinetics, crystal size distribution and Ostwald ripening. *J. Appl. Crystallogr.* **2017**, *50*, 1021–1027.

(154) McPherson, A. In *Methods Enzymol.* Methods in Enzymology C, Vol. 114; Academic Press: 1985, pp 112–120.

(155) Krauss, I. R.; Merlino, A.; Vergara, A.; Sica, F. An overview of biological macromolecule crystallization. *Int. J. Mol. Sci.* **2013**, *14*, 11643–11691.

(156) McPherson, A.; Gavira, J. A. Introduction to protein crystallization. *Acta Crystallogr. Sect. F Struct. Biol. Commun.* **2014**, *70*, 2–20.

(157) Chayen, N. E. Turning protein crystallisation from an art into a science. *Curr. Opin. Struct. Biol.* **2004**, *14*, 577–583.

(158) Ducroix A. and R. Giegé Crystallization of nucleic acids and proteins: a practical approach. *Acta Crystallogr. Sect. D Biol. Crystallogr.* **1994**, *50*, 112–112.

(159) Wlodawer, A.; Minor, W.; Dauter, Z.; Jaskolski, M. Protein crystallography for aspiring crystallographers or how to avoid pitfalls and traps in macromolecular structure determination. *FEBS J.* **2013**, *280*, 5705–5736.

(160) Clegg, W., *X-ray Crystallography*, Second Edi; Oxford University Press: 2015.

(161) Bragg, W. H.; Bragg, W. L. The Reflection of X-rays by Crystals. *Proc. R. Soc. A Math. Phys. Eng. Sci.* **1913**, *88*, 428–438.

(162) Ewald, P. P. Die Berechnung optischer und elektrostatischer Gitterpotentiale. *Ann. Phys.* **1921**, *369*, 253–287.

(163) Arndt, Ulrich Wolfgang; Wonacott, A., *The Rotation Method in Crystallography: Data Collection from Macromolecular Crystals*; 1; North-Holland Pub. Co.: 1977; Vol. 1, p 275.

(164) Blakeley, M. P.; Teixeira, S. C. M.; Petit-Haertlein, I.; Hazemann, I.; Mitschler, A.; Haertlein, M.; Howard, E.; Podjarny, A. D. Neutron macromolecular crystallography with LADI-III. *Acta Crystallogr. Sect. D Biol. Crystallogr.* **2010**, *66*, 1198–1205.

(165) Myles, D. A.; Bon, C.; Langan, P.; Cipriani, F.; Castagna, J. C.; Lehmann, M. S.; Wilkinson, C. Neutron Laue diffraction in macromolecular crystallography. *Phys. B Condens. Matter* **1997**, *241-243*, 1122–1130.

(166) Ren, Z.; Moffat, K. Deconvolution of Energy Overlaps in Laue Diffraction. *J. Appl. Crystallogr.* **1995**, *28*, 482–494.

(167) Powell, H. R. X-ray data processing. *Biosci. Rep.* **2017**, *37*, 1–14.

(168) Leslie, A. G. W.; Powell, H. R. In *Evol. Methods Macromol. Crystallogr.* Read, R. J., Sussman, J. L., Eds., 1st; Springer, Dordrecht: 2007; Chapter Processing, pp 41–51.

(169) Kabsch, W. XDS. *Acta Crystallogr. Sect. D Biol. Crystallogr.* **2010**, *66*, 125–132.

(170) Otwinowski, Z.; Minor, W. Processing of X-ray diffraction data collected in oscillation mode. *Methods Enzymol.* **1997**, *276*, 307–326.

(171) Winter, G.; Waterman, D. G.; Parkhurst, J. M.; Brewster, A. S.; Gildea, R. J.; Gerstel, M.; Fuentes-Montero, L.; Vollmar, M.; Michels-Clark, T.; Young, I. D.; Sauter, N. K.; Evans, G. DIALS: Implementation and evaluation of a new integration package. *Acta Crystallogr. Sect. D Struct. Biol.* **2018**, *74*, 85–97.

(172) Campbell, J. W. Lauegen, an X-Windows-Based Program for the Processing of Laue X-Ray-Diffraction Data. *J. Appl. Crystallogr.* **1995**, *28*, 228–236.

(173) Arzt, S.; Campbell, J. W.; Harding, M. M.; Hao, Q; Helliwell, J. R. LSCALE - The new normalization, scaling and absorption correction program in the Daresbury Laue software suite. *J. Appl. Crystallogr.* **1999**, *32*, 554–562.

(174) Diederichs, K. Some aspects of quantitative analysis and correction of radiation damage. *Acta Crystallogr. Sect. D Biol. Crystallogr.* **2006**, *62*, 96–101.

(175) Weiss, M. S.; Hilgenfeld, R. On the use of the merging R factor as a quality indicator for X-ray data. *J. Appl. Crystallogr.* **1997**, *30*, 203–205.

(176) Diederichs, K.; Karplus, P. A. Improved R-factors for diffraction data analysis in macromolecular crystallography. *Nature* **1997**, *4*, 269–275.

(177) Weiss, M. S. Global indicators of X-ray data quality. *J. Appl. Crystallogr.* **2001**, *34*, 130–135.

(178) Winter, G. Xia2: An expert system for macromolecular crystallography data reduction. *J. Appl. Crystallogr.* **2010**, *43*, 186–190.

(179) Karplus, P. A.; Diederichs, K. Assessing and maximizing data quality in macromolecular crystallography., 2015.

(180) Tronrud, D. E. Introduction to macromolecular refinement. *Acta Crystallogr. Sect. D Biol. Crystallogr.* **2004**, *60*, 2156–2168.

(181) Bernstein, F. C.; Koetzle, T. F.; Williams, G. J. B.; Meyer, E. F.; Brice, M. D.; Rodgers, J. R.; Kennard, O.; Shimanouchi, T.; Tasumi, M. The Protein Data Bank : A Computer-based Archival File for Macromolecular Structures. *J. Mol. Biol.* **1977**, *112*, 535–542.

(182) Engh, R. A.; Huber, R. Accurate bond and angle parameters for X-ray protein structure refinement. *Acta Crystallogr. Sect. A* **1991**, *47*, 392–400.

(183) Steiner, R. A.; Tucker, J. A. Keep it together: restraints in crystallographic refinement of macromolecule–ligand complexes. *Acta Crystallogr. Sect. D Struct. Biol.* **2017**, *73*, 93–102.

(184) Headd, J. J.; Echols, N.; Afonine, P. V.; Grosse-Kunstleve, R. W.; Chen, V. B.; Moriarty, N. W.; Richardson, D. C.; Richardson, J. S.; Adams, P. D. Use of knowledge-based restraints in phenix.refine to improve macromolecular refinement at low resolution. *Acta Crystallogr. Sect. D Biol. Crystallogr.* **2012**, *68*, 381–390.

(185) Emsley, P.; Lohkamp, B.; Scott, W. G.; Cowtan, K. Features and development of Coot. *Acta Crystallogr. Sect. D Biol. Crystallogr.* **2010**, *66*, 486–501.

(186) Afonine, P. V.; Mustyakimov, M.; Grosse-Kunstleve, R. W.; Moriarty, N. W.; Langan, P.; Adams, P. D. Joint X-ray and neutron refinement with phenix.refine. *Acta Crystallogr. Sect. D Biol. Crystallogr.* **2010**, *66*, 1153–1163.

(187) Hamilton, W. C. Significance tests on the crystallographic R factor. *Acta Crystallogr.* **1965**, *18*, 502–510.

(188) Brünger, A. T. Free R value: A novel statistical quantity for assessing the accuracy of crystal structures. *Nature* **1992**, *355*, 472–475.

(189) Ramachandran, G. N.; Ramakrishnan, C; Sasisekharan, V Stereochemistry of Polypeptide Chain Configurations. *J. Mol. Biol.* **1963**, *7*, 95–99.

(190) Carugo, O.; Djinovic Carugo, K. Half a century of Ramachandran plots. *Acta Crystallogr. Sect. D Biol. Crystallogr.* **2013**, *69*, 1333–1341.

(191) Evans, P.; McCoy, A. An introduction to molecular replacement. *Acta Crystallogr. Sect. D Biol. Crystallogr.* **2007**, *64*, 1–10.

(192) Hersleth, H. P.; Andersson, K. K. How different oxidation states of crystalline myoglobin are influenced by X-rays. *Biochim. Biophys. Acta - Proteins Proteomics* **2011**, *1814*, 785–796.

(193) Weiss, M. S.; Panjikar, S.; Mueller-Dieckmann, C.; Tucker, P. A. On the influence of the incident photon energy on the radiation damage in crystalline biological samples. *J. Synchrotron Radiat.* **2005**, *12*, 304–309.

(194) Wilmot, C. M.; Sjögren, T.; Carlsson, G. H.; Berglund, G. I.; Hajdu, J. Defining redox state of X-ray crystal structures by single-crystal ultraviolet-visible microspectrophotometry. *Methods Enzymol.* **2002**, *353*, 301–318.

(195) O'Neill, P.; Stevens, D. L.; Garman, E. F. Physical and chemical considerations of damage induced in protein crystals by synchrotron radiation: A radiation chemical perspective. *J. Synchrotron Radiat.* **2002**, *9*, 329–332.

(196) Wherland, S.; Pecht, I. Radiation chemists look at damage in redox proteins induced by X-rays. *Proteins Struct. Funct. Bioinforma.* **2018**, *86*, 817–826.

(197) Garman, E. Cool data: Quantity AND quality. *Acta Crystallogr. Sect. D Biol. Crystallogr.* **1999**, *55*, 1641–1653.

(198) Murray, J.; Garman, E. Investigation of possible free-radical scavengers and metrics for radiation damage in protein cryocrystallography. *J. Synchrotron Radiat.* **2002**, *9*, 347–354.

(199) Ravelli, R. B. G.; McSweeney, S. M. The 'fingerprint' that X-rays can leave on structures. *Structure* **2000**, *8*, 315–328.

(200) Burmeister, W. P. Structural changes in a cryo-cooled protein crystal owing to radiation damage. *Acta Crystallogr. Sect. D Biol. Crystallogr.* **2000**, *56*, 328–341.

(201) Weik, M.; Ravelli, R. B.; Kryger, G.; McSweeney, S.; Raves, M. L.; Harel, M.; Gros, P.; Silman, I.; Kroon, J.; Sussman, J. L. Specific chemical and structural damage to proteins produced by synchrotron radiation. *Proc. Natl. Acad. Sci. U. S. A.* **2000**, *97*, 623–628.

(202) Pflugrath, J. W. Practical macromolecular cryocrystallography. *Acta Crystallogr. Sect. F Struct. Biol. Commun.* **2015**, *71*, 622–642.

(203) Carugo, O.; Carugo, K. D. When X-rays modify the protein structure: Radiation damage at work. *Trends Biochem. Sci.* **2005**, *30*, 213–219.

(204) Beitlich, T.; Kühnel, K.; Schulze-Briese, C.; Shoeman, R. L.; Schlichting, I. Cryoradiolytic reduction of crystalline heme proteins: Analysis by UV-Vis spectroscopy and X-ray crystallography. *J. Synchrotron Radiat.* **2007**, *14*, 11–23.

(205) Van Thor, J. J.; Gensch, T.; Hellingwerf, K. J.; Johnson, L. N. Phototransformation of green fluorescent protein with UV and visible light leads to decarboxylation of glutamate 222. *Nat. Struct. Biol.* **2002**, *9*, 37–41.

(206) Garman, E. 'Cool' crystals: Macromolecular cryocrystallography and radiation damage. *Curr. Opin. Struct. Biol.* **2003**, *13*, 545–551.

(207) Zwart, P. H.; Banumathi, S.; Dauter, M.; Dauter, Z. Radiation-damage-induced phasing with anomalous scattering: substructure solution and phasing. *Acta Crystallogr. Sect. D* **2004**, *60*, 1958–1963.

(208) Ravelli, R. B.; Nanao, M. H.; Lovering, A.; White, S.; McSweeney, S. Phasing in the presence of radiation damage. *J. Synchrotron Radiat.* **2005**, *12*, 276–284.

(209) Berglund, G. I.; Carlsson, G. H.; Smith, A. T.; Szöke, H.; Henriksen, A.; Hajdu, J. The catalytic pathway of horseradish peroxidase at high resolution. *Nature* **2002**, *417*, 463–468.

(210) Holton, J. M. A beginner's guide to radiation damage. *J. Synchrotron Radiat.* **2009**, *16*, 133–142.

(211) Ravelli, R. B.; Garman, E. F. Radiation damage in macromolecular cryocrystallography. *Curr. Opin. Struct. Biol.* **2006**, *16*, 624–629.

(212) Nave, C.; Garman, E. F. Towards an understanding of radiation damage in cryocooled macromolecular crystals. *J. Synchrotron Radiat.* **2005**, *12*, 257–260.

(213) Garman, E. F. Radiation damage in macromolecular crystallography : what is it and why should we care ? research papers. *Acta Cryst* **2010**, *66*, 339–351.

(214) Hajdu, J.; Neutze, R.; Sjögren, T.; Edman, K.; Szöke, A.; Wilmouth, R. C.; Wilmot, C. M. Analyzing protein functions in four dimensions. *Nat. Struct. Biol.* **2000**, *7*, 1006–1012.

(215) Halsted, T. P.; Yamashita, K.; Gopalasingam, C. C.; Shenoy, R. T.; Hirata, K.; Ago, H.; Ueno, G.; Blakeley, M. P.; Eady, R. R.; Antonyuk, S. V.; Yamamoto, M.; Hasnain, S. S. Catalytically important damage-free structures of a copper nitrite reductase obtained by femtosecond X-ray laser and room-temperature neutron crystallography. *Int. Union Crystallogr.* **2019**, *6*, 761–772.

(216) Owen, R. L.; Axford, D.; Nettleship, J. E.; Owens, R. J.; Robinson, J. I.; Morgan, A. W.; Dore, A. S.; Lebon, G.; Tate, C. G.; Fry, E. E.; Ren, J.; Stuart, D.; Evans, G. Outrunning free radicals in room-temperature macromolecular crystallography research papers. *Biol. Crystallogr.* **2012**, *D68*, 810–818.

(217) Casadei, C. M.; Gumiero, A.; Metcalfe, C. L.; Murphy, E. J.; Basran, J.; Concilio, M. G.; Teixeira, S. C.; Schrader, T. E.; Fielding, A. J.; Ostermann, A.; Blakeley, M. P.; Raven, E. L.; Moody, P. C. Neutron cryo-crystallography captures the protonation state of ferryl heme in a peroxidase. *Science (80-.).* **2014**, *345*, 193–197.

(218) Howard, E. I.; Sanishvili, R; Cachau, R. E.; Mitschler, A; Chevrier, B; Barth, P; Lamour, V; Van Zandt, M.; Sibley, E; Bon, C; Moras, D; Schneider, T. R.; Joachimiak, A; Podjarny, A. Ultrahigh resolution drug design I: Details of interactions in human aldose reductase-inhibitor complex at 0.66 Å. *Proteins Struct. Funct. Genet.* **2004**, *55*, 792–804.

(219) Schoenborn, B. P. In *Neutron Opt. Devices Appl.* Ed. by Majkrzak, C. F.; Wood, J. L., International Society for Optics and Photonics: 2005; Vol. 1738, pp 192–198.

(220) Hoghoj, P.; Anderson, I.S.; Ebisawa, T.; Takeda, T. Fabrication and performance of a large wavelength band multilayer monochromator. *J. Phys. Soc. Japa* **1996**, *65*, 296–298.

(221) Niimura, N.; Podjarny, A., *Neutron Protein Crystallography: Hydrogen, Protons, and Hydration in Bio-macromolecules*, 2011, pp 1–252.

(222) https://www.ill.eu/users/instruments /instruments-list/ladi-iii/description /instrument-layout/.

(223) Niimura, N.; Karasawa, Y.; Tanaka, I.; Miyahara, J.; Takahashi, K.; Saito, H.; Tsuruno, A.; Matsubayashi, M. An imaging plate neutron detector. *Nucl. Instruments Methods Phys. Res. A* **1994**, 521–525.

(224) Wilkinson, C.; Lehmann, M. S.; Meilleur, F.; Blakeley, M. P.; Myles, D. A. A.; Vogelmeier, S.; Thoms, M.; Walsh, M.; McIntyre, G. J. Characterization of image plates for neutron diffraction. *J. Appl. Crystallogr.* **2009**, *42*, 749–757.

(225) Meilleur, F. Characterization of image plates for neutron diffraction. *J. Appl. Crystallogr.* **2009**, *42*, 749–757.

(226) Cipriani, F; Dauvergne, F; Gabriel, A; Wilkinson, C; Lehmann, M. S. Image plate detectors for macromolecular neutron diffractometry. *Biophys. Chem.* **1994**, *53*, 5–13.

(227) De Hoffmann, E.; Stroobant, V., *Mass Spectrometry Principles and Applications*, Third Ed.; 6; John Wiley & Sons, Ltd: Chichester, UK, 2007; Vol. 29, p 489.

(228) Fenn, J. B.; Mann, M.; Meng, C. K.; Wong, S. F.; Whitehouse, C. M. Electrospray ionization for mass spectrometry of large biomolecules. *Science (80-.).* **1989**, *246*, 64–71.

(229) Brockwell, D; Yu, L; Cooper, S; McCleland, S; Cooper, A; Attwood, D; Gaskell, S. J.; Barber, J Physicochemical consequences of the perdeuteriation of glutathione S-transferase from S. japonicum. *Protein Sci.* **2001**, *10*, 572–80.

(230) Meilleur, F.; Dauvergne, M. T.; Schlichting, I.; Myles, D. A. Production and X-ray crystallographic analysis of fully deuterated cytochrome P450cam. *Acta Crystallogr. Sect. D Biol. Crystallogr.* **2005**, *D61*, 539–544.

(231) Artero, J. B.; Härtlein, M.; McSweeney, S.; Timmins, P. A comparison of refined X-ray structures of hydrogenated and perdeuterated rat γE-crystallin in H2O and D2O. *Acta Crystallogr. Sect. D Biol. Crystallogr.* **2005**, *61*, 1541–1549.

(232) Hanson, B. L.; Schoenborn, B. P.; Tomanicek, S. J.; Chen, J. C.-H.; Langan, P.; John, H.; Blum, M.-M.; Rüterjans, H. X-ray structure of perdeuterated diisopropyl fluorophosphatase (DFPase): perdeuteration of proteins for neutron diffraction. *Acta Crystallogr. Sect. F Struct. Biol. Cryst. Commun.* **2010**, *66*, 379–385.

(233) Howard, E. I.; Blakeley, M. P.; Haertlein, M.; Haertlein, I. P.; Mitschler, A.; Fisher, S. J.; Siah, A. C.; Salvay, A. G.; Popov, A.; Dieckmann, C. M.; Petrova, T.; Podjarny, A. Neutron structure of type-III antifreeze protein allows the reconstruction of AFP-ice interface. *J. Mol. Recognit.* **2011**, *24*, 724–732.

(234) Weber, I. T.; Waltman, M. J.; Mustyakimov, M.; Blakeley, M. P.; Keen, D. A.; Ghosh, A. K.; Langan, P.; Kovalevsky, A. Y. Joint X - ray/Neutron Crystallographic Study of HIV - 1 Protease with Clinical Inhibitor Amprenavir: Insights for Drug Design. *J. Med. Chem.* **2013**, *56*, 5631–5635.

(235) Manzoni, F.; Saraboji, K.; Sprenger, J.; Kumar, R.; Noresson, A. L.; Nilsson, U. J.; Leffler, H.; Fisher, S. Z.; Schrader, T. E.; Ostermann, A.; Coates, L.; Blakeley, M. P.; Oksanen, E.; Logan, D. T. Perdeuteration, crystallization, data collection and comparison of five neutron diffraction data sets of complexes of human galectin-3C. *Acta Crystallogr. Sect. D Struct. Biol.* **2016**, *72*, 1194–1202.

(236) Kelpšas, V.; Lafumat, B.; Blakeley, M. P.; Coquelle, N.; Oksanen, E.; von Wachenfeldt, C. Perdeuteration, large crystal growth and neutron data collection of Leishmania mexicana triose-phosphate isomerase E65Q variant. *Acta Crystallogr. Sect. F Struct. Biol. Commun.* **2019**, *75*, 260–269.

(237) Huynh, K; Partch, C. L. Current Protocols in Protein Science: Analysis of protein stability and ligand interactions by thermal shift assay. *Curr Protoc Protein Sci* **2016**, 1–19.

(238) Bai, N.; Roder, H.; Dickson, A.; Karanicolas, J. Isothermal Analysis of ThermoFluor Data can readily provide Quantitative Binding Affinities. *Sci. Rep.* **2019**, *9*, 1–15.

(239) Steinberg, T. H.; Jones, L. J.; Haugland, R. P.; Singer, V. L. SYPRO orange and SYPRO red protein gel stains: One-step fluorescent staining of denaturing gels for detection of nanogram levels of protein. *Anal. Biochem.* **1996**, *239*, 223–237.

(240) Grøftehauge, M. K.; Hajizadeh, N. R.; Swann, M. J.; Pohl, E. Protein-ligand interactions investigated by thermal shift assays (TSA) and dual polarization interferometry (DPI). *Acta Crystallogr. Sect. D Biol. Crystallogr.* **2015**, *71*, 36–44.

(241) Boivin, S.; Kozak, S.; Meijers, R. Optimization of protein purification and characterization using Thermofluor screens. *Protein Expr. Purif.* **2013**, *91*, 192–206.

(242) Dupeux, F.; Röwer, M.; Seroul, G.; Blot, D.; Márquez, J. A. A thermal stability assay can help to estimate the crystallization likelihood of biological samples. *Acta Crystallogr. Sect. D Biol. Crystallogr.* **2011**, *67*, 915–919.

(243) Piszczek, G.; Lee, J. C.; Tjandra, N.; Lee, C. R.; Seok, Y. J.; Levine, R. L.; Peterkofsky, A. Deuteration of Escherichia coli Enzyme INtralters its stability. *Arch. Biochem. Biophys.* **2011**, *507*, 332–342.

(244) Meilleur, F.; Contzen, J.; Myles, D. A. A.; Jung, C. Structural stability and dynamics of hydrogenated and perdeuterated cytochrome P450cam (CYP101). *Biochemistry* **2004**, *43*, 8744–8753.

(245) http://encorbio.com/protocols/AM-SO4.htm.

(246) Petit-Haertlein, I.; Blakeley, M. P.; Howard, E.; Hazemann, I.; Mitschler, A.; Haertlein, M.; Podjarny, A. Perdeuteration, purification, crystallization and preliminary neutron diffraction of an ocean pout type III antifreeze protein. *Acta Crystallogr. Sect. F Struct. Biol. Cryst. Commun.* **2009**, *65*, 406–409.

(247) Di Costanzo, L.; Moulin, M.; Haertlein, M.; Meilleur, F.; Christianson, D. W. Expression, purification, assay, and crystal structure of perdeuterated human arginase I. *Arch. Biochem. Biophys.* **2007**, *465*, 82–89.

(248) Munshi, P.; Chung, S. L.; Blakeley, M. P.; Weiss, K. L.; Myles, D. A.; Meilleur, F. Rapid visualization of hydrogen positions in protein neutron crystallographic structures. *Acta Crystallogr. Sect. D Biol. Crystallogr.* **2012**, *68*, 35–41.

(249) Cuypers, M. G.; Mason, S. A.; Blakeley, M. P.; Mitchell, E. P.; Haertlein, M.; Forsyth, V. T. Near-atomic resolution neutron crystallography on perdeuterated Pyrococcus furiosus rubredoxin: Implication of hydronium ions and protonation state equilibria in redox changes. *Angew. Chemie - Int. Ed.* **2013**, *52*, 1022–1025.

(250) Hazemann, I.; Dauvergne, M. T.; Blakeley, M. P.; Meilleur, F.; Haertlein, M.; Van Dorsselaer, A.; Mitschler, A.; Myles, D. A. A.; Podjarny, A. High-resolution neutron protein crystallography with radically small crystal volumes: Application of perdeuteration to human aldose reductase. *Acta Crystallogr. Sect. D Biol. Crystallogr.* **2005**, *61*, 1413–1417.

(251) Evans, P. In *Acta Crystallogr. Sect. D Biol. Crystallogr.* International Union of Crystallography: 2006; Vol. 62, pp 72–82.

(252) French, B. Y. S.; Wilson, K. On the Treatment of Negative Intensity Observations. *Acta Cryst* **1978**, *A34*, 517–525.

(253) Collaborative Computational Project, N. The CCP4 suite: Programs for protein crystallography. *Acta Crystallogr. Sect. D Biol. Crystallogr.* **1994**, *50*, 760–763.

(254) Evans, P. R.; Murshudov, G. N. How good are my data and what is the resolution? *Acta Crystallogr. Sect. D Biol. Crystallogr.* **2013**, *69*, 1204–1214.

(255) Adams, P. D. et al. PHENIX: A comprehensive Python-based system for macromolecular structure solution. *Acta Crystallogr. Sect. D Biol. Crystallogr.* **2010**, *66*, 213–221.

(256) Moriarty, N. W.; Grosse-Kunstleve, R. W.; Adams, P. D. Electronic ligand builder and optimization workbench (eLBOW): A tool for ligand coordinate and restraint generation. *Acta Crystallogr. Sect. D Biol. Crystallogr.* **2009**, *65*, 1074–1080.

(257) Hurst, D. T.; Griffiths, E.; Vayianos, C. Inhibition of Uricase by Pyrimidine and Purine Drugs. **1985**, *18*.

(258) Zeldin, O. B.; Gerstel, M.; Garman, E. F. Optimizing the spatial distribution of dose in X-ray macromolecular crystallography. *J. Synchrotron Radiat.* **2013**, *20*, 49–57.

(259) Liebschner, D.; Afonine, P. V.; Moriarty, N. W.; Adams, P. D. Evaluation of models determined by neutron diffraction and proposed improvements to their validation and deposition research papers. **2018**, 800–813.

(260) O'Dell, W. B.; Bodenheimer, A. M.; Meilleur, F. Neutron protein crystallography: A complementary tool for locating hydrogens in proteins. *Arch. Biochem. Biophys.* **2016**, *602*, 48–60.

(261) Kovalevsky, A.; Gerlits, O.; Beltran, K.; Weiss, K. L.; Keen, D. A.; Blakeley, M. P.; Louis, J. M.; Weber, I. T., *Proton transfer and drug binding details revealed in neutron diffraction studies of wild-type and drug resistant HIV-1 protease*, 1st ed.; Elsevier Inc.: 2020, pp 1–23.

(262) Dajnowicz, S.; Seaver, S.; Hanson, B. L.; Fisher, S. Z.; Langan, P.; Kovalevsky, A. Y.; Mueser, T. C. Visualizing the Bohr effect in hemoglobin: Neutron structure of equine cyanomethemoglobin in the R state and comparison with human deoxyhemoglobin in the T state: Neutron. *Acta Crystallogr. Sect. D Struct. Biol.* **2016**, *72*, 892–903.

(263) Gerlits, O.; Weiss, K. L.; Blakeley, M. P.; Veglia, G.; Taylor, S. S.; Kovalevsky, A. Zooming in on protons: Neutron structure of protein kinase A trapped in a product complex. *Sci. Adv.* **2019**, *5*, 1–11.

(264) https://web.expasy.org/protparam/.